Uncertainty Quantification and Personalisation of Lumped Parameter Models of the Cardiovascular System

Harry Saxton

Supervisor: Dr. Xu Xu,
Dr. Torsten Schenkel,
Prof. Ian Halliday

A thesis submitted in partial fulfilment of the requirements of Sheffield Hallam University for the degree of
Doctor of Philosophy

January 2025

Declaration

I hereby declare that:

1. I have not been enrolled for another award of the University, or other academic or professional organisation, whilst undertaking my research degree.
2. None of the material contained in the thesis has been used in any other submission for an academic award.
3. I am aware of and understand the University's policy on plagiarism and certify that this thesis is my own work. The use of all published or other sources of material consulted have been properly and fully acknowledged.
4. The work undertaken towards the thesis has been conducted in accordance with the SHU Principles of Integrity in Research and the SHU Research Ethics Policy.
5. The word count of the thesis is 50,743.

Name	Harry Saxton
Award	Doctor of Philosophy
Date of Submission	September 2024
Research Institute	Materials and Engineering Research
Director of Studies	Dr. Torsten Schenkel

Harry Saxton
January 2025

To Millie, mum and nan.

Acknowledgements

I feel honoured by the level of support I have received during my PhD.

Xu Xu – You have been the true director and guardian of this project. Your generosity and warmness that you have shown be during this PhD will be a skill I aim to pass down some day. Both as a researcher and as a person, I have grown tenfold thanks to your guidance and unwavering support. I feel incredibly fortunate to have worked with you, and I hope this collaboration continues for many years to come.

Ian Halliday – My academic inspiration. Your steadfast support and dedication to ensuring I never felt isolated or inadequate is a quality I will carry forward throughout my academic career. Your relentless pursuit of answers, coupled with a deep understanding, speaks volumes about your calibre as a scientist. After all, "*The main thing is the main thing*". I owe many of my professional connections and collaborations to you, and I firmly believe the foundation you have provided will shape the rest of my journey – *sic infit*.

Torsten Schenkel – The computational king. Without your guidance and encouragement to explore new areas, I would never have discovered my second love, "Julia", and my knowledge of computational science would be far more limited. Your ability to ask the critical questions that highlight new directions is truly inspiring, and I can only aspire to achieve the same.

I must also express my gratitude to the institutions that have supported me throughout this journey. Firstly, the Materials and Engineering Research Institute, particularly Francis Clegg and Chris Sammon. Despite the constraints you often faced, you always acted in the best interests of the department and its students. A special mention goes to David Asquith, who, while not part of my supervisory team, often offered me a fresh perspective on academic life and many enjoyable Wednesday evenings.

I also extend my thanks to the University of Sheffield Medical School. The department's strong commitment to impactful research and its infectious enthusiasm have been invaluable.

I am especially grateful to Daniel Taylor, who has given me a renewed appreciation for medical sciences and has consistently asked the most relevant questions to ensure our work is truly translational. Long may our collaboration continue. My final thanks go to the Sano Centre for Computational Personalised Medicine for providing the computational resources necessary for this work and for allowing me to contribute to numerous exciting projects.

My journey through this PhD would have been far more difficult without the support of my friends Kristian Haverson, Joel Hirst, and Raphael Fortulan. Although we are a diverse group of scientists, some of my best memories are with you – whether it be our lunch dates, Thursday celebrations, or chocolate orange at the pub. These are the moments I will cherish for the rest of my life, and I hope our friendship endures.

I cannot overlook my mother. I am forever indebted to you for instilling in me a relentless work ethic and the values that guide my life. Your respect for my passion and your refusal to impose any particular ideology on the direction my life should take mean more to me than words can express.

My final thanks go to my love, Millie Houlton. Your constant love and support have allowed me to pursue my dreams, and you know how much that means to me. I thank you eternally for your patience and unwavering optimism for the future. I am truly a lucky man.

Harry Saxton

Advanced Studies

Publications

Published

- **Saxton, H**., Xu, X., Schenkel, T., Clayton, R. H., & Halliday, I. (2024). Convergence, sampling and total order estimator effects on parameter orthogonality in global sensitivity analysis. *PLOS Computational Biology*, 20(7), e1011946.

- Taylor, D. J., **Saxton, H**., Halliday, I., Newman, T., Hose, D. R., Kassab, G. S., ... & Morris, P. D. (2024). A systematic review and meta-analysis of Murray's Law in the Coronary Arterial Circulation. *American Journal of Physiology-Heart and Circulatory Physiology*.

- **Saxton, H**., Xu, X., Schenkel, T., & Halliday, I. (2024). Assessing input parameter hyperspace and parameter identifiability in a cardiovascular system model via sensitivity analysis. Journal of Computational Science, 79, 102287.

- Tlałka, K., **Saxton, H**., Halliday, I., Xu, X., Taylor, D., Narracott, A., & Malawski, M. (2024, June). Local Sensitivity Analysis of a Closed-Loop in Silico Model of the Human Baroregulation. *In International Conference on Computational Science* (pp. 173-187). Cham: Springer Nature Switzerland.

- Taylor, D. J., **Saxton, H**., Halliday, I., Newman, T., Feher, J., Gosling, R., ... & Morris, P. D. (2024). Evaluation of models of sequestration flow in coronary arteries—Physiology versus anatomy?. *Computers in Biology and Medicine*, 173, 108299.

- Tristano, M., Lenzo, B., **Saxton, H**., Xu, X., & Zhang, X. (2023, August). Physics-Infused Neural Network-Driven Investigation of Vehicle Sideslip Angle. In The IAVSD International Symposium on Dynamics of Vehicles on Roads and Tracks (pp. 358-365). Cham: Springer Nature Switzerland.

- **Saxton, H**., Schenkel, T., Halliday, I., & Xu, X. (2023). Personalised parameter estimation of the cardiovascular system: Leveraging data assimilation and sensitivity analysis. *Journal of Computational Science*, 74, 102158.

- Schenkel, T., **Saxton, H.** (2023). Circulatory System Models (v0.3.1). Zenodo. https://doi.org/10.5281/zenodo.10428848

Under Review

- Talka, K., **Saxton, H**., Taylor, D., Xu, X., Narracott, A., Hose, D. R., Morris, P., Malawski, M., Halliday, I. (2024). Sensitivity Analysis of One-Chamber and Four-Chamber Models with Baroreflex. Target journal: *Plos Computational Biology*

- Otta, M., **Saxton, H**., Halliday, I., Kica, P., Tsui, S.Lim, C., Malawski, M., J., Narracott, A. (2024). Sensitivity analysis of a 0D model of lower limb hæmodynamics. Target journal: *International Journal for Numerical Methods in Biomedical Engineering*

- **Saxton, H**., Taylor, D., Xu, X., Narracott, A., Czechowicz, K., Newman, T., Gosling, R., Hose, D. R., Hellevik, L. R., Halliday, I., Gunn, J., Morris, P. (2024). Derivation and Sensitivity Analysis of a Novel One-Dimensional Model of Coronary Blood Flow Accounting for Vessel Taper & Boundary Slip. Target journal: *Computer Methods and Programs in Biomedicine*

- **Saxton, H**., Taylor, D., Halliday, I., Newman, T., Schenkel, T., Morris, P., Clayton, R., Xu, X. (2024). The impact of experimental designs & system sloppiness on the personalisation process: A cardiovascular perspective. *Computers in Biology and Medicine*

Abstract

Personalised medicine, facilitated by the growing capacity to collect comprehensive patient data, aims to provide personalised therapies for each individual. Computational models are boosting the capacity to draw diagnosis and prognosis, and future treatments will be tailored not only to current health status and data, but also to an accurate projection of the pathways to restore health by model predictions. These models, which are based on physiology and physics rather than on population statistics, enable computational simulations to reveal diagnostic information that would have otherwise remained concealed and to predict treatment outcomes for individual patients. The inherent need for patient-specific models in cardiology is clear and is driving the rapid development of tools and techniques for creating personalised methods to guide pharmaceutical therapy, deployment of devices and surgical interventions.

For computational models to have clinical utility, we must be able to provide a quantification of the risk associated with any predictions or interpretations which are made from the model. Lumped parameter models (LPM) represent the cardiovascular system as a series of electrical segments, each characterised by parameter values that offer insights into the associated health status. Given one can constrain the model with patient specific data such that the parameter values are updated, one obtains a digital representation of a patient's cardiovascular system.

This research investigates the crucial offline stage of uncertainty quantification for models, primarily employing sensitivity analysis, with the goal of achieving personalisation. As such, this work first examines the process of performing a global sensitivity analysis of a cardiovascular LPM, establishing some best practices to ensure accurate model interpretations. Then we assess the impact of the chosen outputs of a model when looking to quantify uncertainty. We demonstrate how variation in the chosen outputs can significantly impact one's interpretation of a model. Following the enhanced understanding of the best practices around sensitivity analysis, we extend a method for obtaining a personalised subset of input parameters, acknowledging the inherent variability among individuals in medicine. Alongside this, a novel examination of the sensitivity indices is proposed within the context of personalised medicine to provide insight associated with the calibration of model parameters. Finally, we investigate a data assimilation technique and explore the method's effectiveness for model personalisation. The primary outcome of this research is the development of an offline model personalisation workflow, designed to reduce the uncertainty associated with calibrating models to patient data to the greatest extent possible.

Table of contents

List of figures

List of tables

Nomenclature

S	Sensitivity Matrix
τ	Heart Cycle length
$\underline{\theta}$	System input parameters
$S_{H,i}$	Higher order sensitivity indices for input parameter i
S_i	First order sensitivity indices for input parameter i
$S_{T,i}$	Total order sensitivity indices for input parameter i
CFD	Computational Fluid Dynamics
CV	Cardiovascular
CVS	Cardiovascular System
ep	End Diastolic/Pulse time
es	End Systolic time
FIM	Fisher Information Matrix
GPU	Graphics Processing Unit
GRV	Gaussian Random Variable
GSA	Global Sensitivity Analysis
la	Left Atrium
LPM	Lumped Parameter Model

LSA	Local Sensitivity Analysis
lv	Left Ventricle
m	Number of model outputs
n	Number of input parameters
pas	Pulmonary Sinus
pat	Pulmonary Arteries
pvb	Pulmonary Vascular Bed
pv	Pulmonary Veins
ra	Right Atrium
rv	Right Ventricle
sas	Systemic Sinus
sat	Systemic Arteries
svb	Systemic Vascular Bed
sv	Systemic Veins
V_s	Stressed Blood Volume
V_T	Total Blood Volume
V_u	Unstressed Blood Volume

Chapter 1

Introduction

Above all, don't lie to yourself.
FYODOR DOSTOYEVSKY, The Brothers Karamazov

Summary
This chapter introduces and surveys cardiovascular physiology and describes the concept of personalised medicine. Section 1.1 provides a brief overview of the vasculature and the heart, describes the volume and pressure distributions in the body and the phases of the cardiac cycle. Section 1.2 reviews a standard clinical workflow, typical cardiovascular research methodologies and begins to formulate a commentary on the role of personalised medicine. Then in section 2.3 we state the main aims and contributions of this work and, to finish section 1.3 provides an outline of the future chapters.

1.1 The Cardiovascular System

The cardiovascular system comprises the heart, the systemic (oxygen rich blood) and pulmonary circulation (deoxygenated blood) as displayed in figure 1.1. Blood vessels are grouped into three categories: arteries, capillaries, and veins. Arteries carry oxygenated blood from the left heart to the organs, veins carry deoxygenated blood back from the organs to the right heart, and the capillaries connecting the arteries and veins facilitate the exchange of oxygen and carbon dioxide [23]. The circulatory system also transports nutrients and metabolites through the blood. The major blood vessels can be grouped as follows

1. **Systemic Arteries**: Transport oxygenated blood from the left side of the heart to the organs both lower and upper body. The main systemic artery is the aorta.
2. **Systemic Capillaries**: Facilitate the exchange of oxygen in the blood for carbon dioxide generated by the tissue.
3. **Systemic Veins**: Transport the now deoxygenated carbon dioxide rich blood back to the right side of the heart. The aggregation systemic veins is the venae cavae.
4. **Pulmonary Arteries**: Transport the deoxygenated blood from the right ventricle into the lungs.
5. **Pulmonary Capillaries**: Facilitate gaseous exchange between the alveoli of the lungs and the blood in the pulmonary capillaries, leading to re-oxygenated blood.
6. **Pulmonary Veins**: Move the blood from the lungs and drain into the left atria for redistribution around the body.

1.1.1 The Heart

The heart is a muscular, periodic pump, driven by mechanical, electrical and chemical processes, that generates the pressure needed to drive blood through the circulatory system. It is located between the lungs, slightly left of the sternum, and surrounded by the pericardium membrane [24]. We will discuss in the below sections, a few relevant internal anatomical features of the heart, including the walls, the arteries which provide blood to the muscle, chambers, and valves.

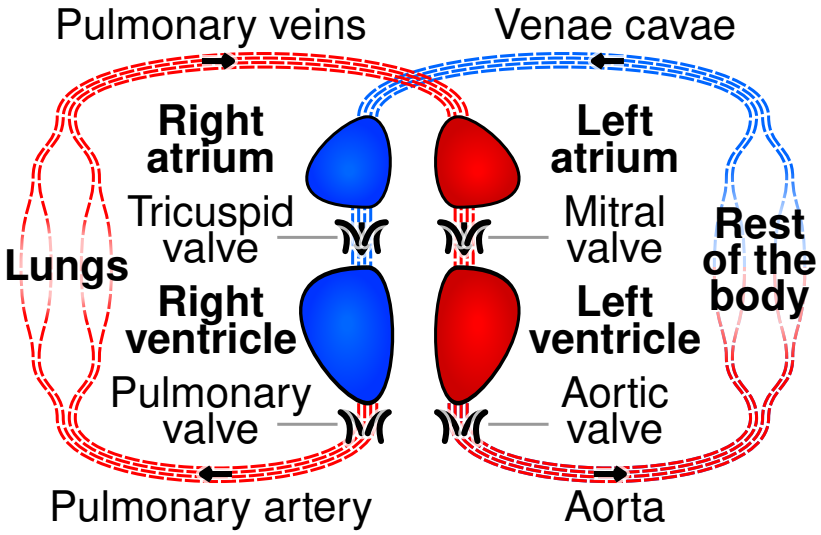

Fig. 1.1 **The human vasculature**: Schematic of the human vascular system displaying both the systemic (red) and pulmonary (blue) circulations. Reproduced from [1].

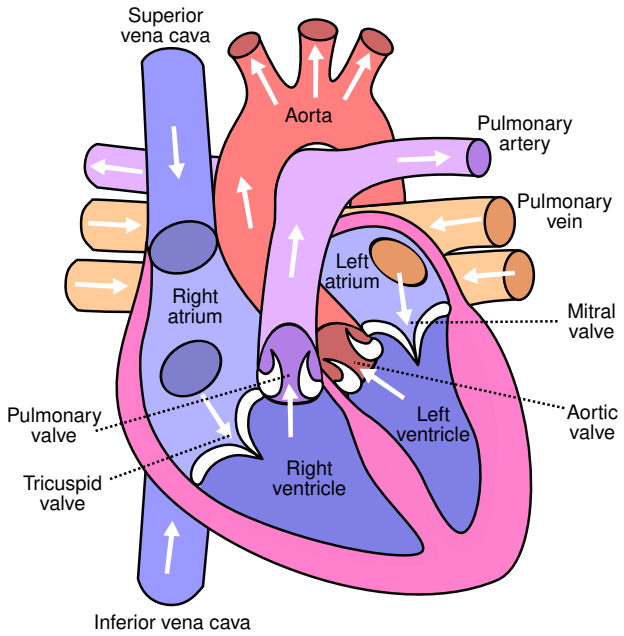

Fig. 1.2 **The human heart**: Diagram highlighting the main heart chambers, valves and veins. Reproduced from [2].

1.1.1.1 Cardiac Tissue

The heart's walls, delineating its four chambers, consist of cardiac muscle tissue, which rhythmically contracts and relaxes to propel blood throughout the body. Structurally, these walls consist of three distinct layers: the epicardium, myocardium, and endocardium. Starting from the outside, the epicardium forms the innermost layer of the pericardium and the outer surface of the heart. Comprised of mesothelial cells, fat, and connective tissue, it provides protection and support to the heart. Next, the myocardium, situated in the middle and being the thickest layer, is predominantly composed of cardiac muscle cells and fibroblasts. Its pivotal role lies in contracting and relaxing, to modulate ventricular volume, thereby facilitating blood circulation throughout the body. The innermost layer, the endocardium, is constituted of endothelial cells and subendothelial connective tissue layers. It lines the four heart chambers and extends over the valves, ensuring smooth blood flow within the heart. Notably, the ventricles have thicker walls compared to the atria, owing to their heightened workload necessitated for generating blood pressure [25]. Among the ventricles, the left ventricle possesses the most robust muscular wall, reflecting its increased workload in pumping blood through the systemic circulation.

1.1.1.2 Coronary Arteries

Coronary arteries supply blood to the heart muscle (see figure 1.3). Like all other tissues in the body, the heart muscle needs oxygen-rich blood to function. Also, oxygen-depleted blood must be carried away. The coronary arteries wrap around the outside of the heart. Small branches dive into the heart muscle to bring it blood. There are two main coronary arteries - the left and right main coronary arteries. The left main coronary artery supplies blood to the left side of the heart muscle (the left ventricle and left atrium). The left main coronary divides into branches: The left anterior descending artery branches off the left coronary artery and supplies blood to the front of the left side of the heart. The circumflex artery branches off the left coronary artery and encircles the heart muscle. This artery supplies blood to the outer side and back of the heart. The right coronary artery supplies blood to the right ventricle and atrium. The right coronary artery divides into smaller branches, including the right posterior descending artery and the acute marginal artery. Together with the left anterior descending artery, the right coronary artery helps supply blood to the middle or septum of the heart [26]. Since coronary arteries deliver blood to the heart muscle, any coronary artery disorder or disease can have serious implications by reducing the flow of oxygen and nutrients to the heart muscle.

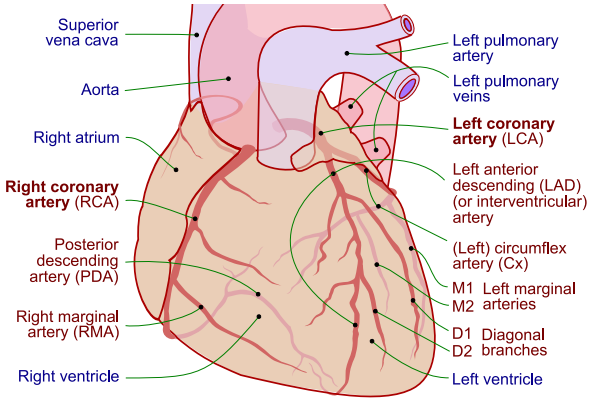

Fig. 1.3 **The coronary arteries**: Diagram highlighting the main coronary arteries of the heart. Reproduced from [3].

1.1.1.3 Heart Chambers

The heart has four chambers; the left and right atria, and the left and right ventricles. The atria are responsible for the filling of the ventricles, where as the ventricles, which operate at a higher pressure, are responsible for the distribution of blood. The septum is a wall of muscular tissue (often considered part of the left ventricle), which separates the deoxygenated blood on the right side of the heart and the oxygenated blood on the left side [27]. As seen in figure 1.1 and 1.2, flow into and out of the two ventricles is facilitated by four heart valves: the tricuspid, mitral, pulmonary, and aortic valves.

1.1.1.4 Heart Valves

To understand the flow characteristics of valves, one must begin with some appreciation of their anatomy and physiology.

Atrioventricular valves, mitral and tricuspid, control flow between the atria and ventricles, while semi-lunar valves, aortic and pulmonary, control flow between the ventricles and the aortic and main pulmonary artery. The valves, shown in figure 1.2, act like trap doors, with opening and closing controlled by pressure differentials. In this manner, the valves only allow blood to flow in one direction. However, in reality back flow of the blood is observed in a healthy patient due to the dynamics of the valve, if there is large amounts of back flow this is often associated with pathophysiology.

Atrioventricular valves: The tricuspid valve, located between the right atrium and right ventricle, consists of three cusps (leaflets) known as the anterior, septal, and posterior cusps.

The tricuspid and mitral valves open when the pressure in the right atria exceeds the right ventricular pressure. The mitral valve, located between the left atrium and left ventricle, consists of only two cusps, anterior and posterior, and is commonly referred to as the bi-cuspid valve. Fibrous ligaments secure the two atrioventricular valves called the chordae tendineae, originating from the papillary muscles on the ventricles' inner surface. During ventricular ejection, the cusps are closed shut, and the papillary muscles contract, securing the cusps from collapsing into the atria [28].

Semi-lunar valves: The pulmonary valve is between the right ventricle and the main pulmonary artery. The pulmonary valve consists of three cusps, the left, right, and anterior cusps. The aortic valve is between the left ventricle and the aorta and consists of three cusps: the left, right and posterior. Unlike the atrioventricular valves, the semi-lunar valves have no chordae tendineae. Instead, the valves are attached to the wall of their corresponding artery and close when the arterial pressure exceeds the ventricular pressure. Thus, open when the pressure in the ventricles exceeds the pressure in the arteries [29].

1.1.2 Volume Distribution

For a healthy adult, the total blood volume is roughly 5 L. Approximately 1 L is in the systemic arteries, 3.5 L in the systemic veins, and 0.5 L in the pulmonary circulation. The total blood volume cannot be easily measured but can be variously estimated from e.g. Hidalgo's formula [30], Nadlers' formula or using Du Bois' [31] definition of body surface area [32, 33].

$$V_{T,H} = \begin{cases} 24.637h^{0.725}w^{0.425} - 1954 \text{ (ml)}, \text{ if male} \\ 23.359h^{0.725}w^{0.425} - 1229 \text{ (ml)}, \text{ if female} \end{cases} \tag{1.1}$$

$$V_{T,N} = \begin{cases} 0.3668h^3 + 0.03219w + 0.6041 \text{ (ml)}, \text{ if male} \\ 0.3561h^3 + 0.03308w + 0.1833 \text{ (ml)}, \text{ if female.} \end{cases} \tag{1.2}$$

Where $V_{T,H}$ and $V_{T,N}$ represent total blood volume, in millilitres (ml), when using the Hidalgo and Nadler formula respectively. Height h is expressed in centimetres (cm) and weight w in kilogram (Kg). Of course, processes like capillary filtration and excretion mean that total blood volume is not conserved on intermediate timescales but for most modelling applications - certainly those considered in this work - it is.

The portion of total blood volume (V_T) that exerts a force on, and causes the stretching, of vessel walls is known as the stressed blood volume (V_s). The remaining volume inside a vessel or heart chamber is denoted the unstressed blood volume V_u. The two quantities are related as follows [34]:

$$V_T = V_s + V_u. \tag{1.3}$$

It is not possible to compare stressed and unstressed volumes by measurements and significant variation exists in determining values. Here, we try to maintain physiological relationships between blood volume [35, 36] where possible, as shown in table 1.1.

Table 1.1 **Human blood distributions**: Total blood volume distributions and stressed volumes in the cardiovascular system. The stressed blood volume percentage is displayed as the percentage of the total blood volume of a compartment.

Blood Vessel	Total Blood Volume (ml)	Stressed Blood Volume (ml)
Systemic Arteries	13%	27%
Systemic Veins	65%	7.5%
Pulmonary Arteries	3%	58%
Pulmonary Veins	11%	11%
Left Atrium	1.5%	62%
Left Ventricle	2.5%	70%
Right Atrium	1.5%	62%
Right Ventricle	2.5%	70%

1.1.3 Blood Pressure

Blood pressure is determined by the amount of stressed blood volume flowing through a vessel or heart chamber and the chambers ability to extend and increase volume, without increased resistance, this is known as **vessel compliance**. In physiology, blood pressure is stated in mmHg (1mmHg = 133.322 Pa = 0.00075 dyne/cm^2). Pressure waves generated by the left and right sides of the heart are propagated throughout the circulatory system all the way to the veins and thus the high pressure waves found in the heart suffer high dissipation thus pressure in the veins is minimal. Example profiles in different parts of the circulatory system are shown in figure 1.4, depicting the approximate maximum and minimum pressures in the *pulse wave* throughout the cardiac cycle. Broadly, the systemic arteries exhibit the largest pressures at approximately 120 mmHg in brachial systole and 80 mmHg in brachial diastole, for a healthy young person. In fact, the pulse wave sharpens like a breaking ocean gravity wave, as it propagates with the result that brachial systolic pressure actually peaks

higher than central aortic systolic pressure. The pressure drops nearly to absolute zero as blood passes through the arterioles passing the capillaries, venules, and veins. The maximum pressure in the right ventricle is about 25 mmHg and remains low, with maximum and minimum pressures in the pulmonary arteries at approximately 30 mmHg and 10 mmHg, respectively. Pulmonary capillary and venous pressures are also near zero; pressure begins to rise in the left ventricle to approximately 120 mmHg [37].

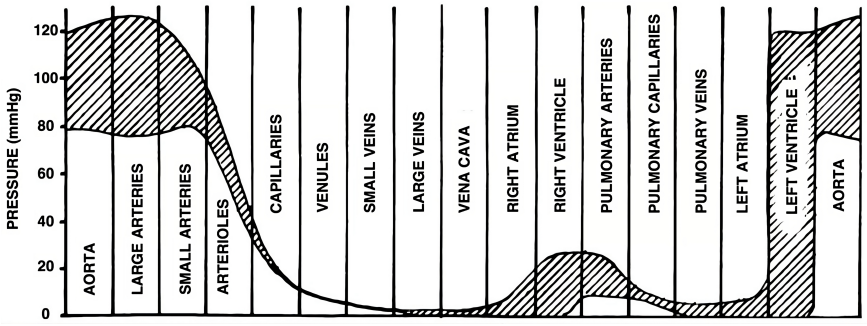

Fig. 1.4 **Cardiovascular pressure profiles**: Pressure profiles across the main blood vessels and chambers. The shaded regions represent the pressure ranges founded in such vessels. Reproduced with permission from [4].

1.1.4 The Cardiac Cycle

A cardiac cycle is defined by pressure and volume changes occurring during systole, the contraction phase, and diastole, the relaxation phase of the heart. The blood is pumped out of the heart at very high pressure, approximately 120 mmHg, and transported through the arteries to the capillaries for oxygen and nutrients exchange. The cardiac output (or blood flow) is about 5L/min, i.e., the total blood volume is pumped through the body in about 1 minute. The duration of the cardiac cycle is the reciprocal of the heart rate,

$$\text{Duration}\left(\text{s/beat}\right) = \frac{60\left(\frac{\text{s}}{\text{min}}\right)}{\text{HR}\left(\frac{\text{beats}}{\text{min}}\right)}. \tag{1.4}$$

The opening and closing of the valves delimit the four main phases of the cardiac cycle. These four phases from the point of view of the ventricles are defined in [5] as:

1. **Inflow Phase**: When the atrioventricular valve is open, and the semilunar valve is closed.

2. **Isovolumetric contraction:** When both valves are closed, there is no blood flow, but ventricular pressure increases.

3. **Outflow Phase:** When the semilunar valve is open and the atrioventricular valve is closed.

4. **Isovolumetrtic Relaxation:** When both valves are closed, there is no blood flow, but ventricular pressure decreases.

Isovolumetric contraction and outflow phases correspond to systole while the inflow and isovolumetric relaxation phases correspond to diastole. Maximum and minimum blood pressures correlate with systole and diastole phases of the cardiac cycle.

As shown in figure 1.5 (which is a form of the famous Wigger's diagram [38]), the cardiac cycle begins at diastole with the atrioventricular (AV) valves (mitral and tricuspid) opening and ventricular volume increasing rapidly, beginning the inflow phase. While the AV valves are still open, the ventricle continues to fill with atrial contraction ejecting more blood at the end of the filling. Then the AV valves close. With both the AV and semi-lunar (SL) (aortic and pulmonary) valves shut, isovolumetric contraction begins and the ventricular pressure increases rapidly. When, the ventricular pressure exceeds arterial pressure this triggers the opening of the SL valves. The ventricles begin ejecting blood, beginning the outflow phase, into the aorta and main pulmonary artery. Ventricular pressure continues rising throughout this phase since contraction is still occurring. When arterial pressures exceed ventricular pressure, the SL valves close. Isovolumetric relaxation also begins, with both sets of valves shut, here the ventricular pressure decreases rapidly, and the cycle repeats itself.

1.2 Personalised Medicine

1.2.1 Standard Clinical Diagnosis

Providing accurate and accessible diagnoses is a fundamental challenge for global healthcare systems. In the UK alone an estimated 5% of outpatients receive the wrong diagnosis every year [39]. These errors are particularly common when diagnosing patients with serious medical conditions, with an estimated 20% of these patients being misdiagnosed at the level of primary care and one in three of these misdiagnoses resulting in serious patient harm [40]. In medicine, a substantial bumper of decisions are made based on statistical and numerical data. To make a diagnosis, prescribe a treatment or a medical procedure, or evaluate a prognosis, clinicians have to reason and decide based on parameters such as disease prevalence, test results, cost/benefit ratio of each intervention, etc [41]. Thus, one

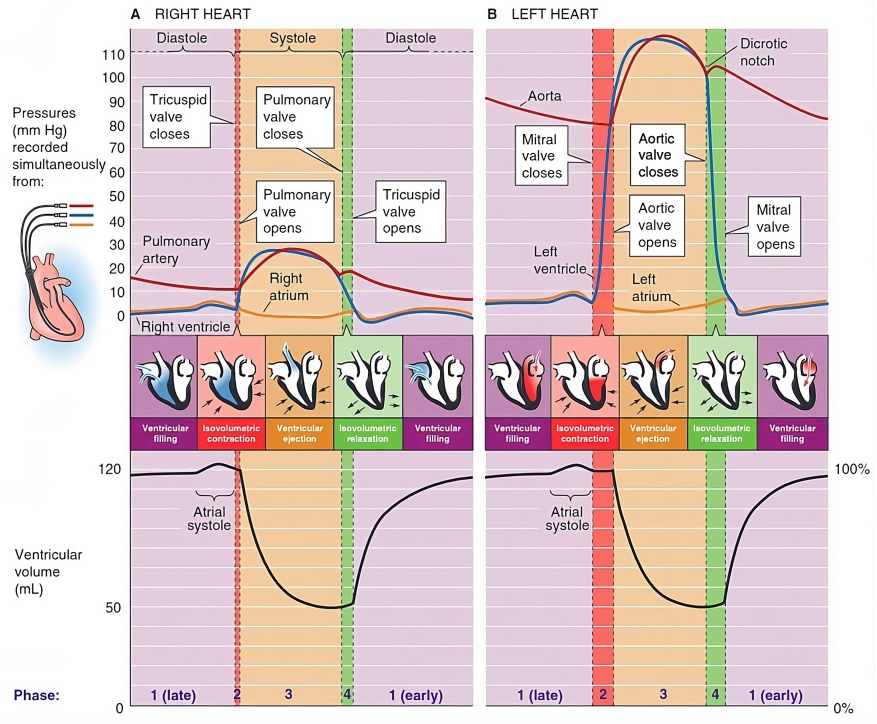

Fig. 1.5 **The cardiovascular cycle**: Arterial, atrial, and ventricular pressures and ventricular volumes during the cardiac cycle. (A) Right heart. (B) Left heart. Ventricular pressures (blue lines) rise during isovolumetric contraction exceeding atrial pressures (orange lines), initiating the opening of the semi-lunar valves. Arterial pressures (red lines) rise during ventricular ejection and then decrease below ventricular pressure, causing the semi-lunar valves to shut and begin isovolumetric relaxation. AV valves open once atrial pressures exceed ventricular pressure. Reproduced with permission from [5].

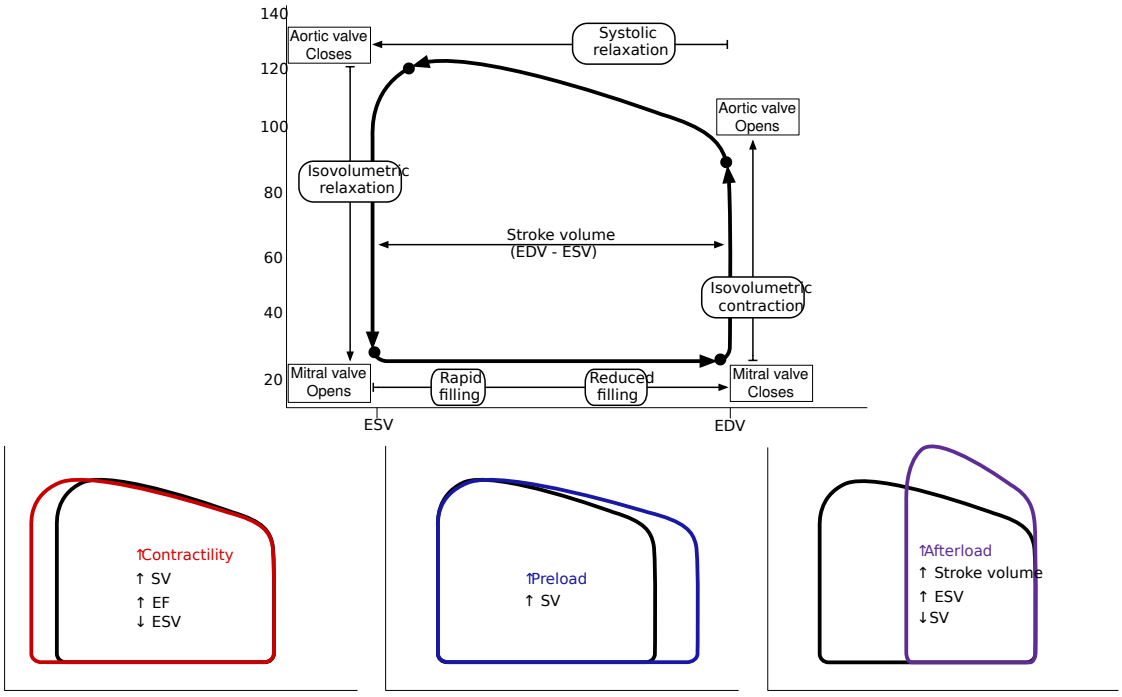

Fig. 1.6 **A pressure-volume relationship**: This diagram illustrates the four phases of the cardiac cycle: (1) isovolumetric contraction, (2) systolic relaxation, (3) isovolumetric relaxation, and (4) diastolic filling (comprising rapid filling and reduced filling phases). Key events such as the opening and closing of the mitral and aortic valves are indicated. The loop demonstrates the relationship between left ventricular pressure and volume throughout the cardiac cycle. End-systolic volume (ESV) and end-diastolic volume (EDV) are marked, with the difference representing the stroke volume (SV). The figure also depicts how changes in contractility, preload, and afterload affect the PV loop. Increased contractility results in increased SV, decreased ESV, and increased ejection fraction (EF). Increased preload leads to increased stroke volume. Increased afterload causes decreased stroke volume and increased end-systolic volume. Reproduced with permission from [6].

of the biggest challenges is how to translate a knowledge of pathophysiology into clinical decision-making that prioritises the patient above the clinician or service. Initially this is accomplished by matching the patient's presenting problem to the best fit condition, known to the doctor.

Thus, a typical diagnostic process proceeds as follows [42]: First, a patient experiences a health problem. The patient is likely the first person to consider their symptoms and may choose at this point to engage with the health care system. Once a patient seeks health care, there is an iterative process of information gathering, information integration and interpretation, and determining a working diagnosis. Reviewing a clinical history and performing an interview, conducting a physical exam, performing diagnostic testing, and referring or consulting with other clinicians are all ways of accumulating information that may be relevant to understanding a patient's health problem. Different information-gathering approaches can be employed at different times, and diagnostic information can be obtained in different orders. Such an iterative process of information gathering, integration, and interpretation involves hypothesis generation (and rejection) and the clinician drawing on their experience of examining previous patients with similar conditions and the statistical success rate of interventions.

The working diagnosis may be either a list of potential diagnoses (a differential diagnosis) or a single diagnosis. Typically, clinicians will consider more than one diagnostic hypothesis or possibility as an explanation of the patient's symptoms and refine this list as further information is obtained in the diagnostic process. As the diagnostic process proceeds, a fairly broad list may be narrowed into fewer options. As the list is narrowed to one or two possibilities, refinement of the working diagnosis transitions to diagnostic verification, in which the lead diagnosis is checked for its adequacy in explaining the signs and symptoms, its coherency with the patient's context (physiology, risk factors), and whether a single diagnosis is appropriate. When considering invasive or risky diagnostic testing or treatment options, the diagnostic verification step is particularly important to avoid exposure to these risk without a reasonable chance that the testing or treatment options will be informative improve patient outcomes.

Throughout the diagnostic process, there is an ongoing assessment of whether sufficient information has been collected. If the diagnostic team members are not satisfied that the necessary information has been collected or that the information available is not consistent with a diagnosis, then the process of information gathering, information integration and interpretation, and developing a working diagnosis continues. When the diagnostic team

members judge that they have arrived at an accurate and timely explanation of the patient's health problem, they communicate that explanation to the patient as the diagnosis.

1.2.2 Cardiovascular Research

Perhaps more than other fields of medicine, cardiovascular research involves experimental studies with mathematical/computational modelling studies. While models are derived (typically from physical and physiological principles), using mathematics, the final equations which express the model are rarely amenable to analytical solution. This necessitates the use of computational methods to solve the equations numerically. Accordingly, we will use the term "computational" henceforth.

Cardiovascular research is dominated by three classes of investigation: *in-silico* studies [43], which are conducted on mathematical models of cardiovascular systems, and *in-vivo* studies [44], which are carried out in animal and human bodies. In *in-silico* studies, mathematical models of various dimensions are developed conceptually to mimic cardiovascular function, aiding the fundamental study of blood flow physics. Examples of this type of research include pulse wave dynamics simulations, whole heart modelling, full body circulation dynamics, and the evaluation of cardiac assist devices for mechanical circulation support [45–48]. *In-vitro* cardiovascular research involves studying cardiovascular systems in controlled laboratory environments outside of a living organism. This approach typically uses biological samples, such as heart cells or blood vessel tissues, grown in culture or tissue-engineered models. By simulating physiological conditions, *in-vitro* research allows scientists to investigate heart functions, test responses to drugs, and understand disease mechanisms, providing valuable insights that can lead to improved treatments and therapies without immediate risks to living subjects. While *in-silico* & *in-vitro* studies provide significant quantitative insights into cardiovascular physiology, the current gold standard of cardiovascular research remains *in-vivo* studies using animal and human subjects [9, 49]. Such studies measure various cardiac, biochemical, and haemodynamic processes to clarify the mechanisms of cardiovascular disease pathogenesis and to unveil the underlying biological processes involved.

In recent years, with the advancement of numerical mathematical science and high performance computing technology, cardiovascular mathematical modelling has developed into a mature research technique [50, 51]. The focus in recent years has been attempting to combine both *in-silico* and *in-vivo* investigations. At the time of writing, the community speaks of "leveraging the model" [52]. This synthesis of approaches allows one to begin to

validate mathematical models by comparing their response to the system dynamics observed through the *in-vivo* investigations [53], or by leveraging the model, by comparing their results at cohort scale, with patient data. Typical modelling studies grapple with the mathematical equations that describe the relevant bio-physical and bio-chemical dynamics in the living system, such that the mathematical solution can predict cardiovascular system responses which are similar to what is observed *in-vivo* [54, 55]. The specific approach varies with biological application and the dimensionality of the model. The latter varies from 3 dimensional computational fluid dynamics models which solve the Navier - Stokes, continuity and wall mechanics equations [52] (see section 4.1) providing detailed insight into specific vessel dynamics, to lumped parameter models (LPMs) (also known as 0D, compartmental or electrical analogue models), which compress the physical space within the cardiovascular system into discrete compartments but leverage this simplification -or coarse-graining- to achieve a quantitative description of global heamodynamics [56, 57]. In this work we shall utilise LPMs which are fully introduced, qualitatively, in Chapter 2 and mathematically in Chapter 4.

In the present context, a mathematical modelling approach can not only predict physiological responses (like arterial pressure and cardiac output) that are measurable *in-vivo*; it can also provide wider information (including venous pressure and flow, vascular impedance etc.) that are important but difficult or impossible to measure in the human cardiovascular system, facilitating augmented diagnoses and deeper insights into the mechanisms of the cardiovascular system *which otherwise would be impossible to observe.* Table 1.2 surveys and compares the mathematical modelling and the *in-vivo* experimental techniques in cardiovascular medicine.

1.2.3 A Patient Specific Outlook

The above commentary converges on the observation that in modern practice, diagnosis operates on a population averaged approach- the team relies on combined experience to ensure a patient's symptoms and personal information gleaned from diagnostic tests are consistent with some pathophysiology, as observed in previous individuals. Then, when prescribing treatment a clinician effectively predicts a patient response to treatment based upon how previous, similar patients have responded - clinicians are trained on the success of previous interventions.

Recognising the variability between patients and the uncertainty associated with diagnostic data and treatment response, there is a shift in the community towards personalised care informed by computational models, given that the computational model in question, which is

Table 1.2 **Comparison of Experimental Approaches:** A comparison of *in-vivo* experiments and mathematical modelling in cardiovascular research.

***In-Vivo* Experiment**	• Risk of harm to a patient, making ethics approval time-consuming. • Experiments may alter the baseline response of a human subject. • Challenging to attribute system response to a single variable. • Provides gold-standard pathophysiological data. • Enables testing of new drugs and treatments. • The signal generated includes all physiological factors contributing to system response.
Mathematical Modelling	• No risk to a patient; simulations can often be run within minutes. • Enables systematic alteration of model parameters to study impact. • Can examine any compartment of the human body and predict responses. • May lack clinical data for validation. • Mathematical formulations may be challenging for clinicians. • Detailed models of specific vessels can require weeks, delaying interpretation.

representative of a patient's physiology, can ingest (i.e. be constrained by) data taken from a patient. This computational model can then, in theory, make predictions and provide insight into a specific patient's health [7, 58–62]. See figure 1.7 for a visual encapsulation of the patient specific outlook - the method in which computational models are personalised to a patient. Henceforth, this will be referred to as the personalisation process.

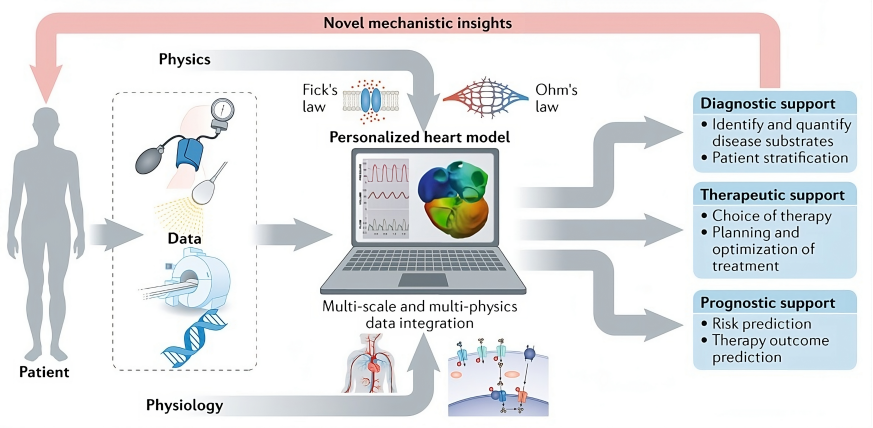

Fig. 1.7 **Personalised cardiovascular models**: A visual representation of how computational models of the cardiovascular system, when constrained by patient data, can improve patient care. Reproduced with permission from [7].

1.3 Thesis Outline

This thesis contains 9 additional chapters summarising the physiological and mathematical insights relevant to addressing the main aims as specified in the next chapter.

- Chapter 2 articulates the key terms associated with the personalisation process, details a brief review of cardiovascular modelling and introduces the cardiovascular LPMs used in this work. Here we also state the main aims of this work given the provided justification in chapter 2.
- Chapter 3 provides a current review of the literature, emphasising the personalisation of LPMs.
- Chapter 4 describes mathematically the model personalisation and analysis methods used.
- Chapter 5 examines the statistical properties associated with Sobol indices (introduced in chapter 4) and examines how convergence of global sensitivity analysis can impact one's interpretation of a model.

- Chapter 6 investigates the impact that varying experimental design (different model outputs used as a surrogate for clinical data) has on the personalisation process.
- Chapter 7 assesses the stability of obtaining personalised subsets of input parameters when different sensitivity methods are used (as introduced in chapter 4). Here, we also define a new methodology leveraging Sobol indices to examine the non-linearity associated with the model response surface providing insight into the personalisation process.
- Chapter 8 considers the unscented Kalman filter and the potential this tool may have for constraining cardiovascular models with patient data.
- Chapter 9 discusses the conclusions drawn in previous chapters and the impact that this may have on the personalisation process.
- Chapter 10 summarises the outcomes of the thesis and discusses future work.

Chapter 2

Background

Books are no more threatened by Kindle than stairs by elevators.
STEPHEN FRY

Summary
This chapter gives an overview of different cardiovascular modelling methodologies and highlights the advantages associated with lumped parameter modelling. Then we proceed to introduce the concepts which are embedded within the personalisation process, covering uncertainty analysis, sensitivity analysis and identifiability.

2.1 Modelling Human Hæmodynamics

In 13th century, Ibn Al-Nafis (1213-1288) was the first physician who described correctly the pulmonary circulation [63]. Before him the prevailing theory of blood circulation was that food is converted into blood in the liver, then that blood operated as fuel which would deplete over time. Later on, in 1628, William Harvey (1578-1657) demonstrated experimentally that the blood is pumped from the heart and circulates. He published “An anatomical study of motion of the heart and of the blood of animals". This was the first publication in the Western world advancing the theory that the heart is responsible for the blood circulation. In 1738, Daniel Bernoulli (1700-1782) investigated the laws governing blood pressure, leading to the well-known Bernoulli invariant, a first integral of the Euler equation [52], which relates blood pressure to blood velocity and potential energy (gravitational forces) [64]. The first pulse wave propagation model for inviscid fluid was introduced by Leonhart Euler (1707-1783) in 1775 [65]. After Euler, Thomas Young (1773-1829) presented a mathematical model describing the wave-like nature of blood flow, that was not recognised in the Euler’s model [66]. In 1838, Jean Léonard Marie Poiseuille (1797-1869) and in 1839, Gotthilf Heinrich Ludwig Hagen (1797-1884), independently derived a physical law that explained the relationship between the pressure drop and blood flow under steady flow conditions within a cylindrical pipe. Later on, the physical law, known as the Hagen - Poiseuille law was published by Poiseuille in 1840 and 1846 [67]. To complicate attribution even further, it seems that Stokes also derived the now eponymous Poiseuille law by solving the Navier–Stokes equation, [52] as early as 1845 but did not publish his work, because he was unsure of the validity of the no-slip condition at the tube walls [68]- a question that persists to the present. The question of the propagation speed of waves in elastic tubes was studied theoretically by Wilhelm Eduard Weber (a noted physicist who is best known for his work on another field theory-electromagnetism) and experimentally by his brother Ernst-Heinrich Weber (an equally noted physiologist who is considered by many to be the founder of experimental psychophysics) and published in 1866 [69, 70]. The theoretical results are based on an independently derived linearised form of Euler’s conservation equations and the assumption of a constant distensibility of the tube. They arrived at the same equation for wave speed as Young proposed 50 years earlier.

In the field of cardiac physiology, several important contributions were made by Otto Frank (1865-1944). Of these, the “Windkessel effect” (that explains how the elastic properties of the arteries help to smooth the pulsatile flow of blood originating in intermittent contractions of the heart) and the “Frank-Starling law of the heart” (the greater the initial length or stretch of the cardiac muscle fibres, or preload, at the end of diastole, preceding systole,

the greater the force of contraction) are undoubtedly the most important. The clergyman Stephen Hales was the first to recognise the importance of the elasticity of the arteries, in 1733. But it was left to Frank, more than a century later, to formalise matters. In 1899, O. Frank published "Fundamental form of arterial pulse", which was first recognisably modern theory of "Windkessel effect" in the field of blood circulation [71]. He considered the arteries as a single compliant compartment and used the conservation of mass to analyse their change of volume during diastole. The solution for pulsatile flow in rigid tubes was first given by Witzig in 1914 in his doctoral thesis [72]. However, in 1955, John R. Womersley (1907-1958) derived the exact solution of viscous fluid in a circular tube under a periodic pressure gradient [73]. Womersley in 1957 went on to provide solutions for pulsatile flow in tubes with elastic walls and to include wall viscoelasticity and longitudinal constraints [74]. Important early work in the time domain was also published by Ling & Atabek [75]. Unlike Womersley's theory, which was formulated in the frequency domain, and allows for analytical solutions, time-domain formulations can only result in approximate solutions obtained by numerical integration. Since the middle of the last century, a steady increase in computer power [76] has provided impetus and focus on creating more complex mathematical models of cardiovascular flow, that can be solved computationally. The first real three-dimensional cardiovascular models were published in the early 1980s, when it became possible to solve the Navier-Stokes and continuity equations on sufficiently large 3D meshes. At the time of writing, fully 3D solutions are still restricted in scope to specific vessel scales while most cardiovascular pathophysiology requires the address of whole system scales such as the systemic circulation. Consequently, there still is - and we believe will remain for the foreseeable future - a pressing need, especially in application-driven research, for alternative models of blood flow. Below we discuss 3-dimensional (3D), one-dimensional (1D) and lumped parameter models (LPMs). Figure 2.1 gives an example of how all 3 modelling methods could be used together. Below we aim to describe their main characteristics with the mathematical definitions given in chapter 4.

2.1.1 3D Models

3D fluid-structure interaction (FSI) models of haemodynamics are recognised as the most insightful models, and several highly complex FSI models exist. See e.g. [77]. However, these models are very computationally expensive, and hence are generally only applied to a small number of vessels or chambers; recent state-of-the art or landmark studies address the whole heart [78, 79], venous valves [80, 81], or coronary arteries [82, 83]. Furthermore, these FSI models require large amounts of input data ranging from but not limited to:

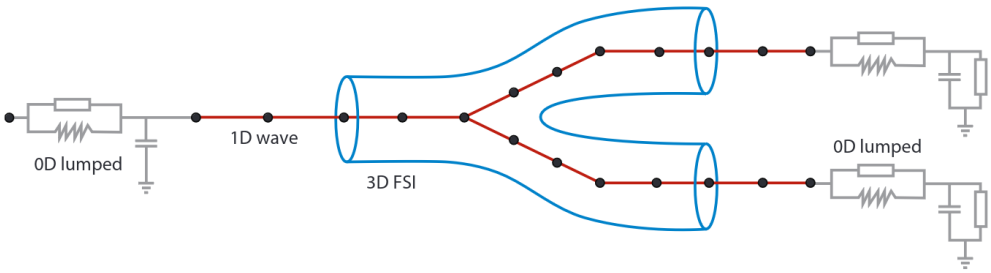

Fig. 2.1 **Multidimensional model representation**: A schematic representation of a typical coupling between 3D,1D and LPM models, designed to investigate coupled flow and wall motion in an arterial bifurcation. Reproduced with permission from [8].

1. Vessel geometry extracted using 3D or 4D radiographic imaging techniques, such as rotational angiography [84], computed tomography (CT) [85] or magnetic resonance imaging (MRI) [86].

2. Haemodynamic quantities such as volumetric flow rate, which often require an assumption of a velocity profile at the inlet and of laminar flow.

3. Pressure measurements, which would generally require the invasive surgical technique of catheterisation.

Material properties of the vessel wall would also be required, to accurately estimate vessel wall motion (compliance) for example. However this is not feasible or ethical, since it would require a sample of a patient's artery. In addition a sample taken outside of the body would exhibit significantly different conditions than the environment in-vivo. The mechanical properties may be estimated from a cadaver but again this step would also be under significantly different conditions than in-vivo. Due to lack of experimental testing, the majority of FSI models assume uniform material properties in a vessel and consider the wall to have isotropic properties [87–89], whereas significant anisotropy has been observed experimentally [90] and computational investigations have shown the vital importance of a compliant vessel wall [91]; or from expensive four-dimensional imaging data such as 4D flow MRI, which can track the three dimensional wall motion and/or blood velocity [92, 93]. This wall motion can be used to either estimate the elastic moduli of the material, or to define wall motion of the vessels during the simulation, essentially avoiding the fluid-structure interface problem as the boundary/interface of the fluid and vessel wall is defined, allowing the vessel wall (solid) model to be neglected. Vessel compliance can also be estimated from the pulse wave speed, by finding the time difference between two measurable waveforms (normally pressure) for specific wave features, such as the initial rise of pressure at the beginning of diastole; however such a method can only be performed non- invasively for a small subset of vessels,

and is typically used to find the overall/average wave speed in the cardiovascular network, rather than the wave speed in a single vessel [94]. Overall 3D FSI models provide us with the intricate details associated with blood flow at vessel scale; despite the scale limitation, these calculations have influenced the clinical workflow for coronary artery disease treatment e.g. the use of virtual fractional flow reserve [95] and the guidelines for coronary artery revascularisation [96, 97]. That said, the need for an address of global heamodynamic scales is of vital clinical importance where the focal effects of hemodynamics perturbations (like stenoses) impact the whole system. To reach a suitable description, one must reduce the dimensionality of the model, to reduce the computational time associated with simulation. In passing we remark that, due to the high degree of detail associated with a 3D simulation investigations, a 3D model is typically subjected to thousands of possible sources of uncertainty. A CFD calculation is only as good as the boundary conditions associated with it.

The simulation of blood flow and red blood cell (RBC) dynamics within complex vascular geometries is essential for advancing our understanding of haematological behaviours in both healthy and diseased states [98, 99]. While traditional 3D computational fluid dynamics (CFD) methods focus on solving the Navier-Stokes equations to model fluid behaviour, multi-component lattice Boltzmann (LB) methods offer a distinct approach, particularly well-suited for capturing the multiphase and particulate nature of blood [100, 101]. Unlike 3D CFD, which relies on continuum assumptions and often requires complex meshing, the LB method represents fluids as collections of particles on a lattice grid, allowing for a more straightforward treatment of complex, deformable structures like RBCs. This approach is ideal for modelling cellular mechanics, aggregation, and plasma-cell interactions within blood flow. Below are examples of 3D RBC or blood flow simulations, along with descriptions of the LB methodology developments that support these sophisticated simulations [102–104].

Two-dimensional (2D) simulations of red blood cells (RBCs), droplets, and other deformable particles provide a streamlined, computationally efficient alternative to more complex three-dimensional lattice Boltzmann (LB) and computational fluid dynamics models. While 3D simulations are essential for capturing detailed spatial interactions and full vascular geometry, 2D models allow researchers to focus on fundamental behaviours like cell deformation, particle collisions, and flow-induced shear stress without the intensive computational demands of 3D frameworks. In 2D, the LB method excels at simulating multiphase flows and interactions within a simpler, planar domain, making it especially valuable for examining isolated dynamics and core behaviours in a controlled environment. This approach offers an effective way to investigate essential haemodynamic characteristics and particle interactions, making

it ideal for rapid, preliminary assessments and cases where full 3D detail is unnecessary.

Two-dimensional (2D) simulations of RBCs, droplets, and other deformable particles provide a streamlined, computationally efficient alternative to more complex 3D LB and CFD models [105, 106]. While 3D simulations are essential for capturing detailed spatial interactions and full vascular geometry, 2D models allow researchers to focus on fundamental behaviours like cell deformation, particle collisions, and flow-induced shear stress without the intensive computational demands of 3D frameworks [107]. In 2D, the LB method excels at simulating multiphase flows and interactions within a simpler, planar domain, making it especially valuable for examining isolated dynamics and core behaviours in a controlled environment [108, 109]. This approach offers an effective way to investigate essential haemodynamic characteristics and particle interactions, making it ideal for rapid, preliminary assessments and cases where full 3D detail is unnecessary.

There are still significant advantages associated with 3D fluid in cardiovascular research due to their capacity to capture complex flow dynamics and spatial variations that are unattainable with lower-dimensional models. Unlike two-dimensional models, 3D simulations can account for the full geometry of blood vessels and chambers, which is crucial for accurately modelling factors like wall shear stress—a key parameter influencing endothelial cell function, vascular remodelling, and atherosclerosis development. These models allow for a detailed assessment of blood flow patterns, including secondary flows and vortices, which are important in regions of complex anatomy, such as arterial bifurcations and the cardiac chambers. This level of detail is essential for evaluating the localised impact of blood flow on vessel walls, making 3D fluid models invaluable in predicting disease progression and designing medical devices, such as stents, with greater precision. By providing a closer approximation of real physiological conditions, 3D models enable researchers to conduct more accurate simulations that enhance our understanding of cardiovascular health and pathology.

2.1.2 1D Models

Propagation of the pressure and flow waves in the vessel network is an intriguing problem in the study of cardiovascular physiology. It is believed that information regarding cardiac function, the elastic properties of the vessels, and the pathophysiological conditions of the important organs (brain, liver, kidney etc.) is encoded in two forward and reflected waveforms, and their relationship. Thus, pulse wave studies have received extensive attention in cardiovascular research [110–112]. 1D models are used to describe vascular components in which distribution of quantities along the vessel axis -the streamwise flow direction- are important,

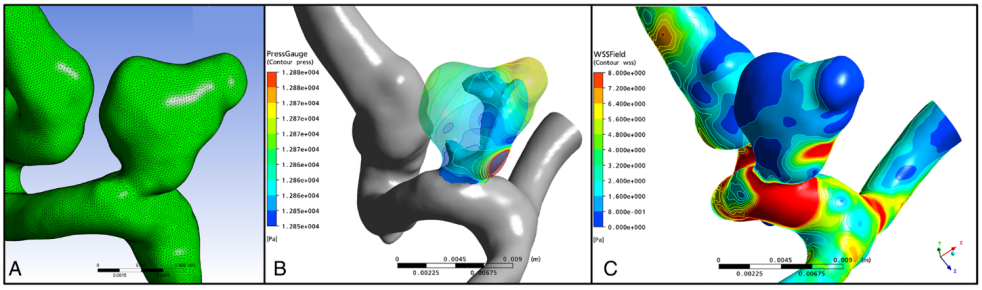

Fig. 2.2 **Example CFD workflow**: Here, the authors treat an intracranial berry aneurysm. Panel (A) demonstrates the reconstructed surface mesh (defining a hydrodynamic no-slip boundary condition) Panels (B) and (C) demonstrate the CFD simulated pressure (B) and wall shear stress (C) acting upon the aneurysm wall. The latter are hypothesised to provide useful risk stratification for rupture, on a patient-specific basis. Reproduced under CC 4.0 BY from [9].

and account for wave effects, including transmission and reflection characteristics. Typically, the dynamics of vessel pressure and flow (the transverse integration of streamwise velocity) are described by two coupled first order partial differential equations in time and a single spatial dimension, representing the curvilinear streamwise coordinate. Often one can find a third equation representing the relationship between transmural pressure, cross-sectional area and vessel wall mechanical properties. Seminal works by Lambert (1958) [113] and Barnard (1966) [114] provided a description of flow in a compliant tube in 1D theory. Later work by e.g. Hughes and Lublinear (1973) [115] derived a set of equations to represent fluid flow in a tapering leaky vessel. Perhaps the most popular 1D model utilised for nearly all of the most recent works is that summarised coherently Mette Olufsen (1998) [116], who reformulated the earlier work by Hughues and Lubliner [115], simplifying to a non-leaky, non-tapering vessel. We defer further discussion of the 1D formulation to chapter 4.

We return to the consideration of the several complications in the study of 1D pulse wave propagation - the tapering of the vessel (causing fluctuation in the convective acceleration), vessel branching, nonlinear pressure/cross-sectional area relationships for the vessel wall axial tension and bending in the vessel wall, boundary slip, vessel leak, transmural pressures, numerical scheme discretisation, collapse of veins and pulmonary vessels *inter alia* [111, 117–125]. The use of 1D blood flow models has become more common, as they have gained traction for analysis of haemodynamic waveforms in the cardiovascular system. One-dimensional modelling provides a computationally viable alternative to the 3D CFD with fluid-structure interaction models, which is able to address the entire circulation while taking considerably less time to run compared 3D model equivalents. The main drawback

with 1D models is that they cannot fully capture local flow fields, as they consider flow only in the axial direction. This has led to several studies coupling 1D and 3D models, enabling the 1D model to act as boundary (inlet) condition, providing some representation of heamodynamics away from the vessel of immediate interest, which is of course covered by 3D model [126–128]. 1D blood flow models have also been used to model particular systemic function e.g.the calf muscle pump [111], cerebral artery flow [129], ductus venosus [130], coronary circulation dynamics [117, 131], the systemic circulation [132], the liver system [133] and -note - the entire human cardiovascular system [47, 134, 135]. Overall, 1D models offer a nice alternative and an ally to 3D models, due almost entirely to their reduction in computational cost and an ability to examine global heamodynamics while preserving a description of wave propagation phenomena. In the clinical setting, where data are constrained, 1D models can be as accurate as an insufficiently parameterised 3D model e.g. in the diagnosis of coronary artery disease [136]. While 1D models lead to a considerable reduction in computational time (to a few minutes, from days) this class of model is still very dependent on the need for a patient specific geometry and it still can contain hundreds of sources of uncertainty, particularly if multiple vessels within the circulatory system are investigated.

2.1.3 Lumped Parameter Models

0D, electrical analogue, compartmental or lumped parameter models divide the circulatory system into compartments within which the primitive problem variables are assumed to be uniformly distributed and to vary only with time. They can be used to represent the whole cardiovascular system physiology, or any portion of it. The physiological variables of compartmental pressure, inter-compartmental flow and compartmental volume can be considered to be formally equivalent to voltage, current and charge, in the electrical analogy of the hydraulic circuit. Blood flow within 0D models is minimally described by:

1. An integrated form of the continuity equation for physical mass conservation.
2. Poiseuille's Law for the steady state momentum equilibrium, derived of course from from the Navier-Stokes equation.
3. A compliance (capacitance) equation accounting for the distensibility, mainly of the great vessels.
4. Then (when necessary) an inertance equation accounting for the inertial of flow.

As we now discuss, using the concepts and terminology which are traditional in the field.

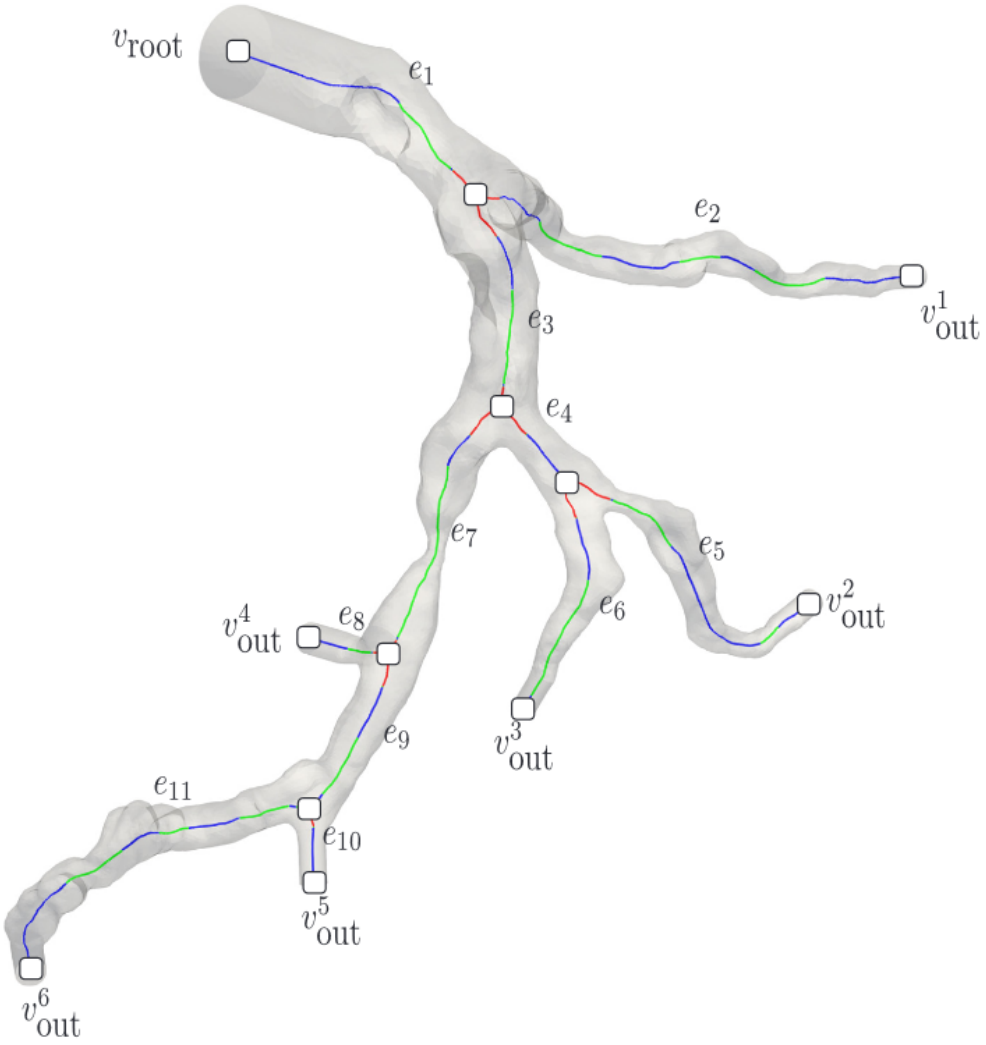

Fig. 2.3 **1D model example**: Centerlines extracted from a 3D geometry for a 1D model simulation. Reproduced under CC 4.0 BY from [10].

After the electric flow concept of current conservation, the hydraulic circuit is assumed to be governed by Kirchhoff's current law for current balance, Ohm's law for the steady state voltage-current relation and the transmission line equation for the high frequency voltage-current relation. By associating blood pressure and flow with voltage and current respectively, we represent the effects of friction and inertia in hemodynamics by a resistance R and inductance L. Vessel elasticity, compliance or distensibility can be represented by a capacitance C. Thus the well-established methods for analysis of electric circuit transients can be mapped across and applied to the investigation of cardiovascular dynamics. LPMs of the cardiovascular system begin, as we have discussed above, with the modelling of arterial flow using the famous Windkessel model. This was subsequently expanded to cover the modelling of other organs such as the heart, heart valves, and other vasculature networks.

Frank introduced what is now termed the two-element Windkessel model in 1899 [71], to relate arterial flow to pressure in a circuit with a resistor and capacitor in parallel (representing arterial ventricular after load) [71]. In 1943, Landes presented a three-element Windkessel model introducing an additional resistor, representing the impedance of the proximal arterial network, in series with the two-element model [137]. Burattini, in 1982, then recognised the 3 element model's inability correctly to capture vessel impedance, and so added an inductor in parallel to the proximal resistor [138]. Several subsequent iteration of these Windkessel models have been proposed, and the reader is directed to the extensive review by Westerhof, Segers and a review by Capoccia for further detail [11, 139, 140]. Interestingly, the term "Windkessel" was derived based on observations that the heart and the arteries behave like an old fire engine in which the pulsatile pumping (equivalent to the heart) is dampened by an air chamber (Windkessel in German) - conceptually equivalent to the large arteries. The 3 most commonly used Windkessel models are displayed below in figure 2.4.

One can relate the Windkessel models as seen in figure 2.4 through a set of coupled ODEs relating pressure and flow. Let Q_a and P_a be flow and pressure at the inlet of the Windkessel model representing the aorta. Q and P then represent the the pressure and flow of the downstream vessels. For the two element Windkessel

$$Q_a = Q + \frac{P}{R},\ Q = C\frac{dP}{dt} \tag{2.1}$$

Combining these equations and applying Kirchhoff's laws

$$Q_a = C\frac{dP}{dt} + \frac{P}{R},\ P_a - P = 0 \tag{2.2}$$

Rearranging to one equation we reach a coupled ODE which may be solved using an integrating factor (IF), analytically

$$\frac{dP_a}{dt} + \frac{P_a}{RC} = \frac{Q_a}{C},\ \text{IF} \rightarrow e^{\int \frac{1}{RC} dt} \tag{2.3}$$

$$\frac{d(P_a e^{\frac{t}{RC}})}{dt} = \frac{Q_a}{C} e^{\frac{t}{RC}} \tag{2.4}$$

Integrating both sides and utilising when $t = 0$, $P_a(0) = P_0$, we obtain:

$$P_a = P_0 e^{\frac{-t}{RC}} + Q_a R(1 - e^{\frac{-t}{RC}}) \tag{2.5}$$

Note during diastole $Q_a = 0$.

For the 3 element Windkessel model where Z_c is the proximal resistance, applying the constitutive equations and Kirchhoff's laws

$$P_a - P = Z_c Q_a,\ Q_a = C\frac{dP}{dt} + \frac{P}{R} \tag{2.6}$$

Replacing the vessel pressure P we obtain

$$Q_a = C\frac{d(P_a - Z_c Q_a)}{dt} + \frac{P_a - Z_c Q_a}{R}, \tag{2.7}$$

$$C\frac{dP_a}{dt} + \frac{P_a}{R} = Z_c C\frac{dQ_a}{dt} + \left(1 + \frac{Z_c}{R}\right) Q_a. \tag{2.8}$$

The four element Windkessel model over comes the inconsistency resulting from the approximation of the characteristic impedance as a resistance by adding an inertial element L either in series or in parallel with RC. The inertance term in Windkessel models represents the overall inertia of the arterial system, effectively capturing the mass-related resistance to changes in blood flow velocity. This approach offers a distinct advantage by focusing on the low-frequency response of the circulatory system, which is crucial for accurately reflecting long-term pressure and flow oscillations due to inertia. At the same time, the resistance and compliance components of the model are dominant at medium-to-high frequencies, where they respond more directly to changes in blood flow and pressure pulses. By separating the frequency contributions of inertance and RC elements, the Windkessel model provides

a comprehensive, frequency-sensitive representation of arterial dynamics. This makes it an efficient choice for applications where the detailed spatial information of 3D models is unnecessary, yet an accurate description of frequency-dependent behaviours, such as pulse pressure propagation and wave reflections, is essential. The 4 elements gives a relative accurate estimation of total arterial compliance from pressure and flow. When L is placed in series we obtain the equations:

$$P_a - P = Z_c Q_a + L\frac{dQ_a}{dt},\ Q_a = C\frac{dP}{dt} + \frac{P}{R} \tag{2.9}$$

Replacing the P terms in the second equation and simplifying we obtain the following second order ODE

$$LC\frac{d^2Q_a}{dt^2} + \big(Z_cC + \frac{L}{R}\big)\frac{dQ_a}{dt} + \big(1 + \frac{Z_c}{R}\big)Q_a = C\frac{dP_a}{dt} + \frac{P_a}{R} \tag{2.10}$$

When adding L in parallel to Z_c the same pressure drop applies however new Kirchhoff laws are now obtained

$$P_a - P = L\frac{dQ_L}{dt},\ Q_a - Q_L = \frac{P_a - P}{Z_c} \tag{2.11}$$

Replacing P in the equation $Q_a = C\frac{dP}{dt} + \frac{P}{R}$ we obtain

$$Q_a = C\frac{d}{dt}(P_a - L\frac{dQ_L}{dt}) + \frac{1}{R}(P_a - L\frac{dQ_L}{dt}) \tag{2.12}$$

$$LC\frac{d^2Q_L}{dt^2} + \frac{L}{R}\frac{dQ_L}{dt} + Q_a = C\frac{dP_a}{dt} + \frac{P_a}{R} \tag{2.13}$$

Replacing Q_L in the equations above and rearranging we obtain

$$LC\frac{d^2}{dt^2}(Q_a - \frac{P_a}{Z_c} + \frac{P}{R}) + \frac{L}{R}\frac{d}{dt}(Q_a - \frac{P_a}{Z_c} + \frac{P}{R}) + Q_a = C\frac{dP_a}{dt} + \frac{P_a}{R} \tag{2.14}$$

$$LC\frac{d^2Q_a}{dt^2} + \frac{L}{R}\frac{dQ_a}{dt} + Q_a + \frac{L}{Z_c}(C\frac{d^2P}{dt^2} + \frac{1}{R}\frac{dP}{dt}) = \frac{LC}{Z_c}\frac{d^2P_a}{dt^2} + (\frac{L}{Z_cR} + C)\frac{dP_a}{dt} + \frac{P_a}{R}. \tag{2.15}$$

Utilising the identity

$$\frac{dQ_a}{dt} = C\frac{d^2P}{dt^2} + \frac{1}{R}\frac{dP}{dt} \tag{2.16}$$

Substituting in and rearranging we obtain

$$Z_cRCL\frac{dQ_a^2}{dt^2} + L(Z_c + R)\frac{dQ_a}{dt} + Z_cRQ_a = RCL\frac{dP_a^2}{dt^2} + (L + Z_cRC)\frac{dP_a}{dt} + Z_cP_a. \tag{2.17}$$

In Figure 2.4, much of the distal systemic vasculature is represented as a single compartment, thus the internal distribution of pressure and flow-rate in the different segments of the filtered

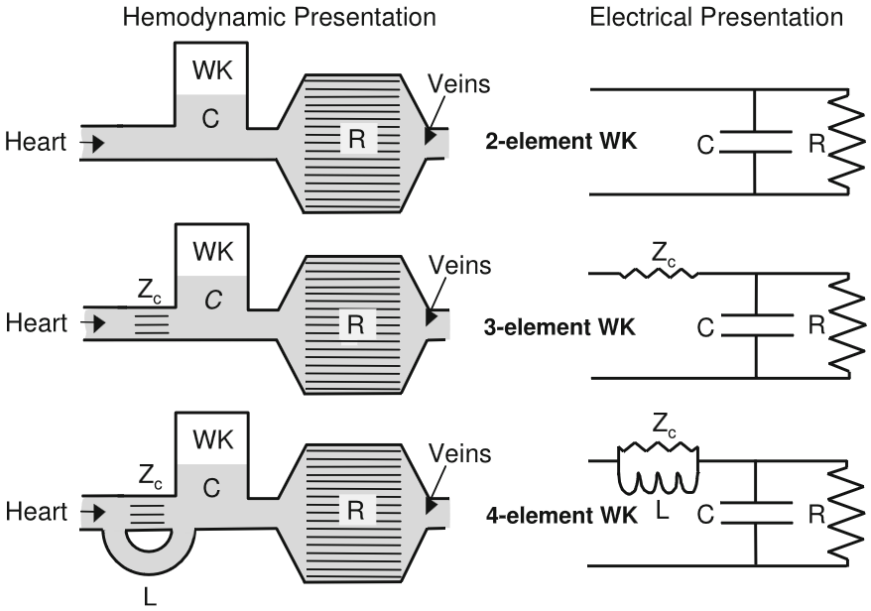

Fig. 2.4 **The Windkessel models**: The two-element Windkessel, the three-element Windkessel, and the four-element Windkessel presented in hydraulic and electrical form Z_c is aortic characteristic impedance, L is the blood inertia, C is the compliance of the large arteries and R is the resistance from the distal vasculature- the cardiologist's systemic vascular resistance. Here the capacitances are represented as in parallel, this is due to the assumption of zero distal pressure which in reality is not true. Reproduced under CC 2.0 BY from [11]

.

output i.e. not computed. Multi-compartment models address these shortcomings. There the systemic vasculature is partitioned into a number of compartments, each described by its own resistance R, compliance C and inductance L, depending on the local vessel group's characteristics. These vessel segments are connected together to form the complete model of the whole vessel network. Depending on the specific aims of any particular study, and the requirement for model anatomical fidelity, the vasculature can be appropriately partitioned to provide detail in the region(s) of interest, whilst other segments can be lumped together using less sophisticated model elements. Clearly, this approach provides a convenient platform for physiological intuition and a flexible and simple description of the vasculature. Accordingly, it is a powerful tool for cardiovascular simulation. In constructing the multiple compartment models for the vessel network, it is necessary to first derive suitable "RLC" (say) models for a vessel segment, as a building block in the development of the whole vessel network model. Formaggia and Veneziani [141] and Milisic and Quarteroni [142] provided detailed derivations of four typical compartment model configurations appropriate for the description of a vessel segment. These include CRL, RLC, RLCLR, CRLC alternaties. Using these network elements as building blocks, several multi-compartment models of the circulatory network have been developed, with various levels of complexity, upwards from the single branch models mentioned above. Most workers take the approach of partitioning the vasculature into segments representing aorta, artery, arteriole, capillary and vein [143–146], characterising the network element to suit local flow features, and then connecting the segments to form the circulation loop. In the aorta and the main arteries the blood vessels are quite elastic, the blood flow is pulsatile, thus the full resistance, compliance and inductance effects (the "RLC" combination) need to be considered. In the arterioles and capillaries, the vessel wall is relatively rigid and flow is steady and frictional loss is the dominant factor, thus the local flow dynamics is adequately described by a pure resistance element. The general veins and vena cava are highly compliant and the blood flow is relative steady, thus the inertial effect is often neglected in venous compartments and an RC combination is considered sufficient to describe their flow characteristics. It might be argued that a model consisting of a series of 0D compartments is, in the limit, a representation of a 1D system, and indeed Milisic and Quarteroni [142] have offered a formal proof that 0D models for the vessel network can be regarded as first order discretisations of 1D linear systems. As discussed earlier, such models are readily interpreted in terms of electrical analogues. In practice the biggest difference between multiple linear LPM and published 1D models is that the latter tend to include the (nonlinear) convective acceleration effects whereas the former cannot which is a significant limitation. One clinical advantage of LPMs is that in clinic the

majority of measurements which are available to us are on the organ scale (pressure and flow with no spatial dependence).

2.1.3.1 Heart Models

Windkessel models are termed passive- they can compute a compartmental pressure (flow) response to a known flow (pressure). For a self-initiating, closed loop model, one must -to exploit the electrical analogue- include the power source i.e. the heart. There have been numerous studies on quantitative characterisation of the heart as a pump, using a range of low order models, all of which attempt in some way to capture the essential biomechanics. As we shall see, these models are independent of LPM representations of passive circulation hemodynamics. But to be useful in the present work, they must clearly be compatible with the LPM description and capable of delivering an integrated description- a self-initiating "closed loop" model.

Leefe and Gentle [147] discuss the characteristics of the left ventricle, exploring whether it was better described as a pressure or as a flow source: of course in truth it is a combination of the two. In the 1974, Suga et al. [148] proposed a varying elastance model for the ventricle. Here, ventricular pressure is presented as a function of a ventricular elastance and the change of the ventricular volume from its unstressed value. The change of ventricular volume is determined by the blood flow into and out of the chamber, and the ventricular elastance is defined as a time-varying function based on the *in-vivo* measurement of the ventricular activity over the cardiac cycle further mathematical details are given in chapter 4. This model is easy to understand and to implement, and it has been widely adopted, especially within the physiological community and by researchers in general e.g. [149–151]. Various alternatives to the varying elastance model have been developed. Žáček and Krause [152] derived a heart model in which muscle mechanics were based on Hill's three parameter model. The ventricular pressure was calculated from the computed muscle force and the volume calculated from the change of muscle length. Werner et al. [153] proposed equations to calculate the myocardial wall tension in systole and diastole by using Hill's model and considering the Frank-Starling effect, and then calculated the ventricular pressure based on the Laplace law by assuming the heart chamber to be spherical in shape. Bovendeerd et al. [154] described the chamber pressure as a function of the muscle fibre contraction in the ventricle, and called this model single fibre model. A simpler model for the heart which does not capture pulsatility is an exponential equation to define the cardiac output as a function of the atrial pressure, with ventricular dynamics details completely neglected [155]. Nevertheless, due to the time varying elastance's concise model structure, pulsatility, clear

physical meaning and intuitive appeal, it remains the most popular [156–160]. In addition to its original use as a descriptor of left ventricle performance, the variable elastance model has also been extended to the simulation of atrial dynamics [48, 161, 162].

We will see in forthcoming chapters that there are several plausible, purely algebraic (polynomial and trigonometric) representations of chamber variable elastance, which are suitable partners to the LPM hemodynamic vessel description.

2.1.3.2 Valve Models

There are four heart valves in the normal heart, the mitral, tricuspid, aortic and pulmonary valves. The valves prevent retrograde flow of blood from the ventricles to the atria during systole (mitral and tricuspid valves) or from the aorta and pulmonary arteries into the ventricles during diastole (the aortic and pulmonary valves). These valves close and open passively under various external effects of pressure gradient across the valve, vortex flow near the valve, shear force acted on the valve leaflet surfaces [163].

The simplest models of the heart valve used in 0D studies represent the valve as a diode with a linear or nonlinear resistance [164–166]. The valve has little resistance to the flow when the pressure gradient across it is positive, while the flow is totally stopped when the pressure gradients across it is negative. This idealised description ignores the more complex features of valve dynamics. Clearly the heart valves have a much more complex dynamics [167]. Žáček and Krause [152] considered the change of heart valve resistance during valve motion by using the concept of a time- dependent drag coefficient. In their work, the drag coefficient was a prescribed function of the valve open area, and it approached infinity when the valve was closed. The drag coefficients were added to the losses of the conduit in which the valve was situated. Werner et al. [153] described the valve behaviour by including the volume of the retrograde flow during the closure phase: in their study this was referred to as the dead space volume, which was a function of the valve leaflet opening angle and became zero when the valve was fully closed. Shi et al. [168] modelled valve dynamics by considering the local flow resistance and the blood inertial effect. The valve was described with an orifice model, and its opening change was prescribed based on previous experimental observations. To further improve the valve dynamics modelling, Korakianitis and Shi [169] proposed a more advanced heart valve model, in which the valve dynamics were described by an ordinary differential equation that considered the different effects of pressure gradient across the valve, vortex flow near the valve, and shear force acting on the leaflet surfaces. In this model, the relative importance of these factors was determined by referring to the

results of previous two dimensional and three dimensional computational fluid dynamics studies. With these improvements, the model could effectively simulate the valve opening and closing procedures, and the numerical results agreed well with the published results on *in-vivo* measurement of valve motions. Mynard et al. [170] presented a simpler valve function based on the work by Korakianitis and Shi, in this work they formulated the valve opening driven by a differential equation based on the pressure gradient. In this formulation they applied a dampening factor to eliminate the flow oscillations present in the previous model which were attributed to a dicrotic notch. More recently, Laubscher et al. [159] developed a new model for the aortic valve in which the parameters representing forces acting on the valves are derived from the geometrical features such as valve cusp thickness, cusp height, valve opening angle and instantaneous valve flow rate.

2.1.3.3 LPM Applications

System models constructed from 0D components generally feature the major components of the system, such as the heart, the heart valves and compartments of the vasculature, and are suitable for examination of global distributions of pressure, flow and blood volume over a range of physiological conditions, including study of interactions between the modelled components. The applications of LPMs are varied. As we have seen, LPMs are used as boundary conditions for 1D and 3D models, to represent the distal vasculature of the vessel of interest, which may be a simple vascular bed [171] or the whole circulatory network, if coupled with a 3D heart model [172]. Independently LPMs have been created to model the systemic, pulmonary, coronary, venous, cerebral, baroreflex regulation, sex differences, ventricular interactions and the whole human circulation [139, 173–179]. A representative LPM can be found in figure 2.5.

Canonically, LPMs can be as parsimonious as possible, given their intended purpose and the difficulty attending their paramterisation (the essential motive of this work, recall). They span a space from simple single ventricle models, up to the complex models of Guyton, which contain not only the mechanical aspects of the heart but also the majority of chemical and biological pathways associated with the human system [180]. This question of the level of detail needed in creating a LPM is central to this work but we defer further discussion to chapter 9. LPMs find applications in examining the impact of cardiovascular disease such as limb amputation, diabetes, pulmonary hypertension, valve stenosis, venous reflux, ischaemic stroke, tachycardia, coronary artery disease, heart disease, vessel collapse, congenital defects, orthostatic stress intolerance and Norwood physiology [159, 181–192].

2.1.3.4 Why LPMs?

Closed-loop LPMs are encapsulated mathematically by a set of simultaneous differential-algebraic equations (DAEs). In representations of the vasculature, there are typically two ordinary differential equations (ODEs) for each compartment, representing the conservation of mass and the conservation of momentum. These are complemented by an algebraic compliance or elastance equation, relating compartment pressure to volume or its time derivative, flow. Due to their relatively simple coupled, first order ODE formulation closed-loop LPMs can be solved much more rapidly than 1D and 3D models. Typically, the problem is expressed in state-space form [193]. As we shall discuss further below, this speed is essential for the problem of personalised medicine. Additionally, LPMs suppress the uncertainty associated with patient geometry, which is a significant issue in the personalisation of 1D and 3D models. Therefore, the only unknowns and sources of uncertainty in the model are the system input parameters that characterise the model and patient e.g the resistance, inductance, and compliance of the LPM's compartments, as well as heart elastance (inverse compliance) function and valve parameters.

Given that we can constrain the model with patient data to provide updated model parameters that characterise a patient, we can develop a virtual representation and personalised model from which we can make predictions and gain insights. For the aforementioned reasons, we choose to investigate the properties associated with personalising lumped parameter models of the cardiovascular system.

2.2 Uncertainty Quantification

Cardiovascular science and medicine are inherently uncertain; each patient differs, resulting in significant variability in medication dosages, treatment reactions, physiological responses and risk [194]. The goal of personalising cardiovascular models is to quantify and suitably communicate these risk to clinicians. A quantification may relate to the risk of making a prediction from a model which contains error or deriving insights from an incomplete model i.e. a corrupted understanding of the mechanisms contributing to a pathophysiological state. Below, we outline the uncertainties which be devil 3D, 1D, and LPMs.

1. **3D models**: Mesh element O(100000), element size and shape, vessel wall mechanics model, terminal boundary conditions, inlet boundary conditions, essentially originating in vessel imaging methodology, image segmentation, vessel reconstruction, flow

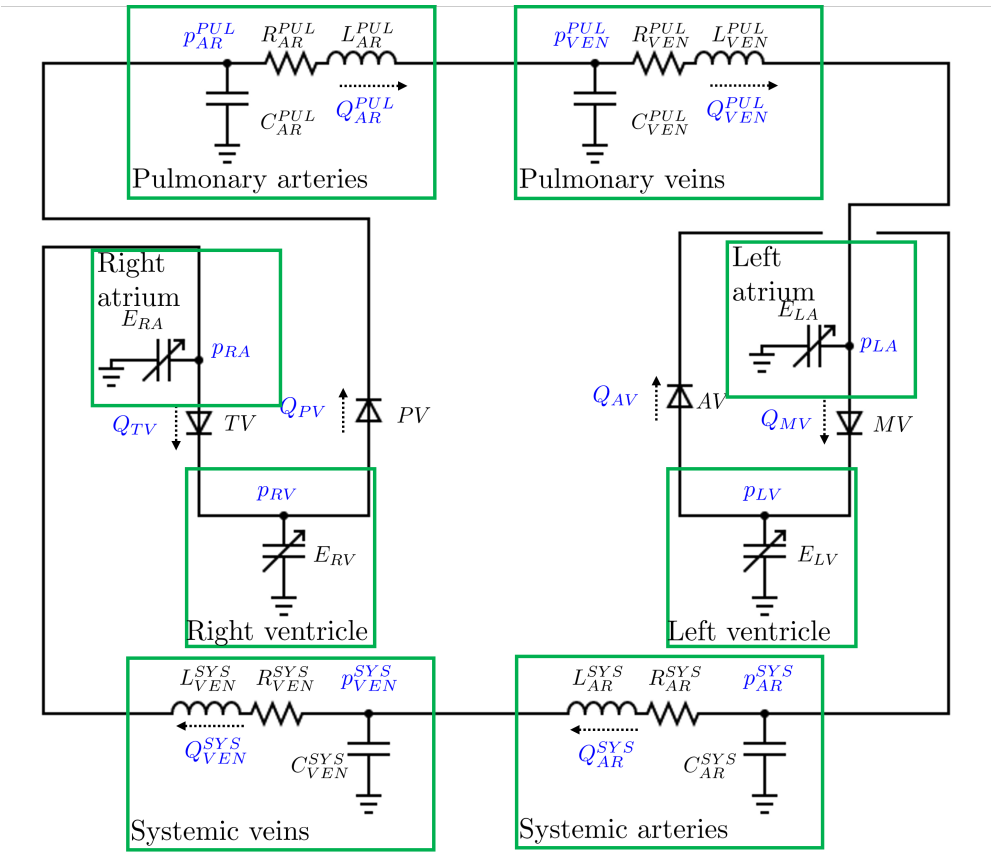

Fig. 2.5 **Example LPM**: A closed-loop LPM model of the human circulation; all 4 heart chambers, heart values and the systemic and pulmonary circulations are explicitly represented. Note, the variable elastance functions which introduce pulsatility into the model. Reproduced from [12].

properties (Newtonian and non-Newtonian models), closure term equation parameters to link larger to smaller scales (turbulence) and missing physics.

2. **1D models**: Mesh elements O(100), wall mechanics model, terminal boundary conditions, inlet boundary conditions, originating in vessel imaging methodology, image segmentation, vessel reconstruction, and missing physics.

3. **LPMs**: Initial volumes, pressures, and flows, missing physics, model input parameters e.g. compartment resistance, compliance, inductance, heart parameters.

LPMs offer a mechanism for quantifying and explaining the uncertainty of cardiovascular responses through a small, countable set of identified input parameters that all have an intuitive physiological interpretation.

2.2.1 Uncertainty & Sensitivity Analysis

Uncertainty analysis (UA), also known as uncertainty propagation, involves generating an ensemble model output distribution (pressures/flows/volumes) within - here - a clinical LPM setting, given some uncertainty in the model input parameters. This process considers possible model output values, considering the input uncertainty [13]. Clinically, this is useful as it informs how changes in model inputs impact the model outputs, which are often surrogates for patient responses. For example one may be able to observe the pressure range which may be expected from a patient given this uncertainty.

There are several definitions of sensitivity analysis (SA). Pathmanathan et al. define SA as “the quantification of the uncertainty in model inputs," where inputs are the parameters characterising an LPM [195]. In this context, the parameters include the resistance, compliance, and inductance values, as well as heart chamber parameters. Saltelli et al. provide an expanded definition of SA as the “study of how uncertainty in the output of a model can be apportioned to different sources of uncertainty in model inputs" [196]. The primary reasons for uncertainty in model inputs are measurement uncertainty (e.g., the inability to measure a quantity exactly) and natural variability (e.g., physiological variability across individuals). Given the significant variability in our cardiovascular models’ inputs, it is important to examine which inputs, within a prescribed range of values, contribute the most to the uncertainty in output quantities of interest (QOIs). From a cardiovascular perspective, QOIs are potential clinical metrics that aid the diagnostic process. For example, ejection fraction can be used to diagnose heart failure, and SA could reveal which model parameters indicate heart failure. Performing SA on a model can highlight the influential mechanisms

contributing to a patient's pathophysiological state.

The aforesaid method is known as global sensitivity analysis (GSA), which considers the entire range of permissible parameter values. Conversely, local sensitivity analysis (LSA) examines how model outputs are affected when parameters are perturbed from a nominal base state. GSA, using empirically derived input ranges, provides a fundamentally different measure of sensitivity compared to LSA, not least because it leverages experimental data (parameter ranges) not considered in LSA. For a detailed introduction to SA, see [196, 197]. Consider the simple model

$$y(x_1, x_2) = x_1 + 10x_2.$$

LSA would conclude that y is ten times more sensitive to x_2 than to x_1. However, GSA leverages information on the distributions of the inputs. Suppose $x_1 \sim N(0,1)$ and $x_2 \sim N(0, 0.01)$. GSA would reveal that 91% of the variance in y can be attributed to the uncertainty in x_1, and 9% to the uncertainty in x_2.

Personalised medicine is a global process that requires identifying model parameter values that best represent patient physiology as well as quantifying the risk associated with model output interpretation, given the input uncertainties. Compared to UA, GSA allows us to identify the primary input parameters that influence the model outputs. These are diagnostically relevant simply in view of their impact on QOIs. UA and SA are complementary investigations with different purposes: SA identifies influential inputs without considering specific output values, while UA generates probability distributions of outputs based on input uncertainties, enabling clinical predictions about system responses to input changes. Figure 2.6 schematically represents the relationship between UA and SA.

In this work, we focus on SA and the practicalities associated with identifying a set of influential, identifiable (to be rigorously defined in Chapter 4), and unique input parameters given a set of model outputs.

2.3 Aims and Contributions

The broad objectives of this work and its contribution to knowledge revolve around the modelling and simulation, quantification of uncertainty through sensitivity analysis (introduced in this chapter), and examination of the personalisation process in cardiovascular LPMs. The focus is on the critical, offline steps of model development where sensitivity analysis (a method for quantifying uncertainty) is employed to understand the behaviour and properties

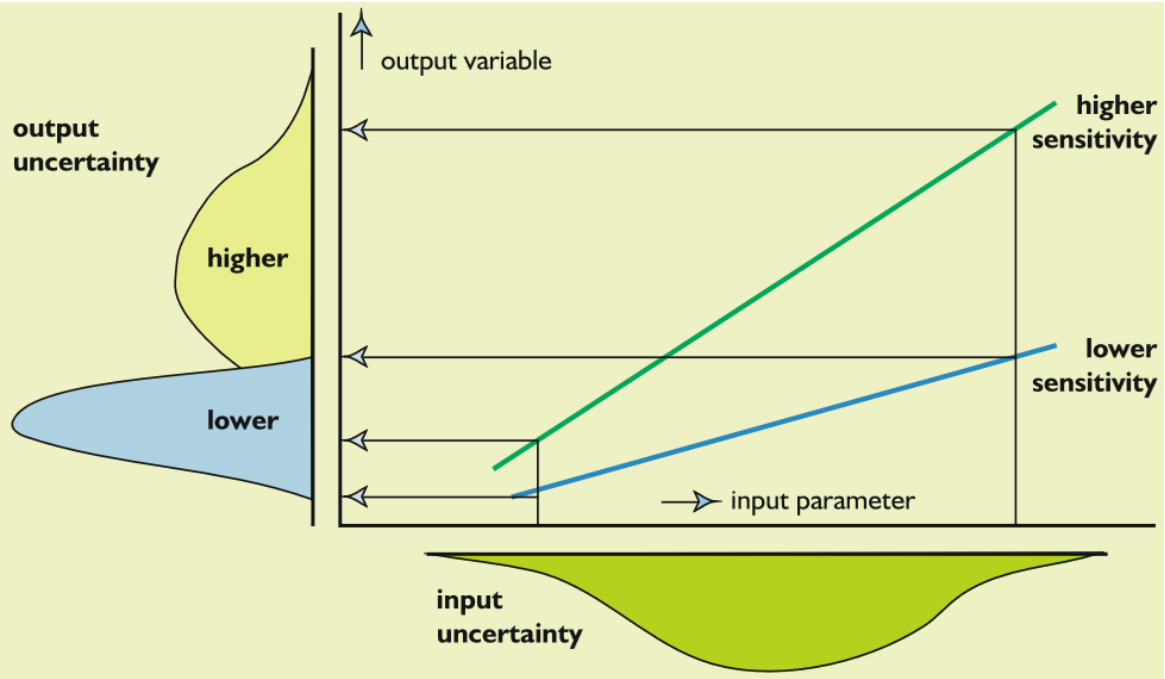

Fig. 2.6 **Model uncertainty representation**: Schematic diagram showing relationship among model input parameter uncertainty and sensitivity to model output variable uncertainty. Reproduced under CC 4.0 BY from [13].

of LPMs, in particular their suitability for personalisation. The key novelty of this work is the development and definition of best practices surrounding global sensitivity analysis and uncertainty quantification. While the application in this work is mostly concerned with the cardiovascular system the work and methods developed here can be applied to any dynamical system in which one looks to quantify uncertainty. The specific aims of this work and the associated contribution to the knowledge can be stated explicitly in five, progressive tiers:

1. Investigate the impact of different statistical estimators, sampling methodologies and convergence when performing a global sensitivity analysis of LPMs.

    - We apply our newly developed computational framework efficiently to investigate methodological choices when computing a global sensitivity analysis, aiming to investigate how different methodological choices impact one's interpretation of LPMs and the consequences of this on the personalisation process.

2. Examine the impact that varying model outputs have on the personalisation process.

    - Having defined best practices for global sensitivity analysis in 1, this work aims to investigate how different model outputs -a proxy for different clinical patient

measurements- can change the interpretation of input parameters in a model and, again, the larger impact this may have on the personalisation process.

3. Investigation of the stability of personalisable/identifiable subsets of input parameters, given varying sensitivity methods and the development of a new methodology which provides insight into the non-linearity associated with a model response surface.

    - The insight provided by 2 above. Is that model interpretation is constrained by the chosen model outputs. Now we aim to extended a subset selection methodology to encapsulate the global nature of the personalisation process and to examine how consistent model interpretation is - given that one varies the sensitivity methodology which is utilised - and develop a method using sensitivity analysis which provides insight into the non-linearity associated with the model response surface, which should aid personalisation when one constrains the model with patient data.

4. Examine the unscented Kalman filter as a method for parameter estimation in the personalisation process.

    - Given the understanding of sensitivity analysis and model interpretation developed from 1,2 and 3, we aim, in this step to investigate a promising data assimilation method for constraining a model (with synthetically generated "forward" patient data) better to personalise the LPM parameters.

Chapter 3

Literature Review

The thing that I fear discriminating against is humour and truth.
— CHARLES BUKOWSKI

Summary
This chapter reviews and critically examines the current literature surrounding the personalisation of cardiovascular LPMs. We end the chapter by highlighting the open questions based on the current literature.

3.1 Introduction

This thesis is concerned with the personalisation of cardiovascular models. We are agnostic towards the structure, application, and methodology by which these models are created and are concerned with uncertainty quantification methods, of both statistical and mechanistic models, as interpretation remains consistent across these types.

In Section 3.2, we review the concept of personalised medicine. We highlight the main challenges in creating cardiovascular models, how to quantify the risk in making predictions with these models, and, most importantly, what is needed for their translational application. We then examine some examples of LPMs that apply sensitivity analysis to identify influential parameters from local (Section 3.3) and global (Section 3.4) bases. While multiple methods exist to assess the global sensitivity of a model, we prioritise global methods that utilise derivative-based measures (Section 3.4.1) and variance-based measures (Section 3.4.2). Then, we review the concept of parameter identifiability, focusing on different methods applied to achieve a personalised cardiovascular model. Section 3.5.1 examines structural identifiability, a theoretical precursor to ensure the possibility of unique parameter identification. We then address practical identifiability in Section 3.5.3. The latter examines the ability to recover unique input parameters in the presence of noisy experimental data. We conclude by discussing identifiability informed by sensitivity analysis or *sensitivity-informed identifiability*. This process examines which input parameters could theoretically be identified, given a specific set of outputs, without accounting for the noise present within clinical data. Theoretical identifiability is reviewed in Section 3.5.2. The concept of model sloppiness is considered in Section 3.6.

Common in pharmacokinetic modelling, sloppiness provides insight into the structure of the input parameter space. We then explore the methods associated with model calibration, examining how parameter values are adjusted to best represent a patient's physiology when experimental data is introduced to a model. Methods for calibrating model parameters through data assimilation are detailed in Section 3.7. The final section, Section 3.8, identifies the gaps in knowledge that this thesis aims to address.

3.2 Personalised Medicine

The last several decades have witnessed lifestyle modifications and evidence-based interventions aimed at decreasing the burden of cardiovascular diseases (CVDs). Despite their success

CVDs continue to place a considerable burden on the healthcare system. At the time of writing, 92.1 million adults in the United States suffer from some form of CVD [198, 9]. Consequently, CVDs dominate healthcare costs and are projected to surpass 1 trillion dollars by 2035, according to the American Heart Association [199, 200]. The methods for diagnosing and preventing CVDs remain largely elusive due to the broad heterogeneity in patient profiles and clinical outcomes, necessitating deeper phenotyping of patient physiology. This gap has paved the way for personalised cardiovascular computational modelling approaches in both basic and clinical cardiovascular research [201]. These models are designed to incorporate the unique anatomy and physiology of a patient to define model parameters, predict patient outcomes, and devise optimal treatment strategies. The application of computational models in other areas of medicine has been incredibly successful, such as in the human immune system, oncology, liver function, and the brain [202–205].

The clinical acceptance of physics-based models in cardiovascular medicine have been accelerated by the work found in [206–210]. The underlying reason for clinical acceptance is augmented diagnosis- a wealth of information provided by physiological flow data, in addition e.g. to the anatomic information which accrues from medical diagnostic imaging data. Patient physiology is the foundation of clinical decision-making and computational models help uncover the complex relationship between patient anatomy and outcomes. Several clinical studies have demonstrated -perhaps unsurprisingly- that anatomy alone does not reveal the underlying pathophysiological mechanisms [211–213]. Physiology-guided interventions have become the cornerstone of modern cardiology practice. However, interventional procedures are generally invasive and expensive, limiting their widespread use [214]. Avoiding invasive procedures not only reduces patient discomfort but also lowers procedural costs and saves time and costs. These factors have inspired the development of physics-based models as fundamental tools in cardiovascular research and motivate efforts to integrate such computational methods into routine cardiovascular practice. Numerous physics-based principles of electromechanics, solid mechanics, and fluid dynamics are currently applied to study cardiovascular electrophysiology and hemodynamics and cellular mechanics [215–219].

Clinical decisions are built on evidence gathered from bench to bedside. Regulatory decisions, however, are often based on heterogeneous, limited, or incomplete human data. Computational model results are now accepted for some regulatory submissions [220, 221]. Digital evidence obtained using computer simulations can be used to ensure the safety of therapies prior to first-in-human use or under scenarios not ethically possible in humans [222].

Computational models play an increasingly important role in overall medical product/drug lifecycle management, proving useful in design optimisation for development and testing, supplemental non-clinical testing, and post-market design changes and failure assessment [223]. The development process for medical devices involves manufacturing and testing samples under a wide range of scenarios, which is often time-consuming and financially overwhelming. Additionally, pre-clinical testing conditions are often very simplified compared to the actual patient environment. Statistical and mechanistic models synergistically streamline this process: statistical models collect a representative virtual patient cohort, while mechanistic models simulate device behaviour under defined scenarios. In this way, new devices can be tested in a representative virtual patient population, decreasing risk before clinical trials. One of the first examples where digital evidence (i.e., an *in silico* trial) replaced additional clinical evidence was the approval of the Advisa MRI SureScan pacemaker (Medtronic, Inc.) [224]. Another important example is a computer simulator of type 1 diabetes mellitus [225], which the FDA accepted as a substitute for animal trials, for pre-clinical testing of control strategies in artificial pancreas studies. Later, the FDA granted an investigational device exemption, solely based on model testing, for a closed-loop control clinical trial assessing the safety and effectiveness of the proposed artificial pancreas algorithm.

Despite such promising results using cardiovascular models to inform clinical practice, one of the professional barriers reported in [226] is generating trust in these models. Improving the reliability of models through validation and sensitivity analysis is crucial to scaling the application of cardiovascular models [227, 228]. This undertaking depends on the amount of data available and the time and cost of the simulations. A lack of validation in computational models has also been noted by Mourato et al. [229] in one context - the modelling of aortic aneurysms. Mourato et al. reported that only 12% of the articles performed numerical validation with patient-specific *in vivo* data, and 76% did not present a meaningful validation process. Regarding UQ and SA, Mourato et al. concluded that there is a paucity of studies of the impact of several parameters in numerical simulations. Rodero et al. recently conducted a systematic review of cardiovascular *in silico* trials and again found a distinct lack of local or global SAs in 81% of the studies analysed. Galappaththige et al. [230] suggested a system to report the different degrees of validation for studies using patient-specific models and virtual cohorts of patient-specific models. Using this system, *in silico* clinical trials could be more aware of limitations concerning validation. Combining conventional clinical trials with modelling tools, as in [231], where *in silico* clinical trial predictions were compared with clinical decisions, can generate trust. Further, combining *in silico* clinical trials with physical and experimental evidence can also build stronger evidence,

as one approach compensates for the limitations of the other [232]. These studies can help spread understanding of computational modelling, provided the corresponding validation and SAs are performed to ensure model robustness.

In the development and application of computational models, especially within the medical field, ensuring credibility is paramount. Verification and validation (V&V) provide essential frameworks to assess the accuracy and reliability of these models, helping to establish their suitability for critical applications, such as medical device design and testing. Through verification, the model's consistency and alignment with its intended purpose are evaluated, while validation examines its accuracy in representing real-world physiological conditions. This paper focuses on employing V&V principles to assess the credibility of computational models in the context of medical devices. By rigorously verifying and validating these models, we can help support their safe and effective implementation in healthcare, where predictive accuracy can have a profound impact on patient outcomes. For validated standards please refer to [233, 234].

Models of natural systems involve parameters either directly measured or indirectly inferred (calibrated) using experimental data. However, even the most carefully conducted experiments exhibit intrinsic variability in their temporal behaviour and extrinsic variability between individual samples. For example, variability is reflected in the intrinsic beat-to-beat fluctuation of action potential duration (APD) in a single cell [235] and extrinsic cell-to-cell differences in APD. Intrinsic and extrinsic variability describe fluctuations due to inherent randomness or natural differences between individuals. Variability is one cause of uncertainty, which is the confidence or precision with which a quantity can be assigned a value. Uncertainty can arise from variability or a lack of knowledge. Natural variation is characterised as aleatory uncertainty, while uncertainty from a lack of knowledge is epistemic uncertainty. Uncertainty is important not only for model calibration, where inputs such as parameter values are derived from experimental data, but also for model validation (where model outputs are evaluated against experimental data not used in the calibration stage) and prediction. Most models treat inputs as fixed values and generate outputs as single values or a time series of single values. However, model parameters and other inputs are usually uncertain because of possible variability and the inherent limitations of experiments and calibration. Uncertainty does not focus solely on model parameters; representing a biological process means that the model may not fully represent it, leading to model discrepancy [236]. Model discrepancy can be seen as the difference between the mathematical description and the true biological process. Thus, as one will always have a simplified model compared to reality, this

discrepancy between the model and the relationship can induce uncertainty into predictions or conclusions drawn from a model. Additionally, as models increase in size to represent more complex processes, how does one choose a set of parameters to calibrate a patient to provide insight? The model's chosen dimension can significantly impact understanding the uncertainty within a model. Do we include uncertainty in image segmentation? Do we include the uncertainty associated with numerical solvers? We formulate some of the main practical questions surrounding the uncertainty of cardiovascular models below:

1. How reliable are cardiovascular models?
2. How do we compare between cardiovascular models rigorously?
3. What type of model should be used?
4. How should uncertainties be communicated to clinicians?

To achieve clinical translation experts (Hose, Holmes, Huberts, Acero, Gray, Viceconti, Peirlinck, Vardhan, Mirams, and Johnstone [237–246]) opine that one needs to account for the uncertainty in cardiovascular models through rigorous sensitivity analysis. Additionally, reducing models to a subset of parameters interpretable by clinicians is essential for making clinical choices. Lumped parameter models (LPMs) of the cardiovascular system currently are the only modelling method with a quick simulation time (avoiding the use of statistical emulation), that have input parameters that are directly clinically relevant, and can provide an examination of global haemodynamics. As stated in the articles above, a global virtual representation of a patient is likely to come from the application of an LPM.

3.3 Local Sensitivity Analysis

Local sensitivity analysis (LSA) varies parameters one at a time, around a base parameterisation for a computational model. Saltelli et al. [196] note that if the model under investigation is linear, then an LSA provides adequate information on the input parameters given a set of inputs. LPMs of cardiovascular systems normally contain a non-linear representation of a heart chamber, while the circulation is represented by linear differential equations and Ohm's law [247]. However, there are exceptions to this. Tang et al. applied non-linear compliance to represent pulmonary hypertension [183]. Pant et al. utilised non-linear resistance to model the effects of a vascular shunt in children with single ventricle physiology [248]. Thus, any interpretation from an LSA outside of an operating point in a model with any non-linearity must be undertaken with caution. Where LSA has been compared to global methods, discussed below and more suitable for non-linear models, researchers have regularly shown

that when a model is linear LSA and GSA results align. However for non-linear models, comparisons between LSA and GSA can lead to misleading conclusions. A majority of the work comparing LSA and GSA has been focused on non medical examples [249–251]. In other systems biology investigations, such as physiologically-based pharmacokinetic (PBPK) modelling, LSA is widely performed. Johnson et al. state that in PBPK modelling, often a drug operating point is known, so LSA is adequate in parameter interpretation [252].

A review by Saltelli et al. [253] highlighted that in medicine, 30% of modelling studies still utilise LSA to make interpretations about model parameters, even in the presence of non-linearity. Another reason for utilising LSA is the complexity of models; the number of input parameters is often too large for any global analysis. In PBPK modelling, Felmlee et al. [254] utilised LSA to obtain clinical markers to look for drug activation markers. In a system with over 250 state variables and 500 parameters, this method has since been utilised many times.

In cardiovascular modelling, Sher et al. [255] performed an LSA on a cardiovascular ionic channel model containing 14 parameters to identify non-influential input parameters which could then be fixed to reduce the parameter space dimensionality, for optimisation. A similar motive is ascribed to Paulsen et al. [256], who to reduce the dimensionality of a complex LPM of the systemic circulation. Ellwein et al. [257] took a complex LPM of the whole human circulation to categorise the sensitive and insensitive parameters against outputs of the human body. An important point regarding LSA studies is that they can be characterised into two distinct categories: some examine parameter influence against a wide range of model outputs; others restrict to particular model outputs, to understand the influence of parameters there.

A good example of trying to understand the general behaviour of parameter influence is the work of Otta et al. [175], who took a 50-parameter resistive model of the venous circulation and applied an LSA to inform potential model reduction. Levin et al. [258] applied LSA to an LPM of the coronary arteries to identify (and subsequently exploit) the impactful parameters in the pressure and flow in the vessels. Sato et al. [259] utilised a multi-scale model of the systemic circulation, including arteries, veins, and peripheral circulation, informed by nutritional and clinical pathways, to investigate the most influential parameters impacting cardiovascular output. Khan et al. [260] sought to personalise a 34-parameter LPM of the carotid artery. Khan was investigating which input parameters of the model are most influential in the case of a stenosis proximal to the bifurcation. By reducing the parameter

space of a specific pathology, Khan proposed a set of inputs that could be used as bio-markers, indicative of the specific pathology. The latter is an example of a model approaching the role of a diagnostic support tool.

3.4 Global Sensitivity Analysis

Global sensitivity analysis (GSA) is a method in which input parameter effect is quantified between prescribed parameter value bounds. Effect is quantified through derivatives, or by examining from the statistical perspective, variation associated with model outputs [196]. In the cardiovascular sciences and biology, sensitivity analysis (SA) is important for several reasons. Biological processes are inherently stochastic [261], and collected data are subject to uncertainty [262]. Additionally, while mathematical models are important tools for formulating and testing hypotheses about complex biological systems [263, 264], a major obstacle confronting such models is that they typically have a large number of free parameters whose values can affect model behaviour and its interpretation. It has been observed that although high-throughput methods are well-suited for discovering interactions, they remain of limited use for the measurement of biological and biochemical parameters [265]. Model parameters can also be approximated collectively through data fitting, rather than direct measurement. However, this often leads to large parameter uncertainties, if the model is unidentifiable. SA methods can be used to ensure identifiability, a property which the model must satisfy for accurate and meaningful (i.e. unique) parameter inference, given the measurement data. Below will review the literature associated with global sensitivities, which can be understood as taking the sensitivities at multiple points in the input space, before taking some measure of the average of these sensitivities. This averaged value then represents the influence that the input in question exerts on the outputs' uncertainty.

While there are many reviews on global sensitivity analysis methods [196, 197, 266, 267], few have emphasised cardiovascular problems. Qian et al. [268] provide a comprehensive review of the global sensitivity methods that exist. They highlight how variance-based measures provide the most intuitive and deep understanding of parameter influence compared to other sensitivity measures. However, Qian makes no comment on how one ensures the sensitivity metric obtained is reflective of the problem under investigation. Gul et al. [269] published a guide to performing SA on a cardiovascular system. In this work, they also advocate for variance-based measures, on the grounds of interpretability.

Olsen et al. [270] examined SA methods in mathematical biology. In this work, they

advocated, in the presence of a highly parameterised model, utilising a derivative-based measure to fix the non-influential parameters, then performing a more extensive variance-based global sensitivity analysis (GSA) to obtain the remaining parameters' true influence. This approach was leveraged by Donders et al. [271], who suggested using derivative-based methods to reduce the parameter space, again by fixing non-influential parameters. They suggested using polynomial chaos expansion to create an emulation of the system, to increase the speed of execution. They argue that an emulator facilitates a larger sample size so one can be more confident in the result of the variance-based method. Eck et al. [272] proposed a guide to uncertainty quantification in cardiovascular models, in which they suggest one should not utilise derivative methods. Instead, these authors recommend focusing efforts on training an emulator, to ensure quick computation. This device means one can perform a variance- based analysis directly; these authors make no quantifiable claims about ensuring convergence (ensuring the estimate one obtains of a sensitivity index is the correct one) other than examining a larger sample size to see if the ranking of input parameters changes. The notion of utilising a larger sample size to ensure convergence was first formalised by Yang [273], who related sensitivity convergence to the central limit theorem. Simply put, the more samples one utilises, the more likely it is to converge on single value, coupled with a small standard deviation value, for the sensitivity. A recent work by Saltelli et al. [253] highlighted how many sensitivity indices fail to utilise variance measures and focus on derivative-based measures, which leads to insufficient exploration of input space which in turn can cause incorrect parameter interpretations.

3.4.1 Derivative Methods

The most popular derivative-based method for biological sciences is the Morris method [274], which is primarily applied to reduce the computation associated with evaluating sensitivity indices [275], or as a screening technique to fix non- influential input parameters. Morris' method has featured heavily in cardiovascular modelling, since the turn of the century. Sher et al. [276] applied it to a 30-parameter cardiovascular cell model to reduce the subset of parameters for optimisation. Once the parameter space was reduced, they then coupled the reduced cell model to a simple lumped parameter model (LPM). Taconne et al. [277] developed a new model for aortic stenosis and implemented this within a four-chamber circulation model. Taconne then utilised the Morris method to reduce the input parameter set, feasibly to optimise against some clinical data. Gul et al. [278] applied the Morris method to study the impact of vessel abnormalities within the systemic circulation. The reason for this was that they needed to compute for numerous different vessel abnormalities, thus the Morris method offered an efficient solution to the problem of obtaining initial insights about the

input parameters. Olsen et al. [279] applied the Morris method and compared these results to the sensitivity indices obtained through a variance- based method, for a baroreceptor model. They highlighted that the Morris method often presented computational challenges in the implementation of the derivatives and attributed to numerical instability their different results, compared to the variance-based methods. Rolle et al. [280] utilised Morris' method to identify biomarkers of heart failure; similar work has been done with the Morris method, to identify pathophysiology in the pulmonary and coronary circulation [281, 282].

There has been a decline in use of Morris' method with the advent of more powerful computation. However, it is still used in some instances where a model contains many parameters. Colebank et al. [283] utilised Morris' method to obtain a subset of parameters to which to apply the profile likelihood method. Colebank also noted how the Morris method sometimes did not return consistent results under different model conditions. Osta et al. [284] applied it to the CircAdapt model [285] to reduce parameters for optimisation, to create a patient-specific model of arrhythmogenic cardiomyopathy-related mutation carriers. When utilising Morris' method to examine parameter effects all scenarios are different and thus the outputs on which the sensitivity metrics are computed on vary significantly between studies. However, in the work to examine biomarkers, it is common to claim parameters' effects are built into the model, the implication here being that the biomarkers of a model are an invariant of the output set utilised. Within Morris' workflow, no rigorous convergence analysis has yet been performed to check the validity of the sensitivity indices obtained.

3.4.2 Variance Methods

Sobol indices, which involve a decomposition of parameter effects into contributions to the total output variance, are widely regarded as the gold standard global sensitivity measure [196, 270, 286–288]. Qian et al. [268] state that Sobol indices are widely used in the life sciences, due to their ease of interpretation by clinicians. As Sobol indices encapsulate a decomposition of the variance, a variety of estimators have been developed for them. For first-order indices (input parameters' independent effects on the output), Saltelli et al. [289] derived a first-order estimator that is now the most commonly used. Recently, a first-order estimator developed by Azzini et al. [290] appeared to give promising results; however, it required twice as many model executions, and thus has not received sufficient attention. The total-order indices (a parameter's complete effects, not just it's independent effect) are commonly used for input parameter fixing [291, 292], to reduce the dimensionality of the input parameter space. Recently, Puy et al. [293] compared eight total-order estimators using non-linear test functions, to examine which estimator could most closely obtain the

analytical sensitivity values. Puy determined that only three out of eight tested obtained the correct values and speculated that this was due to the estimator structure, although this was not explored further.

As stated above, in section 3.4, the most common form of sensitivity convergence is the application of the central limit theorem. However, Archer et al. [294], applied the concept of bootstrapping (resampling with replacement [295]) to show how one could create quantifiable confidence intervals for any Sobol indices calculated. In this work they recommended that one utilises 1000 bootstrapped samples. Another question surrounds how many samples one should utilise; a seminal work by Saltelli et al. [289] recommended that one use 500 samples, which seems, regrettably, to have become canonical- irrespective of model properties. Despite a recommendation by Archer regarding the **interaction** with sample size, often the majority of works use no bootstrapping at all or utilise a sample size as large as possible. This sample size is often restricted by the affordable computational power [296].

Nossent et al. [297] applied 1000 bootstraps and 2500 samples to a 26-parameter environmental linear model. He noted that 500 parameter samples would have led to very different and uncertain interpretations of parameters' influence. Randall et al. [298] applied Sobol analysis to a non-linear model of the Valsalva manoeuvre containing 27 parameters and demonstrated convergence by considering increasing sample sizes of $10^3, 10^4$ and 10^5. To analyse the impact of Sobol indices, Randall considered all state variables of the model as outputs, to gain a general understanding of the model. Sala et al. [299] developed a model to simulate the cardiovascular effects of liver surgery. Here, Sala selected 10 input parameters and 12 pressure and flow measurements in the model to conduct a Sobol analysis. Sala used 10,000 samples and ensured the total-order indices were larger than the first to ensure convergence. Sala then claimed that the sensitive parameters were biomarkers providing insight into the health of a person's liver. Bjordalsbakke et al. [300] performed a Sobol analysis with 2500 samples on a one-chamber, 10-parameter cardiovascular model while examining outputs available in an ICU setting, aiming to reduce the parameter space, so the model could be calibrated to data. Bjordalsbakke utilised aortic blood pressure to rank the parameters for optimisation. No convergence studies or ranking the parameters by other outputs were considered. Karabelas et al. [301] utilised a Gaussian process to create an emulator of a whole-heart, four-chamber model, coupled to the Circ-Adapt LPM. They selected six parameters and 16 outputs to perform a sensitivity analysis, using 1600 samples and no bootstraps. Strocchi et al. [302] utilised a whole-organ to cell-scale model to identify influential parameters on heart function, using 1000 samples across 45 parameters.

The above literature overview provides insight into applications of Sobol indices within cardiovascular modelling. In the sequel, we aim to identify inconsistencies exhibited between the studies performed. In traditional CFD mesh convergence studies are expected- to ensure the accuracy of one's results [303]. In striking contradistinction, in model sensitivity analysis, it appears that despite having the tools (bootstrapping), there is a notable indifference to the certification of results. Furthermore, nobody appears to examine the shift in impact if one changes the set of outputs which parameters are ranked against - which, if the parameter ranking changes, could show impactful clinical interpretations. Our final criticism is that there is little to no interpretation of what the Sobol indices tell the investigator about the structure of the response surface- aside from basic input parameter influence.

3.5 Identifiability

There is a tension in cardiovascular modelling, between the need to incorporate mathematical descriptions of complex physiology, ranging from the cellular to the organ scale, and the necessity of developing robust, predictive, and well-constrained models. Additionally, there is no "gold standard" for model development and assessment. This lack of standardisation can lead to confusion over terminology such as model and parameter identifiability, complex and simple models, virtual populations, and other concepts, which results in potential miscommunication and misapplication of methodologies within modelling communities.

Sher et al. [304] state that the concept of parameter identifiability should be relaxed. They propose that a parameter of a model can be considered identifiable if, when optimised to experimental data, it yields sensible model parameter values. An equally pragmatic definition of identifiability was applied by Nasopoulou et al. [305], who focused on estimating the myocardial material properties. Hui et al. [306] also claimed to have developed an identifiable ionic channel cardiovascular model, as their optimised input parameters were judged to make clinical sense by medical professionals.

However, if one takes the approach outlined above, there is no guarantee that the model parameters are specific to a patient, which is of course important when making clinical stratifications. In our review of the identifiability literature, we split the concept of identifiability into the three conventional parts of the systems biology literature [307]: structural, practical, and theoretical. See Section 4.9 for further details.

3.5.1 Structural

Model parameters, estimated from experimentally measured data illuminate biological processes that are not directly measurable. The relevance of an optimised parameter set to experimental data hinges on its uniqueness—a property known as structural global identifiability. However, conducting a global structural identifiability analysis is not standard practice in biological sciences, due to the lack of user-friendly tools [308].

Performing a global structural identifiability analysis means proving that a model formulation gives a unique model output for any given parameter vector $\underline{\theta}$. However, a model can also be designated locally structurally identifiable. For strictly local structural identifiability, multiple but discretely different vectors of parameters can generate the same model outputs, which clearly raises additional concerns for practical parameter estimation (there may be multiple parameter sets which recreates the output). However, it is not certain that the system has more than one solution within the domain for practical implementation. Practical identifiability analysis needs to be performed to assess this. Given that a model is locally identifiable, it can still be globally identifiable, unless it is explicitly proven not to be. Where locally identifiable is taken to mean there exits a finite number of possible parameter values. This is a common approach within systems biology and by extension cardiovascular models, as often one can utilise expert advice to provide insight into the obtained parameter values, with the reassurance there is a finite number of possible combinations [309–313].

Structural identifiability analysis can be performed by software packages such as STRIKE-GOLD [314] and DAISY [315], which both apply differential algebraic methods to investigate the identifiability of parameters. Structural identifiability is often limited in use for cardiovascular modelling. Kirk et al. [316] utilised DAISY to investigate the identifiability of Windkessel models. However they found that any additional added complexity to the models often led to the parameters becoming only locally identifiable. This observation was confirmed by Bahnsawy et al. [317], who utilised a simple one-chamber model and simulated the effects of insulin in the model. They utilised the STRIKE-GOLD software to highlight the parameters of the model were only locally identifiable. In section 4.2 we consider the one-chamber model, on which a lot of the work in this thesis is based. The one-chamber model developed by Bjordalsbakke et al. [300] was found to only be locally identifiable when the STRIKE-GOLD software was applied to the model. In contradistinction, there have been direct proofs of global identifiability. Pironet et al. [318], directly proved the global identifiability of a simple one-chamber model. Where as Cheung et al. [319], showed that

they have a structurally unidentifiable model to start with but after reparameterizing, found they could make the model parameters identifiable.

3.5.2 Theoretical

Theoretical identifiability is concerned with the situation that, given one has a complex model that is highly parametrised and only a few measurements describing the dynamics of the system. How does one obtain a subset of parameters that, when the model is constrained by clinical (presumably) data the subset obtained will be identifiable [320, 17]? Multiple methods have been developed to address this problem, with a majority based on the formulation of the Fisher information matrix (FIM) [321], see section 4.4. The FIM is a square matrix of $n \times n$ size, where n is the dimension of the input parameter space, and contains all the information about the input parameters' influence, constrained by model outputs.

Shotwell et al. [322], formulated the FIM through local sensitivities, and prescribed a variance between the input parameters based on expert knowledge. Shotwell then examined the condition number of the FIM. They state an estimation problem is ill-conditioned when the condition number of the information matrix is large, and well-conditioned when the condition number is near one. This is then denoted K-optimal criteria of a problem [323]. Arias et al. [324], applied a similar principle of examining the condition number of the FIM. Arias took a more principled approach. They evaluated local sensitivities at many different points in input space to determine which point in parameter space provided the smallest condition number. This was then denoted their base operating point. Pant [325] developed so-called information sensitivity functions, to assess parameter information gain and identifiabilty. The aim of Pant's work was that, given a prescribed covariance matrix for a dynamical system one could relate the evaluation of the covariance matrix to the evaluation of the local sensitivity matrix. This new class of function could then be utilised to identify time intervals or regions in dynamical system behaviour where information on the parameters is concentrated, assess the effect of measurement noise on the information gain for the parameters, assess whether sufficient information in an experimental protocol (input, measurements and their frequency) is available to identify the parameters to identify the sets of parameters that are likely to be indistinguishable then assess identifiability problems for particular sets of parameters.

While the above methods provide insight into the expected difficulty in the calibration of model parameters, we are concerned to reduce input parameter space dimension to an identifiable subset- to reduce the model order. One of the earliest subset reduction methods -and most clearly documented- was developed by Li et al. [19] who presented a simple

parameter selection method, which accounts for input parameter influence derived through local sensitivities and parameter orthogonality. The magnitude of each parameter effect on the measured variables is quantified by applying principal-component analysis to the FIM matrix derived from local sensitivities. The uniqueness of each parameter effect is determined by computing the minimum distance between the sensitivity vector of the particular parameter and the vector spaces spanned by sensitivity vectors of the parameters already selected for estimation. This recursive algorithm provides a trade-off between the magnitude and linear independence of parameter effects and yields a ranking of the parameters according to their inherent ease of estimation. It is important to note here that the main assumption within the algorithm is independence of input parameters so no variance function is prescribed between the parameters. Since the method's development it has only been applied a few times to simple problems in which local sensitivities were also utilised [326–328]. Note here that we hypothesise that the Li method will generalise almost trivially but very productively, based on global sensitivity metrics.

The most utilised method for parameter subset reduction is the structured correlations method (SCM) developed by Olufsen and Ottesen [329]. The SCM has the same philosophy as that of Li et al., in that they wish to obtain a subset of uncorrelated **linearly independent** input parameters, for calibration to experimental data. The SCM first formulates the FIM with a constant variance which denotes relationships between input parameters. One then inverts the FIM to obtain the correlations matrix. Note that the FIM must be of full rank to accomplish this, thus one must fix insensitive parameters first before the inversion can happen. One then implements an iterative scheme examining the correlations between parameters, once the largest correlation is below some set threshold the algorithm is complete. This scheme has been applied widely with local sensitivities [263, 330, 331]. Recently there have been applications of this method to Sobol sensitivities [332, 333]; while the method appeared to provide promising results the assumption of a constant variance is violated by the Sobol method which assumes no correlations between parameters at all. Olsen et al. [270], compared the Li method of orthogonal sensitives to the SCM method utilising local sensitivities on a LPM and found a consistent subset of input parameters.

3.5.3 Practical

Practical identifiability (PI) has emerged as an effective but infrequently employed tool, to support model-based analysis [334, 335]. PI acknowledges variation in parameter estimates resulting from experimental conditions and the model structure, and it is focused on providing useful quantification of parameter uncertainty. The literature contains numerous definitions

of PI that are similar yet ultimately contrasting. The various iterations of measurement inaccuracy are intended to mimic the expected experimental precision. Lam et al. [336] provided a well-cited review of all methods which are "branded" as PI. As stated by Wieland et al. [17], PI can often conflate two ideas: an offline procedure to understand parameter uncertainty and an online procedure to obtain updated parameter values from noisy experimental data. In this section, we denote practical identifiability as the task of obtaining personalised input parameters, given noisy experimental data. This can be viewed as addressing the following question. Can we obtain unique and personalised input parameters given the presence of noisy clinical data?

To assess PI, one performs concurrent parameter optimisations by fixing all parameters except one, for which a cost function is then minimised. This method, denoted practical likelihood method (PL) [307] (see section 4.9.2 for more details), provides an indication of a parameter's identifiability by providing marginalised 1D slices through a response surface where a globally identifiable parameter is denoted by a global minimum cost function value. Simpson et al. [337] developed a Python workflow in which this process is automated. They demonstrated that the PL was the only method that provided interpretable information about model parameters, given experimental data. Casas et al. [338] personalised models of the systemic circulation by utilising non-invasive arterial flow and 4D MRI flow measurements. Applying the PL method, they found that 60% of model parameters were non-identifiable; however, due to their use of only model data, there was no possible explanation of whether the problem was associated with the model formulation or the noise in the experimental data used. Colebank et al. [339] utilised a 49-parameter 4-chamber model to investigate right ventricular dysfunction. Colebank first performed a Morris analysis to reduce the parameter space to 17, then performed a PL analysis on four different output sets commonly collected in clinic to investigate right heart dysfunction. Unsurprisingly, Colebank found that the more data is available, the more the parameters are found to be identifiable. Hardly less intuitive is their observation that output sets should describe different processes in the system; for example volume and flow data from the same model segment describe the same essential model process and so do not associate well. If one has a larger output set, this does not necessarily aid the parameter identification process. Pironet et al. [340] performed a PL analysis on a 7-parameter single chamber model that was previously shown to be globally structurally identifiable. Despite having shown that all parameters of the model could theoretically be found given an output set, the PL revealed that three parameters could not be obtained due to the low quality of the clinical data utilised. Interestingly, when they fixed the unidentifiable

parameters, it did not make all the inputs identifiable, indicating a geometrically complex input parameter space response surface.

3.6 Model Sloppiness

System "sloppiness" refers to anisotropy in the structure of the input parameter space, given a set of model outputs [341]. The insight provided by a sloppy analysis means one can make greater inference about the ease associated with obtaining a personalised subset of parameters. For a full definition see section 4.13.

When seeking to constrain the model parameters with clinical data after obtaining a personalisable subset, as discussed above, one needs insight into the structure of the response surface and thus the complexity of the optimisation one needs to use to calibrate a model. White et al. [18] showed that with increasingly complex biochemical models, the model sloppiness became so great that it was impossible correctly to identify any input parameters within the model when using conventionally simple optimisation methods. The issues surrounding model sloppiness were then further highlighted by Jagadeesan et al. [342] who stated that the impact of model sloppiness and its susceptibility to varying model outputs is still an open question. Jagadeean also then tried to formalise model sloppiness as it is still very much a qualitative analysis method.

In cardiovascular research to date, we could not find any literature examining the sloppiness of cardiovascular LPMs. There have been some works which have examined the sloppiness of cardiovascular electrophysiology models. For example, Fink et al. [343] highlighted that in order for models to be reusable, a quantification of their sloppiness has to be performed to ensure that researchers are not discovering the same things when seeking to personalise models. Whittaker et al. [344, 345], experimented with different model calibration methodologies to obtain personalised ionic channel parameters and commented that they could obtain different results using different optimisation methods. A reason for this was conjectured to be the model sloppiness, which the selected optimiser may struggle with. They also noted how, when different measurements were included in a cost function, this changed the rate at which optimisers were able to obtain the same value for inputs. More recently, Bravo et al. [346], utilised the concept of model sloppiness to reduce an electrophysiological model to a subset of non-sloppy parameters to make model calibration as simple as possible. It is worth noting that model sloppiness is very popular in the life sciences and is often part of many workflows when looking to calibrate model parameters in the life sciences [347–350].

3.7 Data assimilation

Sometimes in cardiovascular modelling, we have the luxury of possessing both experimental data and computational models. However, both have limitations and errors - experimental data are often of low-resolution and noisy and even high-resolution computational simulations have limitations due to uncertainty in model parameters and/or governing equations. The field of data assimilation deals with hybrid models that integrate observed experimental data with computational models. The goal is to use the computational model to advance the solution in time and based on the availability of experimental data, alter the computational model's prediction to improve solution reliability [351]. Kalman filtration methods aim to provide a simple and computationally inexpensive way to estimate the value of state variables and input parameters, given a dynamical system's prediction and experimental data [352]. For a full definition see 4.14.

Arzani et al. [353], state that while Kalman filter methods present a computationally efficient way to perform parameter optimisation, it is often difficult to estimate the error associated with the measurements of states of the system. Canuto et al. [22], utilised the ensemble Kalman filter to estimate the model parameters of a coupled 1D model to a LPM. Canuto obtained some results which were unphysiological, but reasoned that, as these parameters were not of interest in the system, they could be discounted. Julier et al. [354, 355] proposed the unscented Kalman filter (UKF) which is able to cope with the non-linearity found in many dynamical system models. The majority of Kalman filter methodologies have to resort to model approximations or linearisation's, whereas the UKF can adapt to all the features found in a model. Huang et al. [356], compared the ensemble Kalman filter to the UKF in the method's ability to recover the parameters of a 4-element Windkessel model. Huang found that the UKF recovered the known values of input parameters much more accurately than the ensemble method. However, Matzuka et al. [357] showed in a model of baroreflex regulation the ensemble Kalman filter exhibited good properties in recovering patient parameters during a head up tilt test, while no examination of the UKF was examined they propose the ensemble method should be utilised for other applications. The original work that applied the UKF to cardiovascular modelling was conducted by Lombardi [358] who examined the UKF's ability to recover the vessel properties of the 55 largest arteries in the systemic circulation. The application of the UKF to cardiovascular LPMs has been limited with much of the work been conducted by Pant et al. [14, 21, 248, 359] who focused the majority of their work on extracting system parameters from clinical data of infants who exhibited single ventricle physiology. In these works the UKF exhibited exceptional ability to recover clinically insightful parameter values at an efficient speed. It was suggested with

Pant's and Lombardi's [14, 21, 248, 359, 358] work that the UKF could be applied in clinic for continuous monitoring of patients due to the small time required to calibrate a model to data when compared to standard optimisation methods. Pant at al., also mentioned that if this was to happen the UKF has to be examined for its capability to adapt to rapidly changing physiological states.

3.8 Research Questions

The above reviewed literature defines some of the most recent methods applied to the personalisation process, applicable to LPMs. We observe six significant gaps surrounding the personalisation process as follows.

1. **Inconsistency in Best Practices for Sobol Indices:** The consensus of the literature reviewed in section 3.4.2 is that while Sobol indices are acknowledged as the most clinically interpretable global sensitivity method, there is a lack of consistency in (i) the sample sizes used and (ii) the validation of the calculated indices. A set of best practices for Sobol indices could standardise parameter interpretation and provide the community with updated guidelines, enhancing the reliability and validity of the results. This is explored in chapter 6.

2. **Application of Model Sloppiness to Cardiovascular LPMs:** As stated in section 3.6, the theory of model sloppiness has yet to be applied to cardiovascular LPMs. A consideration of sloppiness could yield new insights into the structure of the response surface associated with this class of models, guiding parameter optimisation and addressing the complexities involved in this process. This gap is explored in chapter 5

3. **Impact of Varying Model Outputs in Sensitivity Analysis:** Literature reviewed in sections 3.4.1 & 3.4.2 highlight a lack of scrutiny regarding the impact of changed model outputs, when conducting sensitivity analysis. It is crucial to understand how parameter interpretations from SA are influenced by the choice of outputs, as parameter interpretations often marginalise the impact of model outputs. This gap is explored in chapter 6.

4. **Subset Selection Methods for Personalisation:** Section 3.5.2 highlights how current methods for identifying subsets of parameters for personalisation have predominantly focused on local sensitivities, or have required researchers to prescribe correlations between parameters based on expert knowledge. Developing a subset selection method that respects the scope of clinical endeavour and minimises researchers' intervention

is needed. Additionally, there is a lack of comparison examining the stability of personalised parameters across different global sensitivity methodologies. This gap is explored in chapter 7.

5. **Interpretation of Sobol Indices for Optimisation:** Literature reviewed in section 3.4.2 highlights how Sobol indices have been used to interpret the influence of input parameters. Developing a suitable interpretation of Sobol indices to facilitate insights into the response surface's geometrical complexity can aid the optimisation stage, thereby enhancing the efficiency of the personalisation process. This gap is explored in chapter 7.

6. **Robustness of the Unscented Kalman Filter:** From section 3.7, it is clear that data assimilation methods, particularly the Unscented Kalman Filter (UKF), has received inappropriately limited attention, considering its potential ability to calibrate model input parameters to experimental data. Further investigation into the robustness of the UKF, to perturbations in input parameters and its applicability in a clinical scenario is necessary. This gap is explored in chapter 8.

Addressing these six points will clarify and enrich our perspective on the offline stage of uncertainty quantification, which is, of course, the essential precursor for personalising a model.

Chapter 4

Methods & Materials

Blessed is the man, who having nothing to say, abstains from giving wordy evidence of the fact.
— GEORGE ELIOT, Impressions of Theophrastus Such

Summary
This chapter provides mathematical descriptions of the models and methods used. We outline the theoretical foundations of LPMs and declare the various models used in this work. Proceeding to model analysis, we derive the local and global methods tested in this work, define de facto *model sloppiness, and describe our extended input parameter subset selection method and the unscented Kalman filter approach.*

4.1 Navier-Stokes Equations

4.1.1 3D Formulations

The three-dimensional (3D) incompressible Navier-Stokes (momentum) equations describe the flow of viscous fluid with a constant density, when supplemented with the continuity equation (a principle ensuring that mass is neither created nor destroyed in a fluid flow. For incompressible flow, it simplifies to the condition that the divergence of the velocity field is zero):

$$\nabla \cdot \underline{u} = \frac{\partial u_x}{\partial x} + \frac{\partial u_y}{\partial y} + \frac{\partial u_z}{\partial z} = 0 \tag{4.1}$$

where $\underline{u} = (u_x, u_y, u_z)$ is the fluid velocity in the x, y, z directions. The momentum equations is a principle that states the change in momentum of a fluid particle is equal to the sum of forces acting on it. The Navier-Stokes equation itself is a momentum conservation equation, incorporating both external forces (such as gravity) and internal forces (like pressure and viscous stresses. The equations in three directions are expressed as

$$\frac{\partial u_x}{\partial t} + \left(u_x \frac{\partial u_x}{\partial x} + u_x \frac{\partial u_y}{\partial y} + u_x \frac{\partial u_z}{\partial z} \right) + \frac{1}{\rho} \left(\frac{\partial P}{\partial x} \right) - \left(\frac{\partial \tau_{xx}}{\partial x} + \frac{\partial \tau_{xy}}{\partial y} + \frac{\partial \tau_{xz}}{\partial z} \right) = f_x \tag{4.2}$$

$$\frac{\partial u_y}{\partial t} + \left(u_y \frac{\partial u_x}{\partial x} + u_y \frac{\partial u_y}{\partial y} + u_y \frac{\partial u_z}{\partial z} \right) + \frac{1}{\rho} \left(\frac{\partial P}{\partial y} \right) - \left(\frac{\partial \tau_{yx}}{\partial x} + \frac{\partial \tau_{yy}}{\partial y} + \frac{\partial \tau_{yz}}{\partial z} \right) = f_y, \tag{4.3}$$

$$\frac{\partial u_z}{\partial t} + \left(u_z \frac{\partial u_x}{\partial x} + u_z \frac{\partial u_y}{\partial y} + u_z \frac{\partial u_z}{\partial z} \right) + \frac{1}{\rho} \left(\frac{\partial P}{\partial z} \right) - \left(\frac{\partial \tau_{zx}}{\partial x} + \frac{\partial \tau_{zy}}{\partial y} + \frac{\partial \tau_{zz}}{\partial z} \right) = f_z. \tag{4.4}$$

See [52]. Above, f_x, f_y, f_z are external source/sink body force terms, e.g. gravitational acceleration. ρ is fluid density, τ the fluid viscous stress tensor and P the pressure. The viscous stress tensor is related to the Cauchy stress tensor σ as

$$\sigma_{ij} = -P\delta_{ij} + \tau_{ij} \tag{4.5}$$

Where P is the pressure, δ_{ij} is the Kronecker delta and τ_{ij} is the viscous stress tensor.

We aim to reduce the equations down to a lumped parameter formulation. This is achieved by first reducing to a one-dimensional (1D) description of the Navier stokes equations. To reduce the 3D system into a 1D system suitable for hemodynamics, the 3D incompressible Navier-Stokes equations are first transformed into cylindrical coordinates i.e.

$$x = x, \quad y = r\sin(\theta), \quad z = r\cos(\theta) \tag{4.6}$$

Function $u_r(x,r,\theta)$ is the radial component of motion, $u_\theta(x,r,\theta))$ the circumferential component of motion and $u_x(x,r,\theta)$ the dominant axial, or streamwise component. Making an assumption of a Newtonian fluid, the 3D continuity equation becomes

$$\frac{1}{r}\frac{\partial\left(ru_r\right)}{\partial r}+\frac{1}{r}\frac{\partial u_\theta}{\partial\theta}+\frac{\partial u_x}{\partial x}=0. \tag{4.7}$$

Under the above transformation, the radial component of the momentum equation becomes

$$\begin{aligned}&\rho\left[\frac{\partial u_r}{\partial t}+u_r\frac{\partial u_r}{\partial r}+\frac{u_\theta}{r}\frac{\partial u_r}{\partial\theta}-\frac{u_\theta^2}{r}+u_x\frac{\partial u_r}{\partial x}\right]+\frac{\partial P}{\partial r}\\&-\mu\left[\frac{1}{r}\frac{\partial}{\partial r}\left(r\frac{\partial u_r}{\partial r}\right)-\frac{u_r}{r^2}+\frac{1}{r^2}\frac{\partial^2 u_r}{\partial\theta^2}-\frac{2}{r^2}\frac{\partial u_\theta}{\partial\theta}+\frac{\partial^2 u_r}{\partial x^2}\right]=\rho f_r,\end{aligned} \tag{4.8}$$

the circumferential component becomes

$$\begin{aligned}&\rho\left[\frac{\partial u_\theta}{\partial t}+u_r\frac{\partial u_\theta}{\partial r}+\frac{u_\theta}{r}\frac{\partial u_\theta}{\partial\theta}-\frac{u_r u_\theta}{r}+u_x\frac{\partial u_\theta}{\partial x}\right]+\frac{\partial P}{\partial\theta}\\&-\mu\left[\frac{1}{r}\frac{\partial}{\partial r}\left(r\frac{\partial u_\theta}{\partial r}\right)-\frac{u_\theta}{r^2}+\frac{1}{r^2}\frac{\partial^2 u_\theta}{\partial\theta^2}-\frac{2}{r^2}\frac{\partial u_r}{\partial\theta}+\frac{\partial^2 u_\theta}{\partial x^2}\right]=\rho f_\theta,\end{aligned} \tag{4.9}$$

and the axial component becomes

$$\begin{aligned}&\rho\left[\frac{\partial u_x}{\partial t}+u_r\frac{\partial u_x}{\partial r}+\frac{u_\theta}{r}\frac{\partial u_x}{\partial\theta}+u_x\frac{\partial u_x}{\partial x}\right]+\frac{\partial P}{\partial x}\\&-\mu\left[\frac{1}{r}\frac{\partial}{\partial r}\left(r\frac{\partial u_x}{\partial r}\right)+\frac{1}{r^2}\frac{\partial^2 u_x}{\partial\theta^2}+\frac{\partial^2 u_x}{\partial x^2}\right]=\rho f_x.\end{aligned} \tag{4.10}$$

Above μ represents the dynamic viscosity of the fluid. There are multiple (of course equivalent) ways to derive the 1D blood flow equations from the above 3D formulation [360]:

1. An asymptotic analysis can be performed on the 3D Navier-Stokes equations, under the assumption that the ratio of the vessel radius to length is small. This reduces the dimensionality of the system of equations, and allows higher-order terms to be neglected [114]; one then assumes that vessels are axially-symmetric (an assumption which, strictly, eliminates vessel centre line in-plane curvature, note) and that axial flow is much larger than the flow in the radial and circumferential directions [361].

2. The 1D blood flow equations governing blood flow can be derived directly from first principles on a control volume [115].

In the next subsection, we will approach the 1D formulation in a little more detail, using the mathematically satisfying approach 1, above.

4.1.2 1D Formulations

We follow process (1) declared in the previous subsection, to derive the 1D Navier-Stokes equations. Explicitly then, we make the following assumptions to obtain the well-known 1D Navier-Stokes formulation:

1. Axial symmetry means the solution must be independent of the angle θ.
2. Radial displacement is restricted to the radial direction (no circumferential or axial displacement occurs).
3. The pressure is constant in each cross-section so no radial pressure derivatives are considered
4. Axial velocity is considered much larger than radial velocity allowing radial components of velocity to be neglected.

The momentum equation then becomes

$$\frac{\partial u_x}{\partial t} + u_x \frac{\partial u_x}{\partial x} + \frac{1}{\rho}\frac{\partial P}{\partial x} - \frac{\mu}{\rho}\left[\frac{1}{r}\frac{\partial}{\partial r}\left(r\frac{\partial u_x}{\partial r}\right) + \frac{\partial^2 u_x}{\partial x^2}\right] = f_x. \tag{4.11}$$

Integrating over a section of the vessel gives the accepted form of the 1D momentum equation as

$$\frac{\partial Q}{\partial t} + \frac{\partial}{\partial x}\left(\chi\frac{Q^2}{A}\right) + \frac{A}{\rho}\frac{\partial P}{\partial x} - \int_{CS}\frac{\mu}{\rho}\left(\frac{1}{r}\frac{\partial}{\partial r}\left(r\frac{\partial u_x}{\partial r}\right)\right)d\sigma + \frac{\partial^2 Q}{\partial x^2} = Af_x, \tag{4.12}$$

Above, $Q = Au$ is the volumetric flow rate in a cross sectional area A and u is the average cross-sectional velocity. The quantity χ is a momentum flux correction factor

$$\chi\bar{u}_x^2 = \frac{1}{A}\iint_{A(x)} u_x^2 dA, \tag{4.13}$$

Above, $A(x)$ is the luminal area of a vessel, $\bar{u}_x = \frac{Q}{A}$ is the averaged fluid velocity. χ accounts for the non-uniform velocity distribution (called the Boussinesq co-efficient), and depends on the choice of velocity profile. The continuity equation becomes

$$\frac{\partial A}{\partial t} + \frac{\partial Q}{\partial x} + \psi = 0, \tag{4.14}$$

where A is the cross sectional area and ψ accounts for any source and sink terms, such as leak.

Proceeding, now, through straightforward manipulations of 4.12 and 4.14, then making the assumptions that the vessel has no taper (a cylindrical tube) and no fluid is lost or leaked from the vessel [116], we reach the accepted 1D model for arterial flow [125, 283, 362–364]:

$$\frac{\partial A}{\partial t}+\frac{\partial Q}{\partial x}=0, \text{ Continuity} \tag{4.15}$$

$$\frac{\rho}{A}\frac{\partial Q}{\partial t}+\frac{\rho}{A}\frac{\partial}{\partial x}\left(\chi\frac{Q^2}{A}\right)+\frac{\partial P}{\partial x}-\frac{f}{A}=0, \text{ Momentum.} \tag{4.16}$$

We remark that we have recently modified the 1D Navier-Stokes equation declared above consistently to account for boundary leak, at the expense of introducing an empirical slip boundary condition, consistently to account for an efflux at the luminal boundary (see the section below and appendix A). This formulation is suited to the coronary arteries and it introduces an improved level of self-consistency into recent work [198, 365, 366]. This formulation is as follows.

$$\frac{\partial A}{\partial t}+\frac{\partial Q}{\partial x}+\psi=0, \tag{4.17}$$

$$\frac{1}{A}\frac{\partial Q}{\partial t}+\frac{\partial}{\partial x}\left(\chi\frac{Q^2}{A}\right)+\frac{A}{\rho}\frac{\partial P}{\partial x}+\frac{2(\zeta+2)\pi\mu}{\rho}\frac{Q}{A}\left(1+\left(\frac{\partial R}{\partial x}\right)^2\right)^{-1/2}+\alpha\frac{Q}{A}\psi=0, \tag{4.18}$$

$$Q(0)=Q_0,\ P(0)=P_0,\ \alpha\in[0.4,1.0],\ \chi=\frac{\zeta+2}{\zeta+1},\ f=2(\zeta+2)\pi\mu, \tag{4.19}$$

Above, R is the vessel radius, ψ represents the outflow from the vessel, ζ is a velocity profile shape parameter and α is the level of slip experienced on the boundary. For a full derivation see appendix A. The transverse velocity profile is controlled by the choice of ζ. $\zeta=2$ is a parabolic flow where as $\zeta=9$ is a plug flow.

$$u_x(x,r)=u(x)\left(\frac{\zeta+2}{\zeta}\right)\left[1-\left(\frac{r}{R(x)}\right)^{\zeta}\right],\quad 0\le r\le R(x),\quad \zeta\in[1,9]. \tag{4.20}$$

4.2 Cardiovascular LPMs

Further reducing the 1D formulation to remove the axial direction variation, which can be split the compartments, we arrive at 0D formulations (see section 4.2.3 for further details).

Take continuity and integrate over length of vessel

$$\int_0^L \frac{\partial A}{\partial t}dx + \int_0^L \frac{\partial Q}{\partial x}dx = \frac{d}{dt}\int_0^L A(x)dx + [Q(x)]_0^L dx = \frac{dV}{dt} + Q(L) - Q(0) = 0 \quad (4.21)$$

One can undertake equivalent processes of compartmentalisation on momentum equations. In this way, we retain only the time variable and our chosen set of inter-compartmental flows and compartmental volumes. These equations for these compartments straightforwardly form a coupled system of (non-linear) ODEs. For present purposes, all our LPMs can be conveniently expressed in the state-space form [193]

$$\frac{d}{dt}\underline{X}(t) = \underline{f}(\underline{X}(t);\underline{\theta}), \quad \underline{Y}(t) = \underline{h}(\underline{X}(t)), \quad (4.22)$$

in which $\underline{\theta}$ denotes an input parameter vector, $\underline{X}$ represents the set of state variables of the system $\underline{f}$ is a function describing the system dynamics, $\underline{h}$ is the measurement function where e.g. forward model synthetic measurements are generated, using the computed state variables $\underline{X}$ and $\underline{Y}$ are the measurements of interest. In this work $\underline{X}(t)$ is constituted as follows

$$\underline{X}(t) = (V(t), P(t), Q(t)),\ \underline{\theta} = (\theta_1, ..., \theta_n),\ \underline{Y} = (y_1, ..., y_m). \quad (4.23)$$

Above θ_i and y_j represent an input parameter $i \in [1, ..., n]$ and model output $j \in [1, ..., m]$. n and m represent the number of input parameters and the number of model outputs in the system of interest respectively. V, P and Q represent volumes, pressures and flow rates of the system and are the state variables of the system. Below, the LPMs utilised in this work are declared. Broadly, the models were all solved *in-silico*, as state space coupled ODE problems or as the closely-related differential algebraic equation DAE system.

In figure 4.1A, parametrised by 9 inputs declared in table 4.1 we see our simplest testbench, a single ventricle representation of the systemic circulation without pulmonary representation. The model first proposed by Stergiopulos et al. [367], examined the determinants in aortic pulse pressure and left ventricular stroke volume and showed how such a simple model could be personalised to the *in-vivo* data obtained from dogs. More recently Bjordalsbakke et al, [300, 368] utilised this parsimonious example, first to perform a parameter optimisation investigation and second to show the surprising capability of this model in conjunction with exercise data. The one chamber single ventricle model serves as a test bench for a majority of our investigations. Figure 4.1B, first proposed by Shi et al., [369, 370] is again a representation of the systemic circulation however there is a greater level of detail included with the left atrium and additional vessels. This time there is also explicit representation of

the inertia associated with the blood. The 20 parameters in this LPM are declared in table 4.2.

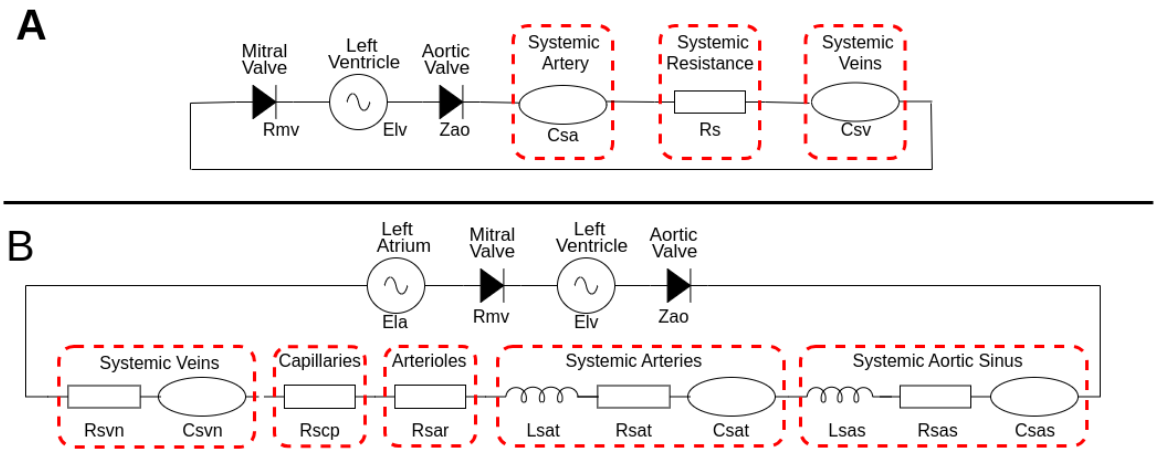

Fig. 4.1 **Simple cardiovascular models**: The 1 chamber model (A) and 2 chamber model (B) utilised in this work.

The 4 chamber models utilised in this work are displayed in figure 4.2. Comunale et al. [162], proposed the 4 chamber model in figure 4.2A and demonstrated its ability to represent human physiology. Thus, this model serves as a test bench with precedent, to facilitate the different measurements which would be available in the clinic. The 36 parameter model values are given in table 4.3. The largest model examined in this work (originally proposed Shi et al, [370]), is a 44 parameter model (figure 4.2B) which serves as popular, detailed model with systemic and pulmonary circulations. Parameters are omitted from this work as this model will serve for computational calibration between programming languages. Full parameterisation can be found in [370].
Below we declare which model was used in the following results chapters and provide a rationale for this choice.

1. **Chapter 4:** This chapter utilises the full complex 4-chamber 44-parameter model in figure 4.2B, first due to its popularity, but also it allows us to demonstrate the computational ability of the Julia language.

2. **Chapter 5:** This chapter uses the 1-chamber 9-parameter model (figure 4.1A) and the 2-chamber 20-parameter model (figure 4.1B), because this choice allows us to compare computationally expensive convergence behaviours between a simple and more complex model with similar properties and (presumably) non-linearities.

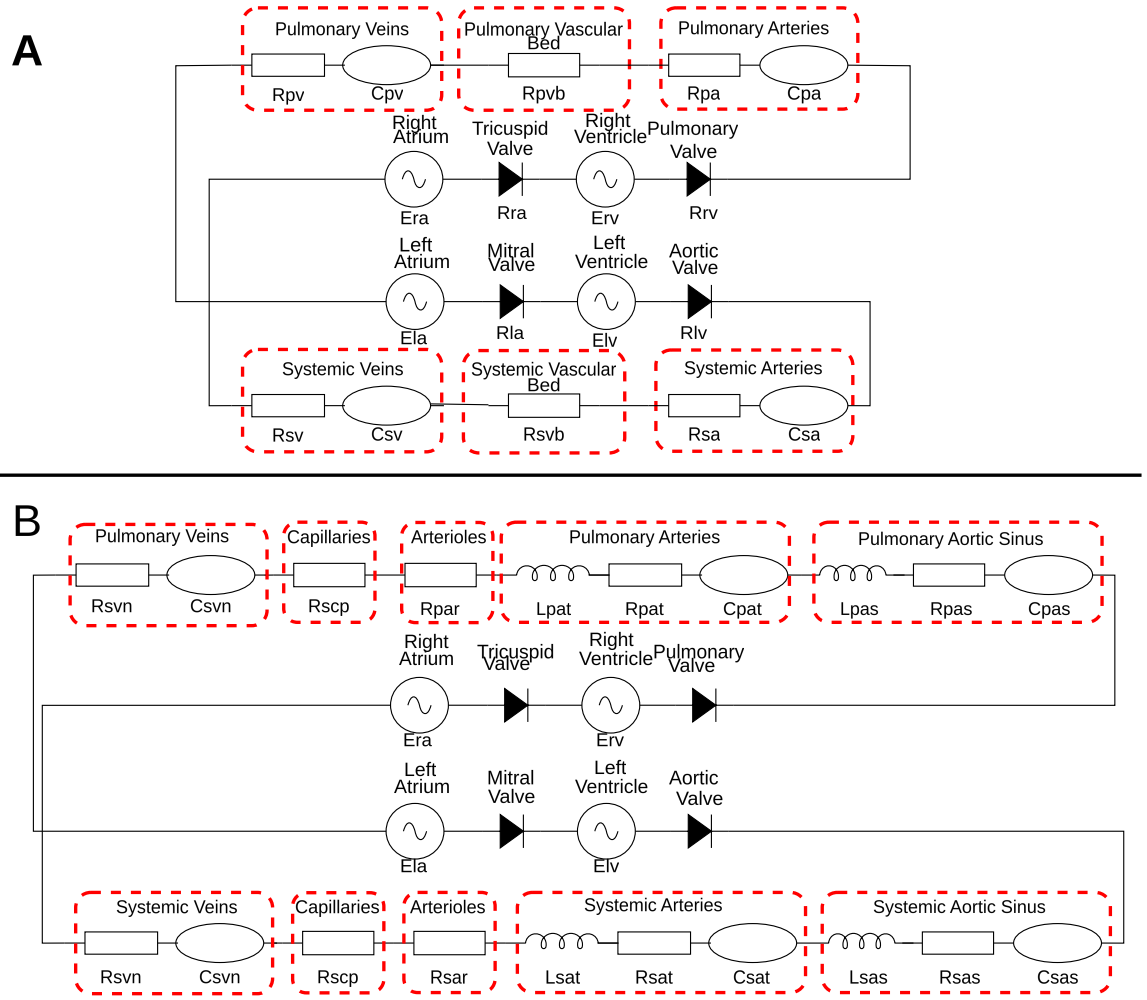

Fig. 4.2 **Complex cardiovascular models**: The 4 chamber models which are utilised in this work. The 36 parameter model in section A and the 44 parameter model in B.

Table 4.1 **Input parameters for our 1 chamber model (figure 4.1A)**: Each input parameter's unit is stated alongside a chosen initial value for the 9 parameter, single ventricle model. τ is the cardiac cycle length and is fixed such that $\tau = 1s$. The ventricular shift parameter $E_{\text{shift}} = 0$ s, as no atrium is present.

Parameter $\underline{\theta}$ (units)	Description	Initial Value
E_{max} $\left[\frac{\text{mmHg}}{\text{ml}}\right]$	Maximal ventricular contractility	1.5
E_{min} $\left[\frac{\text{mmHg}}{\text{ml}}\right]$	Minimal ventricular contractility	0.03
τ_{es} [s]	End systolic time	0.3τ
τ_{ep} [s]	End pulse time	0.45τ
Z_{ao} $\left[\frac{\text{mmHg s}}{\text{ml}}\right]$	Aortic valve resistance	0.033
R_{mv} $\left[\frac{\text{mmHg s}}{\text{ml}}\right]$	Mitral valve resistance	0.006
R_s $\left[\frac{\text{mmHg s}}{\text{ml}}\right]$	Systemic resistance	1.11
C_{sa} $\left[\frac{\text{ml}}{\text{mmHg}}\right]$	Systemic compliance	1.13
C_{sv} $\left[\frac{\text{ml}}{\text{mmHg}}\right]$	Venous compliance	11.0

3. **Chapter 6:** This chapter utilises the 4-chamber 34-parameter model in figure 4.2A because a realistic 4-chamber model facilitates the examination a large variety of cardiovascular measurements, which would not be available with the simpler models.

4. **Chapter 7:** This chapter utilises a parsimonious 1-chamber 9-parameter model, to allow us to address the development of new methodologies and their testings and also to leverage *prior art*.

5. **Chapter 8:** We conclude our results chapters by utilising the 1-chamber 9-parameter model to demonstrate the capability of the unscented Kalman filter, where a simple model allows us again to focus on the methodological development.

The models presented above represent a small fraction of the *prior art* and showcase different ways to represent the cardiovascular system. Below, we explain the choices and definitions for each compartment of the circulatory system. We emphasise at this point that the outputs generated from these cardiovascular models are utilised as a surrogates for plausible clinical measurements. See section 4.9 for further discussion about the different types of data available from the clinic and how these data can be used to provide different levels of insight.

Table 4.2 **Input parameters for our 2 chamber model (figure 4.1B)**: Each input parameter's unit is stated alongside a chosen initial value for the 20 parameter, 2-chamber model. τ is the cardiac cycle length and is fixed such that $\tau = 1s$. The ventricular shift parameter $E_{\text{shift}} = 0.92$ s as an atrium is present in this advanced 20 parameters model.

Parameter $\underline{\theta}$ (Units)	Description	Initial Value
$E_{min_{lv}}$ $\left[\frac{\text{mmHg}}{\text{ml}}\right]$	Minimal Ventricular Contractility	0.1
$E_{max_{lv}}$ $\left[\frac{\text{mmHg}}{\text{ml}}\right]$	Maximal Ventricular Contractility	2.5
$\tau_{es_{lv}}$ (s)	Ventricular Contraction	0.3
$\tau_{ep_{lv}}$ (s)	Ventricular Relaxation	0.45
$E_{min_{la}}$ $\left[\frac{\text{mmHg}}{\text{ml}}\right]$	Minimal Atrium Contractility	0.15
$E_{max_{la}}$ $\left[\frac{\text{mmHg}}{\text{ml}}\right]$	Maximal Atrium Contractility	0.25
$\tau_{es_{la}}$ (s)	Atrium Contraction	0.045τ
$\tau_{ep_{la}}$ (s)	Atrium Relaxation	0.09τ
Z_{ao} $\left[\frac{\text{mmHg s}}{\text{ml}}\right]$	Aortic Valve Resistance	0.033
R_{mv} $\left[\frac{\text{mmHg s}}{\text{ml}}\right]$	Mitral Valve Resistance	0.06
C_{sas} $\left[\frac{\text{ml}}{\text{mmHg}}\right]$	Sinus Compliance	0.08
R_{sas} $\left[\frac{\text{mmHg s}}{\text{ml}}\right]$	Sinus Resistance	0.06
L_{sas} $\left[\frac{\text{mmHg s}}{\text{ml}}\right]$	Sinus Inertia	$6.2 \cdot 10^{-5}$
C_{sat} $\left[\frac{\text{ml}}{\text{mmHg}}\right]$	Arterial Compliance	1.6
R_{sat} $\left[\frac{\text{mmHg s}}{\text{ml}}\right]$	Arterial Resistance	0.05
L_{sat} $\left[\frac{\text{mmHg s}^2}{\text{ml}}\right]$	Arterial Inertia	0.0017
R_{sar} $\left[\frac{\text{mmHg s}}{\text{ml}}\right]$	Arteriole Resistance	0.5
R_{scp} $\left[\frac{\text{mmHg s}}{\text{ml}}\right]$	Capillary Resistance	0.52
R_{svn} $\left[\frac{\text{mmHg s}}{\text{ml}}\right]$	Venous Resistance	0.075
C_{svn} $\left[\frac{\text{ml}}{\text{mmHg}}\right]$	Venous Compliance	20.5

Table 4.3 **Input parameters for our 4 chamber model (figure 4.2A):** Each input parameter is again stated along with the respective units and valves. Here we fix the heart period cycle to $\tau = 0.81$(s).

Heart Parameters					
Parameter Name	Symbol	LV	RV	LA	RA
Maximal Elastance $[mmHg/ml]$	E_{max}	2.8	0.45	0.13	0.09
Minimal Elastance $[mmHg/ml]$	E_{min}	0.07	0.035	0.09	0.045
Unstressed Volume $[ml]$	V_0	20	30	3	7
End Systolic Time $[s]$	τ_{es}	0.269τ	0.269τ	0.11τ	0.11τ
End Diastolic Time $[s]$	τ_{ep}	0.452τ	0.452τ	0.18τ	0.18τ
Atrial Activation Time $[s]$	E_{shift}	0	0	0.85τ	0.85τ
Valve Resistance $[mmHg \cdot s/ml]$	R_{val}	0.01	0.01	0.005	0.005

Circulation Parameters			Initial Volume Values		
Resistance Systemic Arteries $[mmHg \cdot s/ml]$	R_{sa}	0.0448	Initial Volume Systemic Arteries $[ml]$	$V_{sa,0}$	98.3
Resistance Systemic Vascular Bed $[mmHg \cdot s/ml]$	R_{svb}	0.824	Initial Volume Systemic Veins $[ml]$	$V_{sv,0}$	117.996
Resistance Systemic Veins $[mmHg \cdot s/ml]$	R_{sv}	0.0269	Initial Volume Pulmonary Arteries $[ml]$	$V_{pa,0}$	100.5
Resistance Pulmonary Arteries $[mmHg \cdot s/ml]$	R_{pa}	0.003	Initial Volume Pulmonary Veins $[ml]$	$V_{pv,0}$	126.4
Resistance Pulmonary Vascular Bed $[mmHg \cdot s/ml]$	R_{pvb}	0.0552	Initial Volume Left Ventricle $[ml]$	$V_{cv,0}$	149.6
Resistance Pulmonary Veins $[mmHg \cdot s/ml]$	R_{pv}	0.0018	Initial Volume Right Ventricle $[ml]$	$V_{rv,0}$	189.2
Compliance Systemic Arteries $[ml/mmHg]$	C_{sa}	0.983	Initial Volume Left Atrium $[ml]$	$V_{ca,0}$	71
Compliance Systemic Veins $[ml/mmHg]$	C_{sv}	29.499	Initial Volume Right Atrium $[ml]$	$V_{ra,0}$	67
Compliance Pulmonary Arteries $[ml/mmHg]$	C_{pa}	6.7			
Compliance Pulmonary Veins $[ml/mmHg]$	C_{pv}	15.8			

4.2.1 Heart Chambers

Recall, to characterise the contractile state of the heart chambers over the cardiac cycle, we used the concept of time-varying elastance formalised by Suga et al. [148]. This is a well-established formulation quantitatively to describe the filling and the contraction patterns of the chambers. The time-varying elastance relates chamber pressure and volume along the cardiac cycle:

$$E(t) = \frac{P(t)}{V_T(t) - V_u} = \frac{P(t)}{V_s(t)} \tag{4.24}$$

where V_u & V_s represent the unstressed and stressed volumes of the heart chamber. Note that the primitive variables which define elastance are exactly those which define the PV loop. The time varying elastance $E(t)$ may be written as parameterised mono-variate function of time as follows [169]:

$$\begin{aligned} \tilde{t} &= \text{Mod}(t + (1 - E_{shift})\tau, \tau) \\ E(\tilde{t}) &= (E_{max} - E_{min}) \cdot e(\tilde{t}) + E_{min}, \end{aligned} \tag{4.25}$$

where $e(t)$ is the activation function and describes the contraction and relaxation of the heart chamber muscle. E_{shift} is an atrial activation parameter controlling atrial contraction, thus in the case where we model a ventricle $E_{shift} = 0$. Put simply E_{shift} can be interpreted as the delay between ventricular and atrial contraction. τ is the cardiac cycle length, E_{max} and E_{min} are the values of maximal and minimal elastance (i.e., stiffness of the chamber). E_{max} corresponds to the end systolic elastance (the cardiologist's *contractility*)and E_{min} to the passive diastolic elastance of the chamber (the cardiologist's compliance). Several different elastance functions have been evolved to describe chamber contractility, below we identify the most common, usable variants (i.e. those which can be reliably parameterised). Alongside those presented below other methods exist for generating patient specific heart chamber curves. Senzaki et al. [371], utilised 72 PV loops from patients measured invasively, by conductance catheter to generate a normalised elastance curve which accurately represented the majority of pressure volume relationships. Pironet et al. [340], fit 11 Fourier coefficients to measured ventricular volumes and pressures to model the patient specific elastance function. For a full review of other fitting and function based elastance curves see [372]. Within this work we utilise the double cosine activation function for reasons discussed in chapter 9.

4.2.1.1 Double Cosine Activation Function

Here we utilise the popular double cosine function, first publicised by Shi et al. [370, 373]. We choose to utilise this function due to the simple formulation in terms of understandable input parameters:

$$e(\tilde{t}) = \begin{cases} \frac{1}{2}\left[1-\cos(\frac{\pi\tilde{t}}{\tau_{es}})\right], & 0 \leq \tilde{t} < \tau_{es}, \\ \frac{1}{2}\left[1+\cos(\frac{\pi(\tilde{t}-\tau_{es})}{\tau_{ep}-\tau_{es}})\right], & \tau_{es} \leq \tilde{t} < \tau_{ep}, \\ 0, & \tau_{ep} \leq \tilde{t} < \tau, \end{cases} \tag{4.26}$$

where $e(t;\tau_{es},\tau_{ep},E_{shift})$ is the activation function for the heart chamber and is parameterised by the end systolic and end pulse timing parameters τ_{es} and τ_{ep}, respectively. While in the original work an additional function described the addition of the the atrial kick parameter, E_{shift} allows for both ventricles and atria to be described within the same framework. This activation is represented in figure 4.3.

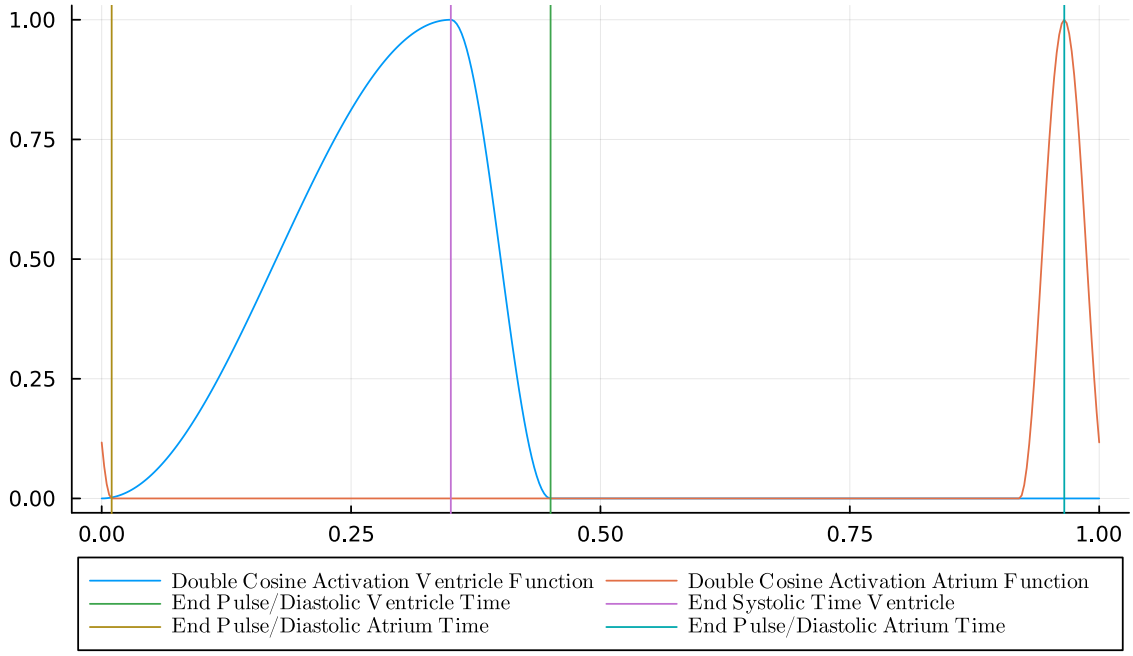

Fig. 4.3 **Double cosine activation function**: The double cosine activation function is represented over a single heart cycle. The timing parameters of the chamber are also represented.

4.2.1.2 Double Hill Activation Function

Another commonly used activation function is the double-Hill function, an extension of the Hill function in quantitative systems pharmacology [367]:

$$e(\tilde{t}) = \alpha \left(\frac{(\frac{\tilde{t}}{\alpha_s \tau})^{R_c}}{1 + (\frac{\tilde{t}}{\alpha_s \tau})^{R_c}} \right) \left(\frac{1}{1 + (\frac{\tilde{t}}{\alpha_d \tau})^{R_r}} \right). \tag{4.27}$$

Here the non-dimensional parameter α_s, R_c, α_d and R_r determine the shape of the curve within each cardiac period. The rate of chamber contraction, reflected as the slope of the ascending part of the curve, is represented by the parameter R_c. R_r corresponds to the rate of chamber relaxation (i.e., the steepness of the descending part of the curve). The systolic and diastolic time constants (τ_s and τ_d respectively) are defined as a function of $\tilde{t}$ and the dimensionless shape parameters α_s and α_d ($\tau_s = \alpha_s \tau$ and $\tau_d = \alpha_d \tau$). α_s and α_d determine the length of systole and diastole relative to each cardiac cycle each cardiac cycle, thereby controlling the time of end-systole. An increase in α_d and/or a decrease in α_s yield an increase in end-systole (i.e., a reduction of the duration of diastole), and vice versa. $\alpha = \alpha(R_c, R_r, \alpha_c, \alpha_d)$ is a normalisation constant, which is determined numerically, such that $\max(e(t)) = 1$. While this activation function provides an arguably more intuitive description of chamber contraction, the calculation of α must be repeated each time the input parameters change value. Thus, as we shall show later a sensitivity analysis requires many model evaluations and this recalculation slows down the calculation process. Finally, we remark on a discontinuity in the $e(t)$ at the time origin. which can create numerical problems with insufficiently careful characterisations. The double Hill elastance is represented in figure 4.4.

4.2.1.3 Single Fibre Elastance Model

A heart chamber can be conceived as a single fibre enveloping the cavity [374, 154]. This model is particularly suitable for lumped modelling as it was shown that under rotational symmetry the shape of the chamber and other geometric parameters had little effect on the relationship between the cavity pressure and fibre stress. This relationship is dominated by the ratio of the cavity volume V to cavity wall volume V_w as follows

$$\frac{\sigma_f}{P} = 1 + \frac{3V}{V_w}, \tag{4.28}$$

where P identifies the pressure of the chamber and σ_f is the stress in the fibre. The fibre stress is composed of two components: an active component σ_a and a passive component σ_p

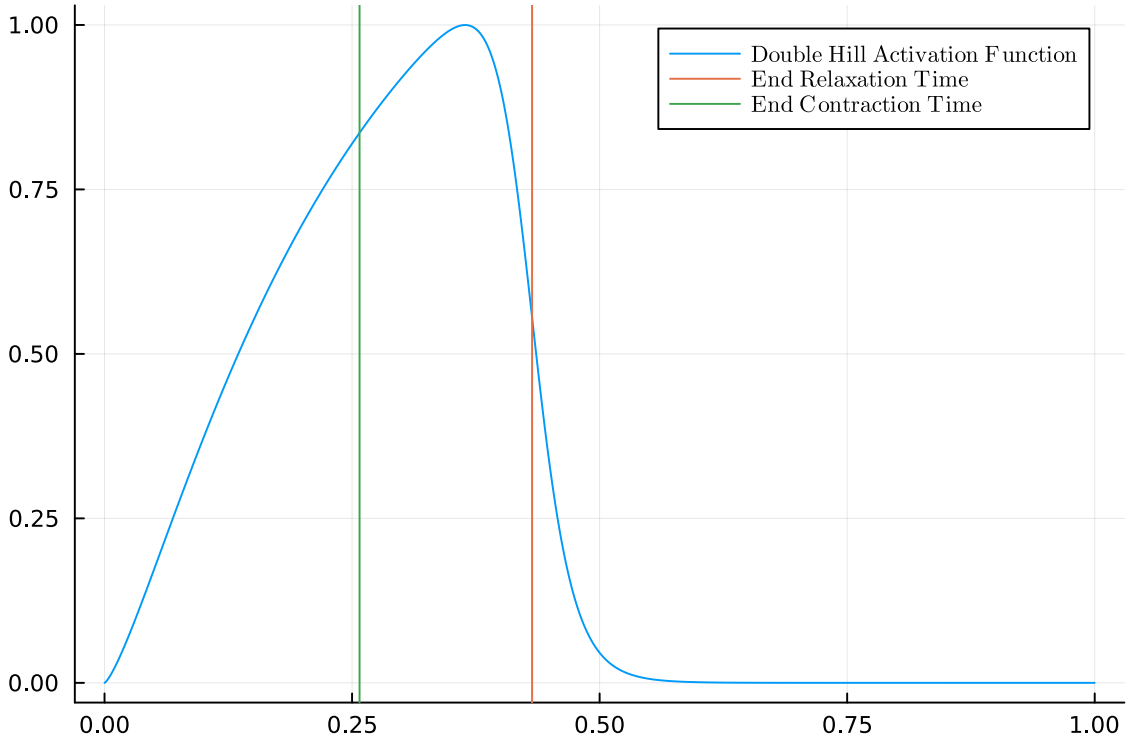

Fig. 4.4 **Double Hill Elastance**: The Double Hill activation function is represented over a single heart cycle. With chamber timing parameters represented also.

such that

$$\sigma_f = \sigma_a + \sigma_p. \tag{4.29}$$

If V_0 and l_0 represent the unstressed cavity volume and sarcomere length respectively, at zero transmural pressure, then at a general state of cavity volume V, the sarcomere [375] length, l, can be written as

$$\frac{l}{l_0} = \lambda = \left(\frac{1+\frac{3V}{V_w}}{1+\frac{3V_0}{V_w}}\right)^{1/3}, \tag{4.30}$$

where λ is the dimensionless fibre stretch ratio. The sarcomere shortening velocity, v_s, is given by

$$v_s = -\frac{dl}{dt} = -\frac{l}{V_w}\left(1+\frac{3V}{V_w}\right)^{-1}\frac{dV}{dt}. \tag{4.31}$$

The active component of stress can be described as

$$\sigma_a = T_{a0} f(l) g(t_a) h(v_s), \tag{4.32}$$

$$f(l) = \begin{cases} 0, & \text{if } l < l_{a0}, \\ \frac{l-l_{a0}}{l_{am}-l_{a0}}, & \text{if } l_{a0} < l \leq l_{am}, \\ 1, & \text{if } l_{am} < l \leq l_{ae}, \\ \frac{l_{af}-l}{l_{af}-l_{ae}}, & \text{if } l > l_{ae}, \end{cases} \tag{4.33}$$

$$g(t_a) = \begin{cases} (\frac{1}{2}(1-\cos(\frac{2\pi t_a}{t_{max}})))^{E_a}, & \text{if } t_a < t_{max}, \\ 0, & \text{otherwise}, \end{cases} \tag{4.34}$$

$$h(v_s) = \frac{1-\frac{v_s}{v_0}}{1+c_v\frac{v_s}{v_0}}, \tag{4.35}$$

where t_a is the time since activation of the cavity, t_{max} is the total time of activation in a cardiac cycle, v_0 is the initial sarcomere shortening velocity, T_{a0} is the maximum active sarcomere stress, and c_v is a prescribed shape parameter. The l parameters are scaromere lengths at different parts of chamber contraction.

The passive stress is given by

$$\sigma_p = \begin{cases} 0, & \text{if } \lambda < 1, \\ T_{p0}(\exp(c_p(\lambda-1))-1), & \text{if } \lambda \geq 1, \end{cases} \tag{4.36}$$

where T_{p0} and c_p are sarcomere material constants. This formulation of chamber contraction is well utilised in the field of elctromechanics (see the book [376]) which model the calcium and ion channels driving ventricular contraction however is outside the scope for this work [343, 377–379]. There have been extensions to the single fibre model, such that sarcomere contraction for segments of the ventricular wall can be computed. For the extensions see [285, 380]. A representation of the single fibre elastnace is given in figure 4.5.

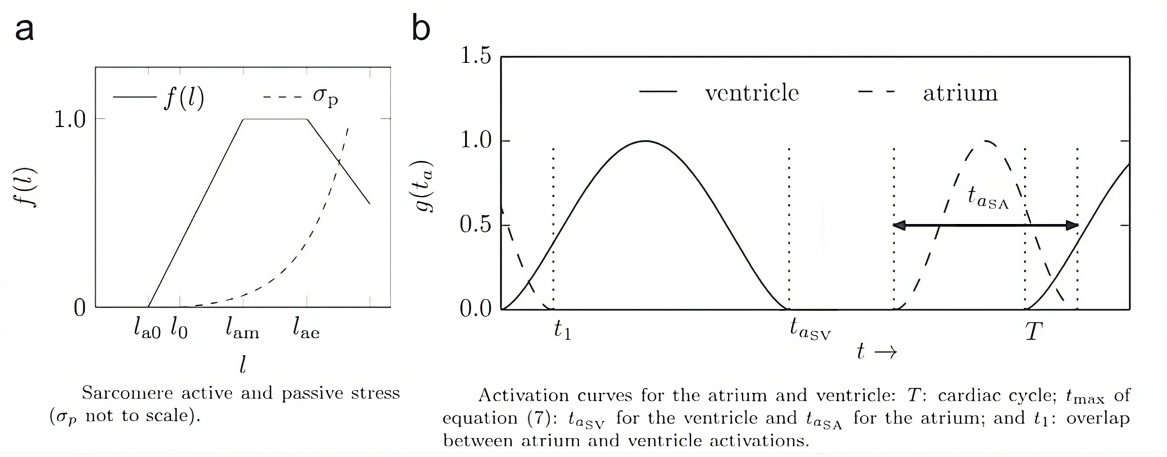

Fig. 4.5 **Single Fibre Elastance**: The single fibre activation function is represented over a single heart cycle. The dynamics of the sarcomere fibres are also represented. Reproduced with permission from [14]

4.2.1.4 Exponential Functions

Smith et al. [179], proposed a time varying elastance function by relating the end systolic pressure-volume relationship (ESPVR) and the end diastolic pressure-volume relationship (EDPVR), which define the upper and lower limits of the cardiac cycle. For reference see the PV loop in figure 1.6.

The equations approximating the ESPVR and EDPVR are:

$$P_{es}(V) = E_{es}(V - V_u) \tag{4.37}$$

$$P_{ed}(V) = A(\exp(\lambda(V - V_u)) - 1), \tag{4.38}$$

Clearly, the end systolic pressure P_{es} stands in a linear relationship with volume V with the elastance E_{es} and unstressed volume V_u. A weighted combination of the above pressures produces an equation for the instantaneous pressure volume relationship in a single chamber in terms of pressure P, volume V and time t and the activation function, which controls the

weight.

$$P(V,t) = e(t)E_{es}(V - V_u) + A(1 - e(t))(\exp(\lambda(V - V_u)) - 1) \tag{4.39}$$

$$e(t) = \sum_{i}^{N} A_i \exp(-B_i(t - C_i)^2). \tag{4.40}$$

Above A_i, B_i, C_i and N determine the shape of the activation function. A representation of the exponential elastance function can be seen in figure

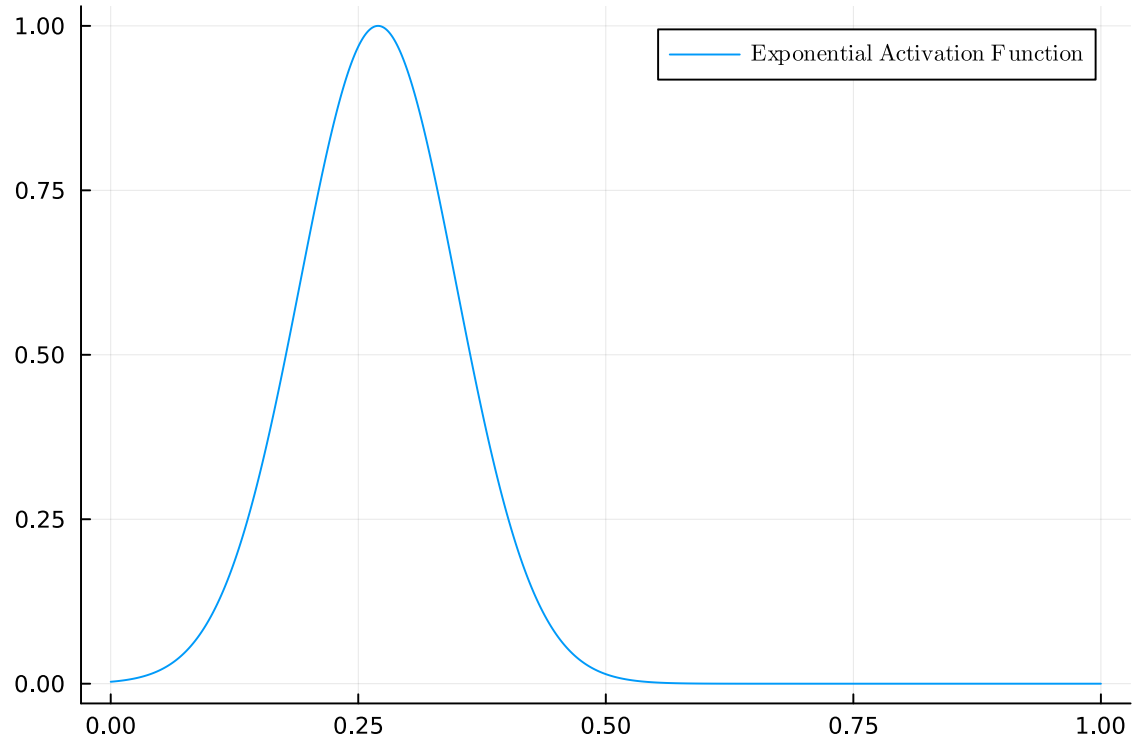

Fig. 4.6 **Exponential Elastance**: The exponential activation function is represented over a single heart cycle.

4.2.2 Heart Valves

We account for the 5 different valve functions which have applications to LPMs. Here, we utilise a diode valve, however the other valves could be applied to diseased valve situations.

4.2.2.1 Diode valve

The simplest formulation of blood flow in and out of the ventricles and atria is modelled as diodes, with Ohmic resistance under a forward pressure drop bias and infinite resistance under reverse bias. Thus, a diode valve has a slope discontinuity at the pressure origin which has the potential to excite numerical instability. Straightforward cubic polynomial interpolation (smoothing) near the pressure origin can overcome this but in the work reported here this has not been necessary. A diode valve was first implemented by Segers et al. [20] and, as mentioned in the introduction, it is still the most common approached when modelling healthy heart valves. The popular formulation is as follows:

$$Q_k = \begin{cases} \frac{P_{k-1}-P_{k+1}}{R_{val}}, & P_{k-1} > P_{k+1}, \\ 0 & P_{k-1} \leq P_{k+1}, \end{cases} \tag{4.41}$$

where $R_{val} = (R_{av}, R_{mv}, R_{pv}, R_{tv})$ represent the resistances across aortic, mitral, pulmonary and tricuspid valves. The subscripts $(k-1), k, (k+1)$ respectively represent the valve's proximal, present and distal system compartments. As there is no pressure associated with the heart valve it effectively constrains the pressure difference across $(k-1)$ and $(k+1)$ compartments. To exemplify our subscript notation,consider the flow across the mitral valve; the valve equation becomes

$$Q_{mv} = \begin{cases} \frac{P_{la}-P_{lv}}{R_{mv}}, & \text{Valve Open}, \\ 0 & \text{Valve Closed}, \end{cases} \tag{4.42}$$

where (k-1) = la (left atrium), k = mv and (k+1) = lv (left ventricle) and the mitral valve is taken to have an infinite reverse bias resistance i.e. permit no regurgitation whatsoever.

4.2.2.2 Orifice vale

Consider some physiological features exhibited by the valves, first introduced by Shi et al. [370]. These authors consider the basic pressure–flow relation in the pulmonary valve and introduce an orifice model:

$$Q_k = \begin{cases} CQ_k \cdot AR_k \cdot (P_{k-1} - P_{k+1})^{\frac{1}{2}}, & P_k \geq P_{k+1}, \\ 0 & P_{k-1} < P_{k+1}. \end{cases} \tag{4.43}$$

For the simple model, the valve opening area (AR_k) is calculated as for a simple diode

$$AR_k = \begin{cases} 1, & P_{k-1} \geq P_{k+1}, \\ 0 & P_{k-1} < P_{k+1}, \end{cases} \tag{4.44}$$

where $AR = 1$ represents the valve at its maximum opening angle. In the orifice model we designate $CQ([\frac{ml}{s \cdot mmHg^{0.5}}])$ to be the flow coefficient (which is different for both the semilunar and atrioventricular valves) and can be written

$$CQ = \sqrt{\frac{2A_{base}^2}{\rho K}}, \tag{4.45}$$

where ρ is blood density k is the flow coefficient, (this is explored in more detail in the next section), and A_{base} is the base area of the inlet conduit to the valve. These values were tuned manually, to produce near physiological cardiovascular behaviour over a range of mitral stenosis and aortic regurgitation cases analysed in [169].

4.2.2.3 Shi valve

We consider a more physiologically realistic model developed in [169]. As above the flow rate depends on the valve flow coefficient CQ but now also the valve opening AR. The valve opening is decided by the angular position of the valve leaflets

$$AR = \frac{(1 - cos(\theta))^2}{(1 - cos(\theta_{max}))^2} \tag{4.46}$$

$\theta = 0$ corresponds to the valve leaflet fully closed and θ_{max} corresponds to the specified fully open position of the valve. The leaflet angular position is computed by considering the various factors that affect the leaflet motion. This leaflet is governed by

$$\frac{d^2\theta}{dt^2} = \frac{Fp - Ff + Fb - Fv}{I}, \tag{4.47}$$

where Fp, Ff, Fb, Fv represent the pressure, frictional, velocity, vortex effects and I is the moment of inertia prescribed to the valve, the following consideration of which relates specifically of the mechanics of the pulmonary valve.

The pressure effect is proportional to the pressure on the valve leaflet surface:

$$Fp_k = (P_{k-1} - P_{k+1}) k_{p,k} \cos(\theta). \tag{4.48}$$

The fluid velocity effect is proportional to the flow rate normal to the leaflet surface

$$Fb_k = k_{b,k} Q_k \cos(\theta). \tag{4.49}$$

The frictional effect due to resistance in the tissue at the valve root is assumed to be proportional to the leaflet angular velocity

$$Ff_k = k_{f,k} \frac{d\theta}{dt}. \tag{4.50}$$

Shi et al. initially developed the valve opening angle considering only pressure force [373, 370] however in their 2006 they work added these additional forces, most notably the vortex force behind the leaflet which was shown to be influential in a number of works [381–383]. The product of the effect of the leaflet angular position and the flow rate is constructed to represent the vortex effect in the heart valve dynamics. We argue that the bigger the flow rate in the valve, the stronger the vortex intensity near the valve. Also, it is assumed that vortex intensity reaches the maximum value when the leaflet is at about $\frac{\pi}{4}$ opening angle. Below $\frac{\pi}{4}$, the smaller the valve opening angle, the more likely it is for the flow to pass the valve as laminar flow. Similarly, above $\frac{\pi}{4}$, the bigger the valve opening angle, the more likely the leaflet will cover the valve root area and restrict vortex formation. A suitable Fv is:

$$Fv_k = \begin{cases} k_{v,k} \sin(2\theta) Q_k, & Q_k \geq 0, \\ 0 & Q_k < 0. \end{cases} \tag{4.51}$$

Combining the above effects and substituting $K = \frac{k}{I}$, the equation for the opening angle of the pulmonary valve is :

$$Fv_k = \begin{cases} K_{p,k}(P_{k-1} - P_{k+1})\cos(\theta) - K_{f,k}\frac{d\theta}{dt} + K_{b,k} Q_k \cos(\theta) - K_{v,k}\sin(2\theta) Q_k, & Q_k \geq 0, \\ K_{p,k}(P_{k-1} - P_{k+1})\cos(\theta) - K_{f,k}\frac{d\theta}{dt} + K_{b,k} Q_k \cos(\theta). & Q_k < 0. \end{cases} \tag{4.52}$$

This very detailed consideration of valve dynamics, considering additional forces and regurgitant flow improves the physical fidelity of the simulation. Modelling of the remaining two valves is implemented in a similar way, with different parameterisation to reflect the changed physiology.

We comment in passing on an implementation issue. Given θ represents the valve opening

angle we define $\frac{d\theta}{dt} = \omega$ to be the angular velocity. The change in ω is acceleration (relative) (i.e. the quotient force/moment) when leaflets are at min/max; this will be zero unless the force direction is away from the min/max position.

4.2.2.4 Mynard valve

The next valve model created by Mynard et al. [170] relates both the flow and pressure difference ΔP using the a relaxed form of the Bernoulli invariant, to form an approximation:

$$\Delta P = BQ|Q| + L\frac{dQ}{dt} \tag{4.53}$$

Here the Bernouill resistance, B, controls the dynamic pressure loss to dissipation with decelerating distal flow to the vena contracta and pressure differences related to convective acceleration. Of course, in the inviscid theory which underpins the Bernoulli invariant, there would be complete recovery of pressure. We write:

$$B = \frac{\rho}{2A_{eff}^2}, \tag{4.54}$$

where ρ is the constant blood density and A_{eff} is an effective cross sectional area on the valve. $L[mmHg \cdot s^2/ml]$, the blood inertia accounts for the pressure difference ΔP related to blood acceleration and is defined as

$$L = \frac{\rho l_{eff}}{A_{eff}}, \tag{4.55}$$

where $l_{eff}[cm]$ is an effective length from the previous compartment to the valve. To control valve dynamics we define a variable, $\psi(t)$ which damps the effective opening area A_{eff}, which is controlled by

$$A_{eff}(t) = [A_{max} - A_{min}]\psi(t) + A_{min}, \tag{4.56}$$

where A_{max} and A_{min} represent the maximum and minimum cross sectional area of the respective valve. To add extra physics to the model which will allow for stenosis and regurgitation we can express these maximum and minimum areas as

$$A_{min} = K_{rg}A_{ann}, \;\; A_{max} = K_{st}A_{ann}, \tag{4.57}$$

where A_{ann} represents the annulus area, held to be constant in the literature [248, 14, 359], and K_{rg} and K_{st} characterise the fitness of a particular patient's valve.

The parameters K_{rg} and K_{st} take values between 0 and 1, where a healthy valve is characterised by $K_{rg} = 0$ and $K_{st} = 1$. $K_{rg} > 0$ corresponds to the level of regurgitation present within the heart valve. In contrast, $K_{st} < 1$ corresponds to a stenosed valve. This valve model is one of a simpler approach only relying on the pressure difference to be the most influential factor on the valve. We therefore say valve opening and closing depends on two variables:

1. The pressure difference ΔP.
2. The damping variable $\psi(t)$.

Assuming that the valve opens/closes when the pressure difference ΔP exceeds a threshold opening/closing pressure value $\Delta P_o, \Delta P_c$. We therefore define the rate of opening and closing as:

$$\frac{d\psi}{dt} = (1-\psi)K_o(\Delta P - \Delta P_o) \tag{4.58}$$

$$\frac{d\psi}{dt} = \psi K_c(\Delta P - \Delta P_c), \tag{4.59}$$

where K_o and K_c are the opening and closing rate coefficients respectively.

In implementation we define two valve functions one for the semilunar and one for the atrioventricvular. Due to $l_{eff} = 0$ for the atrioventricular valves, this causes a singularity when calculating the flow rate of the mitral and tricuspid valve. To accommodate for this we define a valve function in which we assume there are no inertial effects, L. Hence the flow rate is totally dependent on the Bernoulli resistance in the equation below. We set the minimum opening area to $eps()$ which allows us to simulate the smallest regurgitation possible:

$$\Delta p = Bq|q|. \tag{4.60}$$

4.2.3 Circulation Systems

The lumped parameter model equations can be derived using first principles, or can be found by linearising the 1D system in equation 4.15 and then averaging physical properties over the domain length. In order to reduce the 1D system of equations to 0D, the 1D system is linearised around its reference state, which means the non-linear convection term $\frac{\partial}{\partial x}(\chi \frac{Q^2}{A})$ is

first neglected. This leads to the system of equations:

$$\begin{cases} C_{0D}\frac{\partial P}{\partial t} + \Delta Q = 0, & \text{continuity} \\ L_{0D}\frac{\partial Q}{\partial t} + \Delta P + R_{0D}Q = 0, & \text{momentum} \\ C_{0D} = \frac{\partial A_0}{\partial P_0}\Delta x, \quad L_{0D} = \frac{\rho}{A_0}\Delta x, \quad R_{0D} = \frac{8\mu\pi}{A_0^2}\Delta x, & \end{cases} . \tag{4.61}$$

Separating the above equations out into their explicit electrical analogue components we obtain

$$L_k\frac{dQ_k}{dt} = P_{k-1} - P_k \tag{4.62}$$

$$C_k\frac{dP_k}{dt} = (Q_k - Q_{k+1}) \tag{4.63}$$

$$Q_k = \frac{P_{k-1} - P_k}{R_k} \tag{4.64}$$

$$\frac{dV_{s,k}}{dt} = Q_k - Q_{k+1}. \tag{4.65}$$

Here L_k, C_k, R_k are the model parameters for a compartment of interest k. Here, we assume all chambers in the system have a constant compliance ($C = 1/E$).

4.3 Local Sensitivity Analysis

Local, derivative based sensitivities are essentially partial derivatives, evaluated at a base state in input parameter space, $\underline{\theta}_0$. To compare a parameter i's influence evenly against the output j, we scale the absolute sensitivity metric by $\frac{\theta_i}{y_j}$. The result is a relative sensitivity matrix $\mathbf{S}$, of size $(m \times n)$, with entries $S_{j,i}$. For input parameters $i \in (1,...,n)$ and outputs $j \in (1,...,m)$:

$$S_{j,i}(t) = \left[\frac{\theta_i}{y_j}\frac{\partial y_j(t)}{\partial \theta_i}\right]_{\underline{\theta}_0} . \tag{4.66}$$

The relative sensitivity index is a normalised measure and this enables comparisons between input parameters with different units or values at different orders of magnitude.

We define relative sensitivity column vectors associated with a specific model input parameter, i, as follows:

$$\underline{S}_i = (S_{i,1}, S_{i,2}, ..., S_{i,m})^T , \; i = 1,...,n \tag{4.67}$$

where $S_{i,1}$ represents the influence of input parameter i against the measurement 1 (say). To compute the above sensitivity statistics, the inputs are, of course, varied *one at a time* about a base physiological state $\underline{\theta}_0$. LSA is useful in quantifying the impact of input parameters at a well known base state. However, due to the variation associated with human physiology, it is important to understand the global nature of an input parameters' influence.

4.4 Fisher Information Matrix

Another important matrix derived from sensitivity matrices is the square $(n \times n)$ Fisher information matrix (FIM) [270, 321] which was briefly introduced above:

$$F = \mathbf{S}^T \mathbf{S}. \tag{4.68}$$

This is a symmetric matrix representing the information one can extract on input parameters, or factors, from the model outputs which usually correspond to the available measurements [384]. We note that the FIM can be constructed from either global or local sensitivity matrices.

4.5 Global Sensitivity Analysis

The point of GSA is best highlighted with figure 4.7 below. Let us imagine a response surface in figure 4.7 below as describing the physiology of a particular patient - at least in terms of one particular model output; as we traverse such a response surface (changing parameter values as we go) this is going to have an impact on all selected outputs.

If one were to perform a LSA, one would be working at single point in parameter space, observing the rate of change in the output, which amounts to determining the tangent plane to the response surface. Of course, this knowledge tells us nothing about the structure associated with such a response surface. GSA allows one to explore response surface within some sub-space defined by physiological bounds $[\underline{\theta}_{min}, \underline{\theta}_{max}]$ and identify key influential input parameters, impacting the outputs averaged across input parameter space.

4.5.1 Morris Method

The Morris method [385] can be viewed as an extension of the local derivative-based sensitivity measures of the previous section. This extension turns the Morris method into

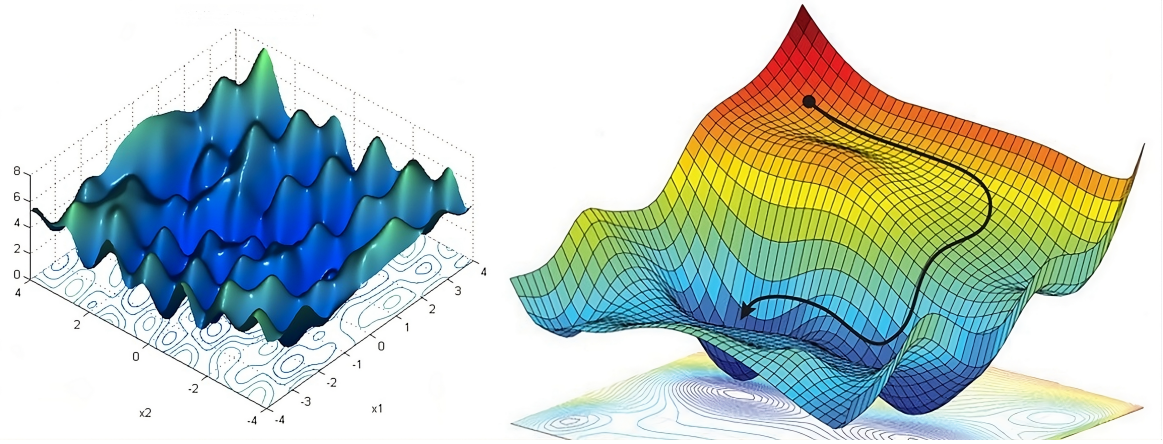

Fig. 4.7 **Example model response surfaces**: Two prototype response surfaces, left : exhibiting complex non-linear behaviour, right : exhibiting less complex structure, with a clear global minimum. Reproduced with permission from [15].

a global technique, making it one of the more widely applied sensitivity methods. Instead of taking the partial derivative of the output with respect to the input parameter of interest θ_i, the Morris method approximates this derivative using a finite difference scheme. The resultant value is called the elementary effect, EE_i of the ith factor:

$$EE = \frac{\underline{f}(\underline{\theta}+\Delta) - \underline{f}(\underline{\theta})}{\Delta}, \; \Delta = \frac{n}{2(n-1)}, \tag{4.69}$$

where the step size is Δ with n the number of input parameters [196].

Each of the inputs is, first, re-scaled to be uniformly distributed in the interval $[0,1]$. Starting from an initial base value, selected at random from a uniform distribution, one random input is incremented or decremented and its elementary effect calculated. From this next position, another random input is again incremented, and this inputs' elementary effect calculated and so on until we have calculated one elementary effect for each factor. The aim of the Morris method is to take the average of a number of elementary effects, each calculated at different points in input parameter space. Denoting this number by r, we would then require a total of r elementary effects per input. Hence, we repeat the process described above $(r-1)$ times to generate the remaining elementary effects. Each repetition, called a run, generates a set, or trajectory, of n elementary effects (one per input). The full algorithm can be found in [385, 287].

Having computed these r elementary effects per input, we find the average of their ab-

solute global values, μ_i^* and the variance of the values σ_i^2:

$$\mu_i^* = \frac{\sum_{k=1}^{r} |EE_i^k|}{r},\ \sigma_i^2 = \frac{\sum_{k=1}^{r} (EE_i^k - \mu_i)^2}{r-1}, \tag{4.70}$$

where EE_i^k denotes the elementary effect of the ith input during the kth model evaluation. μ_i^* is the absolute mean of these elementary effects. The greater the value of μ_i^* the more the ith factor affects the model output, while the greater the σ_i value, the more the input is nonlinear or involved with interactions with other inputs; a low σ_i, by contrast, indicates a linear, additive input. While Morris's original paper [385] used only μ_i, Campolongo et al. [386] introduced the μ_i^* term. They observed that, by using their absolute values, elementary effects of different signs would not cancel each other out in. However, the variance of the elementary effects still use μ_i to calculate σ_i. The Morris method is computationally efficient, requiring $r(n+1)$ model evaluations and can be extended to deal with groups of inputs [196]. The Morris method provides only semi- quantitative information and so is typically used for input screening [196, 386]. However, being a semi- quantitative method, there is no definitive boundary separating the important and unidentifiable parameters. With no ability to check parameter influence convergence this can present significant issues with the reliability of any model interpretations made. The Morris method is at a disadvantage when dealing with input interactions. Though able to detect if an input is involved in nonlinearities or interactions, it cannot determine which of these is present, nor, in the case of interactions, can it identify which input(s) is/are involved. Instead the Morris method gives only one lumped measure, σ_i, of the total magnitude of its interactions and nonlinearities. Despite the Morris methods popularity Saltelli and Annoni [16] showed that in higher parameter dimensions the Morris method can suffer from serious problems in the methods ability to explore input parameter space. This is due to the methods one at a time sampling methodology although improvements to this have been suggested [387, 388]. A visual representation of this problem is displayed in figure 4.8. In situations where more clarity is required, we turn to the more computationally expensive variance-based methods discussed next.

4.5.2 eFAST Method

The extended Fourier amplitude test [389] offers a computationally efficient alternative to Sobol indices (below). eFAST utilises mono- dimensional Fourier decomposition along a

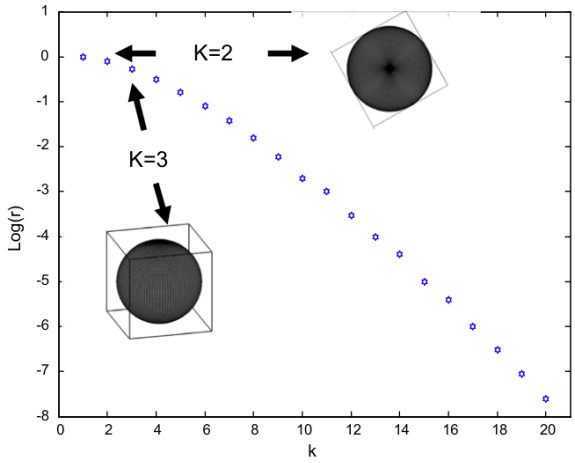

Fig. 4.8 **The curse of dimensionality**: In $k = 3$ dimensions the volume of the sphere internal to a cube and tangent to its face is $r = 0.5$. r goes rapidly to zero with increasing k. Reproduced with permission from [16].

curve exploring the parameter space. The curve is defined by a set of parametric equations:

$$\begin{aligned} \theta_i(s_j) &= G_i(\sin(\omega_i s_j)), \forall i = 1,...,n \\ s_j &= \frac{2j\pi}{N} - \pi, \forall j = 1,...,N \end{aligned} \tag{4.71}$$

where G_i is a transformation function chosen to ensure that the variable is sampled according to the desired probability density function. ω_i is a set of different (angular) frequencies, to be properly selected, associated with each input parameter. As s varies, all the factors change simultaneously along a curve that systematically explores input parameter space. Each θ_i oscillates periodically at the corresponding frequency ω_i, whatever G_i is. The output Y shows different periodicity, combined with the different frequencies ω_i, whatever the model f is. If the i^{th} factor has strong influence on the output, the oscillations of Y at frequency ω_i will be of high amplitude. This provides a basis for computing a sensitivity measure, which, for input θ_i, is founded on the coefficients of the corresponding frequency ω_i and its harmonics. For a full derivation and discussion of frequency choice, see [390, 391].

This GSA methodology allows for parameter interpretations in terms of their independent effects and their collective impact on the chosen inputs. While this method provides an easy way to interpret input effects it is highly dependent on the above hyper-parameters. There is also no known method to evaluate the accuracy of the parameter interpretations. The eFAST methodology requires $k \cdot n$ model evaluations where k is the number of chosen samples and n the number of parameters.

4.5.3 Sobol Indices

Given the state space equation in (4.22) with input parameters $\underline{\theta} = (\theta_1, \theta_2, ..., \theta_n)$ and f the function of a model. Assume the model is composed of independent random variables, the joint probability density function of the input is:

$$P(\theta_1, ..., \theta_n) = \prod_{l=1}^{n} p_l(\theta_l). \tag{4.72}$$

Where p_l is the individual parameter probability distribution. The mean of an output y can be computed as

$$\mathbb{E}(y) = \int \cdots \int f(\theta_1, ..., \theta_n) \prod_{l=1}^{n} p_l(\theta_l) d\theta_l. \tag{4.73}$$

and the variance of an output y

$$\begin{aligned} \mathbb{V}(y) &= \int \cdots \int (f(\theta_1, ..., \theta_n) - \mathbb{E}(y))^2 \prod_{l=1}^{n} p_l(\theta_l) d\theta_l \\ &= \int \cdots \int f^2(\theta_1, ..., \theta_n) \prod_{l=1}^{n} p_l(\theta_l) d\theta_l - \mathbb{E}^2(y). \end{aligned} \tag{4.74}$$

Assume a particular factor θ_j is fixed at value $\hat{\theta}_j$, the resulting variance of y will be equal to:

$$\begin{aligned} \mathbb{V}(y|\theta_j = \hat{\theta}_j) &= \int \cdots \int (f(\theta_1, ..., \hat{\theta}_j, ..., \theta_n) - \mathbb{E}(y|\theta_j = \hat{\theta}_j))^2 \prod_{\substack{l=1 \\ l \neq j}}^{n} p_l(\theta_l) d\theta_l \\ &= \int \cdots \int f^2(\theta_1, ..., \hat{\theta}_j, ..., \theta_n) \prod_{\substack{l=1 \\ l \neq j}}^{n} p_l(\theta_l) d\theta_l - \mathbb{E}^2(y|\theta_j = \hat{\theta}_j). \end{aligned} \tag{4.75}$$

When performing sensitivity analysis one is interested in marginalising out the impact of $\hat{\theta}_j$ by integrating $\mathbb{V}(y|\theta_j = \hat{\theta}_j)$ over the probability density function of $\hat{\theta}_j$, this gives:

$$\begin{aligned} \mathbb{E}(\mathbb{V}(y|\theta_i)) = &\int \cdots \int f^2(\theta_1, ..., \hat{\theta}_j, ..., \theta_n) \prod_{\substack{l=1 \\ l \neq j}}^{n} p_l(\theta_l) d\theta_l \\ &- \int \mathbb{E}^2(y|\theta_j = \hat{\theta}_j) p_j(\hat{\theta}_j) d\hat{\theta}_j \end{aligned} \tag{4.76}$$

Subtracting equation (4.76) from equation (4.74) one obtains:

$$\mathbb{V}(y) - (E)(\mathbb{V}(y|\theta_j)) = \int \mathbb{E}^2(y|\theta_j = \hat{\theta}_j) p_j(\hat{\theta}_j) d\hat{\theta}_j - \mathbb{E}^2(y). \tag{4.77}$$

Utilising the identity below [392]:

$$\mathbb{V}(y) - (E)(\mathbb{V}(y|\theta_j)) = \mathbb{V}(\mathbb{E}(y|\theta_j)). \tag{4.78}$$

The above is a good measure of the sensitivity of y with respect to the input parameter θ_j. Thus we obtain the first order index for an input parameter θ_j,

$$S_j = \frac{\mathbb{V}_{\theta_j}(\mathbb{E}_{\theta_j^c}(y|\theta_j))}{\mathbb{V}(y)}, \tag{4.79}$$

where θ_j^c denotes the complementary set of input parameters excluding θ_j. The inner expectation operator functions such that the mean of y is taken over all possible values of θ_i^c while keeping θ_i fixed. The outer variance is taken over all possible values of θ_i.

Sobol indices were first proposed by I.M Sobol [393], whose problem was that of identifying a subset of the n factors that could account for the most of the variance of an output y. Imagine that the inputs can be partitioned into two subsets $\underline{u} = (\theta_{i_1}, \theta_{i_2}, ..., \theta_{i_m})$ and the remaining set $\underline{v} = (\theta_{l_1}, \theta_{l_2}, ..., \theta_{l_{n-m}})$. Then according to Sobol the overall effect of the subset $\underline{u}$ on the variance of the output can be estimated from:

$$U_v = \int \cdots \int f(\underline{u}, \underline{v}) f(\underline{u}', \underline{v}) d\underline{u} d\underline{u}' d\underline{v}, \tag{4.80}$$

$$\mathbb{V}(\mathbb{E}(y|\underline{v})) = U_v - E^2, \tag{4.81}$$

$$\mathbb{V}(\mathbb{E}(y|\underline{u})) + \mathbb{V}(\mathbb{E}(y|\underline{u}, \underline{v})) = \mathbb{V}(y) - \mathbb{V}(\mathbb{E}(y|\underline{v})). \tag{4.82}$$

In equation (4.82), $\mathbb{V}(\mathbb{E}(y|\underline{u}))$ is the first order effect of the set $\underline{u}$, while $\mathbb{V}(\mathbb{E}(y|\underline{u}, \underline{v}))$ is the interaction term between between the sets $\underline{u}$ and $\underline{v}$. If $\mathbb{V}(y) \approx \mathbb{V}(\mathbb{E}(y|\underline{v}))$, then $\underline{u}$ is non-influential and all inputs in $\underline{u}$ would be conventionally fixed in subsequent analysis of the model.

Equation (4.82) is a particular case of a general variance decomposition scheme proposed by Sobol whereby the total unconditional variance can be decomposed as

$$\mathbb{V}(y) = \sum_i \mathbb{V}_i + \sum_i \sum_{j>i} \mathbb{V}_{ij} + ... + \mathbb{V}_{12...n}, \tag{4.83}$$

where

$$\mathbb{V}_i = \mathbb{V}(\mathbb{E}(y|\theta_i)) \tag{4.84}$$

$$\mathbb{V}_{ij} = \mathbb{V}(\mathbb{E}(y|\theta_i,\theta_j)) - \mathbb{V}_i - \mathbb{V}_j \tag{4.85}$$

and so on. Equation (4.83) contains n terms of first order $\mathbb{V}_i$, $\frac{n(n-1)}{2}$ terms of second order $\mathbb{V}_{ij}$ and so on, till the last term of order n, for a total of $2^n - 1$ terms. The $\mathbb{V}_{ij}$ terms are the second order (or two-way) terms, analogous to the second order effects that capture that part of the effect of θ_i and θ_j that are not described by the first order terms. Equation 4.83 is based on the Sobol-Hoeffding decomposition of the model function f into terms of increasing dimensionality [286].

$$f(\theta_1,...,\theta_n) = f_0 + \sum_i f_i(\theta_i) + \sum_i \sum_{j>i} f_{ij}(\theta_i,\theta_j) + ... + f_{12,...,n}. \tag{4.86}$$

The decompositions in 4.83 and 4.86 are unique, provided that the input factors are independent and that the individual terms in 4.86 are square integrable and have zero mean over the domain existence and have the orthogonality property

$$\int_0^1 f_{1,2,3,..,K} d\theta_k = 0, k = 1,2,...,K.$$

One important aspect of Sobol's development is that similar decompositions can be written by taking the factors into subsets. Thus from 4.84, $\mathbb{V}_i = \mathbb{V}(\mathbb{E}(y|\theta_i^c))$ is the total contribution to the variance of y due to non θ_i. This implies that

$$\mathbb{V}(y) - \mathbb{V}(\mathbb{E}(y|\theta_i^c)) \tag{4.87}$$

is equal to the sum of all terms as shown in 4.82 that include θ_i. By using the relationship in 4.78, we illustrate the case for $n = 3$:

$$S_{T,1} = \frac{\mathbb{V}(y) - \mathbb{V}(\mathbb{E}(y|\theta_1^c))}{\mathbb{V}(y)} = \frac{\mathbb{V}(\mathbb{E}(y|\theta_1^c))}{\mathbb{V}(y)} = S_1 + S_{12} + S_{13} + S_{123}. \tag{4.88}$$

Writing the general form of the index

$$S_{T,i} = \frac{\mathbb{V}(y) - \mathbb{V}(\mathbb{E}(y|\theta_i^c))}{\mathbb{V}(y)} = \frac{\mathbb{V}(\mathbb{E}(y|\theta_i^c))}{\mathbb{V}(y)}. \tag{4.89}$$

This sensitivity index is termed the total effects as they provide insight into the non-linearity associated with the model. It is important to note that for a purely linear additive model

$\sum_{i=1}^{n} S_i = 1$. The sensitivity indices can be computed at a cost of $k(n+2)$ model evaluations. However if we wanted to compute the second order indices also this has an additional associated cost of $k(2n+2)$ model evaluations [287].

For continuous measurements, calculating the sensitivity index produces waveform data which demonstrate the sensitivity of each input parameter over (say) the cardiac cycle [394]. In order to quantify the effects continuous measurements have on the calculation of sensitivity indices, we typically average this sensitivity waveform. Rather than averaging across a time range (which process regions of low variance equally to those of high variance), one seeks to expose differential sensitivities by examining variance-weighted averages:

$$TAS_i = \frac{\sum_k S_i(\underline{Y}^c(t_k))\mathrm{Var}(\underline{Y}^c(t_k))}{\sum_k \mathrm{Var}(\underline{Y}^c(t_k))}, \tag{4.90}$$

where TAS_i is the time averaged first/total order effect of an input parameter i and $\underline{Y}^c(t_k)$ represents the approximated continuous measurement at time step k. The division is performed component-wise such that $TAS_{T,i}$ is of size $(m \times 1)$ and this vector represents the time averaged sensitivity indices for an input parameter i against all outputs m.

4.5.3.1 Bootstrapping

A strong advantage of the Sobol indices is supplement of a bootstrap methodology which can be utilised to produce a confidence interval for the true unknown indices [294]. Clearly, no estimate of sensitivity can be of any use without an estimate of its variability. Bootstrapping is a well-known method within statistics (see chapters 12,13,14 and 22 of [395]). The samples generated for $\{\theta_i\}$ are resampled (i.e sampled with replacement) B times, at each stage and each sensitivity index S_i is recalculated, leading to a bootstrap estimate of the sampling distribution of the sensitivity indices, $\{\tilde{S}_i^b\}_{b=1}^B$ for $i = 1, ..., n$. From this distribution, confidence intervals can then be constructed utilising the moment method. This provides a symmetric 95% interval for S_i as

$$\hat{S}_i \pm 1.96 \times \sqrt{\frac{1}{B-1}\sum_{b=1}^{B}(\tilde{S}_i^b - \tilde{S}_i^*)^2} \tag{4.91}$$

$$\tilde{S}_i^* = \frac{1}{B}\sum_{b=1}^{B}\tilde{S}_i^b. \tag{4.92}$$

Bootstrapping works because sampling with replacement from a set of independent, identically distributed data is equivalent to sampling from the empirical distribution function of

the data. A crucial point is that each bootstrap sample is created directly from the original dataset without needing any further data or model evaluations.

4.6 Hyperspace Investigation

Sobol indices provide the deepest possible insight regarding which input parameters contribute to the variation of the output. They will prove vital in extracting a subset of input parameters which can be personalised. However, the end goal of personalised medicine is to constrain the model parameters using patient data. A wide variety of optimisation routines exist for calibrating models to patient data. The complexity of the optimisation routine which is needed is often decided by the non-linearity of the model which is under investigation. Below we propose a methodology utilising Sobol indices which provides insight into the non-linearity of the model, indicating the complexity of the optimisation routine required.

One can interpret the total order Sobol indices as [297]:

$$S_{T,i} = S_i + \sum_{i \neq j} S_{ij} + \sum_{i \neq j \neq k} S_{ijk} + ...,$$

i.e., for a given input parameter θ_i, the total order indices are the first order indices *plus* all higher order interactions. Subtracting the first order indices

$$\begin{aligned} S_{T,i} - S_i &= \sum_{i \neq j} S_{ij} + \sum_{i \neq j \neq k} S_{ijk} + ... \\ S_{T,i} - S_i &= S_{H,i}, \end{aligned} \tag{4.93}$$

where we nominate the $S_{H,i}$ as the higher order interactions for an input parameter θ_i. If $S_{H,i} \approx 0.0$, one can deduce that the model inputs impact the model outputs in an independent way.

Total order sensitivity indices have been shown to exhibit superior ability to recover the truer sensitivity compared to first order indices [293, 290]. Thus, one can utilise the total order indices to quantify the complexity of the input parameter space.

With the necessary background in place, we are now able to declare an investigative test procedure for our models' sensitivity assessments:

1. Perform an extensive SA at the maximum bounds for our study: $\pm 15\%$ to compute S_1, S_2 and S_T. Calculate the respective confidence intervals.

2. Ensure all sensitivity indices exhibit a statistical variation of less than 5% of the mean value.

3. Calculate S_H.

   (a) if $S_H < 0.01$, proceed using only S_T.

   (b) If $S_H > 0.01$, proceed as follows but examine S_1 and S_T to ensure each sensitivity index has converged.

4. Ensure consistent sampling density and converged sensitivity indices; reduce the input parameters hyperspace volume (hypercube's edge length), recording the ranking and sensitivity values of each input parameter.

5. Once the hypercube volume investigated corresponds to an edge length of less than $\pm 0.05\%$ from base state, finish the investigation.

6. Once all input parameter rankings and values have been recorded, examine the variation between the edges of the input parameter hypercube compared to the minimal variation from the base state.

If a consistent input parameter ranking is exhibited at all hypercube sizes, one can infer a less complex input parameter space, with obvious consequences for model personalisability. On the other hand, if we observe large variations in input parameter rankings when the hypercube sizes are varied, one would infer a more complex input parameter space hyper-surface - a greater encumbrance to personalisation, due to multiple candidate local minima affecting the input parameter ranking variations.

Here, we examine hypercube sizes of $\pm 15\%, \pm 7\%, \pm 3\%, \pm 0.5\%$ and $\pm 0.01\%$ starting with a sample size of $N = 100,000$ at $\pm 15\%$. See chapter 7 for the results of this methodology.

4.7 Sampling Methodology

We turn to a brief description of the input parameter space sampling methodologies to be assessed. We concern ourselves with two popular Monte Carlo (MC) sampling methodologies: Uniform (U) and Latin Hypercube (LH), and three Quasi-Monte Carlo (QMC) sampling methods: Golden Ratio (GR), Lattice Rule (LR) and Sobol Sequence (SS). All

can be generated utilising the QuasiMonteCarlo.jl [396] package provided by Julia lang [397].

For inputs $\underline{\theta}$ which range over a bounded region, we consider a functional $I[\underline{f}](t)$, formed from the integral of $\underline{f}$, as defined in equation (4.22), over the unit hypercube $I^n = [0,1]^n$ where n represents the dimensionality of the input parameter space:

$$I[\underline{f}](t) = \int_{I^n} \underline{f}(\underline{X}(t;\underline{\theta}),\underline{\theta}) d\underline{\theta}. \tag{4.94}$$

The effect of sampling model inputs can be assessed with reference to this integral; in doing so we view the sampling process as an effective quadrature, in which the sampled inputs define the abscissa. The quality of the sampling can then be measured by the quality of the quadrature. The important question of how its accuracy is determined in conjunction with the sampling of the hypercubic region of input parameter space is clearly germane to a robust and reliable sensitivity analysis.

4.7.1 Monte-Carlo Sampling Methods

4.7.1.1 Uniform sampling

The simplest sampling approach is uniform sampling [398]. Input parameters $\underline{\theta}$ are regarded as uniformly distributed random variables, within the hypercube I^n such that:

$$I[\underline{f}](t) = \mathbb{E}[\underline{f}(\underline{X}(t;\underline{\theta})] \approx \frac{\sum_i^N \underline{f}(\underline{X}(t;\underline{\theta}^i),\underline{\theta}^i)}{N} \quad \text{for} \quad i \in [1,N], \tag{4.95}$$

where $\mathbb{E}$ is the expectation operator, $\underline{\underline{\theta}}$ is a $N \times n$ matrix where each row is a parameter vector $\underline{\theta}$ of length n. Whilst mathematically and algorithmically simple, this is deemed a crude approximation with poor convergence rates [399].

4.7.1.2 Latin hypercube sampling

The efficiency of MC methods is determined by the properties of the random samples. A priority for researchers is to develop strategies which ensure points are placed more uniformly, within I^n. One response is to use Latin hypercube (LH) [400]- a very common methodology in life sciences [401–404].

Its main objective is to reduce the variance, and thus the error, associated with evaluating Eq. (4.94). One decomposes the space of inputs into N sub-spaces typically of equal volume, to ensure the space is sampled as uniformly as possible. Let $\{\varepsilon_j^i\}$, for $j = 1,...,n$, be independent random permutations of samples $i = 1,...,N$, each uniformly distributed over all

$N!$ possible permutations. One then sets

$$\theta_j^i = \frac{\varepsilon_j^i + U_j^i - 1}{N}, \;\; j = 1,...,n, \;\; i = 1,...,N, \tag{4.96}$$

where U_j^i are independently randomly sampled points on the [0,1] interval. One can intuit how only one sample point of the input parameters falls between $\frac{i-1}{N}$ and $\frac{1}{N}$ for each dimension $j = 1,...,n$. Here, we use the 'standard' version of LH, but see [405] for other variations.

4.7.2 Quasi Monte-Carlo Sampling Methods

An improvement on the Monte-Carlo sampling methodologies is the low discrepancy sampling (LDS) methods, coupled with the QMC algorithm, as shown in [406, 407]. Discrepancy is a measure of the deviation of sampled points from the uniform distribution [408]. Consider a number of points N_R from a sequence $\{\theta_i\}$, for $i = 1,..,N$, in an n-dimensional rectangle R centred upon an origin 0, whose sides are parallel to the coordinate axes, which is a subset of $I^n : R \subset I^n$, where R is attached with a measure. A sequence has low discrepancy if the proportion of points in the sequence falling into an arbitrary set R is close to the measure of R. LDS satisfies the upper bound condition [409]:

$$D_N \leq k(n)\frac{[ln(N)]^2}{N}, \tag{4.97}$$

where D_N is the sample discrepancy and $k(n)$ is a particular constant depending on the sequence and size of input parameter space. LDS is designed to place sample points as uniformly as possible within a hypercube, instead of the statistical approach adopted in LH. The QMC approximation of the integral in Eq. (4.94) has identical form to Eq. (4.95).

$$I[\underline{f}] = \frac{\sum_i^N \underline{f}(\underline{X}, \underline{\theta}^{i,q})}{N}, \tag{4.98}$$

except in this framework, $\underline{\theta}^{i,q}$ is a quasi sampled parameter vector which has been generated from an LDS and the points are distributed uniformly in the unit hypercube I^n. As a consequence, the sample points generated on I^n have a deterministic nature.

4.7.2.1 Golden ratio sampling

Golden ratio sampling is an LDS sampler in which sample points are based on the fractional part of successive integer multiples of the golden ratio. First introduced by Schretter and Kobbelt [410], using a simple incremental permutation of a generated golden ratio sequence,

they demonstrated equal coverage of a two-dimensional space. Let $\underline{\theta} = (\theta_1, \theta_2, \ldots, \theta_n)$ be a n-dimensional parameter vector, where each parameter θ_i has a lower bound $\theta_i^{\min}$ and an upper bound $\theta_i^{\max}$. We want to generate N samples of $\underline{\theta}$.

First, we define a set of n distinct points $\{\underline{x}_i\}_{i=1}^n$ in $\mathbb{R}^n$ as follows:

$$\underline{x}_i = \left(\frac{\cos\left(\frac{2\pi i}{n}\right) - \theta_i^{\min}}{\theta_i^{\max} - \theta_i^{\min}}, \frac{\sin\left(\frac{2\pi i}{n}\right) - \theta_i^{\min}}{\theta_i^{\max} - \theta_i^{\min}}, \ldots \right), \quad \text{for} \quad i \in [1, n]. \tag{4.99}$$

Then, we define a set of n weights $\{w_i\}_{i=1}^n$ using the golden ratio ϕ:

$$w_i = \frac{\phi^i}{(\phi^n - (-\phi)^{-n})}. \tag{4.100}$$

To generate N samples $\{\underline{\theta}_j^*\}_{j=1}^N$, we use the following procedure:

$$\underline{\theta}_j^* = \sum_{i=1}^{d} w_i \underline{x}_i \odot (\underline{\theta}^{\max} - \underline{\theta}^{\min}) + \underline{\theta}^{\min}, \tag{4.101}$$

where $\odot$ denotes the element-wise product, $\underline{\theta}^{\min}$ and $\underline{\theta}^{\max}$ are the vectors of lower and upper bounds, respectively. In this work, we will test GR sampling for systems with input parameter dimensions much higher than two.

4.7.2.2 Rank-1 lattice rule sampling

Another LDS technique is the rank-1 lattice rule. Let an n-dimensional rank-1 lattice Π be a set of points that contains no limit points and satisfies [411]:

$$\underline{\theta}' \in \Pi \implies \underline{\theta} + \underline{\theta}' \in \Pi \text{ and } \underline{\theta} - \underline{\theta}' \in \Pi, \ \forall \underline{\theta}. \tag{4.102}$$

A general lattice is constructed by a generating matrix $\underline{\underline{G}} \in \mathbb{R}^{n \times n}$:

$$\Pi = \{\underline{\underline{G}} V | V \in \mathbb{Z}^n\}, \tag{4.103}$$

where V is any integer unimodular vector. A generator matrix is not unique to a lattice Π, i.e., Π can be obtained from different generator matrices. A rank-1 lattice is a special case of the general lattice, which has a simple operation for point set construction, instead of directly using Eq. (4.103). A rank-1 lattice point set can be constructed as

$$\underline{\theta}_i := \left\langle \frac{i\underline{z}}{N} \right\rangle, \ i = 0, \ldots, N-1, \tag{4.104}$$

where $\underline{z} \in \mathbb{Z}^n$ is the generating vector and the inner product denotes the operation of taking the fractional part of the input number element-wise. One can then scale $\underline{\theta}_i$ as above to obtain parameter samples between the specified bounds. Compared with the general lattice rule, the construction form of the rank-1 lattice already ensures the constructed points are inside the unit cube, without the need for any further checks.

4.7.2.3 Sobol sequence sampling

Our final sampling methodology is the well-known Sobol LDS technique [412]. The Sobol sequence is widely considered as the optimal sequence for exploration of an input parameter space [403, 413–415]. The Sobol low-discrepancy sequence is quasi-random, and based on the following equation:

$$\theta_i = \sum_{j=1}^{\infty} \frac{a_{i,j}}{2^j} \underline{v}_j, \quad \text{for} \quad i \in [1,n] \tag{4.105}$$

where $a_{i,j}$ is the j-th digit in the binary representation of i, and $\underline{v}_j$ is the j-th direction vector in n dimensions.

To ensure that the samples $\underline{\theta}_i$ lie within specified bounds for each dimension, we can modify the equation as follows:

$$\theta_i = \underline{\theta}^{\min_i} + \left(\sum_{j=1}^{\infty} \frac{a_{i,j}}{2^j} \underline{v}_j \odot (\underline{\theta}^{\max_i} - \underline{\theta}^{\min_i}) \right). \tag{4.106}$$

The direction vectors $\underline{v}_j$ are pre-computed and can be obtained from various sources. One common choice is to use the direction vectors provided by Sobol [412]. Put simply, the Sobol LDS aims to achieve three requirements: (1) best uniformity as $n \to \infty$; (2) good distribution even with small parameter sizes; (3) a very fast computational algorithm.

4.8 Computation of Sobol Indices

Given the first and total order Sobol indices of equations 4.79 and 4.89 and the methods above detailing sample generation for a GSA we now examine how numerically to implement Sobol index calculation. This leads us to consider so-called estimators. For the first order index we utilise the most popular estimator [289]

$$S_i = \frac{1}{k} \sum_{j=1}^{k} f(B)_j (f(A_B^{(i)})_j - f(A)_j). \tag{4.107}$$

Where A and B are independent sampling matrices to be discussed in more detail shortly. Inappropriately, there is little effort directed on furthering first order indices. Recently an impressive estimator authored by Azzini et al. [290, 416] appeared, which had largely superior convergence properties compared to the standard estimator however this estimator required more model evaluations which conventionally increases the computational time (however this apparent failing requires further study).

Here, we shall explore four commonly chosen total order estimators: Homma and Saltelli [417], Sobol [418], Jansen [419] and Janon et al. [420]. While this list is far from exhaustive, it represents a selection of total order estimators which have been practically used within the field and are not costly to execute.

Table 4.4 **Total order estimators**: Formulae to compute S_T, where f_0 and $\mathbb{V}$ represent the mean and variance of the outputs respectively, as defined in Eqs. (4.108) and (4.109).

Authors	Estimator S_T
Homma & Saltelli [417]	$\mathbb{V}(Y) - \frac{\sum_{j=1}^{k} f(A)_j f(A_B^{(i)})_j}{k} + f_0^2$
Sobol [418]	$\frac{\sum_{j=1}^{k} f(A)_j [f(A)_j - f(A_B^{(i)})_j]}{k}$
Jansen [419]	$\frac{\sum_{j=1}^{k} [f(A)_j - f(A_B^{(i)})_j]^2}{2k}$
Janon et al. [420]	$\mathbb{V}(Y) - \frac{\sum_{j=1}^{k} f(A)_j f(A_B^{(i)})_j}{N} - f_0^2$

For the Homma & Saltelli, Sobol and Janson estimators, their mean and variance take the following form:

$$f_0 = \frac{\sum_{j=1}^{k} f(A)_j}{k}, \quad \mathbb{V}(Y) = \frac{\sum_{j=1}^{k} [f(A)_j - f_0]^2}{k-1}, \tag{4.108}$$

and for the Janon estimator:

$$f_0 = \frac{\sum_{j=1}^{k} [f(A)_j + f(A_B^{(i)})_j]}{2k}, \quad \mathbb{V}(Y) = \frac{\sum_{j=1}^{k} [f(A)_j^2 - f(A_B^{(i)})_j^2]}{2k} - f_0^2. \tag{4.109}$$

We imagine having two independent sampling matrices A and B, with a_{ji} and b_{ji} as particular elements. The index i runs from 1 to n, the number of input parameters. The index j runs from 1 to k, the number of model samples generated. The $A_B^{(i)}$ is a matrix where all columns are from A except the ith column which is from B. For a complete estimation of the first and

total order index $2k$ simulations are need to compute the outputs $\underline{Y}$ corresponding to the A and B matrices. Then an additional kN simulations are needed to compute $\underline{Y}$ from the $A_B^{(i)}$ matrices.

4.9 Identifiability Analysis

In addition to the parameters' influence, it is imperative to determine if parameters are identifiable. The identifiability issue confronts the possibility that a large distribution of parameters may exist to describe similar model outputs and behaviours. Within this context, two concepts exist: structural, practical and theoretical identifiability [336, 337, 421, 422].

4.9.1 Structural Identifiability

The concept of structural identifiability was first introduced by Bellman and Astrom [421]. The aim of structural identifiability is to determine to what extent it is possible to gain insight into the internal structure of a system from input-output measurements. This question was studied by identifying "input-output equations" from Laplace transformations of linear ODEs. The study was the first to mention local and global structural identifiability, which was defined formally in the study by Ljung and Glad [423] as follows. Given the state space equation in (4.22), a parameter θ_i is structurally globally identifiable if

$$\underline{f}(\underline{X}(t), \theta_i) = \underline{f}(\underline{X}(t), \tilde{\theta}_i) \tag{4.110}$$

holds true for $\theta_i = \tilde{\theta}_i$. An input parameter θ_i is considered locally identifiable if 4.110 holds true for θ_i within a small neighbourhood of $\tilde{\theta}_i$.

The above statements suggest that if one parameter is structurally unidentifiable, the entire system is structurally unidentifiable. To demonstrate a case of structural non-identifiability, consider the system

$$\frac{du}{dt} = \theta_1 \theta_2 u(t). \tag{4.111}$$

Parameters θ_1 and θ_2 are considered structurally unidentifiable because similar model outputs can be observed by offsetting changes in one parameter by varying the other. Structural identifiability assesses whether model parameters can be uniquely inferred based solely on the model structure without considering actual experimental observations [421]. These analyses assume that model structures are accurate and that no measurement errors exist, assumptions that are clearly not valid in practice.

4.9.2 Practical Identifiability

While structural identifiability captures the maximum possible input parameter information, additional analysis is needed to examine practical identifiability of a model using real, noisy data. A structurally identifiable model may still be practically unidentifiable for example, if the model identifiability is sensitive to measurement error in the data or if measurements are taken too sparsely and miss key features of the system dynamics. Practical identifiability analysis takes into account the quality of the reference output signals, namely their sampling and the measurement and modelling errors. The question is thus whether the input parameters still can be uniquely determined under real experimental conditions. A practical identifiability analysis requires actual reference output signals and effectively probes model response to error. In such cases of noisy data, practically identifiable combinations can often be found. Unidentifiability refers to model outputs observed for multiple parameter values, i.e., there is a non-unique minimum during parameter optimisation [337, 331].

Many other methods have been proposed which have focused on the sensitivity matrix as methods of practical identifiability. However any generated sensitivity matrices are created from forward model solutions. Thus any interpretations do not account for any noise.

For examining the identifiability of the system in the presence of noise associated characteristic of clinical data, there is, insofar as we are aware, only the profile likelihood method introduced by Raue et al [424]. This is a general approach for detecting structural and practical unidentifiabilities not captured by sensitivity approaches. This method “profiles" each parameter θ_i, by estimating all other parameters while keeping θ_i fixed, resulting in the likelihood profile for the fixed parameter given the maximum value of the likelihood of each parameter value [425]. Structurally unidentifiable parameters are characterised by a flat profile likelihood, and practically unidentifiable parameters by a minima of the profile likelihood. See Figure 4.9 for further information for the different diagnostic profiles.

4.9.3 Theoretical Identifiability

From the perspective of personalised medicine, it is essential that one can obtain a set of identifiable input parameters. We suppose that practical identifiability should be split into a third section- theoretical identifiability. This is the class of methods which seeks to obtain subsets of identifiable input parameters from the sensitivity matrix. If one can obtain a theoretically identifiable subset of input parameters based on the sensitivity matrix, when this identifiable subset is shown the clinical data and the identifiability may be assessed

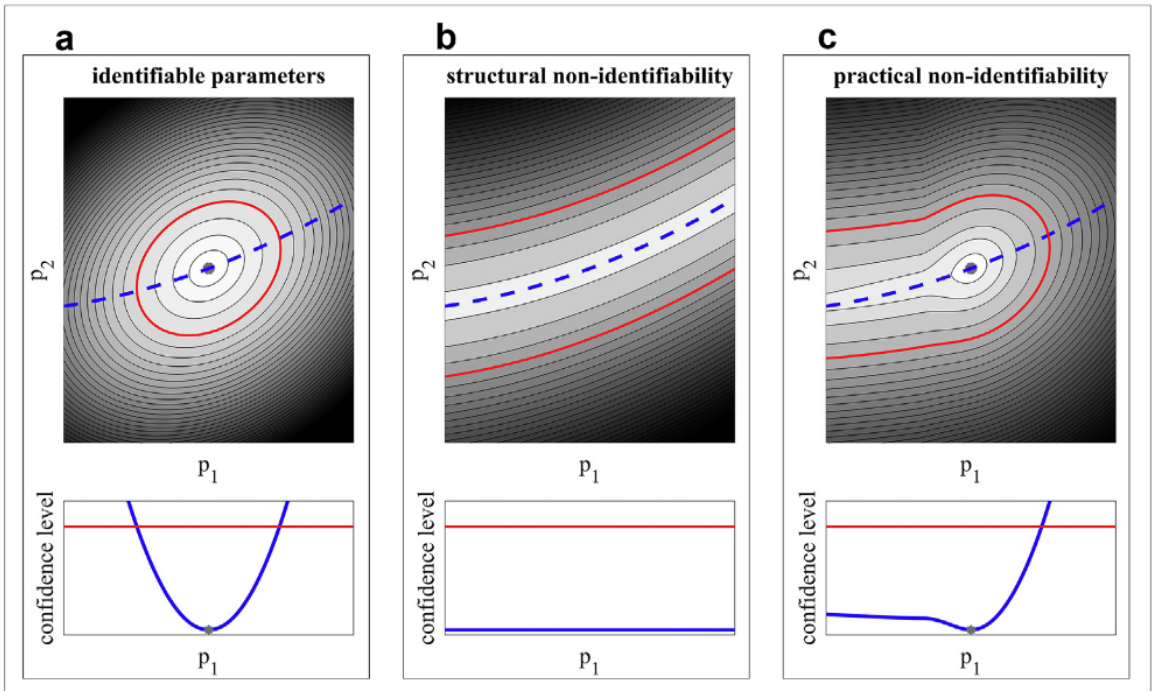

Fig. 4.9 **Various response surface structures**: Subfigures (A), (B) and (C) show contour optimisation plots as well as the profile likelihood versus the parameter below. Lighter colours in the contour plots signify a lower value of a specified cost function. Thresholds for confidence intervals corresponding to a confidence level of 95% are shown in red and plotted both in the contour plots and the profile likelihood plots. The lowest value of the cost function is denoted by a gray asterisk in both the contour plot and the profile likelihood plot. For the identifiable parameter (A), the profile likelihood reaches both an upper and lower threshold, thus leading to a finite confidence interval. For the structurally nonidentifiable parameter (B), the profile likelihood is completely flat, thus yielding infinite confidence intervals. In the contour plot, this translates to a flat path, along which the cost function does not change. The practically nonidentifiable parameter (C) shows an infinite extension of the low cost function region for lower values of the parameter, never reaching the 95% confidence interval threshold. In contrast, a finite upper confidence bound can be derived. Reproduced under CC 4.0 BY from [17].

using the profile likelihood method. Any inputs which are not found to be identifiable can be attributed to noise within the data. Several methods exist to obtain a subset of identifiable input parameters, such as the structured correlations method [426], the singular value decomposition followed by QR factorisation [427], eigenvalue-eigenvector subset selection [422, 428] and the rank deficiency method [429].

4.10 Average Parameter Influence

So far, we have not postulated a metric for the overall influence of an input parameter across all the outputs. In [19], Li et al. derive such a metric based upon the FIM F in equation (4.68). Li's method has only been applied to a FIM derived from LSA. Here we extend to an FIM derived from GSA matrices, to encapsulate the inherent global nature of personalisation problem which by definition is concerned with de-localised searches in input parameter space. We regard it as self-evident that sensitivity information should be consistent with this fact. Put another way, a model personalisation is a search over a hypersurface which is enclosed within a finite volume of input parameters space - and sensitivity information about a point, albeit a point within the correct region is clearly unrepresentative except in the trivial case of an almost featureless hypersurface.

Accordingly, we derive a parameter influence, or *effect* using principal component analysis (PCA) [19, 430], based upon global sensitivity measures. The principal components in question (PCs) are the eigenvectors of the FIM.

Let Q be the matrix of the ordered PC eigenvectors of F, in which the absolute value of each element Q_{ij} reflects the contribution of the i^{th} parameter to the variance of the j^{th} output. We follow Li et al. [19], who measure an overall effect for the i^{th} parameter as:

$$e_i = \frac{\sum_{j=1}^{m} |\lambda_j Q_{ij}|}{\sum_{j=1}^{m} |\lambda_j|}, \tag{4.112}$$

where $0 \leq e_i \leq 1$ and λ_j represents the non-zero eigenvalues of F. This measure reflects the difficulty in determining the i^{th} factor when only a single factor is estimated. Accurate estimation from limited data sets is favoured by large values of e_i.

4.11 Orthogonality Analysis

Using equation (4.67), we can define the orthogonality between two input parameters based on derived sensitivity vectors. Metric $d_{ik} \in [0,1]$ is an orthogonality between two input parameters θ_i and θ_k aggregated across all the chosen outputs.

$$d_{ik} = \sin\left[\cos^{-1}\left(\frac{S_k^T \cdot S_i}{||S_k||||S_i||}\right)\right], \quad i,k = 1,..,n, \quad d_{ik} \in [0,1], \tag{4.113}$$

where, $||.||$ denotes a Euclidean norm. This measure of orthogonality will be utilised below, with vectors S_k based on global sensitivity data, for our extended subset selection method. It will also be used to rank parameters based on the "most independent" effects when ignoring influence altogether. To calculate a rank based on orthogonality, we take the mean orthogonality score for an input parameter with respect to all the others, across all the outputs.

4.12 Extended Subset Selection Method

We require a practical strategy for finding suitable input parameter subsets for the purpose of model personalisation. Our method is based upon a technique dating from 2004, due to Li et al., [19], who originally applied local sensitivity to a bioreactor design; it offers an intuitive balance of parameter influence and orthogonality. We use an aggregated *identifiability index*, which is a simple, scalar product of a measure for (i) parameter influence given in equation (4.112) and (ii) parameter linear independence given in equation (4.113). Essentially, we want a subset, the members of which are optimally influential *and* linearly independent, expressed in the following figure of merit:

$$I_i = e_i \times d_i, \quad 1 \leq i \leq n. \tag{4.114}$$

e_i is our measure of influence, obtained from equation (4.112) and d_i is our measure of the linear independence obtained from equation (4.113).

The concept of orthogonality underlies the method of Li et al. [19], as follows. Parameter dependence is quantified from the FIM equation (4.68)). The rank of F, defined as the dimension of the vector space spanned by its columns [431], gives the number of identifiable combinations of input parameters at any given model operating point (if the sensitivities are local)[324, 432] or, (if the sensitivities are global) within a physiologically bounded bounded region of input parameter hyper space, as in the case of our methodological extension.

Assuming s_r, for $r = 1,..,n$ with $n < m$ are all linearly independent, we find the projection of another vector, s, into the subspace spanned by s_r where $r < m$, effectively by removing out its orthogonal projection (which lies outside that subspace). The remaining part is given by

$$s^{\parallel} = \sum_{r=1}^{n} c_r s_r, \quad n < m. \tag{4.115}$$

Consider, now, a new candidate sensitivity vector s_i, for a generic i^{th} input parameter. The extent to which s_i is linearly dependent upon the already-chosen s_r, is measured by finding the above projection of s_i, onto the subspace spanned by the s_r, that is, by removing from s_i its orthogonal compliment, $s_i^{\perp}$. Accordingly, $s_i^{\parallel}$ is defined by its expansion coefficients, c_r. The latter may, in fact, be efficiently computed in an optimisation process, with solution [19]:

$$\underline{c} = \begin{bmatrix} s_1^T s_1 & \dots & s_n^T s_1 \\ \vdots & \ddots & \vdots \\ s_1^T s_n & \dots & s_n^T s_n \end{bmatrix}^{-1} \times \begin{bmatrix} s_i^T s_1 \\ \vdots \\ s_i^T s_n \end{bmatrix}. \tag{4.116}$$

We summarise our algorithm for optimal input parameter subset selection as follows.

1. For each parameter, θ_i, $i = 1,..,n$, each having relative sensitivity vector s_i, calculate its overall effect, using equation (4.112);

2. Select the parameter with the highest value of e_i, $i = 1,..,n$, to be the first parameter in the selected set;

3. For $n < m$, repeat the following steps until no more parameters can be added to the accumulating set. For the jth candidate:

   (a) Use equation (4.116) to find the nearest vector $s_j^{\parallel}$, to the present candidate, lying in the subspace already spanned by the k (say) currently selected parameters.

   (b) Use equation (4.113) to calculate the orthogonality between $s_j^{\parallel}$ and s_j as follows

$$d_j = \sin\left[\cos^{-1}\left(\frac{s_j \cdot s_j^{\parallel}}{||s_j||||s_j^{\parallel}||}\right)\right]. \tag{4.117}$$

   (Of course, d_j is a proxy for the magnitude of the orthogonal projection of $\hat{s}_j$ which, in turn, measures an overall orthogonality for candidate j relative to the k already-selected parameters.)

(c) Attribute to candidate parameter j a simple aggregate *identifiability index* which reflects both its sensitivity and orthogonality

$$I_j = e_j \times d_j. \tag{4.118}$$

(d) Provided $I_j > 0.05$ [270], include in the set that parameter with $\max_j(I_j)$.

4. If $n \geq m$ form all (m-1) tuples of the already selected parameters. The number of possible candidates is

$$q = \frac{q!}{(m-1)!(n-1+m)!}.$$

Use equation (4.117) to calculate the orthogonality of the input parameter θ_j across all q possible combinations of parameters $d_{q,j}$. Determine the worst case scenario ($d_j = \min(d_{q,j})$) and continue with the calculation of I_j.

5. Continue until no more parameters (elements) can be added.

The main interpretation for this method is in selecting a subset of input parameters for personalisation, one seeks the best set of influential input parameters which span the whole physiology of a patient, available measurements. This set of input parameters are the "team" that work the best collectively instead of the set of input parameters which are either the most influential or the most orthogonal. But it is vital to appreciate that this optimally exists under a constraint of chosen outputs. Were the latter to change one should then repeat the subset selection process again.

4.13 Model Sloppiness

System "sloppiness" refers to anisotropy in the structure of the input parameter space, given a set of model outputs [341]. As discussed above, the main aim in many areas of systems biology is to optimise a dynamical system's input parameters fit to available experimental data. This is normally performed by minimising a cost or loss function, to obtain a point in the input parameter space corresponding to a global minimum of said cost function J [57], typically of the of the broad form

$$J(\underline{\theta}) = \sum_i (y_i(\underline{\theta},t) - y_i^e)^2,$$

where $\underline{\theta}$ is the input parameter set, y_i^e represents the ith experimental measurement available and $y_i(\underline{\theta},t)$ represents the ith dynamical system output (obtained from the model), against

which the experimental data are compared.

Consider an example dynamical system with two input parameters θ_1 and θ_2. When optimising such a system to experimental data, contour plots displaying the closeness of fit are generated as in figure 4.10. Here we see that moving up (in the direction of θ_2) and left in the parameter space rapidly changes the value of the cost function, indicating how good a fit is obtained by a specific value of θ_2. This direction is denoted a stiff direction in the input parameter space. Conversely, if one was to travel up and right (in the direction of θ_1), one could visit a range of θ_1 values without incurring changes of the cost function values. This means the manifold generated by θ_1 is largely linear whereas that generated by θ_2 has steeper gradients, leading to a more easy to identify, unique global minimum. Of course, most real

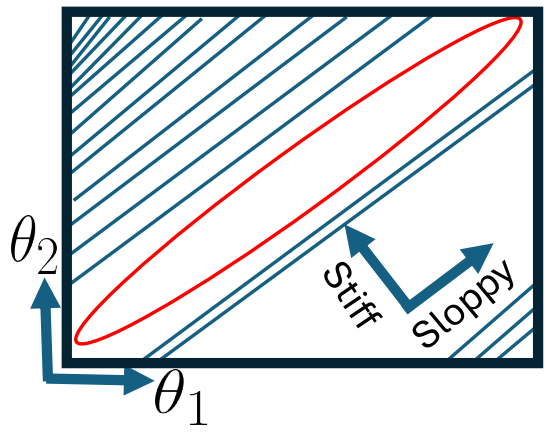

Fig. 4.10 **A two dimensional sloppy model schematic representation:** A two dimensional contour plot displayed as a blue curve, with the minimum contour value displayed in red for input parameters θ_1 and θ_2. Moving up and left in the direction of θ_2 would lead to rapid changes in the contour whereas moving up and right in the direction of θ_1 would lead to slower changes per unit distance moved.

models in systems biology and certainly in cardiovascular modelling cannot be visualised through a two dimensional contour map but Figure 4.10 nevertheless represents a precise analogy.

It is important to quantify the sloppiness which is present within many cardiovascular models. The final stage of personalisation is the optimal estimation of selected input parameters, fitted to patient-specific clinical data. Before this optimisation takes place, if we can quantify the stiffness or sloppiness present within the systems' input parameter space, it would provide perspective on the complexity and facilitate the choice of optimisation

routine (e.g. gradient descent, particle swarm genetic algorithms, unscented Kalman filter) [433, 434].

The related concepts of identifiability and sloppiness provide different but -in both cases- insights on the personalisation process [435]. Identifiability is a binary concept whilst sloppiness quantifies the difficulty associated with obtaining identifiable input parameters. The sloppiness analysis of a model can either distinguish stiff and sloppy regions of the input parameter space, or show that the whole system under investigation can be regarded as sloppy. Note, most system biology models belong to the latter category. Here, we examine the sloppiness associated with the sensitivity matrices, which are defined by input parameter effects on the chosen outputs. Therefore, we also establish a secondary aim of investigating the effects of differing experimental design on a cardiovascular system sloppiness.

We have introduced the concept of sloppiness by examining the contour lines of the cost function. To examine sloppiness in an n-dimensional input parameter space, we consider the eigenvalues of FIM equation (4.68). The eigenvalues of the FIM disclose the variation of input parameters, constrained by the available data. A model can be regarded as sloppy if the eigenvalues of the FIM have a uniform spacing on a log scale i.e. are distributed over many orders of magnitude [341, 18, 436, 437]. On the other hand, if the FIM eigenvalues, denoted λ, have a non-uniform distribution, the model is regarded as stiff. We can then identify stiff directions in the input parameter space which correspond to a set of input parameters where personalisation should occur. See figure 4.11 for a comparison of model sloppiness and identifiability in an n-dimensional space.

4.14 Unscented Kalman Filter

The unscented Kalman filter (UKF) is a data assimilation method iteratively to reconcile model results with available measurements, to provide an improved estimation of a dynamical system's [438] states and parameters (which may be viewed as states). A full derivation of the UKF can be found in [352]. In what follows we use traditional notation, which may conflict with that of the previous section. The UKF consists of two distinct steps, as follows.

First the unscented transform (UT) calculates the statistics of an assumed Gaussian random variable (GRV) that undergoes a non-linear transformation [354]. Both multiplicative and additive noise has been investigated with UKF, we assume additive noise throughout the whole model, which is accepted practice for biological systems [439, 440, 14]. Below we pay

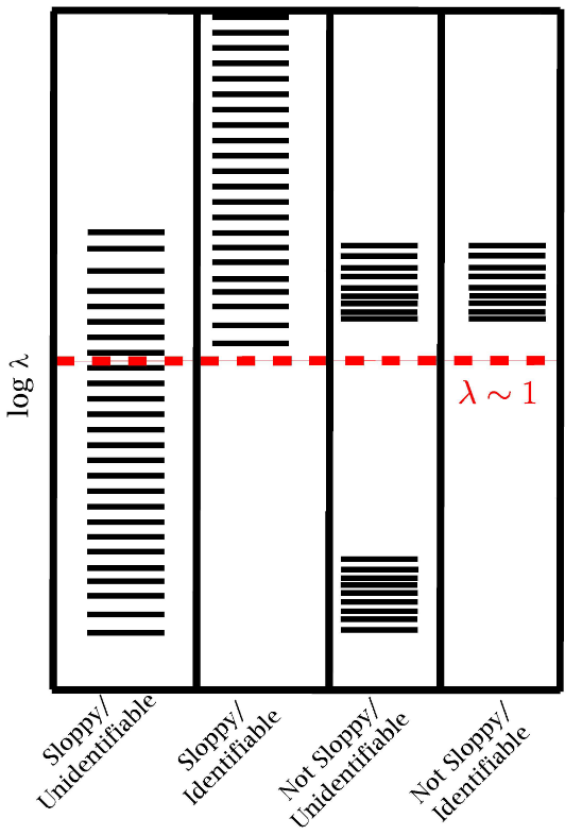

Fig. 4.11 **Sloppiness vs. identifiability:** Although sloppiness and parameter identifiability are closely related, strictly they are distinct. Sloppiness is disclosed by an approximate uniform spacing of FIM eigenvalues spread over many orders of magnitude. In the most common case (first column) many eigenvalues are small and also correspond to unidentifiable parameter combinations. However, it is possible (in principle) for all the eigenvalues to be large (second column) so that sloppy models can be identifiable. It is also possible for model parameters to be unidentifiable and not sloppy (third column) or identifiable and not sloppy (fourth column). We here take $\lambda \sim 1$ as the cutoff between identifiable and unidentifiable designations, after the arguments in [18]. Reproduced under CC 4.0 BY from [18].

particular attention to the influence of patient-specific measurements and how this method could be used to clinical advantage.) We define an augmented vector $\underline{x} = [\underline{X}, \underline{\theta}]$, where $\underline{X}$ and $\underline{\theta}$ are the state variables and input parameters respectively; see (4.22) and assume $\underline{x}$ is a Gaussian random variable (GRV) of dimension L where $L = \dim(\underline{X}) + \dim(\underline{\theta})$. Now consider propagating the augmented state-vector through the non-linear model function $\underline{f}$ as given in equation 4.22. Assume our GRV has a mean $\underline{x}_\mu$ and a covariance $P_{\underline{x}}$. To compute the statistics on the result of the propagation of the GRV through $\underline{f}$, we construct a matrix $\underline{\underline{\chi}}$ of $2L+1$ so-called sigma vectors χ_i, or sigma points, where i represents the ith column of the matrix according to the following, for $t \in [0, \infty)$:

$$\begin{aligned}
\chi_{0,t} &= \underline{x}^A_{\mu,t}, \\
\chi_{i_{1,t}} &= \underline{x}^A_{\mu,t} + \left(\sqrt{(L+\lambda)P^A_{\underline{x},t}}\right)_j, \\
\chi_{i_{2,t}} &= \underline{x}^A_{\mu,t} - \left(\sqrt{(L+\lambda)P^A_{\underline{x},t}}\right)_j, \\
i_1 = j = 1,...,L, &\quad i_2 = L+1,...,2L,
\end{aligned} \tag{4.119}$$

where the superscript A represents the assimilated state-and-parameter vector, λ is now a scaling parameter and P is the covariance matrix relating the states and input parameters. The GRV sigma vectors now represent a minimal set of carefully chosen sample points, which completely capture the true mean and covariance of the GRV. When they are propagated through the true non-linear system, a posterior mean and covariance are captured accurately, to the 3rd order (relative to a Taylor series expansion) for *any* non-linearity. Next, we compute the set of corresponding weights W_i:

$$\begin{aligned}
W^\mu_0 &= \frac{\lambda}{L+\lambda}, \\
W^c_0 &= \frac{\lambda}{L+\lambda} + (1+\beta-\alpha^2), \\
W^\mu_i &= W^c_i = \frac{1}{2(L+\lambda)}, \\
i = 1,...,2L,\ \lambda &= \alpha^2(L+\kappa) - L,
\end{aligned} \tag{4.120}$$

where α determines the spread of sigma points around $\underline{x}_\mu$ (we use $\alpha = 10^{-1}$). κ is another scaling parameter (here $\kappa = 0$) and β incorporate prior knowledge of which distribution $\underline{x}$ follows. Here $\beta = 2$ is used as this is optimal for GRV. The matrix square root is performed using a Cholesky decomposition [441] which requires the matrix to be positive definite.

Second we propagate each sigma vector through the ODE system such that $\Upsilon_i = \underline{f}(\chi_i)$ and determine the mean and covariance of $\underline{Y}$, using the weighted sample mean and covariance of the propagated sigma vectors. Before we can do this, we must first define the prediction step in the algorithm

$$\begin{aligned} \hat{\chi}_{t+1|t} &= \underline{f}(\chi_t), \\ \Upsilon_{t+1|t} &= \underline{h}(\hat{\chi}_{t+1|t}). \end{aligned} \tag{4.121}$$

The above have corresponding mean and sample covariance:

$$\begin{aligned} \underline{x}_{\mu,t+1} &= \sum_{i=0}^{2L} W_i^{\mu} \hat{\chi}_{i,t+1|t}, \\ P_{\underline{x},t+1} &= \sum_{i=0}^{2L} W_i^{c} [\hat{\chi}_{i,t+1|t} - \underline{x}_{\mu,t+1}][\hat{\chi}_{i,t+1|t} - \underline{x}_{\mu,t+1}]^T + \delta_Q I, \\ \underline{Y}^{\mu}_{t+1} &= \sum_{i=0}^{2L} W_i^{\mu} \Upsilon_{i,t+1|t}, \\ P_{\underline{Y},t+1} &= \sum_{i=0}^{2L} W_i^{c} [\Upsilon_{i,t+1|t} - \underline{Y}^{\mu,t+1}][\Upsilon_{i,t+1|t} - \underline{Y}^{\mu,t+1}]^T + R, \\ P_{\underline{xY},t+1} &= \sum_{i=0}^{2L} W_i^{c} [\hat{\chi}_{i,t+1|t} - \underline{x}_{\mu,t+1}][\Upsilon_{i,t+1|t} - \underline{Y}^{\mu,t+1}]^T, \end{aligned} \tag{4.122}$$

where $P_{\underline{xY}}$ is designated the cross correlation matrix. R is the additive noise on the predicted measurements and takes the form $\sigma^2 I_{m\times m}$ (for m measurements), where $\sigma = 5$. This represents the typical clinical error present when measuring e.g. ventricular or aortic pressure and the ventricular volume [442]. $\delta_Q I$ is considered a regularisation term to avoid sigma point collapse [443, 14], where I is an $L \times L$ identity matrix with $\delta_Q = 10^{-8}$. We now correct the prediction that has been made by assimilating with the noisy data. The Kalman gain matrix is calculated as

$$K_{t+1} = P_{\underline{xY},t+1}(P_{\underline{Y},t+1})^{-1},$$

which then leads to:

$$\begin{aligned} \underline{x}^A_{\mu,t+1} &= \underline{x}_{\mu,t+1} + K_{t+1}(\underline{Y}^n_{t+1} - \underline{Y}^{\mu}_{t+1}), \\ P^A_{\underline{x},t+1} &= P_{\underline{x},t+1} - K_{t+1} P_{\underline{Y},t+1} K^T_{t+1}, \end{aligned} \tag{4.123}$$

where $\underline{x}^A_{\mu,t+1}$ and $P^A_{\underline{x},t+1}$ are used to generate new sigma points for the $t+1$ time point. In the assimilation step in equation (4.123), $\underline{Y}^n_{t+1}$ represents the data which are specific to a patient. Therefore we are correcting the value parameter/state estimation with the measured patient data (represented by the noisy synthetic data in this case). This also allows one

to make predictions about compartments in which experimental data are not available, for example aortic valve resistance Z_{ao}. Given the GRV assumption, required for the UKF, we must transform the deterministic input parameters to the Gaussian setting. Each input is then transformed as

$$\theta_i^N \sim N(\theta_i, \sigma_i^2), \tag{4.124}$$

where θ_i^N is the normally distributed input parameter i with an initial mean θ_i and variance σ_i^2, respectively. The mean of the normal distribution is taken from the literature values [20]. The parameter variance is selected to reflect the uncertainty in the mean parameter value and taken from existing literature [22, 21], where larger variances are specified for input parameters with higher uncertainty. This normal distribution reflects the prior belief about the input parameters before any measurements are incorporated. As the UKF iterates, the mean and variance are updated to reflect information gained from new measurements. The initial distribution seeds the estimation process, providing a starting point that is adjusted as more measurement data become available.

To implement the UKF, we take advantage of the versatile SciML ecosystem within Julia. Here we implement a discrete callback which performs the Kalman filtration at each time point and returns the corrected result. This has been shown to contribute negligible computational time associated with the callback, which underwrites our ability to produce the result in close-to-real time. Most previous authors manually discretise the ODE system to transform it into a discrete time system for the implementation of an UKF. Implementing a callback allows us to take advantage of advanced ODE solvers within package DifferentialEquations.jl with improved accuracy. We remark that there are two distinct steps in our computational workflow, (1) we perform a first solve of the dynamical system to generate the synthetic data, including perturbed input parameters along with the synthetically generated personalised HRs. This stage represents experimental data collection. (2) These data are then stored for the second stage, when we solve the model and call the UKF. In this step, we estimate the states and input parameters of the model, given the personalised HRs and perturbed input parameters. The aim is that the algorithm can capture the dynamical effects pf changing input parameters which represent evolving physiological conditions of patients.

To evaluate the effectiveness of the UKF estimation procedure we employ the root mean squared error as found below:

$$RMSE = \sqrt{\frac{(\theta_i - x_{\mu,i}^A)^2}{n}}, \tag{4.125}$$

where θ_i is the true value of the ith input parameter, $x^A_{\mu,i}$ is the assimilated estimate of the ith input parameter and n is the length of the assimilated vector.

4.15 Computational Framework

All of the work in this thesis has been conducted with the Julia language [397]. Above, sensitivity analysis is driven largely by the associated computation. In a nutshell, Julia aims to provide the speed of C but the usability and packages one associates with higher level languages such as Matlab, Python and R. During the work, DifferentialEquations.jl [444, 445] is utilised for its vast array of efficient ODE solvers. Note, this package also facilitates parameter estimation, uncertainty analysis, ML etc. QuasiMonteCarlo.jl [396] is utilised to generate parameter samples for the GSA and GlobalSensitivity.jl [446] for the functions to perform the analysis. We have developed, to facilitate the work of this PhD the package CirculatorySystemModels.jl [447], an Acausal modelling package for LPMs.

This package is built on the acausal modelling framework provided by ModelingToolkit.jl [448], containing all the common elements plus others needed for effective and realistic lumped parameter modelling. Currently CirculatorySystemModels.jl supports common elements such as a capacitor, resistor, inductance and diodes [247], which act as simple valve functions. We also provide extensions to the common elements to include constant compliance chambers, non-linear and Poiseuille resistances as well as the Double-Hill, Shi and Smith activation functions, which are used as the cardiac driving chamber elastances [367, 370] as defined above. We also are the first modelling package to include non-linear valve functions from Shi, Mynard and Laubscher [373, 170, 159]. Alongside individual components we also have created a collection of sub compartments including, full circulatory, systemic, pulmonary and heart models. We decompose these full systems into collections of elements such as the famous Windkessel models [11] to give the user full control over their modelling.

There already exists some popular packages within both Simulink and Modelica such as the “Cardiovascular library for lumped-parameter modeling” [449] and “Physiolibary” [450] respectively. These languages operate a block orientated “drag and drop” approach with Modelica being the common choice due to it’s acausal modelling approach [451]. Other languages, based on XML, exist for lumped parameter modelling such as CellML [452] and SBML [453], while these XML languages are great for exchanging models they are often difficult to implement and model analysis is limited. A common theme within all

current lumped parameter modelling software is the systems inability to deal with complex event handling and non-linear components. Being based on ModelingToolkit.jl, CirculatorySystemModels.jl overcomes these limitations by leveraging the wider SciML framework. [453], while these are great for exchanging models they are often difficult to implement and model analysis is limited. As a result of Julia's architecture, as the complexity of the model increases the model analysis time does not become unreasonable. Other packages exist which allow users to import models from other frameworks, CellMLToolkit.jl [454] and OpenModelica.jl [455]. CirculatorySystemModels.jl goes beyond these by providing a lumped parameter modelling library with seamless integration with the SciML framework [456, 446, 444] which allows for extensive and efficient model analysis. Since both the modelling library and the framework it is built on are pure Julia, new components can be developed in a transparent and consistent manner.

To highlight the computational power associated with our Julia framework we refer the reader to table 4.5. This table displays the relative execution times for the 4 chamber model in figure 4.2B.

Table 4.5 **Computational comparison**: A table displaying the relative speed comparing languages for the 4 chamber model found in figure 4.2B.

CirculatorySystemModels.jl	CellMLToolkit.jl	Matlab	Python
1×	1.6×	272×	963×

4.16 Summary of Methods

Within this chapter many methods and models have been detailed which will be utilised within the following chapters. Below is a tabulated version representing the mapping between the results and which methods will be used. The rational for each model choice can be found in section 4.2.

Table 4.6 **Model and Methods Summary**: Below a tabulated version of the models and methods which are used in each of the results chapters.

Results Chapter	5	6	7	8
Models	1 & 2 Chamber models - Figure 4.1	4 Chamber model - Figure 4.2	1 chamber model - Figure 4.1A	1 chamber model - Figure 4.1A
Methods	Sampling Methods - Section 4.7 Sobol indices - Section 4.5.3 Bootstrapping - Section 4.5.3.1	Sobol indices - Section 4.5.3 Average parameter influence - Section 4.10 Sloppiness - Section 4.13	Global Sensitivity - Section 4.5 Theoretical Identifiability - Section 4.9.3 Extended subset selection - Section 4.12	Sobol indices - Section 4.5.3 Unscented Kalman Filter - Section 4.14

Chapter 5

Convergence, Sampling and Total Order Estimator Effects on Parameter Orthogonality in Global Sensitivity Analysis

It is the mark of an educated person to search for the same kind of clarity in each topic to the extent that the nature of the matter accepts it.
— ARISTOTLE, Nicomachean Ethics

Summary
This chapter introduces the investigation into total order sensitivity estimators and their interaction with sampling methodologies and different classes of data. It highlights the need for converged sensitivity indices and the impact this may have on obtaining personalisable input parameters.[1]

[1]The work conducted in this chapter is published in **Saxton, H**., Xu, X., Schenkel, T., Clayton, R. H., & Halliday, I. (2024). Convergence, sampling and total order estimator effects on parameter orthogonality in global sensitivity analysis. PLOS Computational Biology, 20(7), e1011946.

5.1 Introduction

Various methods exist to calculate model identifiability (see e.g [336]). See section 4.9; here our approach is based on the method of Li et al. [19], which, recall, calculates the *identifiability index* of the *i*th model input I_i as follows:

$$I_i = E_i \cdot d_i, \tag{5.1}$$

where d_i is the *i*th input's orthogonality relative to the current pre-selected set of input parameters- which one is seeking to expand- and E_i is the *i*th input's effect. Here, I_i measures the likelihood of a unique recovery of the *i*th model input. See section 4.12. In our method, both the effect and orthogonality of an input are calculated from the sensitivity matrix which has been generated with respect to model outputs [19, 327, 326, 457]. Clearly, the identifiability index depends on both the effect and the orthogonality which can be disclosed by sensitivity analysis. This prompts an investigation to find the most reliable and robust method for calculation of said sensitivity matrix.

Calculation of inputs' effects and orthogonality are arguably the central area of research for model personalisation. Here we ask three interrelated questions:

1. What is the most reliable estimator on which to compute underlying sensitivity indices?
2. What is the optimal sampling methodology in relation to (i) above which supports accurate exploration a potentially very complex input parameter hyperspace?
3. How do the choices of estimator and sampling methodology interact, e.g. impact indices' convergence?

Prior art [458, 289, 459] almost exclusively prioritises efficient and accurate computation of the total order matrix and the evaluation of different estimators' abilities to reveal the "true" effects of inputs, given their interactions over first order indices'. Recently, Puy et al. [293] reported their examination of several total order estimators - essentially a sensitivity analysis of sensitivity analysis [460]. These authors varied the sampling method, between Monte Carlo and quasi-Monte Carlo, their analytic (note) test model, the dimensionality of input parameter hyperspace, the distribution of input parameters, and the number of model runs. The work provides a comprehensive and systematic assessment of the properties of different estimators.

We focus on the computation of total order indices for varying model dimensionality; we

will consider heterogeneous data, providing both continuous time series and discrete samples. For both the simple nine parameter model defined in Figure 4.1A, and the more complex twenty parameters model in Figure 4.1B we utilise:

$$\underline{Y}^c(t) = (P_{lv}, P_{sa}, V_{lv})^T, \quad \underline{Y}^d(t_k) = (\text{Mean}(P_{lv}), \text{Max}(P_{sa}), \text{Max}(V_{lv}))^T, \tag{5.2}$$

where $\underline{Y}^c$ and $\underline{Y}^d$ represent the continuous and discrete measurement vector. The discrete measurements above are scalar quantities extracted from a continuous waveform solution. The maximum measurement finds the time point t_k at which the output quantity is at its maximum value. The mean measurement averages across the whole waveform which then gives the scalar measurement.

5.2 Results

We present: (i) the convergence of total order indices with respect to both discrete and continuous output measurements; (ii) our investigation outcomes changing the four estimators between the five sampling methodologies defined in Section 4.7. First, the convergence results will be illustrated in Section 5.2.1. Then in the next two subsections, total order Sobol indices and orthogonality of input parameters for the 1-chamber, 9-parameter model (figure 4.1A) and the 2-chamber, 20-parameter model (figure 4.1B) are declared. Between each subsection, we examine what effect the different choices of estimator and sampling methodology have on the orthogonality of input parameters. Within each of the subsections, we make the distinction between the effects of continuous and discrete measurements. All estimators will be referred to in their full form. Sampling methodologies will be simplified to the following:

1. SS - Sobol Sampling
2. LR - Lattice Rule
3. GR - Golden Ratio
4. U - Uniform
5. LH - Latin Hypercube

We present results for input parameters deemed to have potential bio-markers status, for example, low arterial compliance C_{sa} may indicate a stiffening of the vessel. Each subsection considers convergence of a single parameter for brevity.[2].

[2]All other data is available at https://github.com/H-Sax/Orthgonality-SA

5.2.1 Convergence and Uncertainty

Figure 5.1 shows the convergence and the uncertainty of the minimal ventricular elastance E_{min} for the 1-chamber and 2-chamber models. We calculate the Sobol indices using the Jansen estimator and Sobol sampling, which are considered to be best practice [293, 419]. Accordingly, we take this combination as our benchmark and the sample size returned from this initial investigation is used for evaluations on all other estimators and sampling methods. Increasing the sample size and re-sampling with replacement allow us to evaluate the sample size at which the Sobol indices have converged with minimum uncertainty. This is displayed as a band around the index of interest and represents a 95% confidence interval of the index estimate.

For the 1-chamber model, $10,000$ samples ($110,000$ model evaluations) ensured convergence when computed against the discrete measurements defined in Eq. (5.2). Figure 5.1A shows that evaluating the Sobol indices at a higher sample size would provide minimal improvement and at $10,000$ samples the indices have negligible error. Figure 5.1B shows that the continuous indices have minimal error during the cardiac cycle, so when we compute the time averaged indices no excessive error will be present. Using $10,000$ samples we computed the continuous Sobol indices against the measurements defined in Eq. (5.2). For the 2-chamber model, $20,000$ samples ($660,000$ model evaluations) were adequate as seen in Figure 5.1C. The continuous measurements of the 2-chamber model in Figure 5.1D show that the indices were not subject to error for $20,000$ samples. Figure 5.1C appears to indicate that fewer samples may be adequate for the 2-chamber model. However, the adopted sample size ensured all input parameters displayed a consistent rank with less than 5% error.

5.2.2 1-chamber Model

The uncertainty associated with the computation of Sobol total order indices on the 1-chamber model, with $N = 10,000$ samples is presented in Figure 5.2. Only the results for arterial compliance C_{sa} are displayed. The 95% confidence intervals for the Homma and Sobol estimators are considerably wider than that of the Jansen and Janon estimators. The Homma estimator consistently produced estimates of the sensitivity indices which are different to that of the other available estimators. The Jansen and Janon estimators give identical results for their computations of the sensitivity indices and confidence intervals, for every sampling methodology used. When the Homma and Sobol estimators are used, the latin hypercube and uniform sampling methods produce larger confidence intervals compared to the quasi-monte carlo sampling methods.

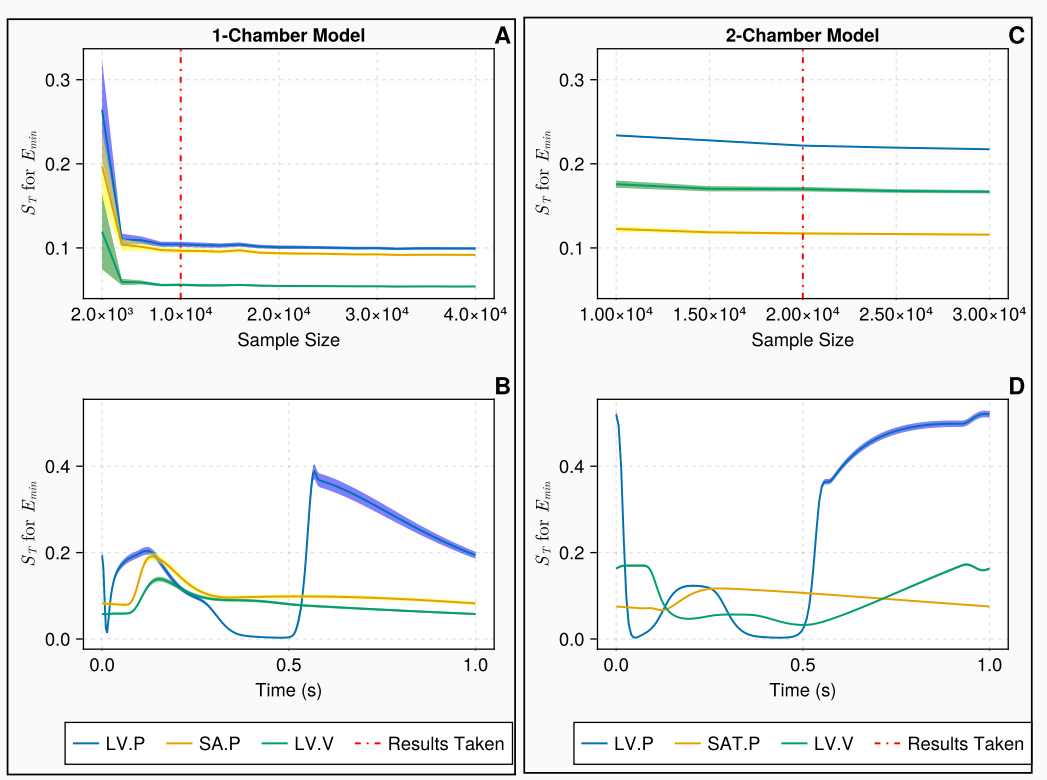

Fig. 5.1 **Convergence and uncertainty of indices associated with the minimum ventricular elastance** E_{min}: Figure **A** displays the convergence and uncertainty of the Sobol indices S_T calculated on discrete measurements for the 1-chamber model against increasing sample size. Here, the vertical line signifies the chosen sample size for the 1-chamber model at $N = 10,000$. Figure **B** presents the continuous Sobol indices with uncertainty bounds, calculated at a sample size $N = 10,000$, on continuous measurements over a single cardiac cycle. Figure **C** displays the convergence and uncertainty of S_T calculated on discrete measurements for the 2-chamber model against increasing sample size. Again, the vertical line signifies the chosen sample size for this model, at $N = 20,000$. Figure **D** shows the continuous Sobol indices with uncertainty bounds for $N = 20,000$, on continuous measurements over a single cardiac cycle. The measurements shown in blue, yellow and green denote the left ventricular pressure, the systemic arterial pressure and the left ventricular volume, respectively. In the discrete settings (i.e., A and C), the measurements are the mean left ventricular pressure, the maximum systemic arterial pressure and the maximum left ventricular volume.

When calculating total order indices on the 1-chamber model with continuous measurements (the histograms for the orthogonality distributions of input parameters are presented in Figure 5.3), we notice that the orthogonality spread for the Jansen and Janon estimators are identical for the golden ratio and Latin hypercube sampling methodologies. The Jansen estimator coupled with lattice rule sampling also shares this orthogonality distribution. The Janon estimator, with Lattice Rule and Sobol sampling, and the Jansen estimator with Sobol sampling, exhibit minor variations from the previous orthogonality distributions generated by Janon and Jansen estimators, however, are identical between themselves. The orthogonality distributions returned from the Homma and Sobol estimators exhibit large variations for each sampling methodology, although the Sobol estimator with the Sobol sampling returns an orthogonality distribution similar to that seen by the Jansen and Janon estimators. These results are summarised in Table 5.1 where the input parameters are ranked based on their orthogonality scores in the parameter space. We see the orthogonality results obtained for the Jansen and Janon estimators are invariant to sampling methodologies. In contrast, the rankings for Sobol and Homma estimators vary amongst different sampling methodologies. The Sobol estimator when coupled with Sobol sampling, returns a parameter ranking almost identical to that of the Jansen and Janon estimators, a result consistent with tha shown in Figure 5.3.

In Table 5.2, a stratification by estimator type and examination of the range of an input parameter across all sampling methodologies reveals, as inferred from Table 5.1, that the Jansen and Janon estimators exhibit no variation for the whole input parameter set, given any sampling methodology. This indicates that the Jansen and Janon estimators are the optimal choices for this model. The Homma and Sobol estimators exhibit variations of 1.33 and 1.67 upon the input parameter set, respectively. These variations mean that using Homma and Sobol estimators will return differing orthogonality rankings when different sampling methodologies are used. When stratifying by sampling types, Table 5.3 reveals that Sobol and Lattice Rule samplings exhibit the smallest mean variations of the input set across all estimator types. It is important to note that these variations are a consequence of the Sobol and Homma estimators which both exhibited different orthogonality rankings for input parameters. These results indicate that given a less than optimal estimator, the Sobol or Lattice rule sampling methodology may produce a ranking which can be considered closer to the ground “truth”. Interestingly, we notice that the life sciences’ most commonly used Latin Hypercube sampling methodology is characterised by the largest variation of an input set of parameters.

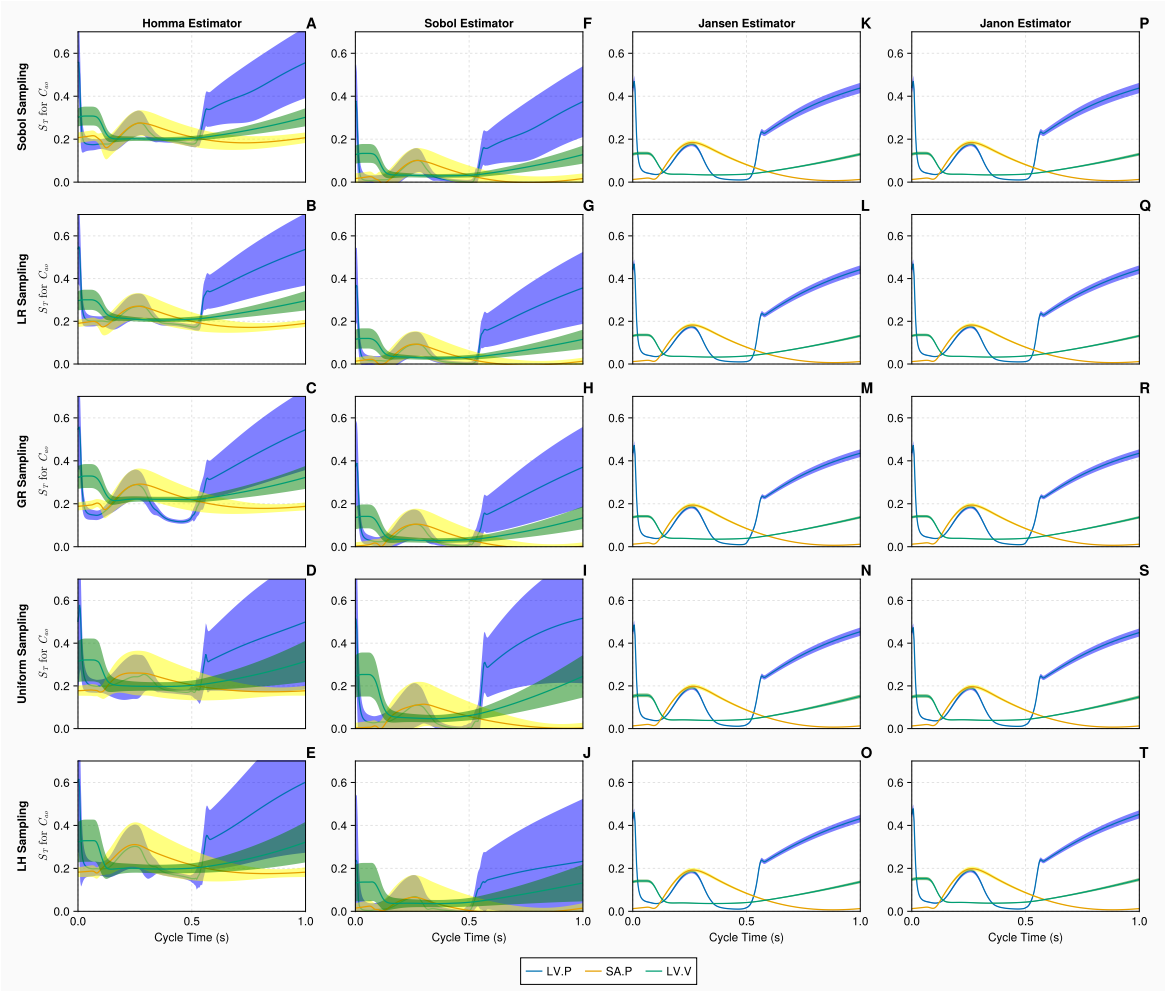

Fig. 5.2 **Total order Sobol indices S_T of the arterial compliance C_{sa} for the 1-chamber model with continuous measurements**: Panels A - T show S_T of C_{sa}, for 3 continuous measurements - left ventricular pressure, systemic arterial pressure and the left ventricular volume (represented in blue, yellow and green curves, respectively), over a single cardiac cycle with differing estimators and sampling methodologies. Measurements are evaluated with $N = 10,000$ samples, using $B = 1000$ bootstrapped samples, to evaluate the uncertainty of the estimate. The bands represent 95% confidence intervals associated with specific indices displayed as solid curves.

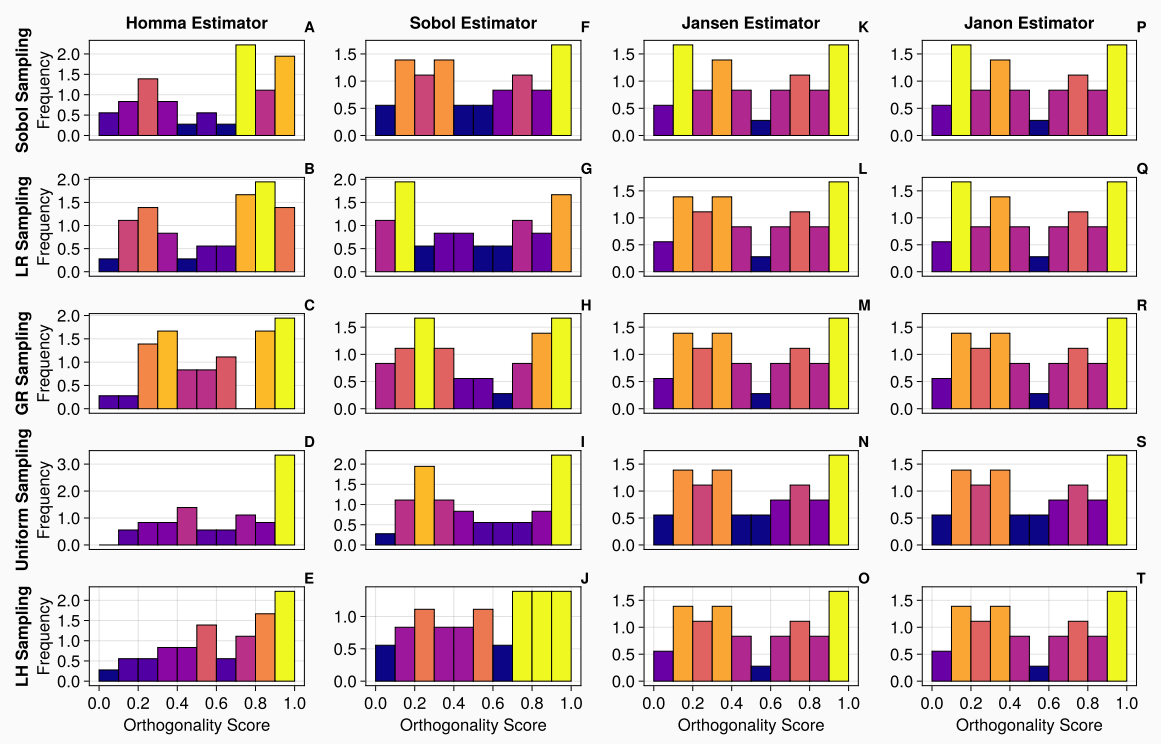

Fig. 5.3 **Orthogonality distributions of input parameters for the 1-chamber model with continuous measurements**: Histograms A-T show the distribution of orthogonality returned from examinations of the sensitivity vectors, calculated from continuous measurements. Here, an orthogonality score of 1 represents total independence, 0 total dependence. Individual diagrams portray a particular combination of sampling methodology and estimator type. The frequency of each histogram is normalised such that it is comparable between plots, i.e., the larger the frequency of a bin, the larger the number of orthogonality scores calculated from the original sensitivity vectors.

Table 5.1 **Input parameter ranking for the 1-chamber model with continuous measurements**: Here, input parameters are ranked based on the averaged orthogonality score returned from the calculated total order sensitivity matrix. In addition, the ranking is stratified by both sampling and estimator types.

		τ_{es}	τ_{ep}	R_{mv}	Z_{ao}	R_s	C_{sa}	C_{sv}	E_{max}	E_{min}
Homma	SS	5	4	9	3	2	8	7	6	1
	LR	5	4	9	3	2	8	6	7	1
	GR	5	4	9	3	1	8	5	6	2
	U	7	4	9	3	1	8	5	6	2
	LH	6	4	8	1	3	9	5	7	2
Sobol	SS	4	3	8	5	1	7	9	6	2
	LR	4	3	9	6	1	8	7	5	2
	GR	4	3	8	7	1	6	9	5	2
	U	5	3	8	4	1	9	7	6	2
	LH	5	4	6	3	1	8	9	7	2
Jansen	SS	4	3	7	5	1	8	9	6	2
	LR	4	3	7	5	1	8	9	6	2
	GR	4	3	7	5	1	8	9	6	2
	U	4	3	7	5	1	8	9	6	2
	LH	4	3	7	5	1	8	9	6	2
Janon	SS	4	3	7	5	1	8	9	6	2
	LR	4	3	7	5	1	8	9	6	2
	GR	4	3	7	5	1	8	9	6	2
	U	4	3	7	5	1	8	9	6	2
	LH	4	3	7	5	1	8	9	6	2

Table 5.2 **Input parameter ranking for the 1-chamber model with continuous measurements**: The ranges of input parameters across 5 sampling types for a specific estimator for the 1-chamber model with continuous measurements.

	τ_{es}	τ_{ep}	R_{mv}	Z_{ao}	R_s	C_{sa}	C_{sv}	E_{max}	E_{min}	Mean variation of input set
Range Homma	2	0	1	2	2	1	2	1	1	1.33
Range Sobol	1	1	3	4	0	2	2	2	0	1.67
Range Jansen	0	0	0	0	0	0	0	0	0	0
Range Janon	0	0	0	0	0	0	0	0	0	0

Table 5.3 **Input parameter ranking for the 1-chamber model with continuous measurements**: The ranges of input parameters across 4 estimator types for a specific sampling method for the 1-chamber model with continuous measurements.

	τ_{es}	τ_{ep}	R_{mv}	Z_{ao}	R_s	C_{sa}	C_{sv}	E_{min}	E_{max}	Mean variation of input set
Range SS	1	1	2	2	1	1	2	0	1	1.22
Range LR	1	1	2	2	1	1	2	0	1	1.22
Range GR	1	1	2	4	0	2	3	2	0	1.67
Range U	3	1	1	2	0	2	4	0	0	1.44
Range LH	2	1	2	4	2	2	4	1	0	2.00

Figure 5.4 displays the convergence and uncertainty associated with the computation of the total order indices of the mitral value resistance R_{mv} for the 1-chamber model against the discrete measurements. In all cases, as the sample sizes are increased, the accuracy of the estimations and uncertainty associated with the indices improve. The Jansen and Janon estimators provide the most efficient convergences and smallest errors when calculating the indices. A sample size of $N = 10,000$ is taken for the discrete measurements, because the columns for the Jansen and Janon estimators (Panels K - T) show that any additional samples would return minimal improvements in terms of accurate calculation of the indices. The Homma and Sobol estimators (Panels A - J) show considerably larger errors than that of the Jansen and Janon estimators. When the upper limit sample size of $k = 40,000$ is reached, the Homma and Sobol estimators appear to have converged, with reduced errors when combined with the Sobol, Lattice Rule and Golden sampling methods, although the errors are still much larger than those exhibited by the Jansen and Janon estimators. The uniform and Latin hypercube sampling methods present the largest errors when combined with the Sobol estimator.

For total order indices on the 1-chamber model with discrete measurements, the histograms presented in Figure 5.5 show that the orthogonality spreads for the Jansen and Janon estimators, across all sampling methodologies other than the Janon estimator and the Latin Hypercube sampling pairing, are identical. We notice, the orthogonality distributions returned from the Homma estimator exhibit large variations for each sampling methodology, as noted for continuous measurements shown in Figure 5.3. The Sobol estimator column (Panels F - J) in Figure 5.5 shows orthogonality spreads which are somewhat similar to that of Jansen and Janon but still quite variable between sampling methodologies. These results are summarised in Table 5.4 where the Jansen and Janon estimators are shown to invariant to

sampling methodologies, whilst the rankings of parameter orthogonality for the Sobol and Homma estimators vary amongst different sampling methodologies.

In Table 5.5, stratifying by estimator type and examining the range an input parameter exhibits across all sampling methodologies reveals that the Jansen and Janon estimators exhibit no variation for any input parameter set for any sampling methodology, once again implying they are the optimum choice. The Homma and Sobol estimators exhibit variations of 5.11 to 2.22, respectively depending on the input parameter set. The variations for the discrete measurements are much greater than the variations seen with continuous measurements. When stratifying by sampling type, Table 5.6 shows the Sobol sampling method exhibits the smallest mean variation of an input set across all estimator types. As previously, since only the Sobol and Homma estimator exhibit significantly variable parameter rankings, stratifying by sampling methodology places more emphasis on the apparently less robust estimators. From this result, it does appear the Sobol sampling method may improve the robustness associated with a parameter orthogonality ranking. One notable observation from Tables 5.1 and 5.4 is that while the robustness of the Jansen and Janon estimator is evidenced in both tables, the ranking associated with the orthogonality of input parameters changes quite dramatically (for example, E_{min}, R_{mv}, Z_{ao} and R_s), highlighting how the change in data type may have consequences in parameter interpretation when conducting a sensitivity analysis.

Overall, for the 1-chamber model with 9 input parameters the Jansen and Janon estimators appear consistently to be the most robust and most reliable which may be attributed to excellent convergence exhibited by these estimators. Sobol and Homma estimators provide very variable parameter rankings across different sampling methodologies, an observation which accords with the poor convergence of these estimators. The Sobol sampling method appears to reduce the level of uncertainty associated with an input parameter's orthogonality ranking, as shown in Tables 5.3 and 5.6. Interestingly, continuous measurements appear to reduce the level of variation associated with parameter orthogonality ranking, when compared to discrete measurements.

5.2.3 2-chamber Model

We present the results of our uncertainty study on the 20 parameters, 2-chamber model. First, the uncertainty associated with the computation of Sobol total order indices, for this more complex model, with $N = 20,000$ samples, is presented in Figure 5.6. Only the results for the left ventricular maximum elastance $E_{max_{lv}}$ are displayed here. The Jansen and Janon estimators give identical index and confidence interval calculations, apart from when com-

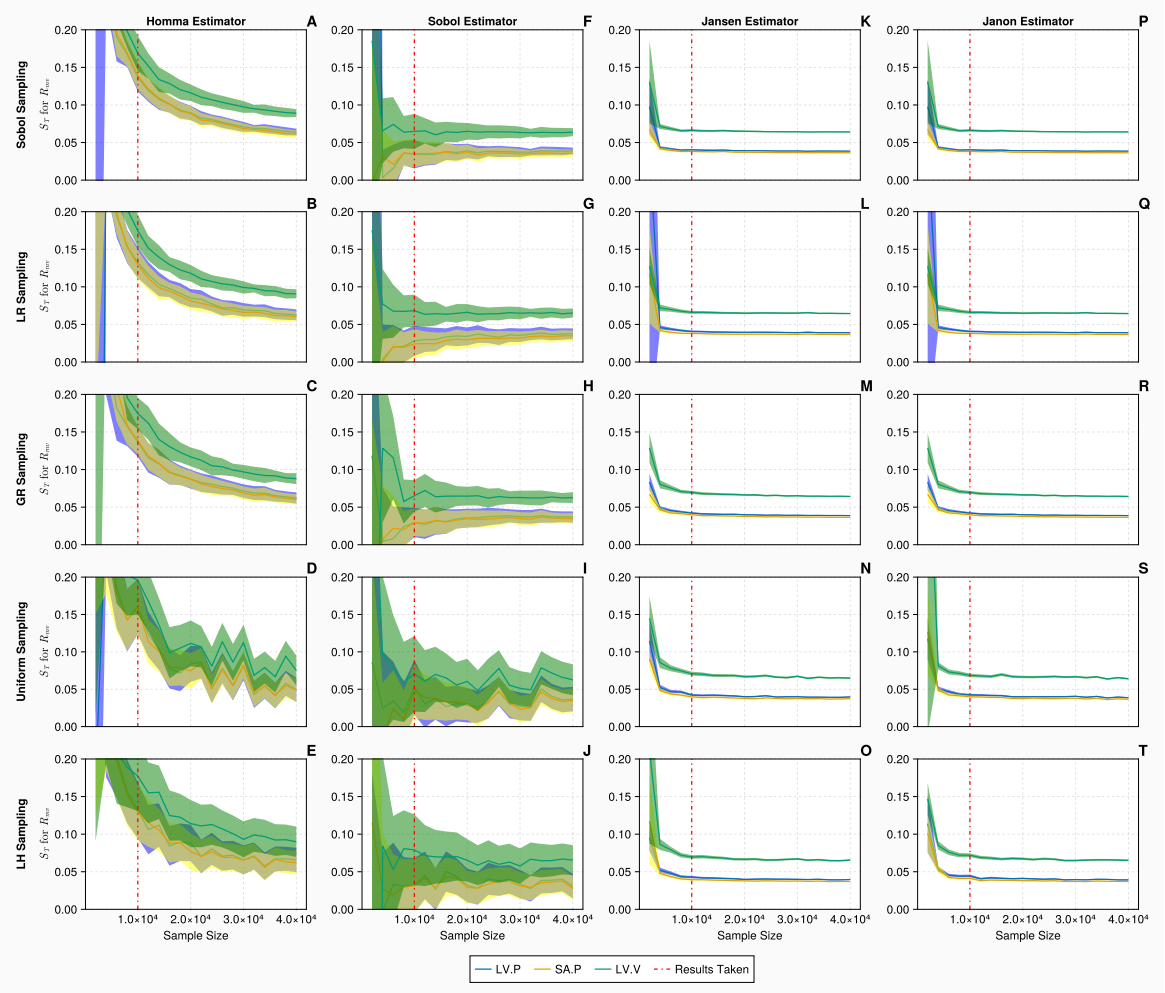

Fig. 5.4 **Total order Sobol indices S_T of the mitral valve resistance R_{mv} for the 1-chamber model with discrete measurements**: Panels A - T show S_T of R_{mv}, for 3 discrete measurements: mean left ventricular pressure, maximum systemic arterial pressure and maximum left ventricular volume (represented in blue, yellow and green, respectively), evaluated at increasing sample sizes ($N \in [2000, 40000]$ using $B = 1000$ bootstrapped samples), with differing estimators and sampling methodologies. The bands represent 95% confidence intervals associated with specific indices displayed as solid curves. The red solid vertical lines represent the point ($N = 10,000$) at which the sample size is taken.

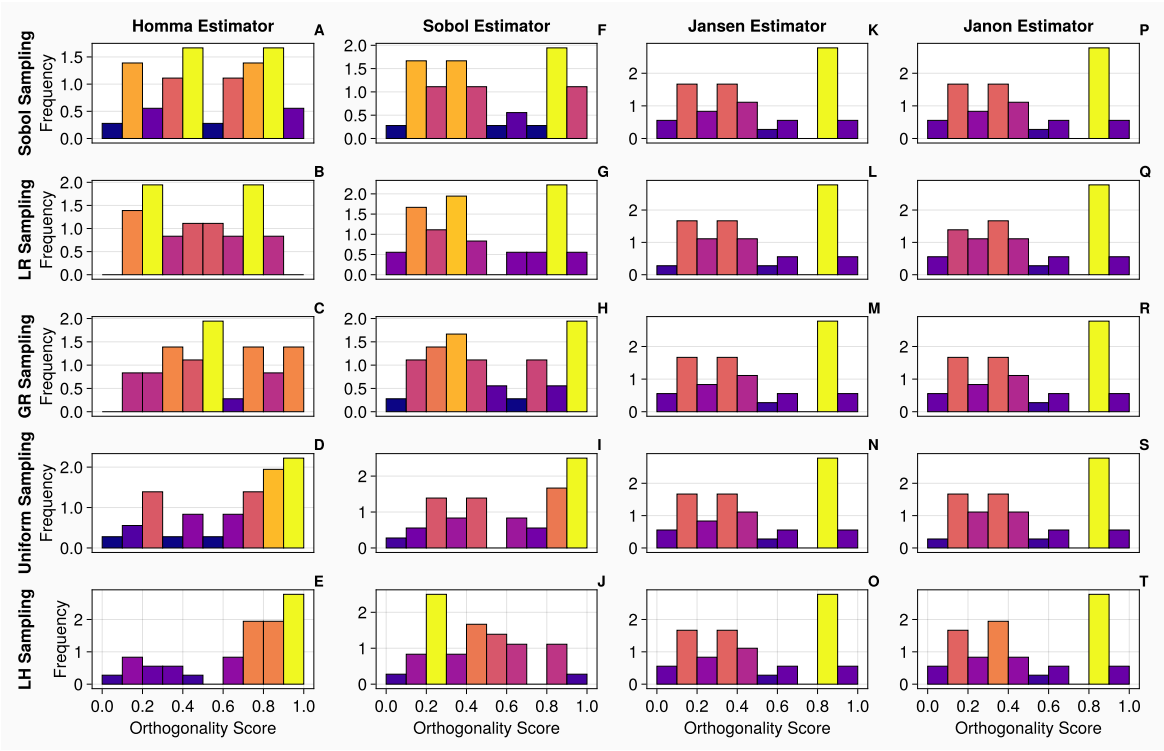

Fig. 5.5 **Orthogonality distributions of input parameters for the 1-chamber model with discrete measurements**: Histograms A-T show the distribution of orthogonality returned from examinations of the sensitivity vectors, calculated from continuous measurements. Here, an orthogonality score of 1 represents total independence of input parameters, 0 total dependence. Each individual diagram denotes a specific combination of sampling methodology and estimator type. The frequency of each histogram is normalised such that it is comparable between plots, i.e., the larger the frequency of a bin, the larger the number of orthogonality scores calculated from the original sensitivity vectors.

Table 5.4 **Input parameter ranking for the 1-chamber model with discrete measurements**: Again, input parameters are ranked based on the averaged orthogonality score returned from the calculated total order sensitivity matrix. The ranking is also stratified by both sampling and estimator types.

		τ_{es}	τ_{ep}	R_{mv}	Z_{ao}	R_s	C_{sa}	C_{sv}	E_{max}	E_{min}
Homma	SS	3	1	4	2	5	9	8	6	7
	LR	3	1	4	2	6	7	9	8	5
	GR	2	4	6	1	7	5	8	9	3
	U	5	2	8	6	7	3	9	4	1
	LH	3	4	5	6	1	8	2	7	9
Sobol	SS	3	2	4	1	5	8	7	6	9
	LR	6	2	4	1	3	9	7	5	8
	GR	3	2	5	1	6	7	8	4	9
	U	1	3	5	2	4	8	7	6	9
	LH	7	1	4	2	3	6	8	5	9
Jansen	SS	5	2	3	1	4	9	7	6	8
	LR	5	2	3	1	4	9	7	6	8
	GR	5	2	3	1	4	9	7	6	8
	U	5	2	3	1	4	9	7	6	8
	LH	5	2	3	1	4	9	7	6	8
Janon	SS	5	2	3	1	4	9	7	6	8
	LR	5	2	3	1	4	9	7	6	8
	GR	5	2	3	1	4	9	7	6	8
	U	5	2	3	1	4	9	7	6	8
	LH	5	2	3	1	4	9	7	6	8

Table 5.5 **Input parameter ranking for the 1-chamber model with discrete measurements**: The range of parameter ranking across 5 sampling types for a specific estimator for the 1-chamber model with discrete measurements.

	τ_{es}	τ_{ep}	R_{mv}	Z_{ao}	R_s	C_{sa}	C_{sv}	E_{max}	E_{min}	Mean Variation of input set
Range Homma	3	3	4	4	6	6	7	5	8	5.11
Range Sobol	6	2	1	1	3	3	1	2	1	2.22
Range Jansen	0	0	0	0	0	0	0	0	0	0
Range Janon	0	0	0	0	0	0	0	0	0	0

Table 5.6 **Input parameter ranking for the 1-chamber model with discrete measurements**: The ranges of input parameters across 4 estimator types for a specific sampling method for the single ventricle model with discrete measurements.

	τ_{es}	τ_{ep}	R_{mv}	Z_{ao}	R_s	C_{sa}	C_{sv}	E_{min}	E_{max}	Mean variation of input set
Range SS	2	1	1	1	1	1	1	0	1	1.11
Range LR	3	1	1	1	3	2	2	3	3	2.11
Range GR	3	2	3	0	3	4	1	5	6	3.00
Range U	4	1	3	5	3	6	2	2	8	3.56
Range LH	4	3	2	5	3	3	6	2	1	3.22

bined with the lattice rule sampling methodology, the plots show slightly larger confidence intervals for the left ventricular volume comparing to the other cases. The Homma and Sobol estimators again display much larger confidence interval estimates compared to the Jansen and Janon estimators. The errors associated with the Sobol sampling methodology when the Homma and Sobol estimator are used, are much smaller compared to the Latin hypercube and uniform sampling methodologies, hence demonstrating the impact sampling methodology can have on the estimations of sensitivity indices.

Next, we calculate total order indices on the 20 dimensional 2-chamber model with continuous measurements. From the histograms presented in Figure 5.7, the orthogonality spreads for the Jansen and Janon estimators are nearly identical across sampling methodologies, excluding the uniform sampling (which shares the same orthogonality spread between the two estimators). With the Homma estimator, the spreads of orthogonality appear more consistent amongst the sampling techniques associated with itself, comparing against the test cases on the 1-chamber model, however, they are largely different from what returned from the Jansen and Janon estimators. The Sobol estimator generated results which appear closer to the orthogonality distributions of the Jansen and Janon estimators, whilst they are not identical, the orthogonality distributions between different sampling methodologies are more consistent than the ones exhibited by the Homma estimator. Considering Table 5.7, the rankings of input parameters are more consistent for the Jansen and Janon estimators, although there are slight discrepancies, as seen on the simple 1-chamber model.

In Table 5.8, stratifying by estimator type and examining the range an input parameter exhibits across all sampling methodologies reveals that the Jansen and Janon estimators

exhibit minimal variations to sampling methodologies - 1.3 and 1.45, respectively. The Homma and Sobol estimators exhibit variations of 8.2 and 7.35 respectively, with the input parameter set. When stratifying by sampling type, Table 5.9 shows the Sobol sampling method exhibits the smallest mean variation of an input set across all estimator types of 7.2. This is still a large variation, due to all estimator types being considered and therefore the range accounts for some of the spurious values generated by the Homma and Sobol estimators.

Table 5.7 **Input parameter ranking for the 2-chamber model with continuous measurements**: Here, input parameters are ranked based on the averaged orthogonality score returned from the calculated total order sensitivity matrix. In addition, the ranking is stratified by both sampling and estimator types.

	Homma					Sobol					Jansen					Janon				
	SS	LR	GR	U	LH	SS	LR	GR	U	LH	SS	LR	GR	U	LH	SS	LR	GR	U	LH
$E_{min_{lv}}$	3	8	8	2	2	12	8	13	9	11	5	5	5	6	5	5	5	6	6	5
$E_{max_{lv}}$	7	11	15	1	1	2	3	3	5	5	1	1	1	1	1	1	1	1	1	1
$\tau_{es_{lv}}$	1	4	6	6	8	8	5	8	8	8	3	3	3	4	3	3	3	3	4	3
$\tau_{ep_{lv}}$	2	5	7	7	9	9	4	6	6	9	2	2	2	2	2	2	2	2	2	2
$E_{min_{la}}$	8	10	1	12	11	13	14	7	2	14	7	7	7	7	7	7	7	7	7	7
$E_{max_{la}}$	9	9	2	11	12	16	17	18	14	15	18	18	18	19	18	18	18	18	19	18
$\tau_{es_{la}}$	19	16	16	18	19	19	19	15	20	13	8	8	8	16	9	8	8	8	16	13
$\tau_{ep_{la}}$	13	1	11	13	17	15	15	20	18	20	16	16	17	17	16	16	16	17	17	15
Z_{ao}	10	2	13	14	13	11	10	12	7	10	4	4	4	3	4	4	4	4	3	4
R_{mv}	17	15	12	3	5	18	16	17	10	18	17	17	16	15	17	17	17	16	15	17
C_{sas}	16	17	18	20	20	7	6	4	17	16	9	9	9	8	8	9	9	9	8	8
R_{sas}	18	18	19	16	16	14	7	14	4	12	6	6	6	5	6	6	6	5	5	6
L_{sas}	14	20	17	17	15	1	2	2	1	1	15	15	15	14	15	15	15	15	14	16
C_{sat}	6	3	3	4	4	6	11	9	12	7	10	10	10	9	10	10	10	10	9	9
R_{sat}	12	12	14	15	18	3	9	5	19	6	13	11	12	11	13	13	11	12	10	10
L_{sat}	15	19	20	19	14	10	1	1	3	2	14	14	14	13	14	14	14	14	13	14
R_{sar}	5	6	4	9	6	5	12	11	16	3	12	13	13	12	12	12	13	13	12	12
R_{scp}	4	7	5	10	7	4	13	10	15	4	11	12	11	10	11	11	12	11	11	12
R_{svn}	20	14	9	5	10	20	18	16	11	19	19	19	19	18	19	19	19	19	18	19
C_{svn}	11	13	10	8	3	17	20	19	13	17	20	20	20	20	20	20	20	20	20	20

Figure 5.8 displays the convergence and uncertainty associated with the computation of the total order indices of the venous compliance C_{svn}, for the 2-chamber model, against our discrete measurements. We see in all cases that, as the sample size is increased, the estimate and uncertainty associated with the indices improve. Similar to the continuous measurement case for $E_{max_{lv}}$ shown in Fig 5.6, the Jansen and Janon estimators provide the most efficient convergence and the smallest error when calculating the indices. A sample size of $N = 20,000$ is taken for the discrete measurements, as seen in the Jansen and Janon columns (Panels K - T), any additional sampling would return minimal improvements in

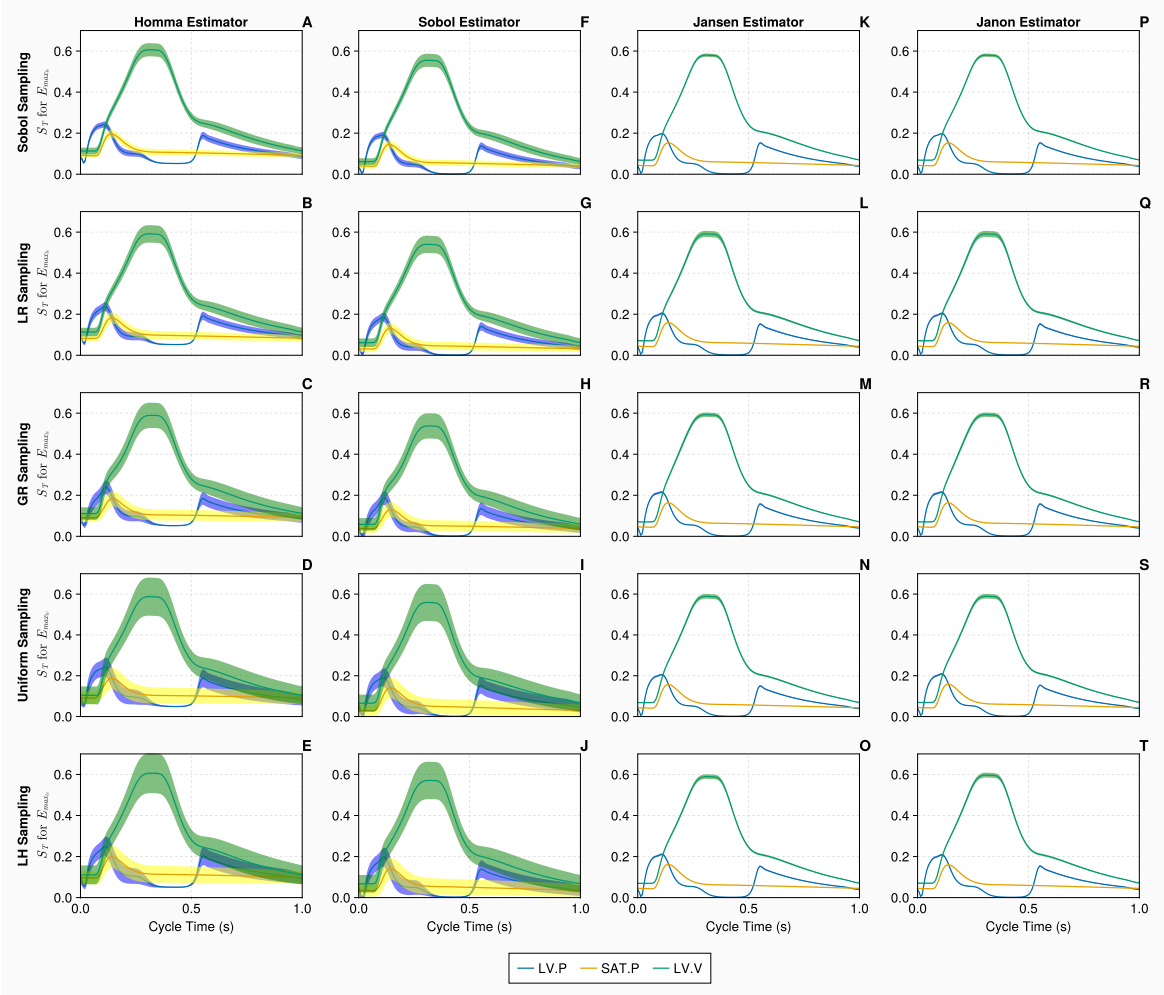

Fig. 5.6 **Total order Sobol indices S_T of the maximal left ventricular elastance $E_{max_{lv}}$ for the 2-chamber model with continuous measurements**: Panels A - T show S_T of $E_{max_{lv}}$, for 3 continuous measurements - left ventricular pressure, systemic arterial pressure and the left ventricular volume (represented in blue, yellow and green curves, respectively), over a single cardiac cycle with differing estimators and sampling methodologies. Measurements are evaluated with N = 20, 000 samples, using B = 1000 bootstrapped samples to evaluate the uncertainty of the estimate. The bands represent 95% confidence intervals associated with specific indices displayed as solid curves. Note all axes are equal for easy comparison however the maximum values for the Homma and Sobol estimators are 0.4.

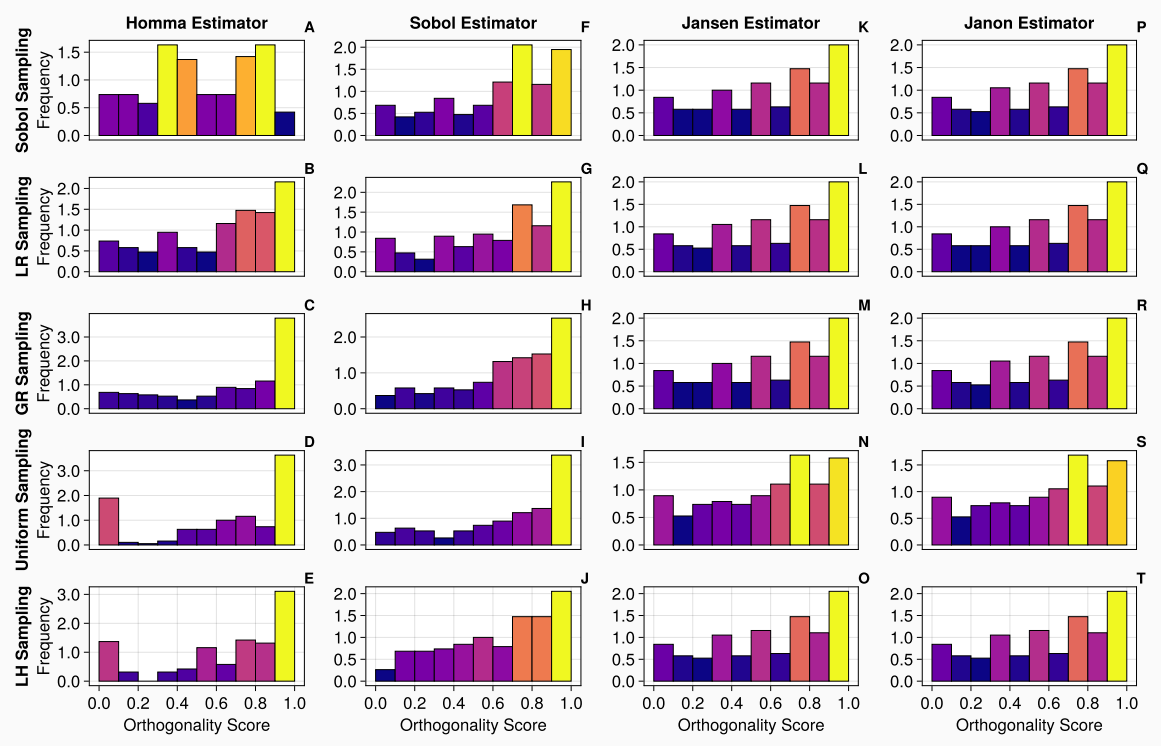

Fig. 5.7 **Orthogonality distributions of input parameters for the 2-chamber model with continuous measurements**: Histograms A-T show the distribution of orthogonality returned from examinations of the sensitivity vectors, calculated from continuous measurements. Here, an orthogonality score of 1 represents total independence of input parameters, whereas 0 represents total dependence. Each diagram denotes a specific combination of sampling methodology and estimator type. The frequency of each histogram is normalised such that it is comparable between plots, i.e., the larger the frequency of a bin, the larger the number of orthogonality scores calculated from the original sensitivity vectors.

Table 5.8 **Input parameter ranking for the 2-chamber model with continuous measurements**: The ranges of input parameters across 5 sampling types, for a specific estimator for the 2-chamber model with continuous measurements.

	Range Homma	Range Sobol	Range Jansen	Range Janon
$E_{min_{lv}}$	6	5	1	1
$E_{max_{lv}}$	14	3	0	0
$\tau_{es_{lv}}$	7	3	1	1
$\tau_{ep_{lv}}$	7	5	0	0
$E_{min_{la}}$	11	12	0	0
$E_{max_{la}}$	10	4	1	1
$\tau_{es_{la}}$	3	7	8	8
$\tau_{ep_{la}}$	16	5	1	2
Z_{ao}	12	5	1	1
R_{mv}	14	8	2	2
C_{sas}	4	13	1	1
R_{sas}	3	7	1	1
L_{sas}	6	1	1	2
C_{sat}	3	6	1	1
R_{sat}	6	16	2	3
L_{sat}	6	9	1	1
R_{sar}	5	11	1	2
R_{scp}	6	11	2	1
R_{svn}	15	9	1	1
C_{svn}	10	7	0	0
Mean Variation Of Input Set	8.2	7.35	1.3	1.45

Table 5.9 **Input parameter ranking for the 2-chamber model with continuous measurements**: The ranges of input parameters across 4 estimator types for a specific sampling method for the 2-chamber model with continuous measurements.

	Range SS	Range LR	Range GR	Range U	Range LH
$E_{min_{lv}}$	9	3	7	7	9
$E_{max_{lv}}$	6	10	14	4	4
$\tau_{es_{lv}}$	7	2	5	4	5
$\tau_{ep_{lv}}$	7	3	5	5	7
$E_{min_{la}}$	6	7	6	10	7
$E_{max_{la}}$	9	9	16	9	6
$\tau_{es_{la}}$	11	11	8	4	10
$\tau_{ep_{la}}$	3	15	4	5	5
Z_{ao}	7	8	8	11	9
R_{mv}	1	2	5	12	13
C_{sas}	9	11	14	12	12
R_{sas}	12	12	14	11	10
L_{sas}	14	18	15	16	15
C_{sat}	4	8	7	8	6
R_{sat}	10	3	9	9	12
L_{sat}	5	18	13	16	12
R_{sar}	7	7	9	7	9
R_{scp}	7	4	7	5	8
R_{svn}	1	5	10	13	9
C_{svn}	9	7	10	12	17
Mean Variation Of Input Set	7.2	8.15	9.3	10.65	9.75

terms of accurate calculation of the indices. The Homma and Sobol estimators display errors which are considerably larger than that of Jansen and Janon estimators. We see when the upper limit sample size of $N = 30,000$ is reached, the Homma and Sobol estimator errors are still large. This results demonstrates that for this complex model, less efficient estimators (such as Homma and Sobol) and a less accurate sampling method (such as Latin hypercube) display large confidence intervals and struggle to return converged index values.

From the histograms presented in Figure 5.9, the orthogonality spreads exhibit similar trends to that of the continuous measurements, shown in Figure 5.7. We note that the histograms are identical for the Jansen and Janon except when the Uniform sampling method is used (which exhibits slight variations from the other histograms). With the Homma and Sobol estimators, although there appears to be low level consistency amongst their orthogonality distributions, they are very different to the ones produced by the Jansen and Janon estimators. Examining Table 5.10, the rankings of input parameters are consistent for the Jansen and Janon estimators apart from the Uniform column which often returns a parameter ranking differing to the other sampling types.

In Table 5.11, stratifying by estimator type and examining the range a input parameter exhibits across all sampling methodologies reveals that the Jansen and Janon estimators exhibit minimal variation to sampling methodologies - 0.9 and 1.0, respectively. This is an improvement on the continuous measurements as the Jansen estimator returns less than 1 parameter range variation. The Homma and Sobol estimators produce variations of 10.9 and 5.55 respectively over the input parameter set. When stratifying by sampling type, Table 5.12 shows the Lattice Rule sampling method exhibits the smallest mean variation of an input set across all estimator types of 5.75. This is still a large variation but is less than that exhibited by the continuous measurements.

Overall, for the more complex 2-chamber model with 20 input parameters, the Jansen and Janon estimators are consistently the most robust and reliable estimators. When using continuous measurements, neither returns an input parameter set mean variation greater than 1. When using discrete measurements, they return a mean variation less than or equal to 1 (see Tables 5.8 and 5.11). This, as in the 1-chamber case, could be attributable to the efficient rate of convergence displayed by the Jansen and Janon estimator. The Sobol and Homma estimators exhibit very different parameter rankings across different sampling methodologies with variations of up to 10.9. These large variations are in line with the poor convergence associated with these estimators. The Sobol and Lattice Rule sampling method appears to

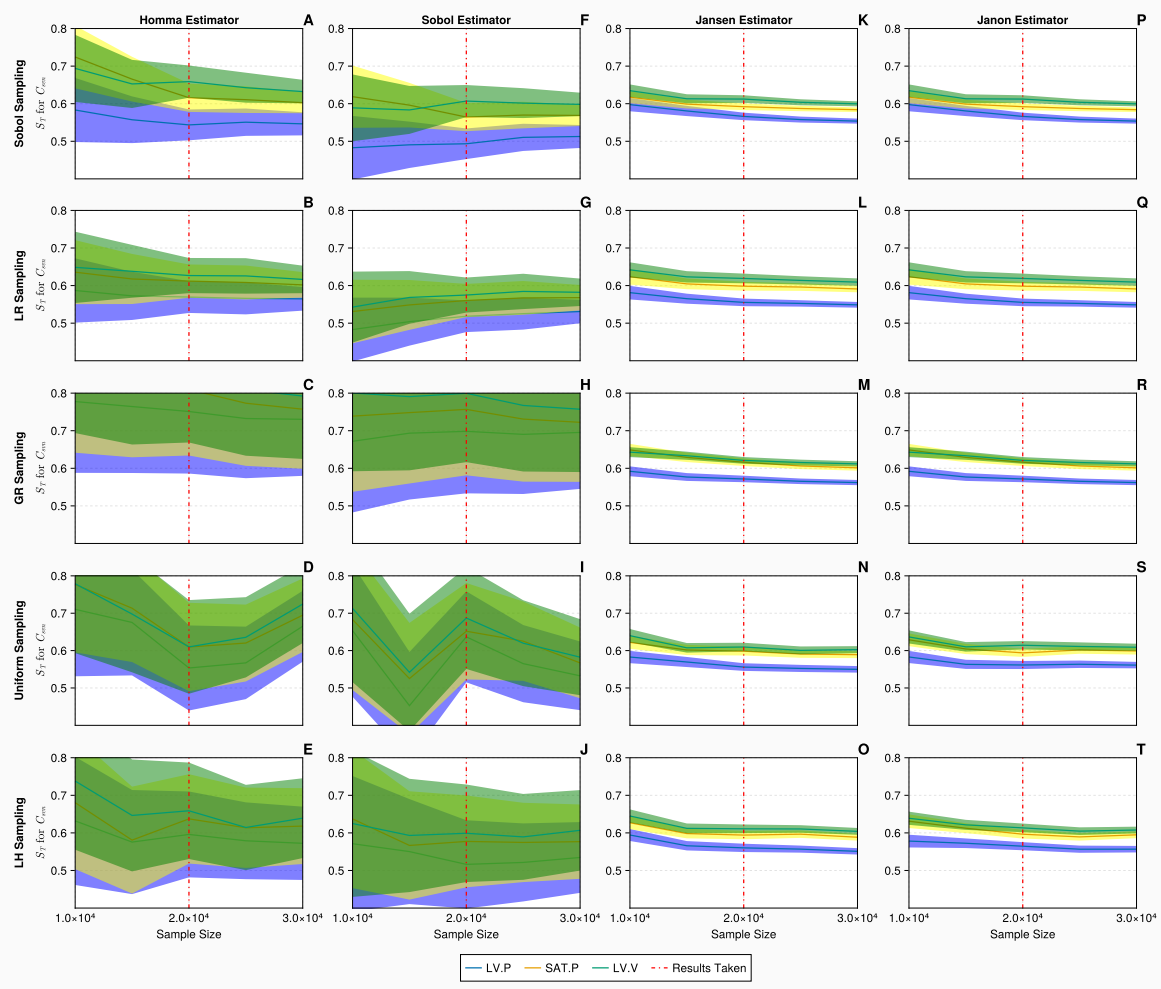

Fig. 5.8 **Total order Sobol indices S_T of the venous compliance C_{svn} for the 2-chamber model with discrete measurements**: Panels A - T show S_T of C_{svn}, for 3 discrete measurements: mean left ventricular pressure, maximum systemic arterial pressure and maximum left ventricular volume (represented in blue, yellow and green, respectively), evaluated at increasing sample sizes ($N \in [10000, 30000]$ using $B = 1000$ bootstrapped samples), with different estimators and sampling methodologies. The bands represent 95% confidence intervals associated with specific indices displayed as solid curves. The red solid vertical lines represent the point ($N = 20,000$) at which the sample size is taken. Note the axes are equal for easy comparison, the range for the Sobol and Homma estimators is [0.4, 1.2].

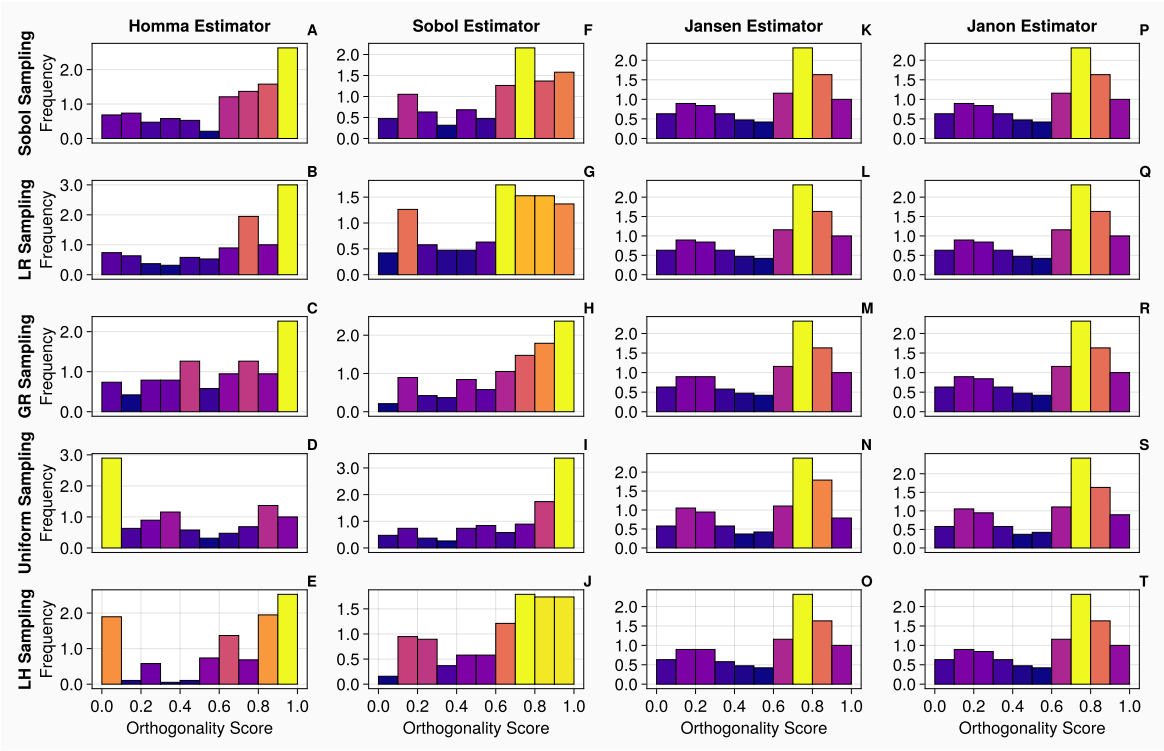

Fig. 5.9 **Orthogonality distributions of input parameters for the 2-chamber model with discrete measurements**: Histograms A-T show the distribution of orthogonality returned from examinations of the sensitivity vectors, calculated from continuous measurements. Here, an orthogonality score of 1 represents total independence of input parameters, whereas 0 represents total dependence. Each individual diagram denotes a specific combination of sampling methodology and estimator type. The frequency of each histogram is normalised such that it is comparable between plots, i.e., the larger the frequency of a bin, the larger the number of orthogonality scores calculated from the original sensitivity vectors.

Table 5.10 **Input parameter ranking for the 2-chamber model with discrete measurements**: Here, input parameters are ranked based on the averaged orthogonality score returned from the calculated total order sensitivity matrix. In addition, the ranking is stratified by both sampling and estimator types.

	Homma					Sobol					Jansen					Janon				
	SS	LR	GR	U	LH	SS	LR	GR	U	LH	SS	LR	GR	U	LH	SS	LR	GR	U	LH
$E_{min_{lv}}$	17	18	14	1	3	7	6	6	9	6	5	5	5	5	5	5	5	5	5	5
$E_{max_{lv}}$	18	14	9	3	7	19	18	19	20	20	20	20	20	19	20	20	20	20	19	20
$\tau_{es_{lv}}$	4	5	4	10	11	8	7	8	6	5	4	4	4	4	4	4	4	4	4	4
$\tau_{ep_{lv}}$	1	1	1	2	8	4	4	7	7	4	3	3	3	3	3	3	3	3	3	3
$E_{min_{la}}$	19	19	8	14	12	14	14	14	1	16	16	16	16	18	16	16	16	16	18	16
$E_{max_{la}}$	20	20	6	9	9	15	13	16	15	9	17	17	17	16	17	17	17	17	16	17
$\tau_{es_{la}}$	9	12	17	19	17	16	19	18	17	15	12	12	12	12	12	12	12	12	12	12
$\tau_{ep_{la}}$	15	17	7	12	15	17	17	17	18	7	15	15	15	17	15	15	15	15	17	15
Z_{ao}	14	6	12	20	13	3	2	5	4	2	1	1	1	1	1	1	1	1	1	1
R_{mv}	13	15	10	4	5	18	15	15	16	17	14	14	14	15	14	14	14	14	15	14
C_{sas}	11	7	16	15	16	12	16	11	2	18	7	7	7	7	7	7	7	7	7	7
R_{sas}	7	10	19	18	20	6	3	4	5	3	2	2	2	2	2	2	2	2	2	2
L_{sas}	8	8	18	17	19	1	1	1	3	1	18	18	18	14	18	18	18	18	14	18
C_{sat}	5	4	5	11	6	5	5	3	12	12	6	6	6	6	6	6	6	6	6	6
R_{sat}	10	11	15	13	14	11	11	2	8	8	10	11	9	9	10	10	11	9	9	10
L_{sat}	6	9	20	16	18	2	10	12	13	13	8	8	8	8	8	8	8	8	8	8
R_{sar}	3	2	2	8	4	9	8	9	11	11	9	9	10	11	11	9	9	10	11	11
R_{scp}	2	3	3	7	2	10	9	10	10	10	11	10	11	10	9	11	10	11	10	9
R_{svn}	16	16	13	6	1	13	12	13	14	14	13	13	13	13	13	13	13	13	13	13
C_{svn}	12	13	11	5	10	20	20	20	19	19	19	19	19	20	19	19	19	19	20	19

Table 5.11 **Input parameter ranking for the 2-chamber model with discrete measurements**: The ranges of input parameters across 5 sampling types for a specific estimator for the systemic circulation model with discrete measurements.

	Range Homma	Range Sobol	Range Jansen	Range Janon
$E_{min_{lv}}$	17	3	0	0
$E_{max_{lv}}$	15	2	1	1
$\tau_{es_{lv}}$	7	3	0	0
$\tau_{ep_{lv}}$	6	3	0	2
$E_{min_{la}}$	11	15	2	1
$E_{max_{la}}$	14	7	1	0
$\tau_{es_{la}}$	10	4	0	2
$\tau_{ep_{la}}$	10	11	2	2
Z_{ao}	14	3	0	0
R_{mv}	11	3	1	1
C_{sas}	9	16	0	0
R_{sas}	13	3	0	0
L_{sas}	11	2	4	4
C_{sat}	7	9	0	0
R_{sat}	5	9	2	2
L_{sat}	14	11	0	0
R_{sar}	6	3	2	2
R_{scp}	5	1	2	2
R_{svn}	15	2	0	0
C_{svn}	7	1	1	1
Mean Variation Of Input Set	10.9	5.55	0.9	1.0

Table 5.12 **Input parameter ranking for the 2-chamber model with discrete measurements**: The ranges of input parameters across 4 estimator types for a specific sampling method for the 2-chamber model with discrete measurements.

	Range SS	Range LR	Range GR	Range U	Range LH
$E_{min_{lv}}$	12	13	9	8	3
$E_{max_{lv}}$	2	6	11	17	13
$\tau_{es_{lv}}$	5	3	4	6	7
$\tau_{ep_{lv}}$	3	3	6	5	5
$E_{min_{la}}$	5	5	8	17	4
$E_{max_{la}}$	5	7	11	7	8
$\tau_{es_{la}}$	7	7	6	7	5
$\tau_{ep_{la}}$	2	2	10	6	8
Z_{ao}	13	5	11	19	12
R_{mv}	5	1	5	12	12
C_{sas}	5	9	9	13	11
R_{sas}	5	8	17	16	18
L_{sas}	17	17	17	14	18
C_{sat}	1	2	3	6	6
R_{sat}	1	0	13	5	6
L_{sat}	6	2	12	8	10
R_{sar}	6	7	8	3	7
R_{scp}	9	7	8	3	7
R_{svn}	3	4	0	7	13
C_{svn}	8	7	9	15	9
Mean Variation Of Input Set	6	5.75	9.35	9.7	9.15

reduce the level of uncertainty associated with an input parameter's orthogonality ranking (see Tables 5.9 and 5.12), despite spurious parameter rankings from the Homma and Sobol estimators leading to large parameter variation when stratified by sampling methodologies.

5.3 Discussion

Utilising two cardiovascular system models, the main aim of our investigation was to test the robustness of the calculation of the input parameter orthogonality, while varying total order estimator types and sampling methodologies, across differing input parameter dimensionalities and types of data on which the total order indices were calculated. The results presented in Section 5.2 show overwhelming robustness for the Jansen and Janon estimators when calculating total order indices, compared to other estimator options. For the 1-chamber, 9-parameter model, we observed that these two estimators gave nearly invariant outcomes across sampling methodology and the data type. When the dimensionality of the model parameters is increased to 20, we noted that the Jansen and Janon estimators still exhibited small variations on the input parameter orthogonality rankings. For the Jansen estimator with discrete measurements, it returned a mean variation of less than 1. We observed that the Homma and Sobol estimators regularly returned mean variations for input parameter sets greater than 1, which is particularly amplified when the model dimensionality is increased. These results indicate that if the used estimator and sampling methodology are not robust and compatible, the calculated optimal parameter set is unreliable. The use of fragile estimators and sampling methods can therefore produce misleading conclusions with real practical consequences, especially in life science applications. Interestingly, we witnessed that the variations attached to the Sobol and Lattice Rule sampling methods were the lowest across all model dimensionalities and data types. Our results also reinforce the findings reported in [296, 461], that the commonly used Latin Hypercube method is sub-optimal in exploring the input parameter space, especially at high dimensionalites.

The Jansen and Janon robustness at calculating total order indices might be attributed to the Jansen estimator never allowing negative values in the numerator (see definitions in Table 4.4), whereas the Janon estimator is the only estimator which is proved to be both asymptotically normally distributed and asymptotically efficient, meaning as the sample size increases the estimation error associated with calculating the indices is negligible [420]. They are both highly optimised estimators with very little room for improvement [419, 420]. Admitting negative indices in both the Sobol and Homma estimators is a reason for the poor performance in the calculations of these indices. From the Hoeffding-Sobol decomposition,

as seen in section 4.5.3, the total order indices can be regarded as a decomposition of the variance. Thus, any negative value obtained from an estimator is impossible. Any negative value returned from an estimator is likely to be due to some points in the parameter space returning unphysiological results. Thus reinforcing the important point of ensuring any sensitivity indices have adequately converged in order to avoid any of these unstable points.

While the robustness of the Homma and Sobol estimators have been questioned within this work, this does not mean they lack the ability to produce accurate estimations of parameter influence. Figure 5.10 shows the Homma and Sobol total order estimator results against the maximum left ventricular volume with an increased sample size comparing to the tests conducted earlier - $N = 100,000$ (which requires $2,200,000$ model evaluations). We observe that, now with a much extended sample size, the confidence intervals (green bands in Figure 5.10) and parameter interpretations from Homma and Sobol estimators are similar to that of the Jansen or Janon estimators, in panels C and D for $N = 40,000$ samples. In principle, this demonstrates a credible convergence- that all estimators can, indeed, produce equivalent results, when 'sufficiently large' samples are used. However, with a limited computational budget, our results indicate a clear estimator choice, to obtain robust and valid parameter interpretations with the best computational efficiency.

With the highly optimised Jansen and Janon estimators, it is evident that they consistently exhibit the most efficient convergence and produce the smallest uncertainties when calculating total order indices. This phenomenon matches the consistent orthogonality observed among input parameters across various sampling techniques when coupled with the Jansen and Janon estimator. Conversely, the Homma and Sobol estimators tend to yield significantly larger uncertainties when sample sizes are held constant among estimators, thus explaining the lack of consistent orthogonality rankings for the input parameters. Increasing the sample size seems to ameliorate the uncertainties associated with the Homma and Sobol estimators, particularly when employing the Sobol, lattice rule, and Golden sampling methods. This observation underscores the resilience of low-discrepancy sequences, demonstrating their effectiveness even in conjunction with a sub-optimal estimator. While the work of Puy et al. [293] did not provide extensive convergence or uncertainty quantification, it is plausible to infer that the Jansen and Janon estimators, with their superior convergence rates and lower uncertainty, played a pivotal role in the authors' conclusion that these estimators are the most efficient at capturing the true effects of input parameters.

Our investigation was based on two highly non-linear stiff differential algebraic equation

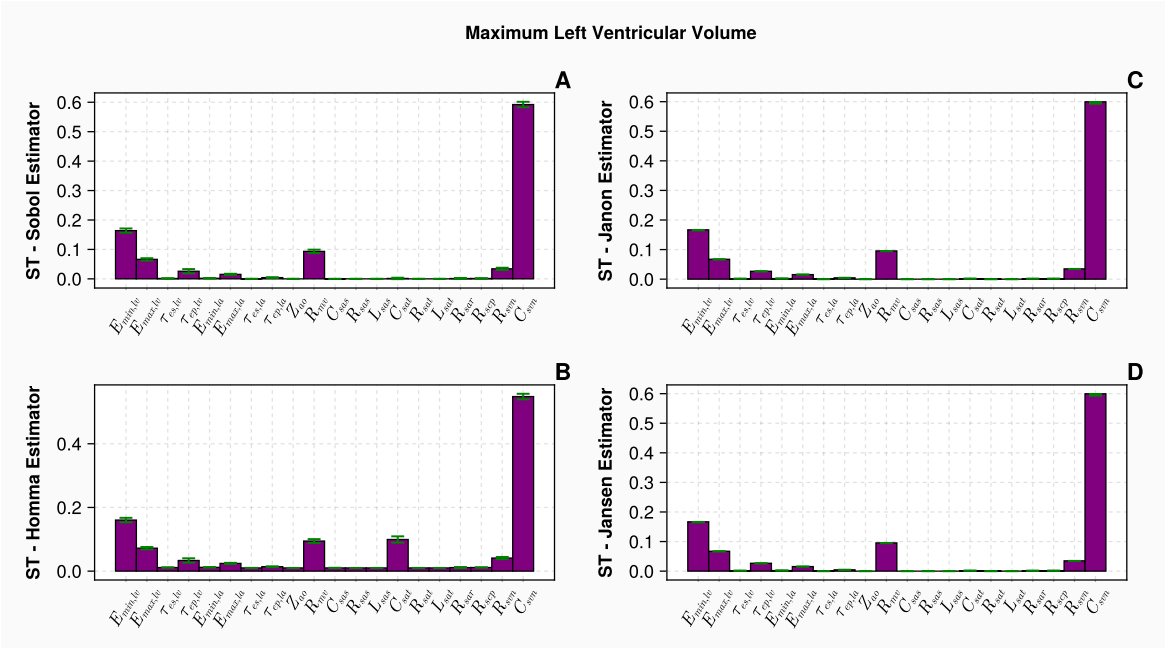

Fig. 5.10 **Estimator comparisons with larger samples for the 2-chamber model with discrete measurements**: The Sobol and Homma estimators results are based on 100k samples, compared to the Jansen and Janon estimators using 40k samples both with 95% confidence. The input parameter effect is displayed against the maximum left ventricular volume as an example here.

systems with a high level of implicit complexity. Good modelling guidelines originating here should therefore be applicable to simpler, more linear models which with a less variable input parameter space. Obtaining sensitivity estimates for linear models is considerably less expensive than what has been conducted here. Convergence and uncertainty quantification have historically been omitted from sensitivity analysis studies, despite being acknowledged as vital, if the results of studies were then to influence policy /societal /clinical decisions [296, 239]. In this study, we have highlighted the impact that convergence has on a total order estimator, alongside this, we have also shown the impact of the level of sampling taken, on the calculation of total order estimators. It is intuitive that the higher density of sampling leads to better resolution of the input parameter space, hence our sensitivity analysis gives a better indication about which input parameters are truly influential. Current literature states that $N > 500$ but this recommendation is based on physical systems which are mostly linear. The work conducted and results shown above suggest for a non-linear system, one needs $N > 5000$. Still more importantly, it is clear that no two systems are the same -even if they are based in similar physiology- so for one to ensure adequate resolution of an input parameter space, convergence and uncertainty quantification through bootstrapping must be an essential step in any modeller's workflow, if accuracy and robustness are an issue. In other fields, such as CFD, it is standard practice for one to perform a mesh convergence study in order to validate the results. The work conducted here advocates for a similar principled approach in order to validate the results and interpretations made from sensitivity investigations.

While it is clear that a large sample size is needed in order to ensure accurate sensitivity estimates, researchers are often restricted by their computational budget. Without sufficient computational speed, it would be infeasible to perform the requisite number of model evaluations to obtain accurate indices interpretation. For our 2-chamber model, 100k samples required 2.2 million model evaluations. Each model evaluation took 0.039 seconds to run in Julia, thus it would require 23.8 hours if this was computed in serial. The Julia language has consistently proved to be 10 to 100 times [444, 445] quicker than other comparable languages for solving systems of this class and the use of parallel computation has further accelerated our simulations. Therefore, in situations with a limited computational budget, the selection of an efficient language and estimators which require fewer samples to reach convergence is key.

Although inexhaustive, the list of estimators investigated in this chapter does represent those that are readily available, practically usable and computationally feasible. Puy et al. [293] also recommended the estimator introduced by Azzini et al. [416], which appeared to produce similar results to the Jansen estimator. The Azzini estimator requires $N = 2k(n+1)$

model evaluations, compared to $k(n+2)$ evaluations needed by our other estimators. The 2-chamber model would require $N = 1,320,000$ model evaluations for an Azzini estimator. For models with higher parameter dimensions, this would be computationally infeasible. As the prospect of digital twins in healthcare grows, more complex and detailed models which accurately represent the true physiological processes are routinely generated. One bottleneck which prevents the progression of these models to the clinic is the computational cost associated with a detailed sensitivity analysis. This cost does not rely on calculation of the indices as much as the process of solving the dynamical system. Therefore, while new estimators may improve accuracy, the focus must remain on efficient resolution of complex dynamical systems and the efficiency of the estimators for low sample numbers, in order to ensure a thorough sensitivity analysis.

All the estimators used here are available in the global sensitivity packages such as SALib, GlobalSensitivity.jl, SenSobol and sbiosobol [462, 446, 463]. It is reassuring to see that the default estimator used to calculate the total order index, in the available packages, is the Jansen estimator. Given the conclusion drawn from Puy et al. [293] and the findings from this work, researchers could straightforwardly use the above packages when performing practical identifiability studies and would obtain a reliable optimal set of input parameters which best describes the experimental data available to them.

A related thread of research is the calculation of total order sensitivity indices where one assumes dependency between input parameters. This is partially investigated by Puy et al. [463] when implementing the method of Glen et al. [464]. This method requires a prescription of linear dependencies between parameters, however, these are often unknown. Consequently, Puy et. al. noted an inaccuracy associated with this method when calculating the true effects. There have been various attempts at deriving variance based sensitivity indices with dependent inputs [465–467], however, like the method of Glen et al. [464], they require knowledge of the dependencies that exist within the model and therefore the computational power needed to simulate these indices is often much larger than the standard Sobol indices. Further, there is no accepted method for how to calculate these dependent indices which should be of interest for future work. Therefore, the need to understand how input parameter orthogonality is affected by varying estimators and sampling methodologies is of significant importance, in order for total order sensitivity indices to be utilised in identifiability studies.

While we have used the method of Li et. al. [19] (see Eq. (5.1)) suitable for practical

identifiability studies, it is also applicable to other methods. Another approach of identifying input parameters is the structured correlations method [331] in which one seeks to identify correlations between parameters and to calculate ranks (based on which parameters can be identified uniquely if they are not strongly correlated with other parameters). This approach used the total order sensitivity matrix to calculate these correlations. Therefore, the need for reliable and robust sensitivity matrices remains- whichever method is implemented.

The work of Puy et al. [293] is conclusive in its findings of the Jansen and Janon estimators being the most reliable in finding a "true" input parameter effect. Our work reinforces these conclusions, in that we find the Jansen and Janon are the most reliable in the calculation of input parameter orthogonality (which appears to be motivated by input parameter convergence). Puy et al. [293] also reported that any choice made on the model has a non-negligible effect. While we agree with these conclusions for the most part, we are able to identify that similar to the model dimensionality, it appears choices we make, such as the sampling methodology and type of data used, have more impactful consequences. The lower variation associated with input parameter sets, when low discrepancy sequences are used, implies their effectiveness in returning robust and reliable input parameter sets. It appears that there is no clear advantage of using either continuous or discrete measurements when choosing how to calculate the total order indices. This may change given the investigation in a different domain.

5.4 Conclusion

This chapter delved into the intricacies of varying sampling methodologies and variance-based total order estimators, aiming to establish best practices for practical identifiability studies. We conducted our investigation using two highly non-linear and stiff LPMs of the human cardiovascular system as different but physiologically unified, complimentary test cases: (i) a 1-chamber, 9-parameter model in figure 4.1A and (ii) a 2-chamber, 20-parameter model in figure 4.1B, both based on differential algebraic equations. Via a thorough assessment of total order estimators and sampling methodologies, we gained valuable insights into their strengths and weaknesses, shedding light on the orthogonality of the input parameters within the models. This analysis complements prior work that focused on the estimators' ability to uncover the "true" effects of a model, enriching our comprehension of their practical identification.

Our findings advocate for the Jansen and Janon estimators as robust choices across dif-

ferent sampling methodologies, measurement data variations, and model dimensions. These estimators emerge as preferred tools for calculating total order indices and, consequently, for identifying the optimal set of input parameters. Their efficient convergence and the resulting reduction in index uncertainty make them the optimal choice for this task. These estimators of the variance and thus will be robust for any dynamical system investigated in any domain. Furthermore, we recommend the use of low-discrepancy quasi-random Sobol and Lattice Rule sampling schemes as optimal sampling methodologies to complement Jansen and Janon estimators.

This work establishes a framework of good modelling practice for practical identifiability studies, considering both the influence of input parameters and their orthogonality. By incorporating these best practices into modelling studies, researchers can consistently and reliably identify the optimal input parameters for dynamical systems. This approach not only enhances the quality and accuracy of parameter identification, but also paves the way for more informed decision-making in various scientific and practical domains.

Chapter 6

Investigating the Impact of Experimental Designs on the Personalisation Process: a Cardiovascular Perspective

I would rather have questions that can't be answered than answers that can't be questioned.
— RICHARD FEYNMAN

Summary
In view of the clear need for converged sensitivity indices, this chapter "reverses" the concept of sensitivity analysis and explores what the impact of changing outputs has on input parameter ranking and model sloppiness, enhancing our understanding of the complexities associated with the personalisation process. [1]

[1]This chapter is currently not published however is under review with the journal *Computers in Biology and Medicine.* **Saxton, H.**, Taylor, D., Halliday, I., Newman, T., Schenkel, T., Morris, P., Clayton, R., Xu, X. (2024). The impact of experimental designs & system sloppiness on the personalisation process: A cardiovascular perspective.

6.1 Introduction

The concept of digital twin (DT) originates in the 1960s with NASA, who created a virtual representation in the Apollo 13 moon exploration mission. There are now many definitions of the DT, one representative example being “a set of virtual information constructs that mimics the structure, context and behaviour of an individual or unique physical asset, which is dynamically updated with data from its physical twin throughout its life-cycle and that ultimately informs decisions that realise value” [468]. In medicine, the potential of the DT is profound, particularly in enhancing patient care and outcomes - clearly, a digital representation of an individual’s physiology or pathophysiology holds immense promise, not least it could empower healthcare professionals to simulate and predict a patient’s disease trajectory, from compensation to decompensation, or in response to various lifestyle changes and treatments [469].

In cardiology, the adoption of heart and circulatory DTs has gradually gained momentum and trust within the clinical community, evidenced by several recent proof-of-concept studies [470, 226, 471]. Traditionally, clinical diagnosis and patient trajectories in cardiology rely heavily on a clinician’s expertise and population-based averages [472]. However, the emergence of DTs in cardiology signifies a shift towards a more personalised approach. These DTs integrate mechanistic (physics-based) models, grounded in physiological understanding of the heart, human circulation, and related physiological processes, with dynamic clinical data collected over time or immediate data from the clinic [7]. This integration enables the DT to provide tailored predictions and clinical decision support. Virtual representations of a patient’s full cardiovascular health in differing states are referred to as their “physiological envelope" [237].

Clinical data are valuable resources, thus the choice or requirement of what data are needed to personalise a LPM (to create a useful cardiovascular DT) is multi-faceted [240]. Within a clinical setting, they range over both continuous and discrete measurement data and the process of obtaining diagnostically useful data often requires invasive tests on a patient. With any data - blood pressure, flow and volume for each compartment (say), one then calculates "derived" clinical metrics (with clinical precedent). Examples include (i) ejection fraction [473] which is traditional stratifier of heart failure; (ii) pulse pressure [474] to stratify arterial stiffening; (iii) maximum blood velocity [475] to stratify heart valve stenosis; (iv) cardiac output [476] to assess overall heart health. One also observes various clinical time series waveforms such as ventricular pressures and volumes [477]. Such metrics can be amalgamated into a DT, enriching the model’s predictions with patient-specific information

with what amounts to a weak form of validation. In general, a plethora of available clinical tests (each carrying its own risks to patients, note) may be ordered, to generate metrics that are of variable importance in creating a faithful virtual representation of a patient; ranking them for importance is a challenging task. Each set of measurements collected and utilised to perform DT related tasks is denoted an experimental design [478].

The integration of clinical data into an LPM, to form a DT is for all practical purposes precisely 'the personalisation process' (or 'model personalisation'). Mathematically, this task is an 'inverse problem' [479]. One can think of the solution to the personalisation process as an input parameter set that locates the global minimum of a hypersurface, spanned by the combination of input parameters of the mechanistic model and the available clinical measurements. These parameters potentially provide unique clinical biomarkers [480], because they define a point in the input parameter hyper space such that the outputs of our mechanistic model most closely match the clinical measurements of a patient. Put another way, the coordinates of this model operating point in the input parameter space define a patient's patho/physiological state.

There remain many very important open questions surrounding the personalisation process, which we distil as explicit questions:

1. What clinical data must be acquired *in-vivo* to obtain patient-specific biomarkers?
2. Is a set of biomarkers invariant in the presence of changed experimental designs?
3. How straightforward is the solution of the personalisation problem under different experimental designs? Does one require a complex genetic algorithm or a simple gradient descent method?
4. Should DTs prioritise individual patient "physiological envelopes" or should they target specific conditions?

These expansive and important question clearly require extensive work from the entire community. We concern ourselves to ask to what extent the above questions can be answered. Before proceeding, it is important to note that all investigations in this work are conducted with forward generated model data first to understand the ideal setting by eliminating the confounding effects of e.g. noise. Clinical data obtain *in-vivo* may provide polluted steer to the *in-silico* data obtained from the model.

6.1.1 Clinical Measures

When varying the experimental design, we adopt medically representative measures i.e. those utilised in diagnosing cardiovascular diseases. To investigate the effect of experimental design, we devise an additive algorithm: each time we move to what we will designate a new measurement level (see below) we add the new measurement to the previous output set, therefore defining a new “unified" output space, of progressively increased dimension, for the analysis of input parameter effects.

In tables 6.1, 6.2 and 6.3, we declare what we define to be progressive, or stratified measurement “levels". See table captions. The latter are essentially sets of increasing cardinality, containing discrete, continuous and mixed measurements.

6.1.1.1 Discrete Measurements

In the discrete case in table 6.1, we utilise only single point metrics. These metrics can be obtained through just 3 clinical tests:

1. Blood Pressure (BP): This can be readily obtained through a cuff reading while a patient is in hospital. In our chosen model, this measurement is obtained by calculating $\frac{\text{Max}(P_{sa})}{\text{Min}(P_{sa})}$ and corresponds to Level 1.
2. Ejection Fraction (EF): This can be obtained through an echocardiogram. In our model, we calculate EF for the left and right ventricle then the left and right atria as $\frac{\text{Max}(V_i)-\text{Min}(V_i)}{\text{Min}(V_i)}$. For $i = lv, rv, la, ra$ this corresponds to Levels 2A, 2B, 2C and 2D.
3. Max(Q_i) - Maximum flow: This could be obtained from either an echocardiogram or a cardiac MRI. This is calculated for the systemic, pulmonary, aortic valve, mitral valve, pulmonary valve and tricuspid valve.

To emphasise the additive process of the experiment in the discrete setting, for example the full output set for Level 3A is defined as follows:

$$\text{Level 3A} = (BP, EF_{cv}, EF_{rv}, EF_{ca}, EF_{ra}, \text{Max}(Q_s)).$$

6.1.1.2 Continuous Measurements

For the continuous measurements displayed in table 6.2, each continuous waveform obtained is made up of 150 time points, obtained though 4 clinical data streams below.

Table 6.1 **Table of Discrete Measurements:** Each discrete *level* (top row) declares which new measurement is added to an increasing model target outputs set. For example, set 2D is the union of all data in sets 1A to 2D; $V_r a$ augments the set of all preceding measurements. Each discrete measurement equates to a single point extracted from the cardiovascular cycle.

Discrete Measurement Levels						
Measurement Level	1	2A	2B	2C	2D	
Measurement Added	BP	EF_{lv}	EF_{rv}	EF_{la}	EF_{ra}	
Measurement Level	3A	3B	3C	3D	3E	3F
Measurement Added	Max(Q_s)	Max(Q_p)	Max(Q_{lv})	Max(Q_{la})	Max(Q_{rv})	Max(Q_{ra})

1. Q_i - Flow rate: can be obtained through a doppler ultrasound, for the systemic, pulmonary, aortic valve, mitral valve, pulmonary valve and tricuspid valve.

2. V_i - Chamber volume: can be obtained through a cardiac MRI, for the two ventricles and two atria.

3. P_{cv}, P_{sa} - Left heart pressures: can be obtained through invasive catherterisation for the left ventricle and systemic artery.

4. $P_{rv}, P_{pa}, P_{ra}, P_{pv}$ - Right heart and circulation pressures: can be obtained by invasive Swan-Ganz catherterisation and wave form pressures are collected in the right heart for the right ventricle, pulmonary artery, right atrium and pulmonary vein.

6.1.1.3 Mixed Measurement Levels

The previous two measurement settings will reveal the difference between continuous and discrete metrics. The mixed measurement level combines both the discrete and continuous measurements but represents a standard diagnosis procedure with increasing invasiveness, i.e., in clinic, a patient would not be subject to invasive chamber pressure measurements unless deemed necessary. Apart from one additional measurement (noisy blood pressure) which will be introduced below, all other metrics and corresponding measurement levels are the same as those defined in sections 6.1.1.1 and 6.1.1.2.

- BPN - noisy blood pressure: This level is added to account for the situation of a patient taking their own arterial blood pressure at home, with noisy readings due to human

Table 6.2 **Continuous Measurements:** Each continuous level shows which new time series measurement is added to the expanding set of outputs which also contains all measurements previous measurements. Each continuous measurement relates to a single converged cardiovascular cycle, consisting of 150 time points.

Continuous Measurement Levels						
Measurement Level	1A	1B	1C	1D	1E	1F
Measurement Added	Q_s	Q_p	Q_{lv}	Q_{la}	Q_{rv}	Q_{ra}
Measurement Level	2A	2B	2C	2D	3A	3B
Measurement Added	V_{lv}	V_{rv}	V_{la}	V_{ra}	P_{sv}	P_{sa}
Measurement Level	4A	4B	4C	4D		
Measurement Added	P_{rv}	P_{pa}	P_{ra}	P_{pv}		

error and lower device accuracy. The analysis of noisy output data will illustrate how global sensitivity indices alter in the presence of noise.

BPN is calculated as

$$\text{BPN} = \frac{\text{Max}(P_{sa})}{\text{Min}(P_{sa})} \times (1+\varepsilon), \;\; \varepsilon \sim N(0, 0.1).$$

In this setting, Level 2 represents an arterial blood pressure measurement obtained in the hospital, not being subject to noise. Slightly different to the measurement levels introduced in sections 6.1.1.1 and 6.1.1.2, here Level 2 will replace Level 1 (instead of adding to it) and Level 2 will be used in all increasing measurement sets for the later levels.

Table 6.3 **Table of Mixed Measurement:** Each level declares which new measurement is added to the increasing output set (apart from Level 2 which replaces Level 1) along with the accumulation of all previous measurements. Each discrete measurement added corresponds to a single cardiovascular cycle. For each continuous measurement added this is a converged cardiovascular cycle resolved on 150 equispaced time points.

Mixed Measurement Levels						
Measurement Level	1	2	3A	3B	3C	3D
Measurement Added	BPN	BP	EF_{lv}	EF_{rv}	EF_{la}	EF_{ra}
Measurement Level	4A	4B	4C	4D	4E	4F
Measurement Added	Q_s	Q_p	Q_{lv}	Q_{la}	Q_{rv}	Q_{ra}
Measurement Level	5A	5B	5C	5D	5E	
Measurement Added	$\text{Max}(Q_{lv})$	$\text{Max}(Q_{la})$	$\text{Max}(Q_{rv})$	$\text{Max}(Q_{ra})$	V_{lv}	
Measurement Level	5F	5G	5H	6A	6B	
Measurement Added	V_{rv}	V_{ra}	V_{ra}	P_{sv}	P_{sa}	
Measurement Level	7A	7B	7C	7D		
Measurement Added	P_{rv}	P_{pa}	P_{ra}	P_{pv}		

6.2 Results

Sections 6.2.1, 6.2.2 and 6.2.3 account for average input parameter influence across all outputs, for varying experimental design, using the method of section 4.10. The average input parameter rank and values are displayed as tables. The corresponding figure in each section shows the eigenvalues of the Fisher information matrix on a $\log_{10}$ scale, for varying measurement levels (see sections 4.4 and 4.13). The sections below present results for the varying discrete, continuous and mixed measurement levels, respectively, as described in section 6.1.1.

6.2.1 Discrete Measures

Table 6.4 ranks each input parameter and their corresponding influence value based upon discrete measurements. We note, from level 1 to level 3F, the resistance of the systemic vascular bed R_{svb} and the systemic arterial compliance C_{sa} rank highest, with the largest influence values with the exception from level 2D in which $E_{shift,ra}$ ranks the most influential. This can be explained by the experimental design. The newest measurement added for level 2D was the ejection fraction of the right atrium. The $E_{shift,ra}$ parameter controls the ejection of blood for the whole system thus if the timing of atrial contraction is wrong this can impact the whole system. However in all the other cases, it appears R_{svb} and C_{sa} still dominate. As more measurements are added to the experimental design, we observe more input parameters record an influence score greater than 0.01. For case 3F where there are 11 outputs, 17 input parameters are recorded with an influence score larger than 0.01. As the measurement set increases, the largest influential value decreases. In addition, as more measurements are added, although more “influential" parameters are obtained, the majority have an influence score of $O(10^{-2})$.

The result in figure 6.1 shows that the model cannot be regarded as sloppy with a discrete output set. With an increasing output set, we observe more input parameters are regarded as stiff. Even with the largest output set, level 3F, the model still exhibits an eigenvalue spectrum spanning >15 orders of magnitude.

6.2.2 Continuous Measures

With an increasing continuous measurement set, in table 6.5, a much higher number of influential input parameters are present, compared to the discrete case (table 6.4). Even with just a single continuous measurement of the systemic flow (Column 1A), 17 input parameters are

Table 6.4 **Input parameter ranking for discrete measurements:** Averaging across all output space, the input parameter rank and its influence value are displayed, for increasing discrete measurements. Here P represents the parameter and E the corresponding average influence value.

Measurement Levels									
1		2A		2B		2C		2D	
P	E	P	E	P	E	P	E	P	E
C_{sa}	0.80	R_{svb}	0.44	R_{svb}	0.34	R_{svb}	0.26	$E_{shift,ra}$	0.24
R_{svb}	0.60	C_{sa}	0.43	C_{sa}	0.33	C_{sa}	0.26	R_{svb}	0.10
$\tau_{es,lv}$	0.04	$E_{max,lv}$	0.24	$E_{max,lv}$	0.18	$E_{max,lv}$	0.14	C_{sa}	0.10
		$V_{0,lv}$	0.04	$V_{0,lv}$	0.03	$V_{0,lv}$	0.03	$E_{max,lv}$	0.06
		$\tau_{es,lv}$	0.02	$E_{max,rv}$	0.02	$E_{max,rv}$	0.02	$E_{max,ra}$	0.04
				$\tau_{es,lv}$	0.02	$\tau_{es,lv}$	0.01	$\tau_{ep,rv}$	0.02
								$E_{min,rv}$	0.01
								$E_{max,rv}$	0.01
								$V_{0,lv}$	0.01

Measurement Levels											
3A		3B		3C		3D		3E		3F	
P	E	P	E	P	E	P	E	P	E	P	E
R_{svb}	0.22	R_{svb}	0.20	R_{svb}	0.19	R_{svb}	0.17	R_{svb}	0.15	R_{svb}	0.13
C_{sa}	0.20	C_{sa}	0.18	C_{sa}	0.17	C_{sa}	0.15	C_{sa}	0.13	C_{sa}	0.11
$E_{max,lv}$	0.10	$E_{max,lv}$	0.09	$E_{max,lv}$	0.09	$E_{max,lv}$	0.09	$E_{max,lv}$	0.08	$E_{shift,ra}$	0.10
$E_{shift,ra}$	0.05	$E_{shift,ra}$	0.06	$E_{shift,ra}$	0.06	$\tau_{es,lv}$	0.05	$E_{shift,ra}$	0.05	$E_{max,lv}$	0.07
$E_{min,lv}$	0.03	$E_{min,lv}$	0.03	$E_{min,lv}$	0.03	$E_{shift,ra}$	0.05	$\tau_{es,lv}$	0.05	$\tau_{es,lv}$	0.04
$E_{max,rv}$	0.02	$E_{max,rv}$	0.02	C_{pa}	0.03	$E_{min,lv}$	0.03	$E_{min,lv}$	0.05	$E_{min,lv}$	0.03
$V_{0,lv}$	0.02	$V_{0,lv}$	0.01	R_{pvb}	0.03	$E_{max,rv}$	0.02	$E_{max,rv}$	0.03	$E_{max,ra}$	0.03
C_{sv}	0.01	C_{sv}	0.01	$E_{max,rv}$	0.02	$E_{max,la}$	0.02	$\tau_{es,rv}$	0.02	$E_{max,rv}$	0.03
$E_{max,la}$	0.01	$E_{max,la}$	0.01	$E_{shift,la}$	0.02	$E_{shift,la}$	0.02	$E_{max,la}$	0.02	$\tau_{es,rv}$	0.03
$E_{shift,la}$	0.01	$E_{shift,la}$	0.01	$E_{max,la}$	0.02	C_{sv}	0.01	$E_{shift,la}$	0.02	$E_{min,ra}$	0.02
$\tau_{es,lv}$	0.01	C_{pa}	0.01	C_{sv}	0.02	$V_{0,lv}$	0.01	C_{sv}	0.02	C_{sv}	0.02
R_{pvb}	0.01	R_{pvb}	0.01	$V_{0,lv}$	0.01	C_{pa}	0.01	$E_{min,rv}$	0.01	$E_{shift,la}$	0.02
$E_{min,rv}$	0.01	$E_{min,rv}$	0.01	$E_{min,rv}$	0.01	$E_{min,rv}$	0.01	$V_{0,lv}$	0.01	$E_{max,la}$	0.02
$\tau_{es,lv}$	0.01	$\tau_{es,lv}$	0.01	$E_{max,ra}$	0.01	R_{pvb}	0.01	C_{pa}	0.01	$E_{min,rv}$	0.01
						R_{pvb}	0.01	R_{pvb}	0.01	R_{ra}	0.01
										C_{pa}	0.01
										R_{pvb}	0.01

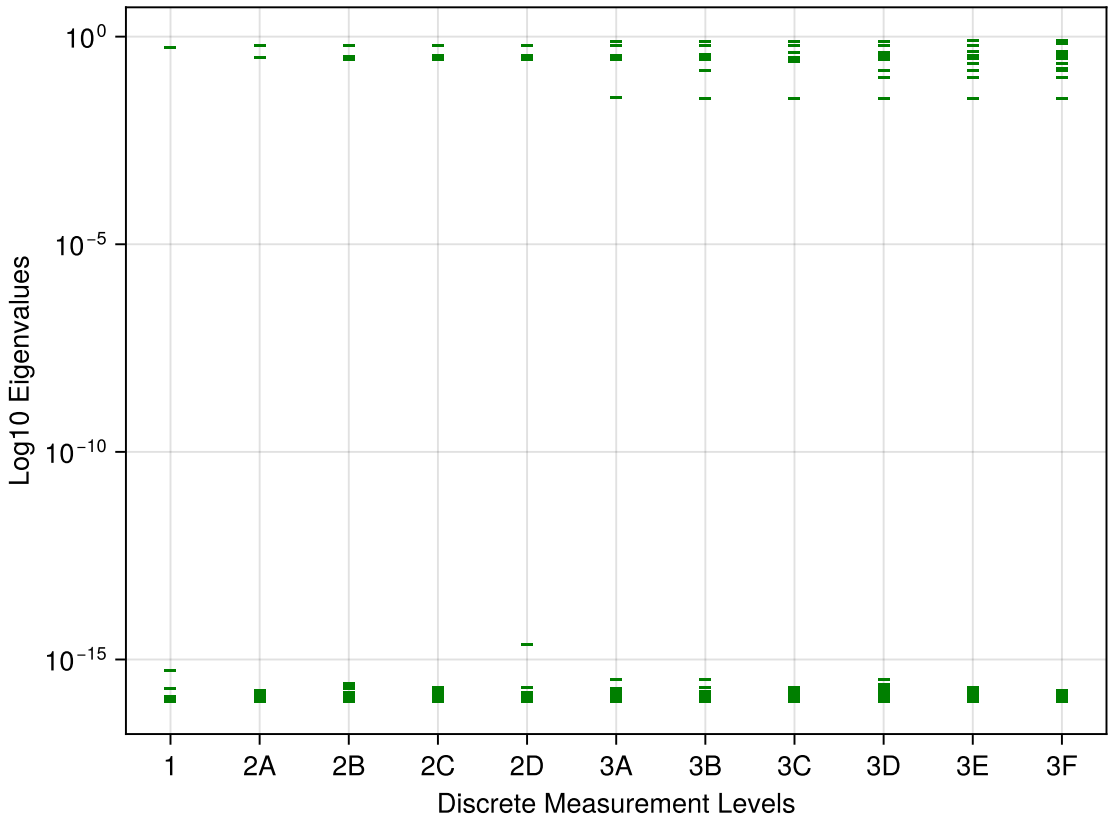

Fig. 6.1 **Discrete measures - sloppy analysis:** The eigenvalues of the Fisher information matrix for increasing discrete measurements are displayed here on a $\log_{10}$ scale.

regarded as influential. In level 4D, where there are 16 continuous output measurements, 20 input parameters are recorded as influential. Here, the ranking of influential input parameters shows much less consistency, compared to table 6.4. The most influential parameters appear loosely to correlate with the latest output added to the measurement list. For example, in level 3B, the left ventricular pressure and systemic arterial pressure are new additions to the output set, and then the top ranking parameters are the minimal ventricular elastance $E_{min,lv}$ and the end pulse time for the left ventricle $\tau_{ep,lv}$. Whereas in level 4C, pressures associated with the pulmonary system have just been added, then the top ranking parameters are the right atrial activation time $E_{shift,ra}$ and the minimal elastance for the right ventricle $E_{min,rv}$. Despite the change in rankings, we note that a similar set of input parameters qualify as influential, with just minor changes when new output measurements are added. As observed in the discrete measurement set, when more input parameters are influential, the concentration of influence decreases and is more evenly spread between the input parameters with an influence value >0.01.

Figure 6.2 shows that for any continuous measurement set, the system can be regarded as sloppy. When increasing the output measurements, the level of sloppiness decreases, with the eigenvalue spectra contracting from a range of 10^{-16} to 10^{-6}. Compared to the discrete sloppy analysis (figure 6.1), input parameters in the stiff direction exhibit larger values than observed previously.

6.2.3 Mixed Measures

When combing both discrete and continuous measurements, the results in table 6.6 show a similar structure to that observed when only continuous measurements are utilised. When BPN is the only output, all input parameters record an influence greater than 0.01, despite the noise, there are still clear influence parameters (C_{sa}, R_{svb} and $\tau_{es,lv}$) which might be regarded as biomarkers. However, when we introduce the noise free BP, the influence values associated with the biomarkers increase significantly. At level 4A, the first continuous measurement is introduced alongside the previous discrete ones. As a consequence, we observe the number of input parameters with influence greater than 0.01 grows from 9 in level 3D to 17 in level 4A. In level 7D (which contains all discrete and continuous measurements) the exact same ranking as level 4D in table 6.5 manifests, although the values of influence vary slightly. This indicates that continuous measurements dominate, when obtaining influential input parameters for a set of measurements. This pattern is also present in figure 6.3, where once continuous measurements are introduced to the output list, sloppiness appears and the

Table 6.5 **Input parameter rankings for continuous measurements:** Averaging across all output space, we declare input parameter rankings and their respective influence value, for increasing continuous measurements.

Measurement Levels											
1A		1B		1C		1D		1E		1F	
P	E	P	E	P	E	P	E	P	E	P	E
$E_{min,lv}$	0.57	$E_{min,lv}$	0.32	$\tau_{es,lv}$	0.38	$E_{shift,la}$	0.21	$E_{shift,la}$	0.19	$E_{shift,la}$	0.11
R_{svb}	0.26	$E_{shift,la}$	0.16	$E_{min,lv}$	0.14	$\tau_{ep,lv}$	0.18	$\tau_{ep,lv}$	0.15	$E_{shift,ra}$	0.1
C_{sa}	0.23	R_{svb}	0.16	R_{svb}	0.1	$E_{min,lv}$	0.07	$E_{min,lv}$	0.06	$\tau_{ep,lv}$	0.08
$\tau_{es,lv}$	0.16	C_{pa}	0.14	C_{sa}	0.06	$\tau_{es,lv}$	0.06	$\tau_{es,lv}$	0.05	$E_{min,lv}$	0.04
C_{pv}	0.15	C_{sv}	0.12	$E_{max,lv}$	0.06	R_{svb}	0.03	$\tau_{es,rv}$	0.05	$\tau_{es,rv}$	0.04
$E_{shift,la}$	0.13	C_{sa}	0.11	$E_{shift,la}$	0.05	C_{pa}	0.03	R_{svb}	0.03	$\tau_{es,lv}$	0.03
$E_{max,lv}$	0.13	R_{pvb}	0.11	C_{sv}	0.04	$E_{min,la}$	0.03	C_{pa}	0.03	$\tau_{ep,rv}$	0.03
C_{sv}	0.12	$\tau_{es,rv}$	0.1	C_{pa}	0.04	C_{sv}	0.02	$E_{min,la}$	0.02	R_{svb}	0.02
$E_{shift,ra}$	0.08	C_{pv}	0.1	C_{pv}	0.04	$E_{max,la}$	0.02	C_{sv}	0.02	C_{pa}	0.02
$E_{max,la}$	0.08	$E_{max,lv}$	0.09	R_{pvb}	0.03	R_{pvb}	0.02	$E_{max,la}$	0.02	C_{sv}	0.02
$E_{min,rv}$	0.08	$\tau_{es,lv}$	0.09	$E_{shift,ra}$	0.03	$\tau_{es,rv}$	0.02	R_{pvb}	0.02	R_{pvb}	0.01
$E_{max,rv}$	0.07	$E_{shift,ra}$	0.07	$\tau_{es,rv}$	0.03	C_{sa}	0.01	C_{sa}	0.02	$E_{min,la}$	0.01
C_{pa}	0.07	$E_{min,rv}$	0.07	$E_{min,rv}$	0.03	$E_{max,lv}$	0.01	$E_{max,lv}$	0.02	$E_{min,rv}$	0.01
R_{pvb}	0.04	$E_{max,la}$	0.06	$\tau_{ep,lv}$	0.02	C_{pv}	0.01	C_{pv}	0.01	$E_{max,la}$	0.01
$E_{max,ra}$	0.03	$E_{max,rv}$	0.05	$E_{max,la}$	0.02	$E_{shift,ra}$	0.01	$E_{min,rv}$	0.01	$E_{max,lv}$	0.01
R_{sv}	0.02	$\tau_{ep,lv}$	0.04			$E_{min,rv}$	0.01	$E_{shift,ra}$	0.01	C_{sa}	0.01
$E_{min,la}$	0.02	$E_{min,la}$	0.03							C_{pv}	0.01
		$E_{max,ra}$	0.02								

Measurement Levels											
2A		2B		2C		2D		3A		3B	
P	E	P	E	P	E	P	E	P	E	P	E
$\tau_{ep,lv}$	0.18	$\tau_{ep,lv}$	0.12	$E_{shift,la}$	0.11	$E_{shift,ra}$	0.16	$\tau_{ep,lv}$	0.12	$E_{min,lv}$	0.1
$E_{shift,la}$	0.06	$E_{shift,ra}$	0.1	$\tau_{ep,lv}$	0.1	$E_{shift,la}$	0.06	$E_{min,lv}$	0.09	$\tau_{ep,lv}$	0.08
$E_{min,lv}$	0.04	$E_{shift,la}$	0.06	$E_{min,lv}$	0.08	$E_{min,lv}$	0.05	$E_{shift,ra}$	0.08	R_{svb}	0.08
$E_{shift,ra}$	0.04	$E_{min,lv}$	0.05	$E_{shift,ra}$	0.06	$\tau_{ep,lv}$	0.04	$E_{shift,la}$	0.07	$E_{shift,ra}$	0.07
$\tau_{es,lv}$	0.03	$\tau_{es,rv}$	0.03	$E_{min,la}$	0.05	$E_{min,rv}$	0.03	$E_{min,la}$	0.04	$E_{shift,la}$	0.07
$E_{max,lv}$	0.02	$\tau_{es,lv}$	0.03	$E_{max,lv}$	0.03	$E_{min,la}$	0.03	$\tau_{es,lv}$	0.03	$\tau_{es,lv}$	0.07
$\tau_{es,rv}$	0.02	$\tau_{ep,rv}$	0.03	$\tau_{es,lv}$	0.02	$\tau_{ep,rv}$	0.03	$E_{max,lv}$	0.03	$E_{min,la}$	0.04
R_{svb}	0.02	$E_{max,lv}$	0.02	C_{sv}	0.02	C_{sv}	0.02	C_{sv}	0.02	$E_{max,lv}$	0.03
C_{sv}	0.02	C_{sv}	0.02	$\tau_{es,rv}$	0.02	$E_{min,ra}$	0.02	$E_{min,rv}$	0.02	C_{sv}	0.03
C_{pa}	0.01	R_{svb}	0.02	R_{svb}	0.02	$\tau_{es,rv}$	0.02	R_{svb}	0.02	$E_{min,rv}$	0.03
C_{sa}	0.01	$E_{max,rv}$	0.02	$E_{max,la}$	0.02	$E_{max,rv}$	0.02	$E_{max,rv}$	0.02	C_{sa}	0.03
$E_{min,la}$	0.01	C_{pa}	0.01	$E_{max,rv}$	0.02	$E_{max,lv}$	0.02	C_{pv}	0.02	C_{pv}	0.03
C_{pv}	0.01	$E_{min,rv}$	0.01	C_{pa}	0.02	R_{svb}	0.02	C_{sa}	0.02	$E_{max,rv}$	0.02
$E_{min,rv}$	0.01	C_{sa}	0.01	C_{sa}	0.02	$E_{max,ra}$	0.02	$\tau_{es,rv}$	0.02	$E_{max,la}$	0.02
		C_{pv}	0.01	C_{pv}	0.02	C_{pa}	0.01	C_{pa}	0.02	C_{pa}	0.02
		$E_{min,la}$	0.01	$E_{min,rv}$	0.02	$\tau_{es,lv}$	0.01	$E_{max,la}$	0.01	$\tau_{es,rv}$	0.02
				$\tau_{ep,rv}$	0.01	C_{pv}	0.01	$\tau_{ep,rv}$	0.01	$\tau_{ep,rv}$	0.01
				R_{pvb}	0.01	$E_{max,la}$	0.01	$E_{min,ra}$	0.01	$E_{min,ra}$	0.01
						C_{sa}	0.01	$E_{max,ra}$	0.01	$E_{max,ra}$	0.01

Measurement Levels							
4A		4B		4C		4D	
P	E	P	E	P	E	P	E
$E_{min,lv}$	0.09	$E_{min,lv}$	0.09	$E_{shift,ra}$	0.18	$E_{shift,ra}$	0.16
$E_{shift,ra}$	0.08	$E_{shift,ra}$	0.09	$E_{min,rv}$	0.05	$E_{min,lv}$	0.08
R_{svb}	0.07	R_{svb}	0.07	$E_{min,lv}$	0.05	$E_{min,rv}$	0.05
$\tau_{ep,lv}$	0.06	$\tau_{ep,lv}$	0.06	R_{svb}	0.04	R_{svb}	0.04
$E_{shift,la}$	0.06	$E_{shift,la}$	0.05	C_{sv}	0.03	$E_{shift,la}$	0.04
$E_{min,rv}$	0.04	$E_{min,rv}$	0.04	$E_{shift,la}$	0.03	C_{sv}	0.03
$\tau_{es,lv}$	0.03	C_{sv}	0.04	$E_{min,ra}$	0.03	$\tau_{ep,lv}$	0.03
$E_{min,la}$	0.03	$E_{min,la}$	0.03	$\tau_{ep,rv}$	0.03	$E_{min,la}$	0.03
C_{sv}	0.03	$\tau_{es,lv}$	0.03	$\tau_{ep,lv}$	0.02	$E_{min,ra}$	0.03
$E_{max,lv}$	0.03	$E_{max,lv}$	0.03	$E_{max,rv}$	0.02	$E_{max,rv}$	0.03
$\tau_{ep,rv}$	0.02	$\tau_{es,rv}$	0.03	$\tau_{es,rv}$	0.02	$E_{max,lv}$	0.02
$\tau_{es,rv}$	0.02	$\tau_{ep,rv}$	0.03	$E_{max,ra}$	0.02	$\tau_{ep,rv}$	0.02
$E_{max,rv}$	0.02	$E_{max,rv}$	0.02	$E_{min,la}$	0.02	$\tau_{es,rv}$	0.02
C_{sa}	0.02	C_{pv}	0.02	$E_{max,lv}$	0.01	C_{pv}	0.02
C_{pv}	0.01	C_{sa}	0.01	C_{pv}	0.01	$E_{max,ra}$	0.02
C_{pa}	0.01	C_{pa}	0.01	C_{pa}	0.01	$\tau_{es,lv}$	0.02
$E_{min,ra}$	0.01	R_{pvb}	0.01	$\tau_{es,lv}$	0.01	C_{sa}	0.02
$E_{max,la}$	0.01	$E_{min,ra}$	0.01	R_{pvb}	0.01	C_{pa}	0.02
$E_{max,ra}$	0.01	$E_{max,ra}$	0.01	C_{sa}	0.01	R_{pvb}	0.01
		$E_{max,la}$	0.01			$E_{max,la}$	0.01

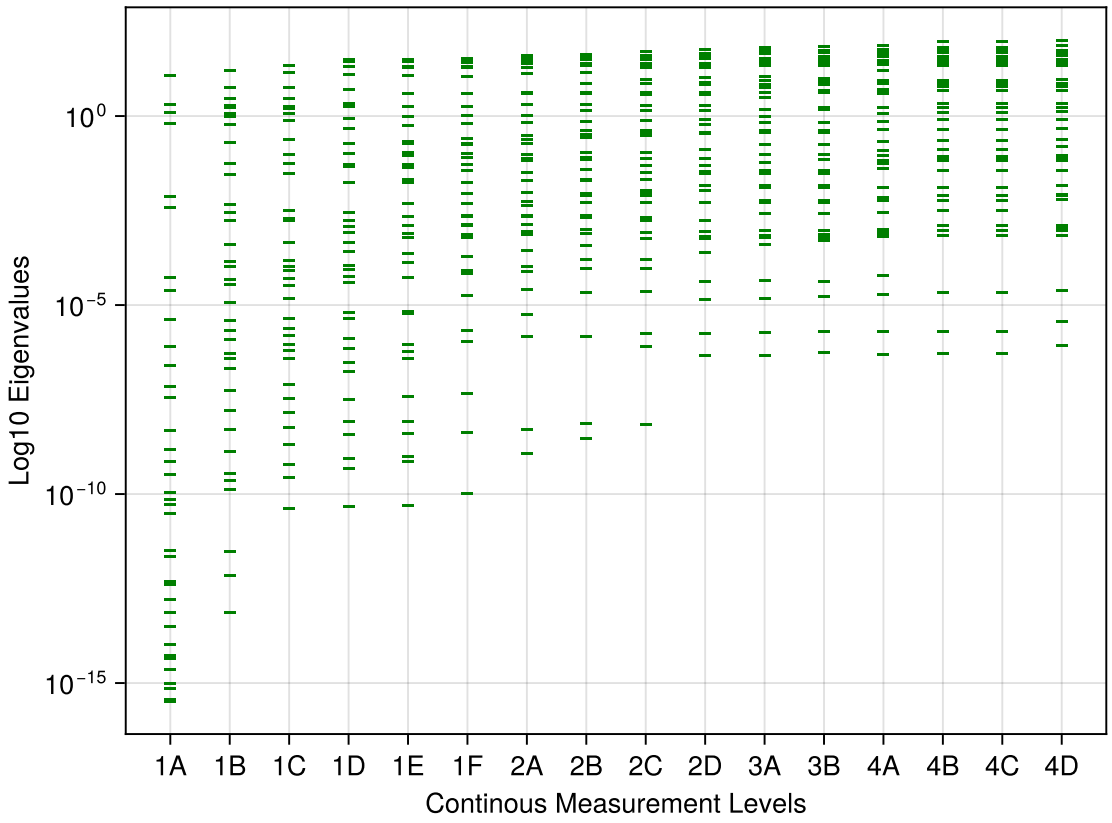

Fig. 6.2 **Continuous measures - sloppy analysis:** The eigenvalues of the Fisher information matrix for increasing continuous measurements, displayed on a $\log_{10}$ scale.

eigenvalues are greater than 10^0 with an eigen-spectrum ranging from 10^{-12} for level 4B decreasing down to 10^{-6} for level 7D.

Table 6.6 **Input parameter ranking for mixed measurements:** The input parameter ranking and its influence value, averaging across all outputs, for increasing mixed measurements.

Measurement Levels																								
1		2		3A		3B		3C		3D		4A		4B		4C		4D		4E		4F		5A	
P	E	P	E	P	E	P	E	P	E	P	E	P	E	P	E	P	E	P	E	P	E	P	E	P	E
C_{sa}	0.22	C_{sa}	0.80	C_{sa}	0.44	R_{svb}	0.34	R_{svb}	0.26	$E_{shift,ra}$	0.24	$E_{min,lv}$	0.44	$E_{min,lv}$	0.27	$\tau_{ep,lv}$	0.38	$\tau_{ep,lv}$	0.25	$\tau_{ep,lv}$	0.20	$\tau_{ep,lv}$	0.11	$\tau_{ep,lv}$	0.11
R_{svb}	0.21	R_{svb}	0.60	R_{svb}	0.43	C_{sa}	0.33	C_{sa}	0.26	R_{svb}	0.10	R_{svb}	0.29	C_{pa}	0.16	$E_{min,lv}$	0.11	$E_{shift,la}$	0.16	$E_{shift,la}$	0.14	$E_{shift,la}$	0.09	$E_{shift,la}$	0.09
$\tau_{es,lv}$	0.17	$\tau_{es,lv}$	0.04	$E_{max,lv}$	0.24	$E_{max,lv}$	0.18	$V_{0,lv}$	0.14	C_{sa}	0.10	C_{sa}	0.23	R_{svb}	0.16	R_{svb}	0.09	$E_{min,lv}$	0.06	$\tau_{es,rv}$	0.05	$E_{shift,ra}$	0.09	$E_{shift,ra}$	0.09
				$V_{0,lv}$	0.04	$V_{0,lv}$	0.03	$V_{0,lv}$	0.03	$E_{max,lv}$	0.06	C_{sv}	0.22	$E_{shift,la}$	0.16	C_{sv}	0.06	$\tau_{es,lv}$	0.05	$E_{min,lv}$	0.05	$\tau_{es,rv}$	0.05	$\tau_{es,rv}$	0.05
				$\tau_{es,lv}$	0.02	$E_{max,rv}$	0.02	$E_{max,rv}$	0.02	$E_{max,ra}$	0.04	$\tau_{es,lv}$	0.17	C_{sv}	0.14	$E_{max,lv}$	0.06	C_{pa}	0.03	$\tau_{es,lv}$	0.04	$E_{min,lv}$	0.04	$E_{min,lv}$	0.04
						$\tau_{es,lv}$	0.02	$\tau_{es,lv}$	0.02	$\tau_{ep,rv}$	0.02	$E_{shift,ra}$	0.13	$\tau_{es,rv}$	0.12	C_{sa}	0.05	R_{svb}	0.02	C_{pa}	0.03	$\tau_{ep,rv}$	0.03	$\tau_{ep,rv}$	0.03
										$E_{min,rv}$	0.02	$E_{max,lv}$	0.13	R_{pvb}	0.11	$E_{shift,la}$	0.05	C_{sv}	0.02	R_{svb}	0.02	$\tau_{es,lv}$	0.03	$\tau_{es,lv}$	0.03
										$E_{max,rv}$	0.01	$E_{min,rv}$	0.12	C_{sa}	0.10	C_{pa}	0.04	$E_{min,la}$	0.02	C_{sv}	0.02	C_{pa}	0.02	C_{pa}	0.02
										$V_{0,lv}$	0.01	C_{pv}	0.11	$E_{shift,ra}$	0.09	$E_{shift,ra}$	0.03	$\tau_{es,rv}$	0.02	$E_{min,la}$	0.02	R_{svb}	0.02	R_{svb}	0.02
												$E_{shift,la}$	0.10	$E_{max,lv}$	0.08	$E_{min,rv}$	0.03	R_{pvb}	0.02	R_{pvb}	0.02	C_{sv}	0.02	C_{sv}	0.02
												$E_{max,rv}$	0.08	$E_{min,rv}$	0.08	C_{pv}	0.03	$E_{max,la}$	0.02	$E_{max,la}$	0.01	$E_{min,rv}$	0.01	$E_{min,rv}$	0.01
												$E_{max,la}$	0.06	C_{pv}	0.08	R_{pvb}	0.03	$E_{max,lv}$	0.01	R_{pvb}	0.01	R_{pvb}	0.01	R_{pvb}	0.01
												$E_{max,ra}$	0.04	$\tau_{es,lv}$	0.07	$\tau_{es,rv}$	0.03	$E_{shift,ra}$	0.01	$E_{min,la}$	0.01	$E_{min,la}$	0.01	$E_{min,la}$	0.01
												R_{sv}	0.04	$E_{max,rv}$	0.05	$E_{max,rv}$	0.02	$E_{min,rv}$	0.01	$E_{shift,ra}$	0.01	$E_{max,lv}$	0.01	$E_{max,lv}$	0.01
												C_{pa}	0.03	$E_{max,la}$	0.04	$E_{max,la}$	0.02	C_{sa}	0.01	C_{sa}	0.01	$E_{max,la}$	0.01	$E_{max,la}$	0.01
												R_{pvb}	0.03	$\tau_{ep,lv}$	0.04	$\tau_{ep,lv}$	0.01	C_{pv}	0.01	C_{pv}	0.01				
												$E_{min,la}$	0.01	$E_{max,ra}$	0.03	$E_{max,ra}$	0.01								
														R_{sv}	0.03	R_{sv}	0.01								
														$E_{min,la}$	0.03										

All input parameters register $F < 0.01$

Measurement Levels																									
5B		5C		5D		5E		5F		5G		5H		6A		6B		7A		7B		7C		7D	
P	E	P	E	P	E	P	E	P	E	P	E	P	E	P	E	P	E	P	E	P	E	P	E	P	E
$\tau_{ep,lv}$	0.11	$\tau_{ep,lv}$	0.11	$\tau_{ep,lv}$	0.11	$\tau_{ep,lv}$	0.17	$\tau_{ep,lv}$	0.11	$E_{shift,la}$	0.11	$E_{shift,ra}$	0.16	$\tau_{ep,lv}$	0.12	$E_{min,lv}$	0.10	$E_{min,lv}$	0.09	$E_{min,lv}$	0.09	$E_{shift,ra}$	0.18	$E_{shift,ra}$	0.16
$E_{shift,la}$	0.09	$E_{shift,la}$	0.09	$E_{shift,la}$	0.09	$E_{shift,la}$	0.06	$E_{shift,ra}$	0.10	$\tau_{ep,lv}$	0.09	$E_{shift,la}$	0.06	$E_{min,lv}$	0.09	$\tau_{ep,lv}$	0.08	$E_{shift,ra}$	0.09	$E_{shift,ra}$	0.09	$E_{min,rv}$	0.05	$E_{min,lv}$	0.08
$E_{shift,ra}$	0.09	$E_{shift,ra}$	0.09	$E_{shift,ra}$	0.09	$E_{min,lv}$	0.05	$E_{shift,la}$	0.06	$E_{min,lv}$	0.07	$E_{min,lv}$	0.05	$E_{shift,la}$	0.08	R_{svb}	0.08	R_{svb}	0.07	R_{svb}	0.07	$E_{min,lv}$	0.05	$E_{min,rv}$	0.05
$\tau_{es,rv}$	0.05	$\tau_{es,rv}$	0.05	$\tau_{es,rv}$	0.05	$E_{shift,ra}$	0.04	$E_{min,lv}$	0.05	$E_{shift,ra}$	0.06	$\tau_{ep,lv}$	0.04	$E_{shift,la}$	0.07	$E_{shift,ra}$	0.07	$\tau_{ep,lv}$	0.06	$\tau_{ep,lv}$	0.05	R_{svb}	0.04	R_{svb}	0.04
$E_{min,lv}$	0.04	$E_{min,lv}$	0.04	$E_{min,lv}$	0.04	$\tau_{es,lv}$	0.03	$\tau_{es,rv}$	0.03	$E_{min,la}$	0.05	$E_{min,la}$	0.03	$E_{min,la}$	0.04	$E_{shift,la}$	0.06	$E_{shift,la}$	0.06	$E_{shift,la}$	0.05	C_{sv}	0.03	$E_{shift,la}$	0.04
$\tau_{ep,rv}$	0.03	$\tau_{ep,rv}$	0.03	$\tau_{ep,rv}$	0.03	$E_{max,lv}$	0.02	$\tau_{ep,rv}$	0.03	$E_{max,lv}$	0.03	$\tau_{es,lv}$	0.03	$\tau_{es,lv}$	0.03	$\tau_{es,lv}$	0.04	$E_{min,rv}$	0.04	$E_{min,rv}$	0.04	$E_{min,ra}$	0.03	C_{sv}	0.03
$\tau_{es,lv}$	0.03	$\tau_{es,lv}$	0.03	$\tau_{es,lv}$	0.03	$\tau_{es,rv}$	0.02	$\tau_{es,lv}$	0.03	$\tau_{es,lv}$	0.03	$\tau_{ep,rv}$	0.03	$E_{max,lv}$	0.03	$E_{min,la}$	0.03	$\tau_{es,lv}$	0.03	C_{sv}	0.03	$E_{shift,la}$	0.03	$\tau_{ep,lv}$	0.03
C_{pa}	0.02	C_{pa}	0.02	C_{pa}	0.02	R_{svb}	0.02	$E_{max,lv}$	0.02	C_{sv}	0.02	C_{sv}	0.03	C_{sv}	0.02	$E_{max,lv}$	0.03	$E_{min,la}$	0.03	$E_{min,la}$	0.03	C_{sv}	0.03	$\tau_{ep,rv}$	0.02
R_{svb}	0.02	R_{svb}	0.02	R_{svb}	0.02	C_{sv}	0.02	R_{svb}	0.02	$\tau_{es,rv}$	0.02	$E_{min,ra}$	0.02	$E_{min,rv}$	0.02	C_{sv}	0.03	C_{sv}	0.03	$\tau_{es,lv}$	0.03	$\tau_{es,lv}$	0.02	$E_{min,ra}$	0.02
C_{sv}	0.02	C_{sv}	0.02	C_{sv}	0.02	C_{pa}	0.01	C_{sv}	0.02	R_{svb}	0.02	$\tau_{es,rv}$	0.02	R_{svb}	0.02	$E_{min,rv}$	0.02	$E_{max,lv}$	0.03	$E_{max,lv}$	0.03	$\tau_{es,lv}$	0.02	$E_{max,rv}$	0.02
$E_{min,rv}$	0.01	$E_{min,rv}$	0.01	$E_{min,rv}$	0.01	C_{sa}	0.01	$E_{max,rv}$	0.02	$E_{max,la}$	0.02	$E_{max,rv}$	0.02	$E_{max,rv}$	0.02	C_{sa}	0.02	$\tau_{ep,rv}$	0.02	$E_{max,rv}$	0.02	$E_{max,rv}$	0.02	$E_{max,lv}$	0.02
R_{pvb}	0.01	R_{pvb}	0.01	R_{pvb}	0.01	$E_{min,la}$	0.01	C_{pa}	0.02	$E_{max,rv}$	0.02	$E_{max,lv}$	0.02	$\tau_{es,rv}$	0.02	C_{pv}	0.02	$\tau_{es,rv}$	0.02	$\tau_{ep,rv}$	0.02	$\tau_{es,rv}$	0.02	$\tau_{ep,rv}$	0.02
$E_{min,la}$	0.01	$E_{min,la}$	0.01	$E_{min,la}$	0.01	C_{pv}	0.01	$E_{min,rv}$	0.02	C_{pa}	0.02	R_{svb}	0.02	C_{pv}	0.02	$E_{max,rv}$	0.02	$E_{max,rv}$	0.02	$E_{max,rv}$	0.02	$E_{max,ra}$	0.02	$\tau_{es,rv}$	0.02
$E_{max,lv}$	0.01	$E_{max,lv}$	0.01	$E_{max,lv}$	0.01	$E_{min,rv}$	0.01	C_{pa}	0.02	C_{sa}	0.01	C_{pa}	0.02	C_{sa}	0.02	$E_{max,la}$	0.02	C_{sa}	0.02	C_{pv}	0.02	$E_{min,la}$	0.02	C_{pv}	0.02
$E_{max,la}$	0.01	$E_{max,la}$	0.01	$E_{max,la}$	0.01			$E_{min,rv}$	0.01	C_{pv}	0.02	$\tau_{es,lv}$	0.02	$E_{max,la}$	0.01	$\tau_{es,rv}$	0.01	C_{pv}	0.02	C_{sa}	0.02	C_{pv}	0.01	$E_{max,ra}$	0.02
								$E_{min,la}$	0.01	$E_{min,rv}$	0.01	C_{pa}	0.02	C_{pa}	0.01	C_{pa}	0.01	C_{pa}	0.02	C_{pa}	0.02	$E_{max,lv}$	0.02	$E_{min,lv}$	0.02
										$\tau_{ep,rv}$	0.01	C_{pv}	0.01	$\tau_{ep,rv}$	0.01	$E_{min,ra}$	0.01	$E_{min,ra}$	0.02	R_{pvb}	0.02	$\tau_{es,lv}$	0.02	C_{sa}	0.02
										R_{pvb}	0.01	$E_{max,la}$	0.01	$E_{min,ra}$	0.01	$\tau_{ep,rv}$	0.01	$E_{max,ra}$	0.01	$E_{min,ra}$	0.02	R_{pvb}	0.01	C_{pa}	0.02
												C_{sa}	0.01	$E_{max,ra}$	0.01	$E_{max,ra}$	0.01	$E_{max,ra}$	0.01	$E_{max,ra}$	0.01	C_{sa}	0.01	R_{pvb}	0.01
																				$E_{max,ra}$	0.01			$E_{max,la}$	0.01

6.3 Discussion

Our study aims to assess the impact of experimental design on the input parameter influence and the system sloppiness. Overall, the results accord with *prior art*: continuous measurements lead to a larger selected subset of input parameters as plausible candidates for personalisation in a cardiovascular DT [300, 333, 339]. When only discrete measurements are used, there is a smaller and more concentrated subset of identifiable input parameters. Perhaps surprising is the extent of this disparity. Only when the largest discrete measurement level, 3F, is examined do we obtain the same number of input parameters with a value greater than 0.01, compared to the first continuous measurement level 1A.

We further observe that as the size of the output set increases, the influence between input parameters appears to become more evenly distributed. For example, for the discrete mea-

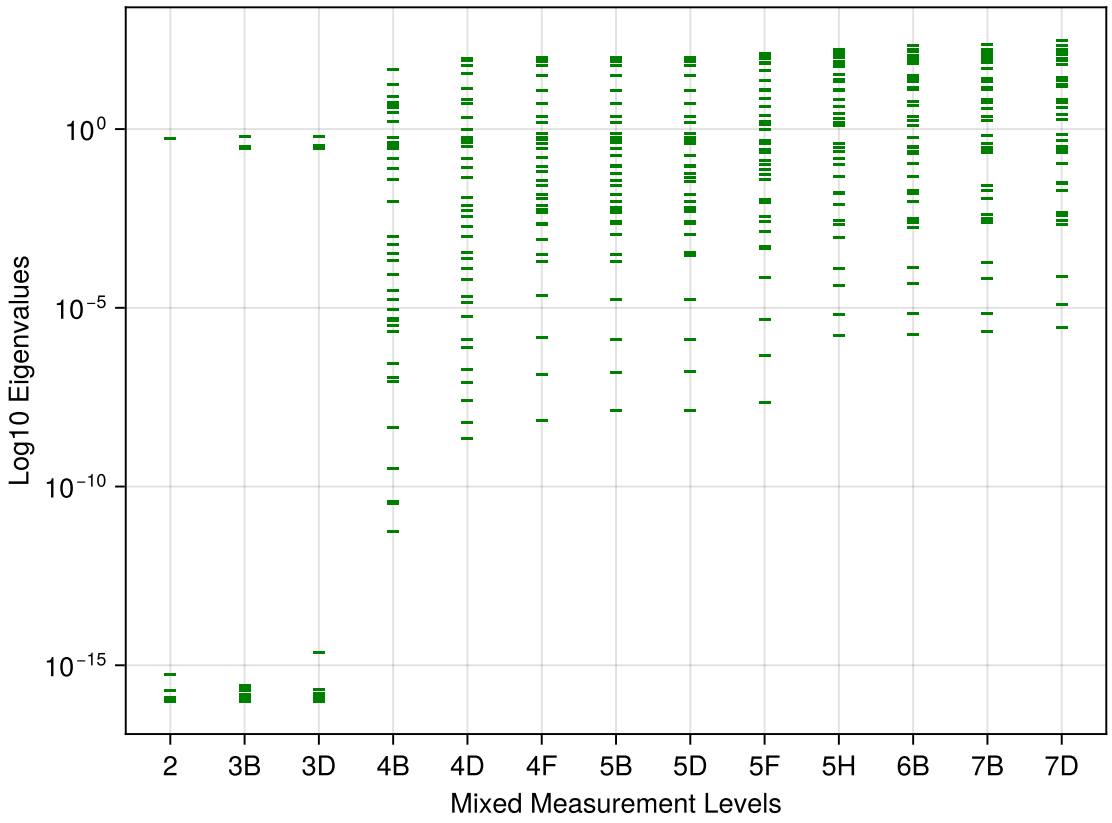

Fig. 6.3 **Mixed measures - sloppy analysis:** The eigenvalues of the Fisher information matrix for every other increasing mixed measurements, displayed on a $\log_{10}$ scale.

surements results shown in table 6.4, the systemic vascular bed resistance R_{svb} and arterial compliance C_{sa} rank as the most influential parameters for all measurement levels except 2D. In level 1, C_{sa} and R_{svb} have influence values of 0.8 and 0.6 respectively. However, in level 3F, when the dimensionality of output space increases to 11, these two parameters' influence decreases to 0.11 and 0.13.

The first sloppy analysis of the cardiovascular model under test indicates that discrete measurements do not introduce sloppiness into the system, whereas for continuous measurements, the system begins to exhibit sloppy behaviour. Through the lens of creating DTs, the stiff input parameters are clearly identified using discrete measurements which would lead to easier identification of a personalised global minimum parameter set. When using the combination of both the continuous and discrete measurement sets, as they increase in size, the number of stiff input parameters which can be considered as prime candidates for personalisation increases. Sloppiness provides a view into the structure of the input parameter space and an insight for why more "influential" input parameters appear when the dimensionality of the outputs grows. As more measurements are added, there is a noticeable change in the structure of the response surface, providing more information on the personalisable global minimum location.

When creating a virtual representation of a patient, it is still an open question whether the DT should be personalised to a specific condition or encapsulate the full physiological envelope of a patient [239, 237, 469]. Our experiments and analysis provides some insight there. If one wishes to capture a full physiological envelope with a DT, a number of continuous measurements are essential. This is due to the larger number of influential input parameters, along with the higher values of stiff eigenvalues, when compared to the discrete measurement setting. This approach brings practical problems of course, because of the invasive nature associated with obtaining some continuous measurements (e.g. ventricular pressure, recall). A patient would have to be subject to a serious of invasive tests with associated risks to generate the data to for a personalised DT. Alongside this, continuous measurements have shown a higher level of sloppiness, indicating that a computationally expensive optimisation routine may have to be utilised to generate the virtual patient representation. Conversely, if the purpose of a DT is to target specific conditions, a set of non-invasive discrete measurements poses as an alternative. Although there is a smaller number of identifiable input parameters in this case, the influence is concentrated strongly around the biomarkers relevant to the discrete metrics. In addition, because the system does not exhibit sloppy behaviour, the personalisation process using discrete measurements may

be more efficient than its continuous counterparts.

One problem of the sloppy analysis is the subjectivity in diagnosing whether sloppiness is present within a system. In this work, we have used the common definition of evenly spaced eigenvalues on a log scale, distributed over a minimum range of 10^6 orders of magnitude [342, 18]. The lack of sloppiness is clear in the discrete measurements setting (see figure 6.1). In the case of continuous measurements, when the measurement level increases, the distribution of eigenvalues (figure 6.2), while still evenly spaced, reduces from a spread of 10^{16} to just 10^6 (i.e., more input parameters are in the stiff direction than before). But does this change in an apparent reduction in sloppiness actually align with intuition? Given the increase of parameters in the stiff direction, one would assume more accurate optimisation of the input parameters when compared to level 1. However, this remains an open question and requires an additional study to investigate.

The study of sloppiness is common practice in most other areas of systems biology, however, this is not the case for cardiovascular models. The concept of sloppiness provides an important insight for examining the personalisability of cardiovascular models. By assessing the stiff and sloppy directions generated from the input parameters, sloppy analysis provides an alternative approach to identify optimal subsets for personalisation, compared to other methods such as profile likelihood and combining sensitivity and orthogonality [481, 339, 482]. This is an interesting area which should be explored in future research. When attempting to personalise a DT, there are several stages and sloppy analysis belongs to the vital off-line stage in which prime candidates for personalisation are identified. This off-line stage enables us to identify biomarkers which can be personalised to produce the virtual representation of a patient. The off-line stage is vital because once patient data are introduced, any additional issues occurring during personalisation can then be attributed to issues within the clinical data.

For the personalisation of cardiovascular DTs, the process in which this happens must operate on a multi-dimensional input parameter space in which some points give accurate representation of a patient's physiological and pathophysiological state. Currently, analysis on the input parameter space and the identification of the optimal parameter subset for personalisation are conducted on a local basis [270, 483, 484]. For example, it is still the norm to form the sensitivity matrices through local methods when analysing system sloppiness [346, 265]. If sloppy analysis is to be utilised more in the identification of biomarkers, local analysis should not be adopted for larger, more complex circulatory models. Personalisation is a global process, therefore it is vital to understand and quantify the global behaviour and

the structure present within the input parameter space. This is why we have conducted our sloppiness analysis using the global sensitivity analysis outcomes in this work.

To perform such an extensive study, the associated computational expense is another important factor to consider. In total, we have tested 48 individual experimental designs, for each of which a sensitivity analysis has been performed with 75,000 samples to ensure convergence [485]. As our chosen global sensitivity method is Sobol indices [482, 270, 299], this means for each experimental design, $75000 \times (36+2) = 2.85 \times 10^6$ model evaluations are required. Thus for 48 independent experimental designs, we have solved the 4-chamber model 136.8 million times. This study has only been made feasible due to the superior computational speed exhibited by DifferentialEquations.jl within Julia. Solving the dynamical system for a single model run including 30 cycles took 0.060246(s). When personalising DTs, computationally efficient and accurate tools should be utilised where possible, for the most effective allocation of computational resources for all stages of DT development.

Alongside LPMs, there is also interest in higher dimensional (e.g. 1D, 2D and 3D) cardiovascular models which can be utilised as DTs [7, 486, 487]. The level of physiological details in these models is usually far superior to what can be established in LPMs. The main drawback or compromise, is the lack of ability to simulate global haemodynamics because of the astronomical computational cost.

Physiologically detailed models of a single piece of vessel or a compartment are of course of great importance, to further biological understanding where invasive clinical assessments are inappropriate or unethical. One promising area of the cardiovascular digital twin development is in the creation of multi-scale, multi-modal models, combining both LPMs and physiologically detailed higher dimensional representations of specific vessels or valves [302, 487]. This approach combines the advantages of both modelling domains and forms an attractive avenue for future research in cardiovascular personalisation and building DTs.

6.4 Conclusion

Our study highlights the importance of experimental design in the quantification of input parameter influence and the associated model sloppiness, for a LPM-based personalised cardiovascular digital twin. Using a 4-chamber 36-parameter LPM as a test bench, we investigated 48 independent experimental designs. The most significant findings, are: (i) Input parameter identifiability is not consistent when the model is subject to varied measurement

data, and depends on the chosen experimental design. (ii) Sloppiness is present in LPMs when the chosen experimental design contains continuous measurements. (iii) The personalisation of a digital twin to encompass the complete physiological envelope necessitates invasive tests to obtain continuous measurements. Although this approach offers an increased number of identifiable parameters with the potential to be biomarkers, it comes at the expense of a sloppy system which in turn increases the difficulty in parameter identification. Conversely, discrete metrics may provide a simpler personalisation approach, yielding less identifiable but more targeted biomarkers, due to the absence of sloppiness in the system.

Chapter 7

Assessing Input Parameter Hyperspace Structure and Parameter Identifiability in a Cardiovascular System Model using Sensitivity Analysis.

The difference between a democracy and a dictatorship is that in a democracy you vote first and take orders later; in a dictatorship you don't have to waste your time voting.
— CHARLES BUKOWSKI

Summary
Having considered the impact of experimental design and convergence when quantifying the uncertainty present within lumped systems, we next compare various subset selection methods to evaluate the rank stability of the resulting personalised subsets. Further, we expand upon a subset selection method, accounting for parameter influence and orthogonality to incorporate the global nature of the personalisation problem. Through the application of Sobol indices, we propose a domain-agnostic algorithm offering an informal but intuitive and interpretable map of input parameter space, which lends insight into the personalisability of a model.[1]

[1]The work in this chapter is published in: **Saxton, H.**, Xu, X., Schenkel, T., & Halliday, I. (2024). Assessing input parameter hyperspace and parameter identifiability in a cardiovascular system model via sensitivity analysis. Journal of Computational Science, 79, 102287.

7.1 Introduction

Mathematically, input parameter identification is an inverse problem; clinically it is the personalisation process [488, 489]. It amounts to taking a highly detailed dynamical system model with its input parameters (usually prescribed realistic bounds) and supplying the model with *target* observations i.e. experimental or clinical to match, data that correspond to model outputs. The process returns a new set of input parameters which - in some sense - best describe the observed data. This new set allows for new inferences to be made about the physical process under investigation [237] or the condition of the patient from whom the target data was taken. In the clinic, LPMs show promise as diagnostic and treatment planning aids in CV diseases, such as coronary artery disease, pulmonary arterial hypertension and aortic valve stenosis [187, 490, 159]. If one can ingest into CVS LPMs measurements specific to patients and can personalise quickly and robustly, one may hope to e.g. broaden the uptake and evaluation of information in the diagnostic process to the extent the need for invasive diagnostic tests diminishes. The diagnostic challenge requires that a model be able to personalise to pathophysiological states, as well the physiological. Further, if personalised input parameters can be used to e.g. stratify an individual or cohort, the uptake of LPMs might rise still further to meet the prognostic challenge [239].

The mathematical essence of the personalisation process is a solution, for an input parameter coordinate set, that locates the global minimum of a hyper-surface, or landscape, spanned by the input parameters and computed from the target clinical measurements. Patient-specific data are typically sparse and mathematically insufficient, so many off-line investigations must be performed to ensure the optimal accuracy, efficiency and uniqueness of the solution to the personalisation process. Despite progress there remain many open questions surrounding the key personalisation issues, which we distil as questions

- What is the most effective and stable methods for mapping the bounded, physiologically realistic input parameter space?
- How does one ensure biomarkers extracted from input parameters are truly patient specific?
- What is the surface complexity of input parameter space corresponding to the available measurements?

This chapter aims to provide methodologies and limited answers for these three questions. It is important to note our investigation uses *forward data* (synthetic model outputs) from

the prescribed dynamical system, in order to understand the methods in an ideal setting. Of course, without this critical, off-line step, misleading results may be obtained which would then lead to ill-informed clinical decisions.

The personalisation process is a large and detailed procedure with many choices to be made to ensure unique and patient specific input parameters. Patients cohorts may exist at many different pathophysiological states so one must explore the input parameter space globally [237, 239]. Off-line assessment of a LPM is a necessary prelude, as it ensures as complete an understanding as is practically feasible for a complex numerical model, in an ideal setting. Thus, when practical identifiability is performed, using profile likelihood or global optimisation, any problem in parameter identififablity can be attributed to issues surrounding available data. We aim to extend the sensitivity–based identifiability stage of the procedure, to utilise global sensitivities, and to provide a practical investigative test able to quantify the complexity of input parameter, which has obvious utility. The essential contributions here are as follows:

1. **Extension of Parameter Selection Method:** We extend the parameter selection method of Li et al. [19], incorporating global sensitivities, to respect the global nature of the personalisation process.

2. **Stability of Optimal Input Parameter Subset Selections:** We address the stability of optimal input parameter subset selections by considering competing considerations and various parameter sensitivity methods, both local and global.

3. **Quantification of Input Parameter Space Complexity:** We set-out an investigative test based in global sensitivity analysis, able to quantify the complexity of the input parameter space.

These contributions are intended to enhance the understanding and robustness of the personalisation process, offering evolved tools for parameter identification in patient-specific models.

7.2 Results

For the 9 parameter single ventricle model in Figure 4.1A and 4 model outputs of

$$\underline{Y} = (\text{Mean}(Q_s), \text{PP}(LV), \text{PP}(SA), \text{SV}(LV)).$$

Where PP and SV represent the pulse pressure and stroke volume of a compartment. Sections 7.2.1 and 7.2.2 respectively consider LSA and GSA results. Sections 7.2.2.1, 7.2.2.2 and 7.2.2.3 consider the Morris, eFAST and Sobol GSA methods defined in section 4.5. In section 7.2.3 the overall effect of input parameters is compared between sensitivity methods, utilising equation 4.112. We then compare the ranking of input parameters, based solely on their orthogonality score, between methods utilising equation 4.113, in section 7.2.4. Section 7.2.5 examines the stability of input parameter identifiability when we extend subset selection to GSA methods and finally section 7.2.7 examines the complexity of the input parameter space of our single ventricle model, using the method of section 4.6.

7.2.1 Local Sensitivity

Figure 7.1 is the local sensitivity matrix. The minimal elastance of the left ventricle E_{min} is most influential across all measurements, followed by the maximal elastance E_{max} and windkessel factors R_s, C_{sa} and C_{sv}. The end diastole timing parameter τ_{ep} and the valve parameters Z_{ao} and R_{mv} are the least influential.

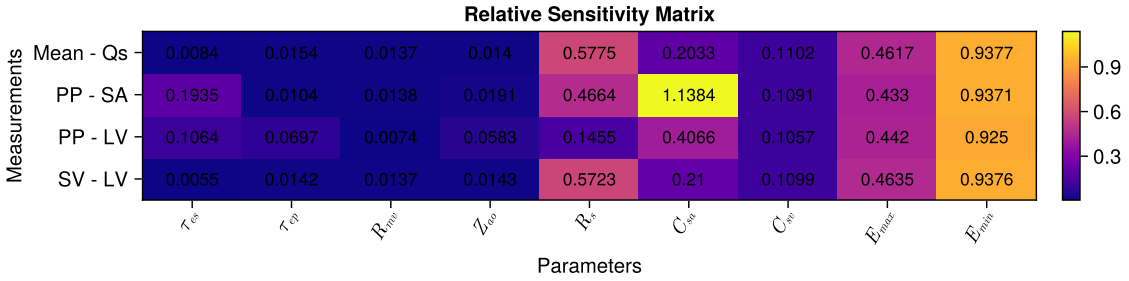

Fig. 7.1 **Local relative sensitivity matrix**: Shows the local relative sensitivity matrix, measuring input parameters' (column headings) influence on specific model outputs (row headings).

7.2.2 Global Sensitivity

The mean vs. variance plots are shown for Morris' method in figure 7.2. Figure 7.3 and 7.4 show first order indices (panel A), total order indices (panel B) and the higher order indices (panel C) as defined in equation (4.5.3), for the eFAST and Sobol methods, respectively.

7.2.2.1 Morris Method

Figure 7.2, plotted on a log 10 scale note, shows using Morris' method, that both valve parameters Z_{ao}, R_{mv} and the minimal elastance E_{min} have high mean and variance values against all 4 measurements, implying these inputs are influential and have either a non-linear relationship with the output, or non-linear interactions with other inputs. Here the venous compliance C_{sv} has a low mean and variance for all 4 measurements, implying C_{sv} has little influence and may be fixed.

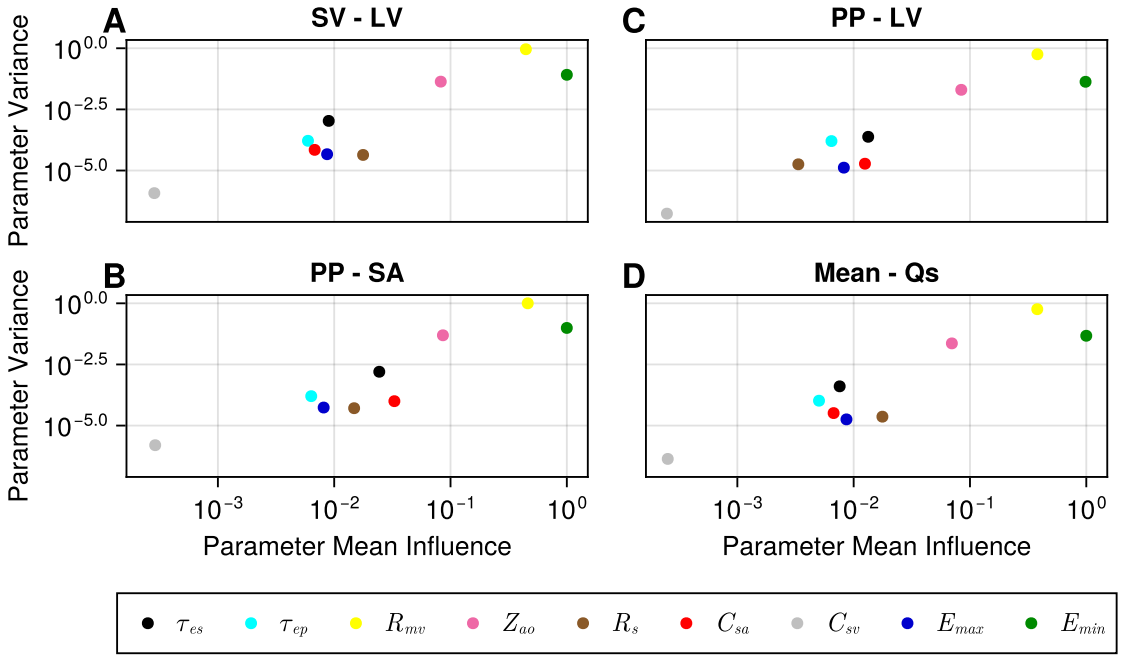

Fig. 7.2 **Morris' method scatter plots**: Each plot displays a normalised mean value plotted against the variance value for each input parameter using a log 10 scale. Panel A: Morris' method results for the stroke volume of the left ventricle. Panel B: Morris' method results for the pulse pressure. Panel C: Morris' method result for the pulse pressure in the left ventricle. Panel D: Morris' method results for the mean systemic flow.

7.2.2.2 eFast Method

The sensitivity indices generated from the eFAST method are shown in figure 7.3. Panel C displays the higher order sensitivity indices $S_h \approx 0$ with the highest order interaction value of 0.0066, for E_{min}, impacting the pulse pressure of the systemic artery. Thus, using the eFAST method, we infer the inputs to act independently on the outputs. Examining panels A and B, the ventricular elastance parameters E_{min}, E_{max} appear influential across all 4

measurements. The systemic resistance R_s appears influential across all measurements apart from the ventricular pulse pressure. The arterial compliance C_{sa} appears influential when the measurement includes a pressure. The other system parameters appear to have little influence across all outputs.

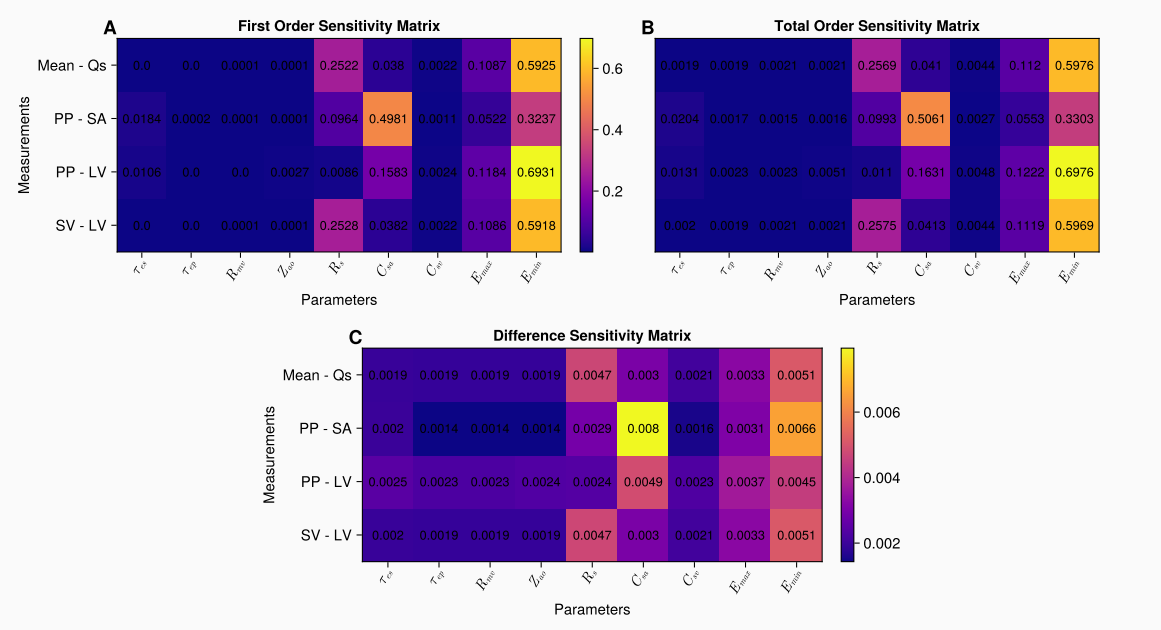

Fig. 7.3 **eFAST sensitivity matrices**: Each matrix, with input parameters as column headings and specific model outputs as row headings, shows an influence value for an input parameter against a specific output. Panel A: the first order indices. Panel B: the total order indices. Panel C: the difference sensitivity matrix.

7.2.2.3 Sobol indices

Figure 7.4 shows the Sobol indices. As in the eFAST case, we note that panel C, for the higher order indices, are all approximately 0. The largest higher order interaction is the minimal elastance E_{min}, with a value $S_h = 0.0099$, impacting the stroke volume of the left ventricle. Because the higher order indices are of very low value, the second order indices are minimal as shown in figure 7.5. Panels A and B show the first and total order indices (their respective convergences are displayed in figures (7.6 and 7.7). E_{min} appears most influential across all measurements, with the system parameters R_s, C_{sa} and C_{sv} next.

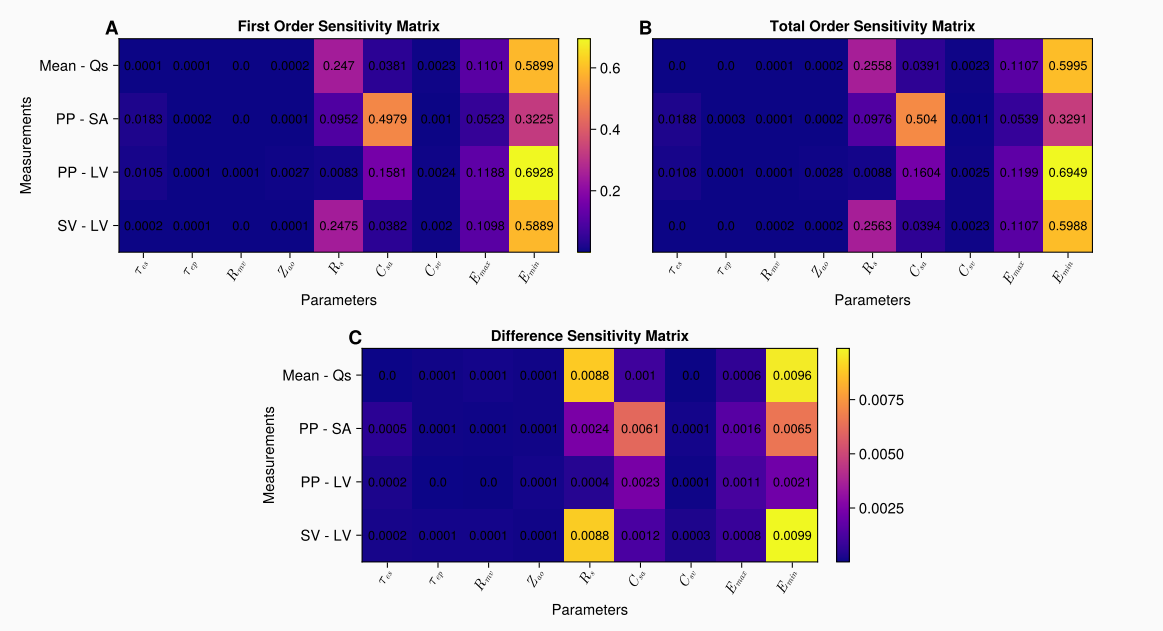

Fig. 7.4 **Sobol sensitivity matrices**: Each matrix, with input parameters as column headings and specific model outputs as row headings, displays an influence value for an input parameter against a specific output. Panel A: the first order indices. Panel B: the total order indices. Panel C: the difference sensitivity matrix.

7.2.3 Input Parameter Influence Comparisons

Figures 7.1, 7.2, 7.3 and 7.4 show our sensitivity matrices for each input parameter, using different methods. Using the method in section 4.10, table 7.1 shows the average influence ranking of all input parameters across all 4 measurements. Although exact influence values differ, all sensitivity measures rank the minimal elastance E_{min} as the most influential across all measurements. All sensitivity measures, except Morris' method, rank the arterial compliance C_{sa} as second most influential, with Morris' method attributing an influence measure and order of magnitude lower than all other methods. Interestingly, the Morris sensitivity measure ranks the valve parameters as the next most influential. All global measures apart from Morris' rank input parameters in the same orders, apart from the parameters with negligible influence values. The first order and total order indices exhibit the same ranking, which once again is indicative of a system driven by independent input factors $S_h \approx 0$. The Local sensitivity matrix displays a very similar ranking to the global measures, with small differences in positions.

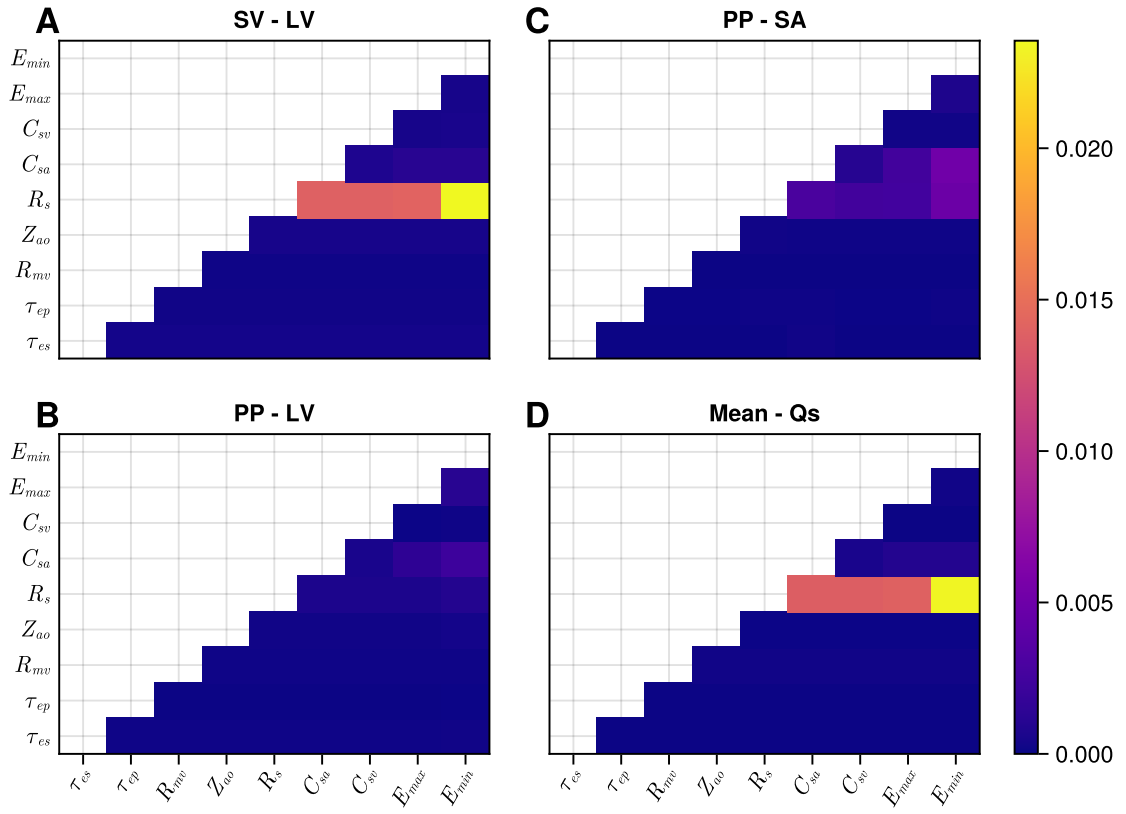

Fig. 7.5 **Second order Sobol indices**: The second order Sobol indices are presented as lower triangular matrices, due to their symmetric nature. Each matrix element displays the influence an interaction between two input parameters have on a selected output. Panel A: the second order indices stroke volume for the left ventricle. Panel B: the second order indices for the pulse pressure for the left ventricle. Panel C: the second order indices pulse pressure for the systemic artery. Panel D: Displays the second order indices for the mean systemic flow.

Table 7.1 **Parameter influence ranking**: A table displaying the ranking of each input parameter influence, averaged across all 4 measurements. Rankings are displayed for both local, global, first order and total order sensitivity measures.

Sensitivity Metric	Parameter Ranking	Parameter Influence Value
Local	$E_{min}, C_{sa}, E_{max}, R_s, C_{sv}, \tau_{es}, \tau_{ep}, Z_{ao}, R_{mv}$	0.674, 0.388, 0.324, 0.322, 0.078, 0.062, 0.018, 0.018, 0.009
Morris	$E_{min}, R_{mv}, Z_{ao}, C_{sa}, \tau_{es}, R_s, E_{max}, \tau_{ep}, C_{sv}$	0.919, 0.384, 0.074, 0.014, 0.013, 0.012, 0.008, 0.005, 0.001
eFAST S1	$E_{min}, C_{sa}, R_s, E_{max}, \tau_{es}, C_{sv}, Z_{ao}, R_{mv}, \tau_{ep}$	0.796, 0.223, 0.213, 0.141, 0.009, 0.003, 0.001, 0.000, 0.000
eFAST ST	$E_{min}, C_{sa}, R_s, E_{max}, \tau_{es}, C_{sv}, Z_{ao}, R_{mv}, \tau_{ep}$	0.794, 0.228, 0.216, 0.144, 0.012, 0.006, 0.004, 0.003, 0.003
Sobol S1	$E_{min}, C_{sa}, R_s, E_{max}, \tau_{es}, C_{sv}, Z_{ao}, \tau_{ep}, R_{mv}$	0.796, 0.224, 0.209, 0.142, 0.009, 0.003, 0.001, 0.000, 0.000
Sobol ST	$E_{min}, C_{sa}, R_s, E_{max}, \tau_{es}, C_{sv}, Z_{ao}, R_{mv}, \tau_{ep}$	0.795, 0.224, 0.214, 0.142, 0.009, 0.003, 0.001, 0.000, 0.000

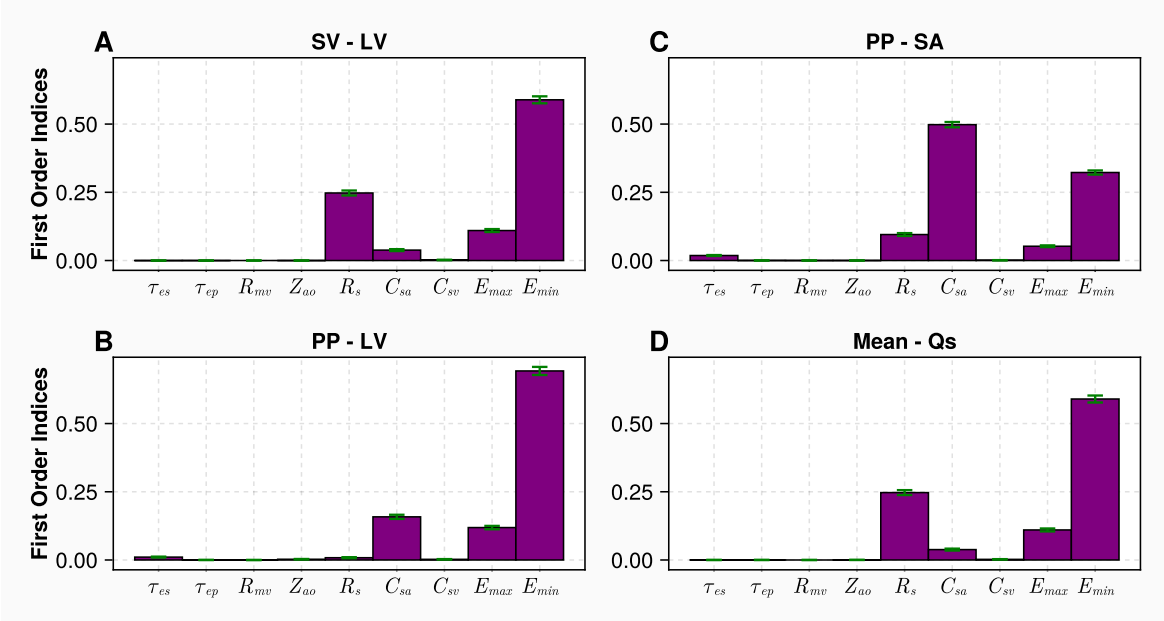

Fig. 7.6 **First order Sobol indices' convergence**: Panel A,B,C and D display, for each individual input parameter, the first order convergence for the stroke volume of the left ventricle, the pulse pressure of the left ventricle, the pulse pressure of the systemic artery and the mean systemic flow, respectively.

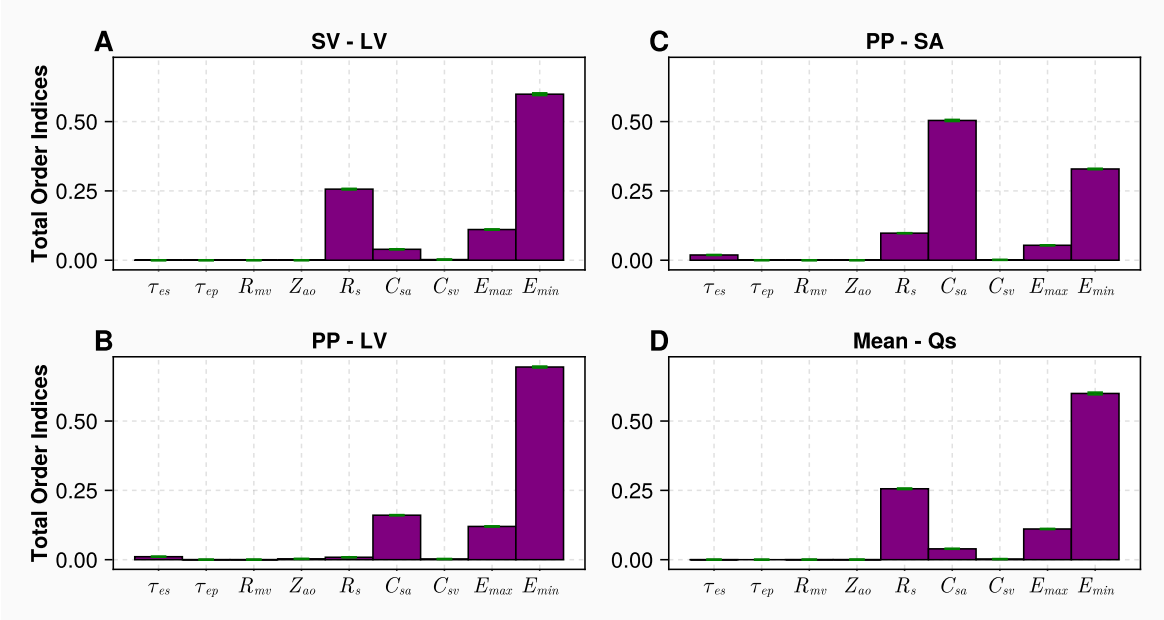

Fig. 7.7 **Total Order Sobol indices' convergence**: Panel A,B,C and D display, for each individual input parameter, the total order convergence for the stroke volume of the left ventricle, the pulse pressure of the left ventricle, the pulse pressure of the systemic artery and the mean systemic flow, respectively.

7.2.4 Orthogonality Analysis

Figure 7.8 (Panels A-F) display the orthogonality matrices for the respective sensitivity measures. Overall, the orthogonality rankings of input parameters are different using different sensitivity measures. In some instances, for example, for the eFAST and Sobol methods, there are very different orthogonality scores between the first and total order indices, e.g. τ_{ep}. Despite this, there are still common trends in the orthogonality scores: τ_{es} being consistently independent, R_s having independent effects from C_{sa}, and E_{min}, E_{max} having dependent effects. Panels G-L report varied orthogonality scores between different sensitivity measures. Sobol first order, Sobol total order, eFAST first order and the local measure are consistent with more orthogonal parameters. Morris' and eFAST total order produce orthogonality rankings which suggest that the input parameters are more dependent on each other.

Table 7.2 displays the mean averaged input parameter ranking based on orthogonality matrix in figure (7.8). In contradistinction to the influence case shown in Table 7.1, no clear patterns in the ranking emerge. Z_{ao} appears the most orthogonal for the eFAST first order, Sobol first order and Sobol total order methods. The venous compliance C_{sv} ranks as least orthogonal in all sensitivity measures, apart from the eFAST total order and the Sobol first order, but even in these settings, the rank of C_{sv} is low. Examining the parameter orthogonality value column in table 7.2, we see a large variation in the average values of orthogonality for each input parameter, with the lowest ranked parameter exhibiting an average orthogonality score between (0.21-0.549).

Table 7.2 **Parameter orthogonality ranking**: the rank of input parameters based on their average orthogonality score, calculated by taking the mean orthogonality score for each input parameter across all outputs for each sensitivity measure.

Sensitivity Metric	Parameter Ranking	Parameter Orthogonality Value
Local	$\tau_{ep}, \tau_{es}, C_{sa}, Z_{ao}, R_s, R_{mv}, E_{max}, E_{min}, C_{sv}$	0.694, 0.686, 0.635, 0.620, 0.566, 0.465, 0.405, 0.398, 0.398
Morris	$C_{sa}, R_s, \tau_{es}, E_{max}, \tau_{ep}, E_{min}, Z_{ao}, R_{mv}, C_{sv}$	0.537, 0.468, 0.410, 0.236, 0.229, 0.223, 0.218, 0.212, 0.210
eFAST S1	$Z_{ao}, \tau_{ep}, R_s, \tau_{es}, C_{sa}, R_{mv}, E_{min}, E_{max}, C_{sv}$	0.865, 0.770, 0.730, 0.729, 0.714, 0.631, 0.553, 0.552, 0.549
eFAST ST	$C_{sa}, R_s, \tau_{es}, Z_{ao}, E_{max}, \tau_{ep}, E_{min}, C_{sv}, R_{mv}$	0.761, 0.701, 0.693, 0.517, 0.370, 0.361, 0.357, 0.348, 0.347
Sobol S1	$Z_{ao}, R_s, C_{sa}, \tau_{es}, R_{mv}, \tau_{ep}, C_{sv}, E_{max}, E_{min}$	0.798, 0.768, 0.754, 0.732, 0.647, 0.614, 0.534, 0.529, 0.520
Sobol ST	$Z_{ao}, \tau_{ep}, R_s, \tau_{es}, C_{sa}, R_{mv}, E_{min}, E_{max}, C_{sv}$	0.863, 0.742, 0.729, 0.726, 0.706, 0.623, 0.547, 0.545, 0.545

7.2.5 Indentifiability Analysis

Utilising equation (4.68), for every sensitivity matrix generated from LSA and GSA, we find the FIM to be singular, i.e., certain model parameters' effects are totally dependent on others. $Rank(F) = 4$ for the single ventricle model defined in Eqs. (2-6) implies $9 - 4 = 5$

Fig. 7.8 **Orthogonality matrix and histograms**: panels A-F show the orthogonality matrices for the local, Morris, eFAST first order, eFAST total order, Sobol first order and Sobol total order methods, respectively. A value of 1(0) indicates that the two input parameters have orthogonal effects on across all the outputs (contribute the same effect on the output). Panels G-L are histograms of the respective orthogonality matrices, indicating the distribution of orthogonality present within the input parameters, when computed through the different sensitivity measures.

non-identifiable parameter combinations. Thus, we expect 4 identifiable input parameters. From the definition of the identifiability index (equation 4.114), we use a cut off of $I < 0.05$ [270] although further investigation of the reliability of this measure is indicated. We note all sensitivity methods, except Morris' obtain the expected number of identifiable input parameters in table 7.3. All global methods identify the minimal elastance (E_{min}) and arterial compliance (C_{sa}) as the most identifiable parameters. The local sensitivity measure agrees with the global methods, with the minimal elastance as the most identifiable and the arterial compliance as identifiable (but this is ranked 4th). Sobol first order indices and the local measure are the only methods that find the systemic resistance R_s as identifiable. eFAST and the Morris method first order indices are the only methods to find the maximal elastance as also identifiable. Both total order indices for the global methods give the same set of identifiable input parameters. Examining the identifiability index value of each input parameter, all global methods except Morris' attribute a similar value for each rank position, indicating that although the input parameter rankings may vary between methods, their quantifiable identifiablity value remains constant.

Table 7.3 **Identifiable input parameters**: the identifiable input parameters calculated using the global subset selection method. Parameters in red indicate an unidentifiable input parameter utilising a cut off of $I < 0.05$.

Sensitivity Metric	Identifiability Parameter Ranking	Identifiability Index Value
Local	$E_{min}, R_s, Z_{ao}, C_{sa}, C_{sv}, \tau_{es}, E_{max}, R_{mv}, \tau_{ep}$	0.703, 0.169, 0.097, 0.068, 0.023, 0.017, 0.016, 0.003, 0.000
Morris	$E_{min}, C_{sa}, E_{max}, C_{sv}, R_s, \tau_{es}, Z_{ao}, R_{mv}, \tau_{ep}$	0.919, 0.396, 0.114, 0.008, 0.005, 0.002, 0.000, 0.000, 0.000
eFAST S1	$E_{min}, C_{sa}, C_{sv}, E_{max}, \tau_{es}, R_s, Z_{ao}, \tau_{ep}, R_{mv}$	0.814, 0.210, 0.085, 0.040, 0.034, 0.034, 0.003, 0.000, 0.000
eFAST ST	$E_{min}, C_{sa}, C_{sv}, \tau_{es}, E_{max}, R_s, \tau_{ep}, Z_{ao}, R_{mv}$	0.812, 0.201, 0.079, 0.050, 0.045, 0.017, 0.000, 0.000, 0.000
Sobol S1	$E_{min}, C_{sa}, R_s, C_{sv}, Z_{ao}, E_{max}, \tau_{es}, R_{mv}, \tau_{ep}$	0.815, 0.150, 0.078, 0.076, 0.006, 0.003, 0.000, 0.000, 0.000
Sobol ST	$E_{min}, C_{sa}, C_{sv}, \tau_{es}, E_{max}, \tau_{ep}, R_s, R_{mv}, Z_{ao}$	0.813, 0.192, 0.086, 0.069, 0.036, 0.010, 0.000, 0.000, 0.000

7.2.6 Rank Stability

The extended subset selection algorithm specified in section 4.12 assumes (reasonably) that the most influential input parameter is the automatically identifiable and so is a sensible - but not necessary - first choice, from which to construct a subset. How dependant are the outcomes of the method, on this choice? Table 7.4 shows the results of performing the subset selection method, based on the first order Sobol indices, while changing the first input parameter. Strikingly, we see that the same subset of identifiable input parameters is obtained in all cases for any input parameter which is fixed. We note that the ranking in which the parameters appear identifiable is not consistent however with the calculation of orthogonality

in the response surface one would expect this to influence the result given a change in the assumed identifiable parameter.

Table 7.4 **Rank stability test**: Table showing the stability of the rank associated with the extended subset selection. Parameter fixed indicates the parameter which is taken to be identifiable and the extended subset algorithm is then performed.

Parameter Fixed	Identifiable Subset
E_{min} - Default	$E_{min}, C_{sa}, R_s, C_{sv}$
E_{max}	$E_{max}, E_{min}, C_{sa}, R_s$
C_{sv}	$C_{sv}, E_{min}, R_s, C_{sa}$
C_{sa}	$C_{sa}, E_{min}, R_s, C_{sv}$
R_s	$R_s, E_{min}, C_{sa}, C_{sv}$
Z_{ao}	$Z_{ao}, E_{min}, C_{sa}, R_s$
R_{mv}	$R_{mv}, E_{min}, R_s, C_{sa}$
τ_{ep}	$\tau_{ep}, E_{min}, C_{sa}, C_{sv}$
τ_{es}	$\tau_{es}, E_{min}, C_{sa}, R_s$

7.2.7 Hypercube dimension

In Table 7.5, we extend the input parameter space volume, from local to one characterised by a parameter variation of $\pm 15\%$, revealing an input parameter ranking which remains constant from a boundary $\pm 0.01\%$ upward. From the local sensitivity measure, we note a ranking similar to the global setting, with the minimal elastance E_{min} and arterial compliance C_{sa} ranking first and second. The other input parameters, when using the local measure, appear to vary by only a single rank position compared to the global setting. As each hypercube dimension is sampled with the same density, one would expect to see the parameter influence value to remain the same. Here, as the hypercube dimension is extended, we observe some slight variation in the influence value. This shows that, as the hypercube is extended, there is some quantifiable change in an input parameter's influence.

7.3 Discussion

Aiming to address the stability of input parameter identifiability, we extended the subset selection method of Li et al., [19] to global sensitivities, then took various global sensitivity methods to interrogate the input parameter space. Tables 7.6 and 7.7 disclose issues around this problem. Comparing influence and orthogonality rankings directly, we noted that influence had a much more consistent ranking with all methods, except the local and the

Table 7.5 **Hyperspace dimension**: input parameter rankings for varying sizes of input parameter space explored when computing total order Sobol indices. Both the ranking and the value of the influence are displayed.

Hypercube Dimension	Parameter Ranking	Parameter Influence Value
Local	$E_{min}, C_{sa}, E_{max}, R_s, C_{sv}, \tau_{es}, \tau_{ep}, Z_{ao}, R_{mv}$	0.674, 0.388, 0.324, 0.322, 0.078, 0.062, 0.018, 0.018, 0.009
±0.01%	$E_{min}, C_{sa}, R_s, E_{max}, \tau_{es}, C_{sv}, Z_{ao}, \tau_{ep}, R_{mv}$	0.788, 0.227, 0.210, 0.167, 0.009, 0.003, 0.001, 0.001, 0.000
±0.5%	$E_{min}, C_{sa}, R_s, E_{max}, \tau_{es}, C_{sv}, Z_{ao}, \tau_{ep}, R_{mv}$	0.785, 0.236, 0.222, 0.141, 0.009, 0.003, 0.001, 0.000, 0.000
±3.0%	$E_{min}, C_{sa}, R_s, E_{max}, \tau_{es}, C_{sv}, Z_{ao}, R_{mv}, \tau_{ep}$	0.792, 0.226, 0.215, 0.140, 0.009, 0.003, 0.001, 0.000, 0.000
±7.0%	$E_{min}, C_{sa}, R_s, E_{max}, \tau_{es}, C_{sv}, Z_{ao}, R_{mv}, \tau_{ep}$	0.792, 0.226, 0.214, 0.141, 0.009, 0.003, 0.001, 0.000, 0.000
±15.0%	$E_{min}, C_{sa}, R_s, E_{max}, \tau_{es}, C_{sv}, Z_{ao}, R_{mv}, \tau_{ep}$	0.795, 0.224, 0.214, 0.142, 0.009, 0.003, 0.001, 0.000, 0.000

Morris methods. When the ranks are based on orthogonality, we observe that no methods exhibit a consistent ranking of input parameters. This is further apparent when the extended parameter subset selection method is applied. Table 7.3 highlights that all global methods except Morris' found the minimal elastance E_{min}, the arterial compliance C_{sa} and the venous compliance C_{sv} to be identifiable, however the 4th parameter found to be identifiable varied between each method. The total order indices for eFAST and Sobol produced the same subset of identifiable parameters in the same order, which is reassuring, although we see that the model is driven mainly through independent effects ($S_h \approx 0$), where the total order indices capture all contributing affects to the output variance. Thus, the identifiable subset returned is the same.

Table 7.6 **The mean rank and range of the input parameters**: The effect of different parameter subset methodologies (influence, orthogonality and our extended Li methodology [19]) when we stratify across all sensitivity metrics

		Input Parameters								
		τ_{es}	τ_{ep}	R_{mv}	Z_{ao}	R_s	C_{sa}	C_{sv}	E_{max}	E_{min}
Influence	Mean	5.2	8.3	7.3	6.5	3.6	2.3	6.3	3.6	1.0
	Rank									
	Range	6-5	9-7	9-2	8-3	6-3	4-2	9-6	7-3	1-1
Ortho	Mean	3.3	3.6	6.6	3.0	2.8	3.0	8.5	6.6	7.3
	Rank									
	Range	4-2	6-1	9-6	7-1	5-2	5-1	9-7	8-4	9-6
Li Method	Mean	5.3	8.0	8.3	6.5	4.8	3.0	8.5	6.6	7.3
	Rank									
	Range	7-4	9-6	9-8	9-3	7-2	4-2	5-3	7-3	1-1

From the way each sensitivity method aggregates, orthogonality has a clear impact on an input parameter's identifiability and therefore should be examined further. However, it is

Table 7.7 **The mean rank and the range of input parameters**: Across all subset selection methodologies when we stratify by different sensitivity methods.

		Input Parameters								
		τ_{es}	τ_{ep}	R_{mv}	Z_{ao}	R_s	C_{sa}	C_{sv}	E_{max}	E_{min}
Local	Mean Rank	4.6	5.6	7.6	5.0	3.6	3.0	6.3	5.6	3.3
	Range	6-2	9-1	9-6	8-3	5-2	4-2	9-5	7-3	8-1
Morris	Mean Rank	4.6	7.3	6.0	5.6	4.3	2.3	7.3	4.6	2.6
	Range	6-3	9-5	8-2	7-3	6-2	4-1	9-4	7-3	6-1
eFAST S1	Mean Rank	4.6	6.3	7.6	5.0	4.0	3.0	6.0	5.3	3.0
	Range	5-4	9-2	9-6	7-1	6-3	5-2	9-3	8-4	7-1
eFAST ST	Mean Rank	4.0	7.3	8.6	6.3	3.6	1.6	5.6	5.0	3.0
	Range	5-3	9-6	9-8	8-4	6-3	2-1	8-3	5-5	7-1
Sobol S1	Mean Rank	5.3	7.6	7.3	4.0	2.6	2.3	5.6	6.0	3.6
	Range	7-4	9-6	9-5	7-1	3-2	3-2	7-4	8-4	9-1
Sobol ST	Mean Rank	4.3	5.0	7.3	5.6	4.3	3.0	6.0	5.6	3.0
	Range	5-4	9-2	8-6	9-1	7-3	5-2	9-3	8-4	7-1

important to note that the extended subset methodology (with results in table 7.3) utilises the concept of orthogonality differently to the way it was analysed in table 7.2. Once the number of the selected input parameters is greater than the number of measurements available, the orthogonality score used to calculate the identifiability index from equation 4.114 (i.e., the worst case/maximum orthogonality) is chosen. Thus, for input parameters deemed unidentifiable, the rank should not be examined too closely, as there are an infinite number of unidentifiable ranking positions for the input parameters. Moreover, with the extended subset methodology, we examine orthogonality against groups of input parameters, so the rankings presented in table 7.2 (which are based on averages of orthogonality pairings of the parameters) may not translate directly to the extended subset methodology.

The Morris method has failed to return consistent results for both the influence and an identifiable subset. While it is still popular for higher dimensional models, its inability to explore input parameter space is here exposed. This ability deteriorates exponentially with increasing dimensions [16]. Ideally, one would use a variance based method such as eFAST or Sobol indices to characterise input parameter, however this is often not utilised due to the associated computational expense. Sensitivity analysis is driven by the speed in which a dynamical system can be solved. The time taken to compute Morris, eFAST and Sobol indices on 28 threads was $3568.6, 3325.1$ and 6893.0 seconds respectively. Thus, eFAST presents itself as a reliable and efficient GSA method. Note, for the Sobol method, the time quoted above included the computation of second order indices also; if we were only interested in the first and total order the number of model evaluations would be the same as Morris' method. Thus, given one can optimise the model solution time, efficient GSA is assured. This may be achieved through use of surrogates [288, 491] or by utilising the efficient ODE solvers in DifferentialEquations.jl [445], as here.

Overall, eFAST is a reliable method to assess the uncertainty of the single ventricle model. However it relies on a sinusoidal function to sample input parameter space, which creates two problems. This sampling method produces a zigzag pattern in the input parameter space and it can struggle to capture the extremes of the input parameter space [492]. When the size of the input parameter space increases, and with more physiologically detailed models, the eFAST method may also struggle to return true input parameter sensitivities. On the other hand, the Sobol methodology utilises Quasi-Monte Carlo sampling strategies, which allow for an easy computation of the confidence intervals associated with the sensitivity index. No such method exists for the eFAST methodology, due to the sampling nature of the method [493]. Therefore, for assessing uncertainty, the Sobol method is still preferred, because of its

ability to compute confidence intervals using the bootstrapping methodology alongside the sensitivity indices.

A secondary aim of our investigation was to develop a GSA based methodology to map input parameter space. We have shown in table 7.5 that as one migrates from base state, input parameters' influence rank is constant over an extended region. The simplest explanation for the change in parameter rank moving from the point that is base state to an albeit small by extended region of $\pm 0.01\%$ is that local SA is by construction a linearisation - a tangent plane - taken at a point with all non-linear curvature effects neglected. The total order Sobol indices method captures all effects and these *are* present, though intentionally neglected in local SA. Further, in table 7.5 the value quantifying parameters' influence remains largely constant with minor variations, implying that as the size of the hyperspace is extended, new domains of parameter influence are reached. However, the effects as a whole do not change because of the extension of the hyperspace dimensions. This indicates a largely additive model, representing a flat input parameter hyperspace. A (mostly) additive nature suggests that the single ventricle model is a good candidate for personalisation. Validation of this conclusion can be performed from patho–physiological patient measurements; however, our present model is only shown to be effective in identifying patient's characteristics from exercise data using local optimisation [368]. Our findings, utilising the hyperspace dimension test are consistent with this.

Despite the promising findings of our hyperspace dimension test, there are important issues to consider. First, we use a GSA method to quantify the input parameter space. Often, GSA is performed without any assessment of the error associated with the sensitivity value. It has been shown that in order to achieve the true input parameter influence, convergence must be achieved. Thus, we propose Sobol indices are used for the hyperspace dimension test. Second, one should ensure the same density of sampling at every hyperspace dimension size. The selection of samples suffers from'the curse of dimensionality' [494]. But if a large enough sample size over the hypercube was used, consistent sample densities close to the base state would become too small. Here, we have utilised the total order indices due to $S_h \approx 0$. If this was not the case, one would have to perform investigations with both the first and total order indices. The first order indices are much harder to converge [293, 297, 290], thus for a model with slightly more complexity and higher non-linearity, it may not be possible to perform such a convergence test. However, for dynamical systems where the outputs are driven by independent effects of the inputs, this test will prove useful.

For personalisation, investigations must be assumed to rely on a fixed set of measurements. In reality, one may not have access sufficient data. While our methodology defines the ideal off-line scenario to investigate identifiability –before using *live* patient data– it should be acknowledged every investigation is constrained by available measurements. So, every time new data become available, a new study is indicated. This also has implications for parameter inference, because parameter identifiability is only valid in the presence of a set of measurements.

7.4 Conclusion

Our study provides a clear and intuitive investigation of a key stage of the personalisation process. We have used a single ventricle, 9 parameter, 0D model, to probe the identifiability of its input parameters in the presence of 4 synthetic but representative clinical surrogate measurements. We have: (i) extended the parameter subset selection method of Li et al., [19] to reflect the global nature of the personalisation process, (ii) shown how a different set of globally identifiable input parameters could be obtained and (iii) provided novel perspectives relative to previous local studies. Assessing the stability of this identifiable input parameter subset, we employed various global and local measures of input parameter sensitivity, revealing how alternative sensitivity methods which depict input parameter space in contrasting ways lead to similar but subtly different identifiable input parameter subsets (driven mainly by the dissimilar orthogonality between input parameters). Finally, we have detailed a novel and intuitive input parameter hyper-surface structure investigation, utilising Sobol indices. The connection with Sobol index error evaluation provides a guide for mapping of the complexity of input parameter space, with a view to aid the inverse problem. When applied to the single ventricle model, within the presence of the 4 chosen measurements, the single ventricle model revealed itself as a prime candidate for personalisation, due to its stable input parameter rankings, in the presence of expanding hyperspace boundaries.

Chapter 8

Personalised Parameter Estimation of the Cardiovascular System: Leveraging Data Assimilation and Sensitivity Analysis.

Product of optimism and knowledge is a constant.
— LEV LANDAU

Summary
From investigations examining how to derive input parameters suitable for identification in personalised medicine, we now turn to the Unscented Kalman Filter (UKF) as a tool for efficient, adaptive parameter estimation in the presence of disturbances. Our findings demonstrate an exceptional adaptability in the UKF, to severe parameter perturbations which representing large physiological fluctuations. We offer novel insights into the continuous sensitivity of model input parameters, illustrating the robustness and efficacy of the UKF. The real time monitoring of a patient's physiological state, with minimal delay, becomes more feasible, by incorporating patient- specific measurements by leveraging the UKF. The workflow presented here facilitates prompt identification of pathophysiological conditions. [1]

[1]The work in this chapter is published in: **Saxton, H**., Schenkel, T., Halliday, I., & Xu, X. (2023). Personalised parameter estimation of the cardiovascular system: Leveraging data assimilation and sensitivity analysis. Journal of Computational Science, 74, 102158.

8.1 Introduction

There is an accelerating trend towards utilising established data assimilation (DA) methods to aid estimation of personalised model input parameters. While DA methods do not have a direct metric for assessing the influence of input parameters, they have demonstrated effectiveness in their recovery from experimental data [495], stemming from an ability to leverage time-varying measurements. DA has been successfully applied to various CV problems, including the estimation of Windkessel model input parameters [22, 356] and closed-loop models of single ventricle physiology [21]. Here, our focus lies on the Unscented Kalman Filter (UKF) [355], detailed in chapter 4.14, primarily due to its ability to handle the non-linearities introduced by the valvular and ventricle functions of the LPM. Here we utilised the 1-chamber 9 parameter model as seen in figure 4.1A in order to demonstrate the efficiency of the method.

8.2 Parameter Perturbations & Synthetic Data

We derive noisy synthetic patient waveform data from forward model solutions characterised with notionally ground truth parameter values of lv pressure P_{lv}, lv volume V_{lv} and systemic pressure P_{sa}, for 15 cycles, representing plausible continuous clinical measurements from (say) echocardiography for V_{lv} [496] and arterial line measurements for P_{sa} [497] (cardiac catheterisation can be performed to extract P_{lv} [498]). To align with the purpose of a UKF, our forward numerical solutions are subject to multiplicative Gaussian corruption as follows:

$$\underline{Y}_j^m = \underline{h}(\underline{X}(t_j, \underline{\theta}_t)), \qquad \underline{Y}_j^n = \underline{h}(\underline{X}(t_j, \underline{\theta}_t)) \cdot (1 + \psi_j). \tag{8.1}$$

Above, subscript j denotes sampling time, deemed to be the discrete time of the numerical solution, superscript n indicates a noisy solution and superscript m denotes the measured, un-corrupted numerical solution. ψ_j is an independent, normally-distributed random variable, with zero mean and a standard deviation 0.025, which is typical [22].

We propose two types of perturbation to the input parameters, applied from $t > 8$ (having run the model to steady state) until the end cycle. The first perturbation we apply is to the elastance timing parameters of the chamber, such that for every cycle $t > 8$ we apply a random value for τ_{es} and τ_{ep} satisfying the distributions

$$\tau_{es} \sim N(0.3, 0.03^2), \ \tau_{ep} \sim N(0.45, 0.03^2). \tag{8.2}$$

The second parameter perturbation applied to the non-timing parameters of the model describes a gradual increase from $t > 8$ and is represented in Figure 8.1 and equation (8.3):

$$\theta(t) = \frac{1}{2}\sin\left(\frac{t-t_0}{4}\right) + \theta_0, \tag{8.3}$$

where $\theta(t)$ represents the value of an input parameter (see Table 4.1) at time t. t_0 represents the time at which the perturbation is applied. $t_0 = 8$. θ_0 represents the true value of the input parameter, before it is perturbed, i.e., for E_{min}, $\theta_0 = 0.03$.

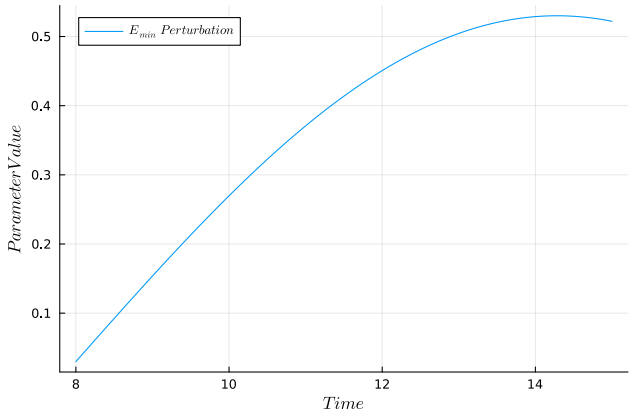

Fig. 8.1 **Parameter Perturbation** : the perturbation applied to the minimal contractility parameter E_{min}. From $t > 8$, the perturbation becomes positive, demonstrating an increase in minimal ventricular contractility.

Table 8.1 **Normal (Gaussian) distribution parameters of the single ventricle model**: θ - Initial mean from [20] . σ - Standard deviation from [21, 22].

Parameter	θ	σ
τ_{es}	0.3	0.01
τ_{ep}	0.45	0.01
R_{mv}	0.06	0.01
Z_{ao}	0.033	0.01
R_s	1.11	0.3
C_{sa}	1.13	0.3
C_{sv}	11.0	0.3
E_{max}	1.5	0.3
E_{min}	0.03	0.01

8.3 Results

We conduct a continuous sensitivity analysis of our model, examine the UKF's ability to recover input parameters when no perturbations are present and analyse the robustness of the model investigated (section 8.3.1). We proceed to examine the ability of UKF to recover true input parameters when they are perturbed from base states (section 8.3.2). For each case explored we tabulate RMSE for each input parameter, before and after a perturbation has been applied. The values presented in the tables below are accurate to 1sf. All results presented below are discussed in full within section 8.4.

8.3.1 Base State

Figure 8.2 shows the case where a patient may be haemorrhaging blood, so blood volume drops and as a consequence, systemic resistance increases to maintain arterial pressure (denoted by the orange curve). To represent this scenario, initial blood volume was halved and the systemic resistance was doubled. The mean values of the arterial pressure for the base state and the pathophysiological state were 97.8 mmHg and 98.2 mmHg. Given, this case examined is very unlikely to occur in clinic, the model response is in line with expectation providing confidence of the affected model to adapt to other pathophysiological states.

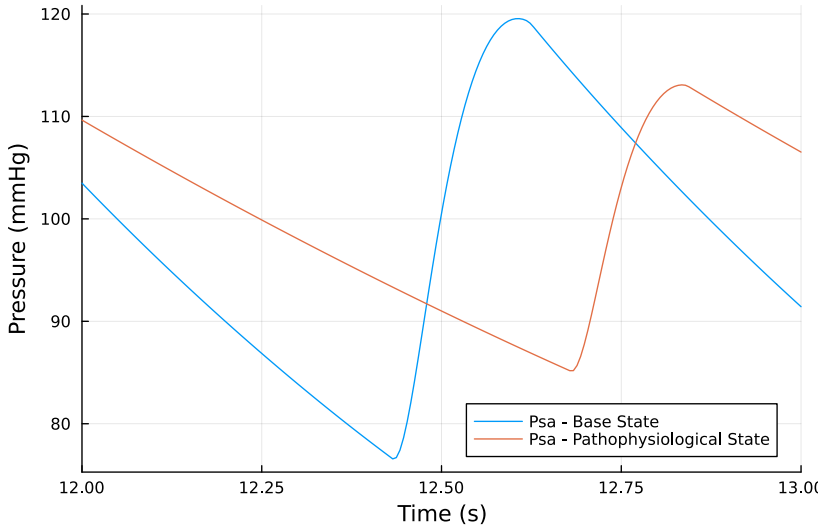

Fig. 8.2 **Systemic arterial pressure** : the arterial pressure for a base state simulation (blue) and when blood volume is halved and systemic resistance is doubled (orange).

Figure 8.3 summarises our implementation of the UKF when no parameter perturbations are present- only beat-to-beat variability. Evidently, the input parameters are estimated with

remarkable precision from the outset. The only parameter that deviates beyond 1% of its true value is C_{sv}, as depicted in Figure 8.3G. Also, R_{mv} (Figure 8.3C) and R_s (Figure 8.3E) exhibit noticeable deviations from their true parameter values, indicated by the yellow line. However, these data still demonstrate superior accuracy compared to existing medical devices where the standard error is 20%[499]. Most input parameters exhibit consistent variance, with the exceptions in Figures 8.3N, 8.3P, and 8.3Q, which correspond partially to the input parameters that were not estimated within 1% accuracy. Notably, certain input parameters, as shown in Figures 8.3J, 8.3K, 8.3L, 8.3M, 8.3O, and 8.3R, exhibit consistent periodic variation. These input parameters, characterised by steady variance, also demonstrate excellent accuracy, except for R_{mv} in Figure 8.3C. In Table 8.2 the root mean squared error (RMSE) is displayed for all input parameters. E_{min} displays the smallest RMSE. C_{sv} exhibits RMSE values an order of magnitude larger than the rest of the input parameters. We remark that the RMSE, as defined in equation 4.125, decreases by an order of magnitude in the second half of the observed time span.

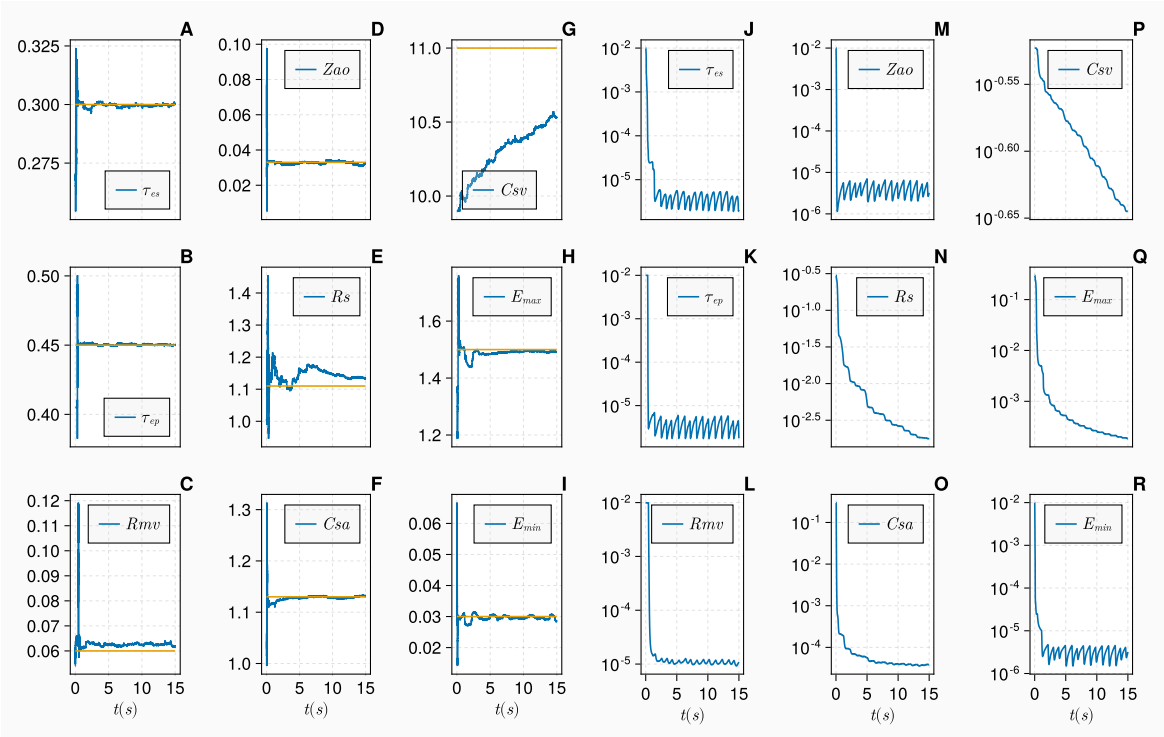

Fig. 8.3 **Single Ventricle Base State Estimation** : figures **A** - **I** display the parameter estimations over the 15 cardiac cycles. The yellow and blue line represent the true and estimated parameter values respectively. Figures **J** - **R** display the parameter covariances over the 15 cardiac cycles.

Table 8.2 **Single Ventricle Base State RMSE** : first row shows the RMSE values of input parameters for $t \leq 8$s. The second row displays the RMSE values of the input parameters for $t > 8$s.

Parameter	τ_{es}	τ_{ep}	R_{mv}	Z_{ao}	R_s	C_{sa}	C_{sv}	E_{max}	E_{min}
RMSE $t \leq 8$s	0.005	0.009	0.005	0.003	0.05	0.01	0.8	0.04	0.003
RMSE $t > 8$s	0.0005	0.0004	0.002	0.001	0.03	0.02	0.6	0.007	0.0006

Figure 8.4 reports the continuous sensitivity of the input parameters, where no perturbations are applied with respect to arterial pressure. See Appendix for the sensitivity analysis of input parameters to the other measurements (similar to Figure 8.4). We note the sensitivity of input parameters follows a dynamics which mimics a cardiac cycle, that some parameters, such as τ_{es}, R_{mv}, R_s and C_{sa} in Figures 8.4A, C, E, F, exhibit a consistent level of sensitivity over the full CV cycle, the τ_{es} Figure 8.4A being the most influential during overall and that the parameters E_{min}, E_{max}, Z_{ao} and C_{sv} exhibit orders of magnitude change in sensitivity during the cycle. In Figure 8.4B we see the end pulse time τ_{ep} appears to have no influence of the arterial pressure during the whole cardiac cycle.

8.3.2 Parameter Perturbations

We examine the UKF's ability to estimate input parameters accurately, when they are perturbed away from the "baseline" value during each cardiac cycle, applying the perturbations defined in equations (8.2) and (8.3) from $t \geq 8$.

8.3.2.1 τ_{es} & τ_{ep}

Figure 8.5 demonstrates the UKF's ability to adapt to perturbations of the timing parameters τ_{es} and τ_{ep}. The UKF adapts to the perturbed points with exceptional ability -see Figures 8.5A and 8.5B. The original parameter values were $\tau_{es} = 0.35$ and $\tau_{ep} = 0.45$, the perturbed values for the cycles were $\tau_{es} = [0.35, 0.27, 0.27, 0.28, 0.34, 0.28, 0.31, 0.26]$ and $\tau_{ep} = [0.43, 0.46, 0.47, 0.44, 0.46, 0.44, 0.43, 0.43]$ to 2dp. The variance of the parameters in Figures 8.5J and 8.5K appear to be consistent, despite the perturbations. Figures 8.5I and 8.5R represent the estimation and variance of the parameter E_{min} respectively. There is disruption to the parameter estimation, despite the true value of E_{min} being found during each cardiac cycle. There is minimal disruption to the parameter variance. Note similar behaviour with the aortic valve resistance Zao, and maximal contractility E_{max} in Figures 8.5D, 8.5M, 8.5H and 8.5Q respectively. The common theme between both is that the parameter estimations return to the true parameter values during each cardiac cycle. Estimates of all input

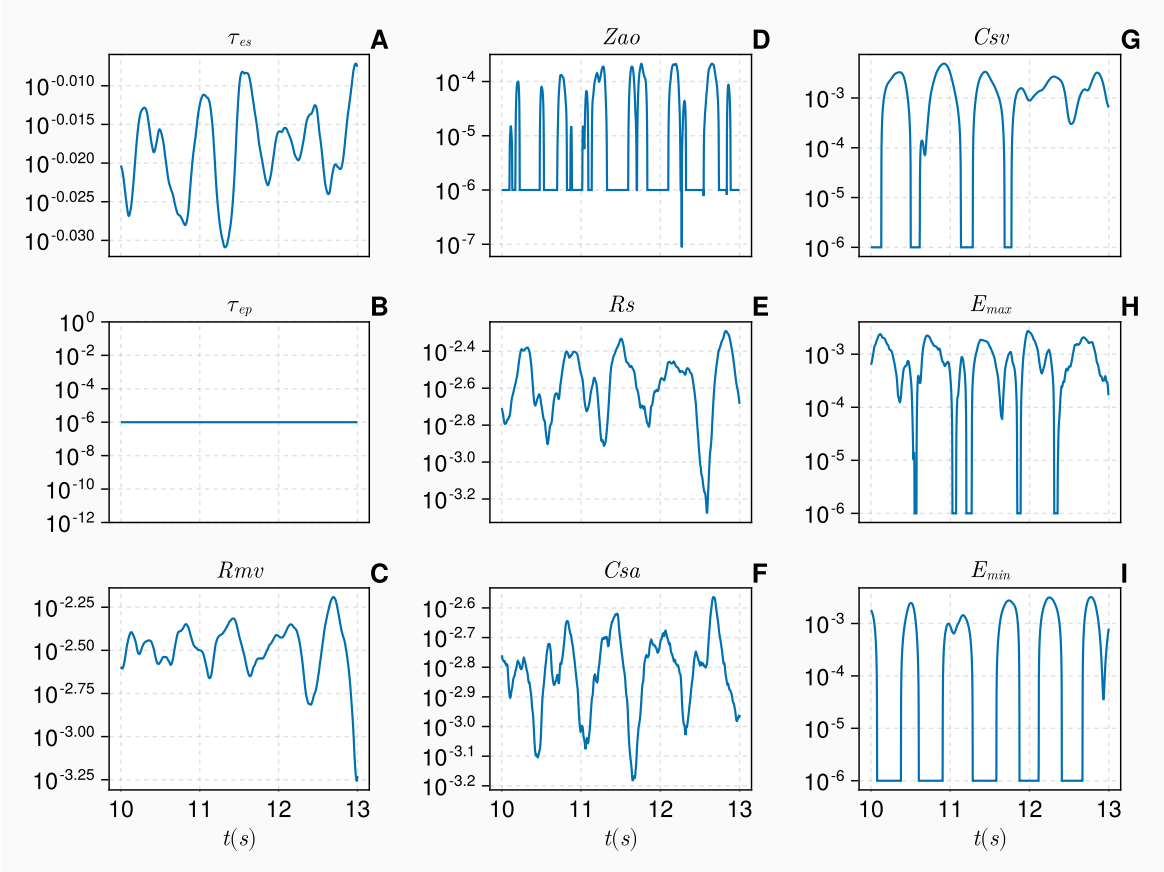

Fig. 8.4 **Single Ventricle Base State Sensitivity** - Figures **A** - **I** display the continuous parameter sensitivities with respect to the arterial pressure. All parameters which returned 0 for sensitivity are set to a value of 10^{-6} in order to plot a log scale.

parameters apart from C_{sv} have minimal errors. The RMSE values in Table (8.3) indicate that no input parameter estimations suffer as a result of perturbing the timing parameters (of the elastance function). Some input parameter estimates improve as the simulation progresses. C_{sv} exhibit the worst RMSE by an order of magnitude when compared to the other input parameter estimates.

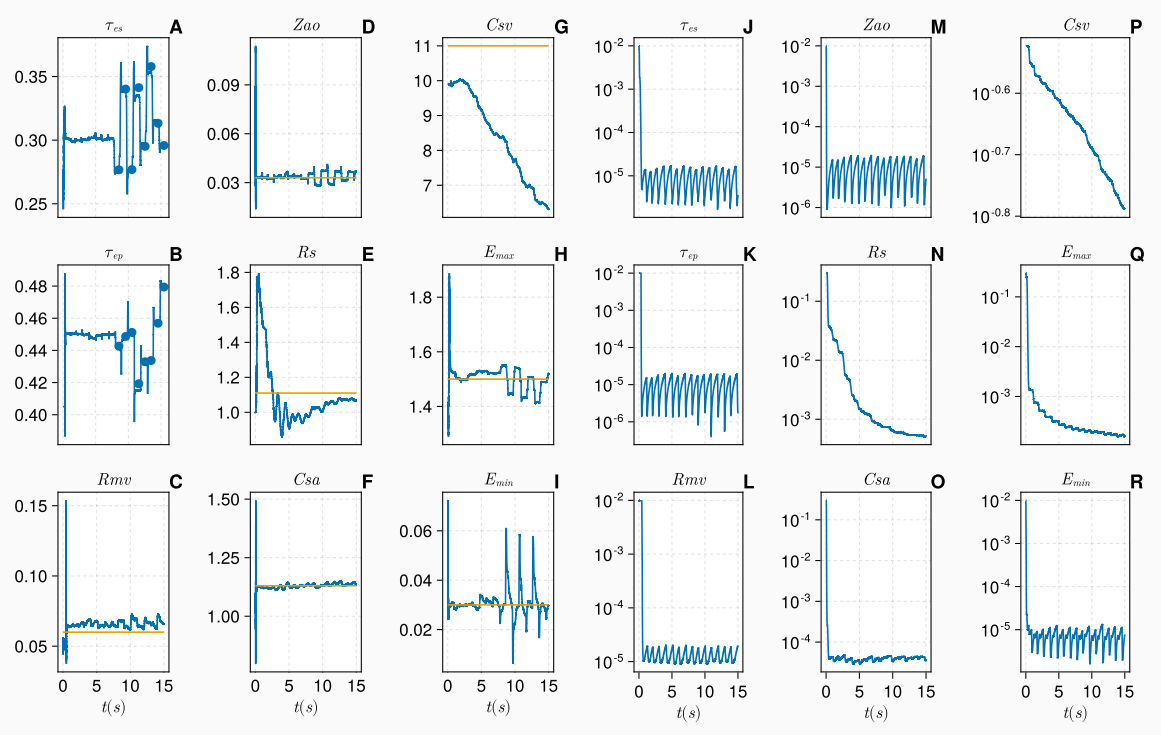

Fig. 8.5 τ_{es} & τ_{ep} : Figures **A** - **I** show parameter estimations over 15 cardiac cycles with varying values for τ_{es} and τ_{ep}. The yellow and blue line represent the true and estimated parameter values respectively, the blue dots represent the perturbed values on the input parameters. Figures **J** - **R** display the parameter covariances over the 15 cardiac cycles.

Table 8.3 τ_{es} & τ_{ep} RMSE : first row, RMSE values of input parameters for $t \leq 8$, second row, displays the RMSE values of the input parameters for $t > 8$ after a continuous perturbation has been applied to E_{min}.

Parameter	τ_{es}	τ_{ep}	R_{mv}	Z_{ao}	R_s	C_{sa}	C_{sv}	E_{max}	E_{min}
RMSE $t \leq 8$	0.01	0.009	0.008	0.003	0.2	0.02	2	0.04	0.005
RMSE $t > 8$	0.03	0.02	0.007	0.004	0.06	0.009	4	0.05	0.008

8.3.2.2 E_{min}

Figure 8.6 reports the UKF's ability to estimate ventricular compliance, E_{min}, given the perturbation defined in equation (8.3). In Figure 8.6I, we see E_{min} traces the perturbation with high accuracy, and that the perturbation also impacts the variance of the parameter, causing a gradual increase, from when it is applied. This increase in parameter variance is also present in other input parameters (where the perturbation is not applied), seen in Figures 8.6J, K, L, M, O, R. The timing parameters of the elastance function, τ_{es} and τ_{ep}, appear to diverge from the true parameter values when the perturbation is applied, as seen in Figures 8.6A and 8.6B. We remark that all input parameter estimates return to the true parameter value by the final cycle at $t = 15$. All other input parameters, apart from C_{sv}, tend towards their true values with minimal error after the perturbation is applied to E_{min}. Table 8.4 indicates that the UKF copes with the perturbation with great efficiency as the RMSE value of the perturbed parameter E_{min} increases minimally. Overall most input parameters do not suffer significantly, with some actually improving their estimation, after the perturbation applied to E_{min}, with only τ_{es} exhibiting a $2.5\times$ increase in error. C_{sv} as in the base state is the input parameter with the largest RMSE error.

Table 8.4 E_{min} RMSE - The first row shows the RMSE values of input parameters for $t \leq 8$. The second row displays the RMSE values of the input parameters for $t > 8$ after a continuous perturbation has been applied to E_{min}.

Parameter	τ_{es}	τ_{ep}	R_{mv}	Z_{ao}	R_s	C_{sa}	C_{sv}	E_{max}	E_{min}
RMSE $t \leq 8$	0.004	0.008	0.007	0.003	0.2	0.01	1	0.03	0.01
RMSE $t > 8$	0.01	0.009	0.009	0.009	0.03	0.008	2	0.03	0.03

8.3.2.3 C_{sa} & τ_{ep}

In Figure 8.7, we report perturbations applied to τ_{ep} and equation (8.3) applied to C_{sa}. Figure 8.7B demonstrates the UKF's ability to adapt to differing times which are applied to the end pulse time, τ_{ep}. In Figure (8.7 F) we see that C_{sa} is not found as accurately when the same perturbation is applied to E_{min}, Figure 8.6I. Despite C_{sa} not being determined as efficiently, the trend of gradual increase is still present in the estimated parameter. We observe small disruption to other input parameters in the presence of this parameter perturbation case. C_{sv} and R_{mv} appear to diverge from the true parameter estimate. In Table (8.5) the RMSE values indicate the UKF struggles to capture the perturbation to C_{sa} accurately, with a $5\times$ increase in the RMSE. The perturbation applied to τ_{ep} appears to cope with a small increase in the error. Most input parameters appear to improve their estimate of the input parameter value

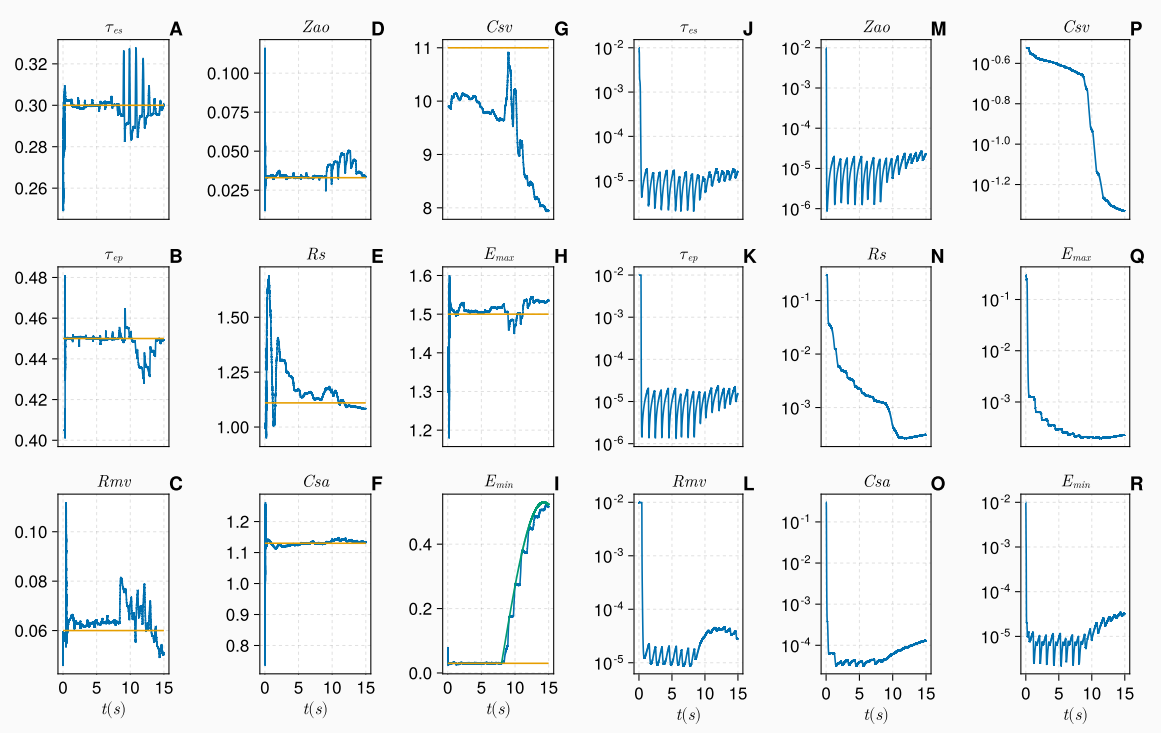

Fig. 8.6 E_{min}. Figures **A** - **I** show the parameter estimations over the 15 cardiac cycles with perturbed E_{min}. The yellow, blue and green line represent the true, estimated and perturbed parameter values respectively. Figures **J** - **R** display the parameter covariances over the 15 cardiac cycles.

apart from E_{min}, where the error increases by $2\times$ and R_{mv} where we see the same increase in the error, however in this case it appears R_{mv} may be diverging. C_{sv} again is the input parameter with the largest RMSE value.

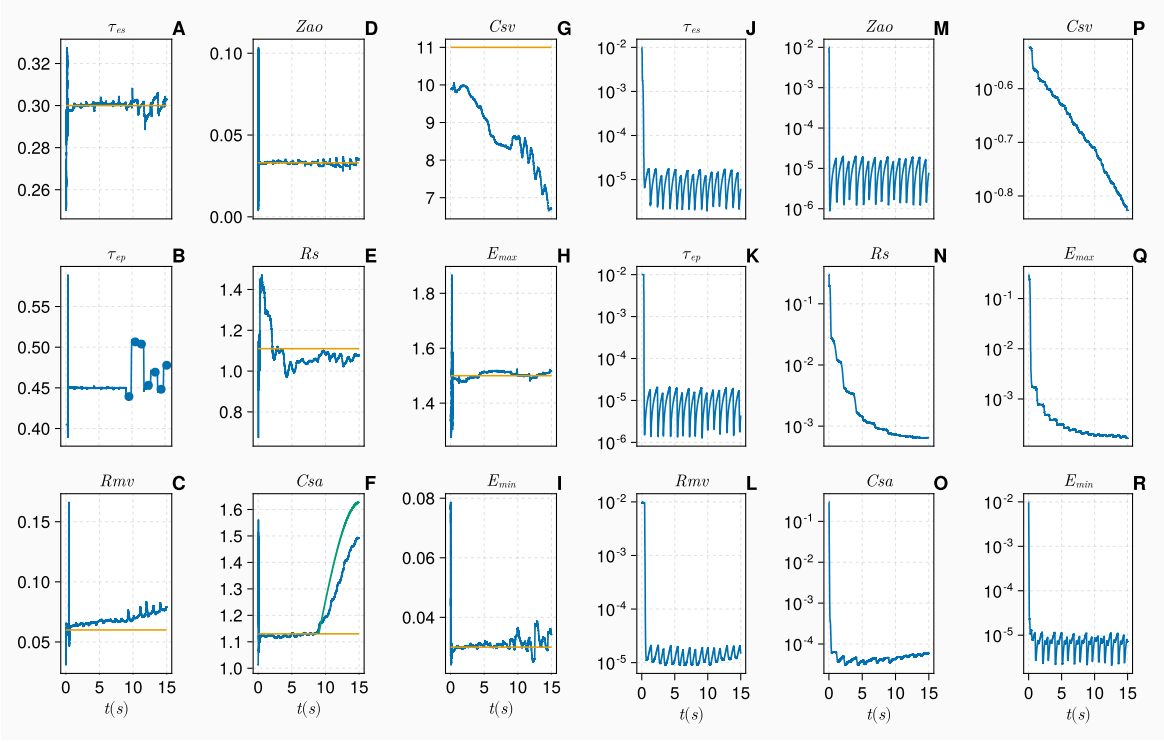

Fig. 8.7 C_{sa} & τ_{ep} - Figures **A** - **I** show the parameter estimations over 15 cardiac cycles with perturbed C_{sa} and τ_{ep}. The yellow and blue line represent the true and estimated parameter values respectively. The blue dots and green line represent the perturbed parameter values for τ_{ep} and C_{sa}. Figures **J** - **R** show the parameter covariances over the 15 cardiac cycles.

Table 8.5 C_{sa} & τ_{ep} RMSE : first row, RMSE values of input parameters for $t \leq 8$. Second row : RMSE values of the input parameters for $t > 8$ after a continuous perturbation has been applied to C_{sa} and discretely we perturb τ_{ep}

Parameter	τ_{es}	τ_{ep}	R_{mv}	Z_{ao}	R_s	C_{sa}	C_{sv}	E_{max}	E_{min}
RMSE $t \leq 8$	0.004	0.01	0.009	0.003	0.1	0.02	2	0.03	0.002
RMSE $t > 8$	0.003	0.03	0.02	0.002	0.04	0.1	3	0.007	0.004

8.3.2.4 R_s & E_{min}

Here, R_s and E_{min} are perturbed. We see exceptional ability of the UKF to adapt to E_{min} being perturbed by equation (8.3) but R_s fails to track the perturbation as accurately as E_{min}.

A majority of input parameters in Figure 8.8 converge to the ground truth value, with little error apart from R_{mv} and C_{sv}. This parameter perturbation combination causes increases in all parameter variances. The RMSE values of Table (8.6) indicate -once again- that all none-perturbed parameters are fairly resistant to the changes applied to the input parameter space, we see a $1.67\times$ and $1.25\times$ increase in the RMSE for τ_{es} and τ_{ep}, a $2\times$ increase in the perturbed E_{min} parameter and a $3.33\times$ increase on the RMSE value for Z_{ao}. The perturbed systemic resistance R_s retains the same level of error pre and post perturbation which we believe is due to R_s failing accurately to find the true parameter value in the first 8 cycles. Then, after the perturbation is applied the R_s estimation fails to track the perturbation to the higher values, $R_s > 1.3$. C_{sv} exhibits the largest values of the RMSE, notably for $t > 8$ we see our smallest value of the RMSE yet for C_{sv}. From Figure 8.8G we see C_{sv} appears to tend towards the true value before diverging again.

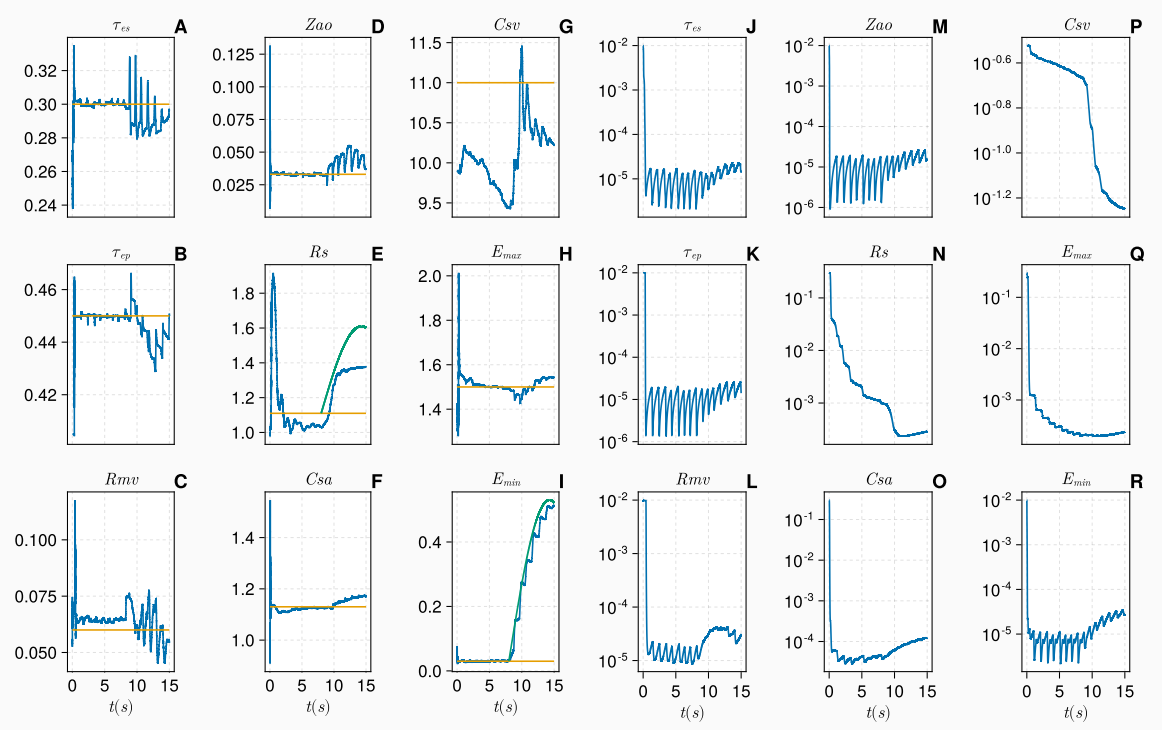

Fig. 8.8 R_s & E_{min} - Figures **A** - **I** show the parameter estimations over the 15 cardiac cycles with perturbed E_{min} and R_s. The yellow and blue line represent the true and estimated parameter values respectively. The green lines represent the peturbed input parameter values. Figures **J** - **R** display the parameter covariances over the 15 cardiac cycles.

Table 8.6 R_s & E_{min} RMSE : first row, RMSE values of input parameters for $t \leq 8$. Second row : RMSE values of the input parameters for $t > 8$ after a continuous perturbation has been applied to E_{min} and R_s.

Parameter	τ_{es}	τ_{ep}	R_{mv}	Z_{ao}	R_s	C_{sa}	C_{sv}	E_{max}	E_{min}
RMSE $t \leq 8$	0.006	0.008	0.007	0.003	0.2	0.02	1	0.04	0.02
RMSE $t > 8$	0.01	0.01	0.008	0.01	0.2	0.03	0.6	0.03	0.04

8.3.2.5 τ_{es}, τ_{ep} & E_{min}

Figure 8.9 shows the outcome after both the timing parameters τ_{es} and τ_{ep} and the minimal contractility parameter E_{min} are perturbed. The timing parameters τ_{es} and τ_{ep} struggle to adapt to the differing timing parameters shown in Figures 8.9A and 8.9B. Perturbing E_{min} leads to an accurate estimate during every cardiac cycle. We notice the parameter estimates for other input parameters converge with minimal error. C_{sv} diverges from the true value in Figure 8.9G. The mitral valve resistance R_{mv} appears to diverge from the true parameter value when the perturbation is applied, but towards the final cardiac cycle it appears to converge back towards the true parameter value. We also notice that the variance appears to increase in all parameters except C_{sv} - see Figures 8.9 J-R. This is mirrored in the RMSE values found in Table (8.7) we see a $16.7\times$ and $50\times$ increase in the RMSE value for τ_{es} and τ_{ep}. E_{min} appears robust to the perturbation with the same value of the RMSE being found before and after the perturbation has been applied. All over input parameters suffer from increases to their RMSE value with the exception of the systemic resistance which has a $10\times$ improvement. C_{sv} exhibits the largest RMSE value.

Table 8.7 τ_{es}, τ_{ep} & E_{min} RMSE : first row, RMSE values of input parameters for $t \leq 8$. Second row : the RMSE values of the input parameters for $t > 8$ after a continuous perturbation has been applied to E_{min} and then a discrete perturbation to the timing parameters τ_{es} and τ_{ep}.

Parameter	τ_{es}	τ_{ep}	R_{mv}	Z_{ao}	R_s	C_{sa}	C_{sv}	E_{max}	E_{min}
RMSE $t \leq 8$	0.006	0.008	0.006	0.003	0.2	0.01	2	0.04	0.04
RMSE $t > 8$	0.1	0.4	0.02	0.005	0.02	0.02	3	0.04	0.04

8.3.2.6 C_{sv}

Next, we perturb the venous compliance parameter C_{sv}. In Figure 8.10, the parameter estimate diverges from the ground truth value whist all other parameter estimates in Figure 8.10 appear to converge as accurately as in the base state, a fact mirrored by constant variance. The RMSE values found in Table (8.8) reflect the accuracy of estimation observed in the base state case, see Table (8.2). In this case we obtain our smallest value of the RMSE obtained by

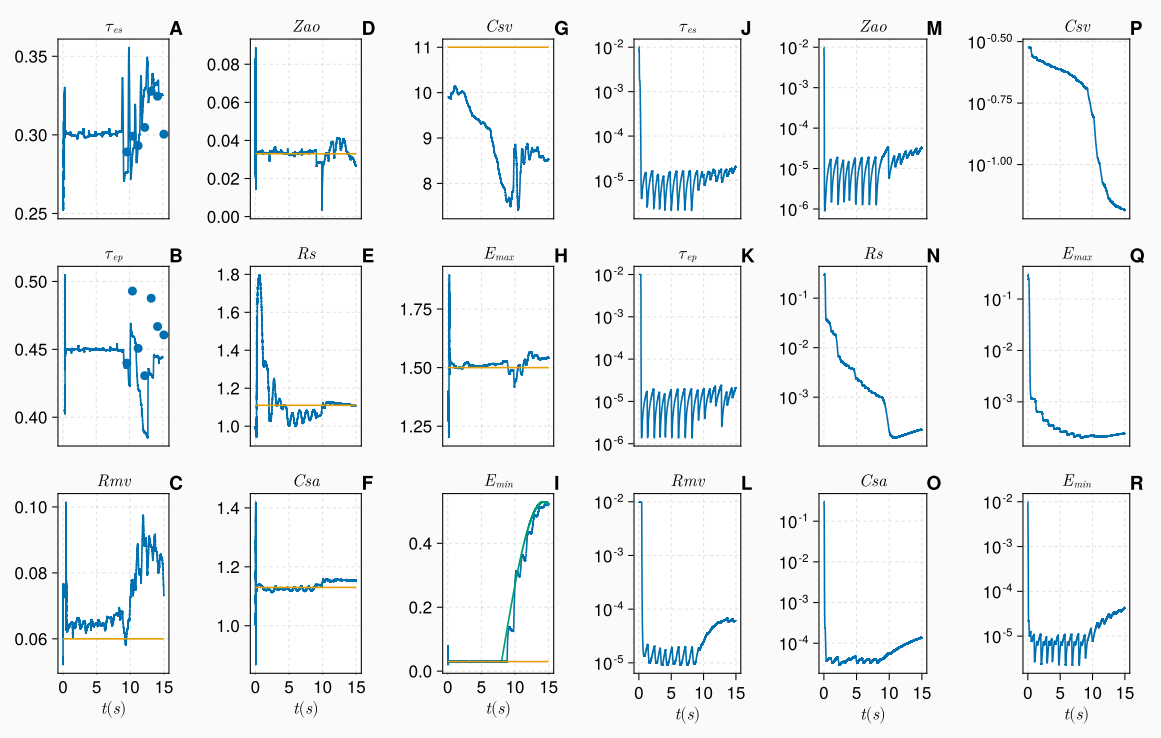

Fig. 8.9 τ_{es}, τ_{ep} & E_{min} - Figures **A** - **I** exhibit parameter estimations over 15 cardiac cycles with perturbed timing parameters τ_{es} and τ_{ep} and E_{min}. The yellow and blue lines represent the true and estimated parameter values respectively. The blue dots represent the perturbed values of the timing parameters τ_{es} and τ_{ep}. The green line represents the continuous parameter perturbation. Figures **J** - **R** display the parameter covariances over the 15 cardiac cycles.

τ_{ep} after the perturbation was applied to C_{sv}. Figure (8.10) displays a uniform trend that as the simulation runs longer the estimation improves, seeming to indicate the perturbation applied to C_{sv} makes no difference to the estimation of the other input parameters. C_{sv} appears to take no notice of the perturbation and continues to diverge.

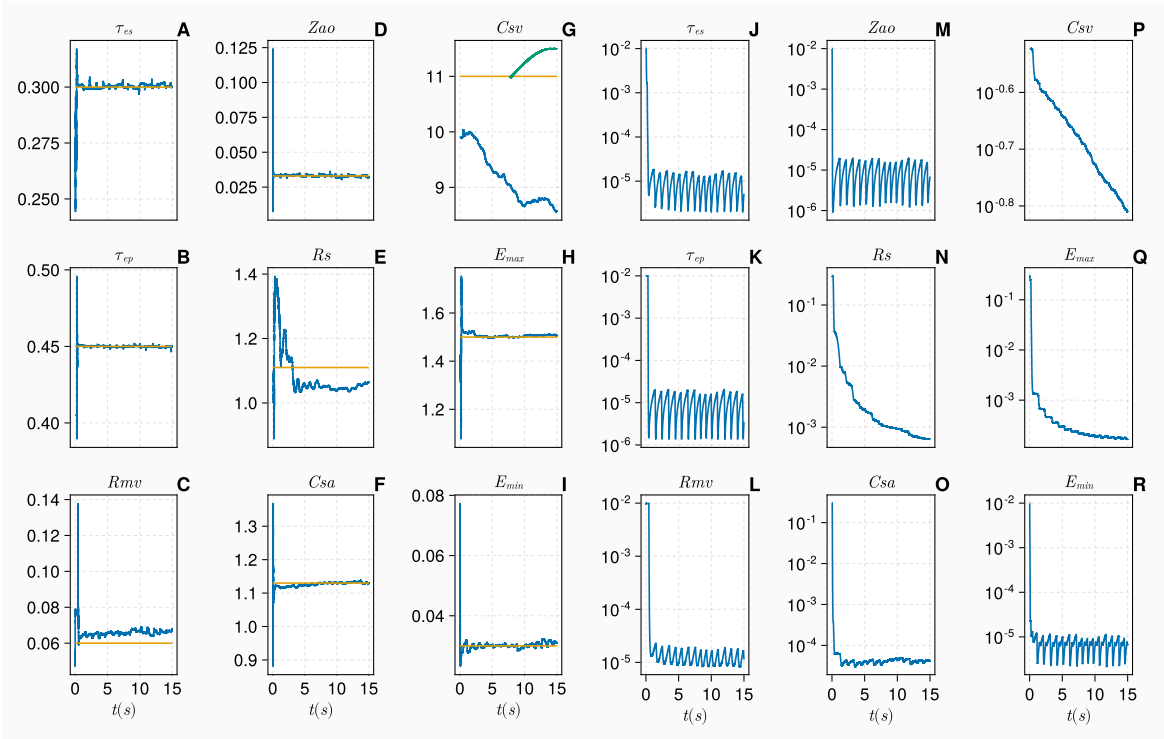

Fig. 8.10 C_{sv}: Figures **A** - **I** show parameter estimations over the 15 cardiac cycles with perturbed E_{min}. The yellow and blue line represent the true and estimated parameter values respectively. The green line represents the perturbed value of C_{sv}. Figures **J** - **R** display the parameter covariances over the 15 cardiac cycles.

Table 8.8 C_{sv} RMSE : first row RMSE values of input parameters for $t \leq 8$. Second row : the RMSE values of the input parameters for $t > 8$ after a continuous perturbation has been applied to C_{sv}.

Parameter	τ_{es}	τ_{ep}	R_{mv}	Z_{ao}	R_s	C_{sa}	C_{sv}	E_{max}	E_{min}
RMSE $t \leq 8$	0.004	0.008	0.007	0.003	0.09	0.02	2	0.03	0.002
RMSE $t > 8$	0.001	0.0004	0.006	0.0007	0.06	0.003	3	0.008	0.001

8.4 Discussion

Our main intention was to test the robustness of the UKF in the presence of beat-to-beat variability and physiological parameter perturbations. Overall, we see it presents as a good choice for the identification of input parameters, both in terms of accuracy and efficiency. The results in section 8.3 demonstrate that all the input parameters exhibit adaptive behaviour, towards their ground truth value in the presence of perturbed and non-perturbed input parameters (note: always for synthetic personalised varying cardiac cycle length times). Most remarkably, when certain input parameters are perturbed, namely, the minimal ventricular elastance or compliance, E_{min}, and the ventricle timing parameters τ_{es} and τ_{ep}, the UKF often finds the perturbed values exceptionally well (see Figure 8.6 and Figure 8.5). This provides assurance that, given a similar data set measured in clinic, these important parameters may be feasibly estimated, given the same set of clinical measurements are used. Note, given a different set of measurements it is likely the accuracy of the estimations may change for specific input parameters. Other input parameters such as the systemic compliance, C_{sa} and the systemic resistance R_s do not return such accurate estimations (see Figures 8.7 and 8.8). Despite this, it appears the general trend of the added perturbation is still present in the estimation of the input parameters.

All cases considered reveal that when a perturbation is applied to a parameter, this normally introduces some disturbance to the other parameter estimations in the model (see the Figures in section 8.3) where the disturbance of other parameters in magnitude is often smaller than the magnitude of the perturbed parameter. Further, the disturbance introduced on certain input parameter estimates is a residual effect of another parameter perturbation and not a direct change in our synthetic patient's physiological state.

The non-perturbed parameter estimations tend towards their true values during a cardiac cycle after a perturbation has been applied. This is evident in the RMSE values, in section 8.3. Clinical expertise is essential to ensure that this minimal disturbance can be distilled from true parameter perturbations, for example, in a head-up tilt, one observes a significant drop in systemic resistance before recovery [357]. In Figure 8.9, we perturb 3 input parameters and observe the estimations on the timing parameters break down dramatically while the other input parameters appear to be estimated with sufficient accuracy. This is likely to be caused by the 3 parameters being linked by the analytical description of the ventricle in equation (4.25), which highlights the need to identify dependencies and identifiable parameters, before estimation, to ensure that accurate and unique parameter estimations can occur.

We examined the continuous sensitivity of input parameters to give an indication on how this may relate to the accuracy of estimation performed by the UKF. The continuous sensitivity analysis (CSA), with results shown in Figure 8.4, reveals that most input parameters have a well-defined "cycle of importance" which corresponds to the phases of the cardiac cycle. Two tentative conclusions can be drawn: first, this may explain why most input parameters are estimated with outstanding accuracy, even when their time averaged influence is small compared to the most influential parameter τ_{es}. Therefore an accurate estimation of input parameters is due to either a well-defined cycle of importance or being consistently important. This means the input parameters' effects are observable in the outputs, such that they would be accurately identified by the UKF. Our second conclusion from the CSA relates to what choice of measurements should be made. It is accepted practice to investigate discrete measurements. The CSA indicates that there are distinct moments within the cardiac cycle where certain parameters exert a stronger influence compared to their influence at other instants. Our work provides a guide for what one should consider, when deciding on which measurements to use to interrogate an input parameter space, i.e., one would choose measurements which are applicable to the time points where all input parameter effects are at their largest, hence improving the chances of making the parameters identifiable.

Notably, two input parameters exhibit surprising results. In the CSA (Figure 8.4), we note that the end pulse time, τ_{ep}, exhibits minimal sensitivity across the whole time period investigated. Due to personalised cardiac cycles being included, the effects of end pulse time are truncated. The end pulse time signifies the start of passive filling of the ventricle and due to the passive filling phase of of the ventricle being isolated between cycles, this leads to the effects being neglected. Despite the lack of sensitivity, τ_{ep} is found accurately in nearly all cases investigated. One explanation is that the variance of the parameter is consistently low, hence the UKF finds the local minimum estimate and therefore the accurate estimate. Due to this factor, our estimate of τ_{ep} should be considered with more caution than other input parameters.

Within the clinical setting, the end systolic time, τ_{es} is that which is considered to have more impact, as it relates to a QT interval [500, 501], which is reflected in the high level of sensitivity seen in Figure 8.4. In section 8.3, we notice that the estimates of the venous compliance C_{sv} appear to diverge in all cases. C_{sv} even diverges in the base state where no parameter perturbations have been applied (see Figure 8.3). The variance of the venous compliance is the highest in all parameter estimations, whereas the parameters with accurate estimations have steady minimal variances. One explanation for this is that venous

compliance has no direct influence over any of the measurements present in our analysis [502]. As a consequence the parameters' effects cannot be observed independently in our synthetic measurements and subsequently the parameter estimate is poor. Despite these special cases, the CSA and UKF results are robust and consistent to all other input parameters.

In the presence of personalised cardiac cycle lengths and parameter perturbations, the average computation time is 90.4 seconds under serial execution, which corresponds to an average of 6 seconds per cardiac cycle. If the goal is to implement this approach in the clinic it is important to reduce the computation time to real-time levels, ensuring a one-to-one relationship between the computational time and the cardiac cycle time. Recently, a real time implementation without perturbations is available to clinicians [502]. Although the estimates in this study demonstrate exceptional accuracy, it is possible to decrease the computational time by reducing the tolerance, complexity of the differential equation solver, and the size of the time step. However, this would inevitably lead to a decrease in the accuracy of the parameter estimate. Currently, no adaptive time step Kalman filtration approach exists for this purpose, but its development would significantly enhance the efficiency of the algorithm. Additionally, it would be intriguing to investigate the optimal time step required to ensure sufficient accuracy of the parameter estimate. If either of these issues could be developed, it would lead to an increase in the algorithm's efficiency while still maintaining the accuracy level presented within this work.

It is worth noting that the computational expense of this approach is low compared with other computational tools for direct clinical applications [21, 82, 368, 503]. Even though the computational time of this work does not currently meet real-time requirements, clinicians can still obtain prompt insights into a patient's physiological state, compared to other tools. Therefore, when pathophysiological conditions are present within the patient data, the UKF should be capable of providing state and parameter estimates that accurately emulate the pathophysiological conditions depicted in the data. The only drawback with this current workflow is that the personalised cardiac cycle lengths must be recorded, say through an ECG. However, when the pathophysiological condition is not severe, this workflow (of collecting personalised cardiac lengths and patient data, feeding them to the UKF, and interpreting the results) remains an efficient approach to personalised patient-centred care.

A primary perturbation employed in this study involves a random scattering of the timing parameters of the elastance function, specifically τ_{es} and τ_{ep}, as defined in equation (8.2). In reality, there presumably exists some function that enshrines the complex relationship

between the length of the cardiac cycle τ, the end systolic time τ_{es}, and the end pulse time τ_{ep}. However, in this work, these parameters are treated as independent parameters of the elastance function. By perturbing τ_{es} and τ_{ep} independently, we are able to demonstrate the robustness associated with the UKF in accurately estimating the timing parameters, even under extreme and non-physiological conditions. hence defining a worst case scenario. This highlights the excellent capability of the UKF to handle perturbations and effectively estimate the timing parameters, despite their independence from the underlying physiological relationships within the cardiac cycle. The other parameter perturbation used (defined in equation (8.3)) applies a steady increase to a parameter value. The results are also tested using a steady decrease in the parameter value and the same conclusions hold. This parameter perturbation is more realistic and similar parameter dynamics have been reported in models which have built-in physics which causes time-varying behaviour of input parameters, such as in models of head-up tilt, microgravity and stochastic versions of the Windkessel model [504–506].

The UKF utilised to estimate input parameters can only perform within a local context. While it excels in providing efficient parameter estimations, there are advanced global optimisation techniques, such as particle filters and genetic algorithms which offer additional benefits such as independence from initial conditions, which the UKF can be sensitive to, and they are better suited at coping with non-linearities in the system, so global optimisation techniques can often explore a wider input parameter space [507, 508]. Use of carefully chosen sigma vectors to represent a GRV reduces the need for numerical derivative evaluations, which are computationally expensive in global optimisations. A UKF's computational advantage is particularly valuable in clinical situations where a decision may required under a time constraint. However, relying solely on the UKF's local approach has certain limitations. Since the UKF heavily relies on initial conditions and model assumptions, there is a potential for introducing bias into the estimates.

Within this chapter, all parameter distributions and initial co-variances were chosen with the physiology of the input parameters in mind. See section 4.14. The dynamical system noise was set to $Q = 10^{-8}$, reflecting the cardiovascular system's largely deterministic nature and to avoid sigma point collapse, a problem associated with the UKF [21, 443]. The measurement noise used in this work was $R = 5^2 \times I_{3\times3}$ to represent the uncertainty within our chosen measurements, as defined in section 8.2. The local nature of the UKF restricts its ability to explore the entire parameter space, limiting its capability to find the global optimum. In contrast, global optimisation techniques can better navigate multi-modal parameter spaces,

potentially yielding more accurate estimates.

The estimates provided by the UKF could be evaluated by the clinical expert with specialised knowledge, to determine if the estimated parameters align with physiological expectations and reflect their assessment of the patient's physiological state. Such an evaluation process ensures that the estimates are not only mathematically sound but also relevant. By incorporating the interpretive expertise of clinical professionals, the UKF's estimates can be validated, enhancing the interpretation of clinical data and providing a more comprehensive assessment of the patient's condition. This collaborative approach between the UKF and the clinical expert fosters an efficient, reliable and clinically relevant decision-making process.

8.5 Conclusion

We have analysed a tractable nine-dimensional closed loop, single ventricle LPM of the systemic circulation. Our approach to this LPM may be generalised to a range of dynamical systems and our observations are in principle applicable to any model - not just one in a cardiovascular setting. We present a *de novo* computational algorithm, designed to incorporate patient-specific beat-to-beat variability into model investigations. Utilising this algorithm, we have efficiently implemented the Unscented Kalman Filter, demonstrating its exceptional adaptability to severe parameter perturbations, representing significant changes in a patient's physiological state.

Our investigation into the computationally efficient, continuous sensitivity of model input parameters explains the exceptional capability of the UKF accurately to estimate input parameter values, within a single cardiac cycle. This insight contributes to our understanding of the UKF's robustness and efficacy. Our research showcases potential clinical applications of the UKF. By utilising patient-specific measurements and employing the close to real-time UKF, it becomes feasible to monitor a patient's physiological state with minimal delay, offering promise to medical professionals, to promptly identify the onset of a (patho)physiological condition.

Chapter 9

Discussion

It was written I should be loyal to the nightmare of my choice.
— JOSEPH CONRAD, Heart of Darkness

Summary
This chapter discusses the results presented in this thesis and examines how lumped parameter models fit into a clinical workflow and what one must do to obtain a personalised medicine. We also examine alternative approaches for quantifying uncertainty within cardiovascular models.

We have examined the offline investigation of sensitivity analysis and parameter subset selection of cardiovascular LPMs and unveiled the UKF as a promising methodology for online parameter calibration, to a patient. Our results reveal important new considerations for personalising these models. To obtain the greatest impact, computational models must be incorporated into a clinical workflow. LPMs appear to be a good candidate as a components of a cardiovascular digital twins. As demonstrated in chapter 6, the data which parameter influence estimates are computed against can lead to very different interpretations. Thus if one were to apply a LPM to create a virtual patient representation, to e.g. track a pathophysiology over time, say as the patient decompensates, one would need to recompute the personalisable subset at every update of the model, incurring a large, on-going computational expense. Still, due to the efficient computational properties, a LPM remains an attractive conduit.

Another attractive property of LPMs for personalisation is that they provide insight into the physiology for which no clinical measurements are available or ethical. Due to the efficient computation time of LPMs,as demonstrated above with high-fidelty complex models. Using an LPM to study pathophysiology in (say) a specific vessel or compartment by performing a GSA, the results may reveal new influencing factors which would not have been otherwise exposed.

A limitation associated with LPMs is their neglect of spatial factors in the cardiovascular system. There are accepted clinical diagnostic metrics associated with wall shear stress that are impossible recover with LPMs. As mentioned above, when seeking to apply computational modelling in a clinical setting this has to be completed within an acceptable time frame. Higher dimensional models may be suitable for the diagnosis of pathophysiological conditions, their interrogation of clinical scans (MRI/CT) scans allowing for the close examination of patient specific vessel structure [509, 510]. However, were one to need to personalise a higher dimensional model requiring continuously updates of new data sources, this would require very considerable computing power- and would become logistically unfeasible. Alternatively, high fidelity models provide us the opportunity to visualise the impact of including multiple different biological processes such as material, chemical and electrical models of heart function or vessel dynamics. Thus while we have been concerned with the *tractable* inverse problem in this work, the high dimensional modelling still cannot be discarded for a future in which resource that are currently classified as exascale become more accessible.

Recently, there has been an upswing in the use of high performance computing in car-

diovascular models. Here, all the sensitivity analysis has considered how efficiently one can solve a model. For our LPMs, we have used only a single node with multiple CPUs (26 & 48). In Julia, one should use Distributed.jl to extend to multiple nodes which would then allow us to gain multiple speed-ups. For more complex models, for example, of the whole human circulation, the parameter subset selection methodologies could then be applied. Another potential improvement to the whole subset selection methodology would be to use the new differential equation solvers which are adapted to GPUs, from DiffEqGPU.jl. This would then, on average, provide us with an additional order of magnitude acceleration, leading to quicker and more efficient model personalisation. This has been recently utilised with higher dimensional models,reducing the computational time to hours instead of days for a single model execution, which improves clinical prospects; however this is still unusable for sensitivity analysis investigations unless coupled to an emulator methodology. It is also important to note that higher dimensional models contain hundreds of thousands sources of error compared to LPMs, which possibly contain hundreds at most. These are present in the form of additional model parameters which are likely to be attributed to the segmented arterial geometry created from a medical image. If one has an interest in quantifying the uncertainty using Sobol indices the number of model executions would quickly become infeasible. Recall, Sobol indices require $k(n+2)$ model executions, where n is the number of parameters.

Turning to the application of computational models to the clinic, while access to HPC opens up opportunities for further process investigation and the personalisation of more highly detailed LPMs, one has to acknowledge the limit on resources available. If a model were to be integrated into a routine clinical checkup (say) or a DT to monitor the evolution of a patients health, such resource is not going to be readily available in the medium term. Further, another common barrier to the implementation of technical solutions into cardiovascular care is the barrier to entry and the staff up-skilling required for HPC training would be too large. Thus, while HPC offers an academic technical or off-line solution for further research, the focus for clinical translation of cardiovascular models has to be on the efficient solving of models locally. Otherwise, while the technology and methods are available to simulate large scale complex models the computational resource may not be.

To perform the vital offline stage investigating the sensitivity of the model parameters, we have already highlighted the vital importance of efficient model solving. Apart from utilising the HPC systems as discussed above, the steady models can be executed at a fraction of the speed associated with pulsatile models thus making them a prime candidate for personalisation. Another approach is statistical emulators of the model which is under investigation,

namely Gaussian processes. A Gaussian process (GP) s a flexible non parametric regression tool widely used for machine learning, which effectively interpolates an output surface. The GP is initially trained using a set of design data composed of inputs and the desired output. Once trained, a GP can be evaluated very quickly to estimate an output for a new and unseen set of inputs, and so can emulate a cardiac cell model, or simulator [511]. A GP can treat uncertainty and variability explicitly, providing a probabilistic (mean and variance) estimate of the output, and so is an ideal tool for sensitivity and uncertainty analysis. It can be trained on a relatively small number of simulator runs, and so offers advantages over other approaches, such as Monte Carlo methods that require large numbers of simulator runs. The emulator is a probability distribution for the model. Given any point in parameter space θ the emulator encodes our knowledge about the corresponding model output $\underline{Y}$. If we have run the simulator at x, then we know the corresponding model output with certainty. Note that this does not mean that we know with certainty the “true" value of the quantity we are modelling, just that we know what value the computer model will return given input parameters $\underline{\theta}$. When training the GPE it allows for us to associate an uncertainty associated with points in input space. Work has shown that Sobol indices can be directly calculated from the outputs of the emulator [512, 288]. There are many other theories of model emulation such as neural network and polynomial chaos expansion [513, 514]. Statistical modelling allows for categorising patients based on the probability of an outcome, mechanistic modelling provides the insight into whether we should support or reject this such categorisation.

The whole focus of the personalisation process is situated around the integration of computational tools into a clinical workflow. If one is to provide clinicians with predictions or advice based on computational models, we must quantify the risk associated with these deductions. This means that every aspect of uncertainty in the modelling process must be understood and quantified. Thus, this presents a dichotomy between looking to minimise the uncertainty of the personalisation process and trying to obtain quick and efficient solutions to the cardiovascular systems under investigation. While emulators solve models efficiently and offer an attractive alternative methodology the effects and uncertainty of the hyperparameters associated with the training of an emulator need also to be quantified when they are been used to make deductions from cardiovascular models. In this work we have avoided the use of emulators due to the speed associated with the system solvers in Julia. However, when examining the UKF’s efficiency in the personalisation process, there are multiple hyperparameters associated with this methodology. Thus further investigation should be performed to examine the impact of the associated hyperparameters of the UKF. An interesting future direction would be to include the hyperparameters into a GSA to examine their influence

against the mechanical model parameters. Although these hyperparameters carry no clinical insight, if they are to be incorporated into the personalisation process it would begin to allow us to provide clinicians with a greater more reasoned quantification of the risk associated with model interpretations.

In this work we have been able to focus on Sobol indices, due to the rapid computation of the models investigated. However, given a wish to investigate more complex models with multiple paths (regulation, chemical, electrical), would Sobol indices still be usable? There have been other attempts at simplifying the computational burden associated with Sobol indices' computation, such as hybrid local-global sensitivity analysis method termed the Distributed Evaluation of Local Sensitivity Analysis (DELSA). DELSA uses derivative-based "local" methods to obtain the distribution of parameter sensitivity across the parameter space and has been shown to be in good standing with respect Sobol indices interpretation. However, the intuitive understanding provided by the first and total order indices Facilitates insight into the complexity of input space, as described in section 4.6. Derivative based global measures (DGSM) (first introduced by Sobol and Gershman), have a strong link with the Morris screening method and Sobol' sensitivity indices and have several advantages over them. DGSM are very easy to implement and evaluate numerically. The computational time required for numerical evaluation of DGSM is generally much lower than that for estimation of Sobol' sensitivity indices. Most importantly it can be shown that the total order Sobol indices are bounded above by the DGSM sensitivity metrics. DGSM is based on averaging local derivatives using Monte Carlo or Quasi Monte Carlo sampling methods. This technique is much more accurate than the Morris method as the elementary effects are evaluated as strict local derivatives with small increments compared to the variable uncertainty ranges. Local derivatives are evaluated at randomly or quasi-randomly selected points in the whole range of uncertainty and not at the points from a fixed grid. The estimator is defined as a normalised integral of partial derivatives.

The question of why this is important rests depends on one's view of utilising more complex models in future. When performing parameter subset selection, the parameters which are found to be unidentifiable are fixed at their nominal value, a practice denoted "factor fixing" by Saltelli [196]. If one obtains models with $O(10^3)$ input parameters, in a preliminary investigation using DGSM (as a proxy for the total order indices which is the gold standard for factor fixing) before performing a full global analysis one may be able to significantly reduce the parameter space for which a full Sobol analysis can be performed and the identification of inputs for personalisation is plausible. This is something which should be tested in the

future, to identify a best practice where possible.

There are also differing interpretations when seeking to assess the sensitivity of Y to $\underline{\theta}$. A way of exploring the sensitivity of a model output in the presence of uncertainty is by distribution-based techniques (also called moment independent). A technique is distribution-based (or moment independent) if the associated global sensitivity measures explicitly consider the entire model output distribution (either the cumulative distribution function or the density) instead of relying on a particular moment of this distribution (e.g., variance). They are well suited to address the decision maker's state of knowledge in the model output, especially when distributions are skewed or multi-modal. If one utilises a variance-based method then one is implicitly framing the SA within the following SA setting: we are betting on the factor that, if determined (i.e., fixed to its true value), would lead to the greatest expected reduction in the variance of $\underline{Y}$. In a distribution-based sensitivity analysis, originally proposed by Park and Ahn [515], a different setting is proposed. Now the SA setting is: we are betting on the factor that, if determined, would lead to the greatest expected modification in the distribution of Y. The sensitivity measure of interest is defined as

$$\delta_i \coloneqq \frac{1}{2}\mathbb{E}_{\theta_i}[s_i(\theta_i] \tag{9.1}$$

$$s_i(\tilde{\theta}_i) \coloneqq \int_{\Omega_Y} |f_Y(y) - f_{Y|\theta_i=\tilde{\theta}_i}(y)|dy \tag{9.2}$$

$s_i(\tilde{\theta}_i)$ is the shift the model output distribution $f_Y(y)$ and the conditional model output distribution, $f_{Y|\theta_i=\tilde{\theta}_i}(y)$, given that input θ_i is fixed at $\tilde{\theta}_i$. As underlined by Iman and Hora [516], in the presence of long tail input/output distributions robustness problems might emerge in the estimation of statistical quantities as, e.g. variance-based sensitivity measures. The results in this thesis have all been based on a variance based interpretation, however in reality we have access to many long tailed outputs, with the moment independent approach this may provide a more accurate insight into the sensitivity of continuous outputs which may influence our results when performing parameter subset selection methods.

A major assumption associated with the work here is that all input parameters are independent of each other i.e. none are correlated. A sensitivity approach that has gained more traction recently is that of the Shapley Value. The Shapley value, from economics, provides an alternative way to define variable importance. As we describe below, Shapley value provides a way to attribute the value created by a team to its individual members. In our context the members are individual input variables. Owen [517] derived Shapley value importance for independent inputs where the value is variance explained. The Shapley value

of a variable turns out to be bracketed between two different Sobol' indices. Song et al. [518] recently advocated the use of Shapley value for the case of dependent inputs. They report that it is more suitable than Sobol' indices for such problems. They use the term "Shapley effects" to describe variance based Shapley values. Although Shapley value solves the conceptual problems, computational problems remain challenging [519]. The Shapley value is defined in terms of $2^n - 1$ models where n is the dimension of $\underline{\theta}$. Shapley values offer an interesting approach to allow us to identify the marginal influence of each input parameter given specified correlations between parameters. The human body is a complex interconnected system thus the personalisation process should be carefully considered, leveraging clinical knowledge about correlations between compartments to observe if a different personalisable set of input parameters are obtained.

Following chapter 2, there is a difference between sensitivity and uncertainty analysis. In GSA, one prescribes bounds on the input parameters, which in theory should be informed by e.g clinical constraints. Then by utilising a GSA method, one identifies the input parameters which most greatly impact a chosen set of outputs. An issue associated with GSA is that we have no insight into the value of the outputs which we are investigating. Were one to use a range on input parameters which does not encapsulate the full range of (patho)physiology of a patient, deductions from a GSA may not reflect reality. One could style personalisation as the task of obtaining a region within input parameter space which characterises a patient. If the objective is long term monitoring of a patient tracking changes in a condition one must have investigated and identified the whole of the implicated region. A simple example is a heart valve resistance if one considers a range which subsumes a sub-region for which no blood can flow through the valve. When performing a GSA one would be picking up influence of unphysiological regions that -clinically- are of no consequence, thus when performing a parameter subset reduction, one may reach false conclusions with serious consequences.

How does one identify regions of input space that are of interest? This is an open question. As we shall cement below, we propose that GSA should be used in collaboration with uncertainty analysis. A promising method is tha of Bayesian history matching - a statistical method for calibrating mathematical models. The basis of history matching is to use observed data to rule-out any parameter settings which are "implausible". For a potential parameter set $\underline{\theta}$, their implausibility $I(\underline{\theta})$ is calculated as

$$I(\underline{\theta}) = \frac{|\mathbb{E}[f(\underline{\theta})] - \underline{Y}^o|}{\sqrt{\mathbb{V}[f(\underline{\theta})]}} \tag{9.3}$$

where $\underline{Y}^o$ is the observed outputs, $\mathbb{E}[f(\underline{\theta})]$ is the expected output of the model and $\mathbb{V}[f(\underline{\theta})]$ represents the uncertainties of the model for that parameter sample. Due to the extensive number of simulations needed, often one uses an emulator as described above. An implausibility of 3 is considered a good threshold for rejecting parameter settings. For models with more that one output other thresholds can be used. A key component of history matching is the notion of iterative refocusing, where new computer model simulations can be chosen to better improve the emulator and the calibration, based on preliminary results.

We have focused exclusively on parameter uncertainty and made the assumption that the models we use reflect reality. Another important consideration is that of model discrepancy - the difference between a model's predictions and reality. Another major source of uncertainty in modelling is uncertainty in the model structure, i.e. the form of the governing equations. There is always a difference between the imperfect model and reality and reality which is termed model discrepancy. Assessment of the robustness of model predictions given our uncertainty in the model structure, and methods to characterise model discrepancy, has received relatively little attention anywhere in mathematical/systems biology. For calibration, the existence of model discrepancy can change the meaning of the estimated parameters. If we fail to account for the model discrepancy in our inference, our parameter estimates, instead of being of physically meaningful quantities, will have their meaning intimately tied to the model used to estimate them. The estimated parameter values depend on the chosen model form, and the uncertainty estimates obtained during inverse parameter UQ tell us little about the true value (only how confident we are about the "pseudo-true" values). In other words, there is no guarantee that the obtained $\underline{\theta}$ will match the true physiological values of any parameters that have a clear physiological meaning. We can try to restore meaning to the estimated parameters by including a term to represent the model discrepancy in our models. While this term does not tell us what physics we are missing, it allows us to gain insight into that we are missing some. See [236] for more details.

Alongside model discrepancy we are often limited with the amount of data available in cardiovascular systems. So, we seek a method in which we can leverage mechanistic modelling but accounting for model discrepancy. This workflow falls into the burgeoning field of "scientific machine learning" which integrates machine learning derived idea into traditional engineering-related methods to utilise domain knowledge and physical constraints into the learning process. It has recently been shown to advantage merging differential equations with machine learning. Physics-Informed Neural Networks (PINNs) use differential equations in the cost functions of neural networks to incorporate prior scientific knowledge [520]. While

this has been shown to be a form of data -efficient machine learning for some scientific applications, PINNs frame the solution process as a large optimisation. While this formalism incorporates the knowledge of physical systems into machine learning, it does not incorporate the numerical techniques which have led to stable and efficient numerical solvers. Treating the training process as fully implicit is compute-intensive which, recent results have shown, is increasingly difficult as the stiffness of the model increases [521]. While work has demonstrated that efficiency is greatly improved when incorporating classical discretisation techniques into the training process (as "discrete physics-informed neural networks", such as in multi-step neural networks [522]). Common PINN frameworks do not have the ability automatically to combine scientific machine learning training with highly efficient differential equation solvers and adjoint techniques developed over the last century. Thus, as a basis for scientific machine learning that incorporates the efficient numerical solver and adjoint techniques, developed by Julia lang they denote these as universal differential equation (UDE). UDEs are differential equations which are defined in full or part by a universal approximator. A universal approximator is a parameterised object capable of representing any possible function in some parameter size limit. Mathematically the UDE can be seen as

$$\frac{d}{dt}\underline{X}(t) = \underline{f}(\underline{X}(t);\underline{\theta}) + NN(\underline{X}(t),\underline{\theta}). \tag{9.4}$$

Above, the *NN* represents the missing physics within our mechanistic model. The Julia framework allows us to utilise the adaptive differential equation solvers and advanced automatic differentiation frameworks - advantages that lead to a more efficient training procedure and should be investigated further in the final model calibration stage to patient data. Here UDEs offer an interesting approach, we could still calibrate the model parameters which can provide clinical insight while utilising a neural network to account for any model discrepancy.

Our results embellish the vital offline stage of personalisation and the important considerations that one must make to ensure the results' validity. Figure 9.1 is a proposal for the personalisation of a cardiovascular LPM which emphasises the recursive nature of the personalisation process. For example, once a personalisable subset of parameters have been obtained, if said subset does not contain the biomarkers, one must work with clinicians to establish what additional data can be obtained for a patient and thus GSA and subset selection can be iterated. This proposal also highlights one of our key findings - that personalisation outcomes must be constrained with the available data. But when UA or model sloppiness is performed we can repeat the whole process again by either developing a new model or incorporating clinical data. From figure 9.1 we propose that the personalisation process should

be a largely offline process to obtain the best case personalisable set of input parameters. Once we subsequently begin to constrain the model with data, to personalise the model, this stage involves the optimisation and calibration of the model parameter values (informed by model sloppiness investigations). Also, one can then begin to examine the practical identifiability of the model parameters which allows one to examine the uniqueness of the personalisable subset of model parameters given noisy clinical data. The proposed workflow below defines a novel approach to quantifying the uncertainty associated with cardiovascular models constrained by computational time. This work has examined the combination of GSA and orthogonality in chapter 5 and 7. Model sloppiness was examined in chapter 6 and the UKF online optimisation stage was examined in chapter 8.

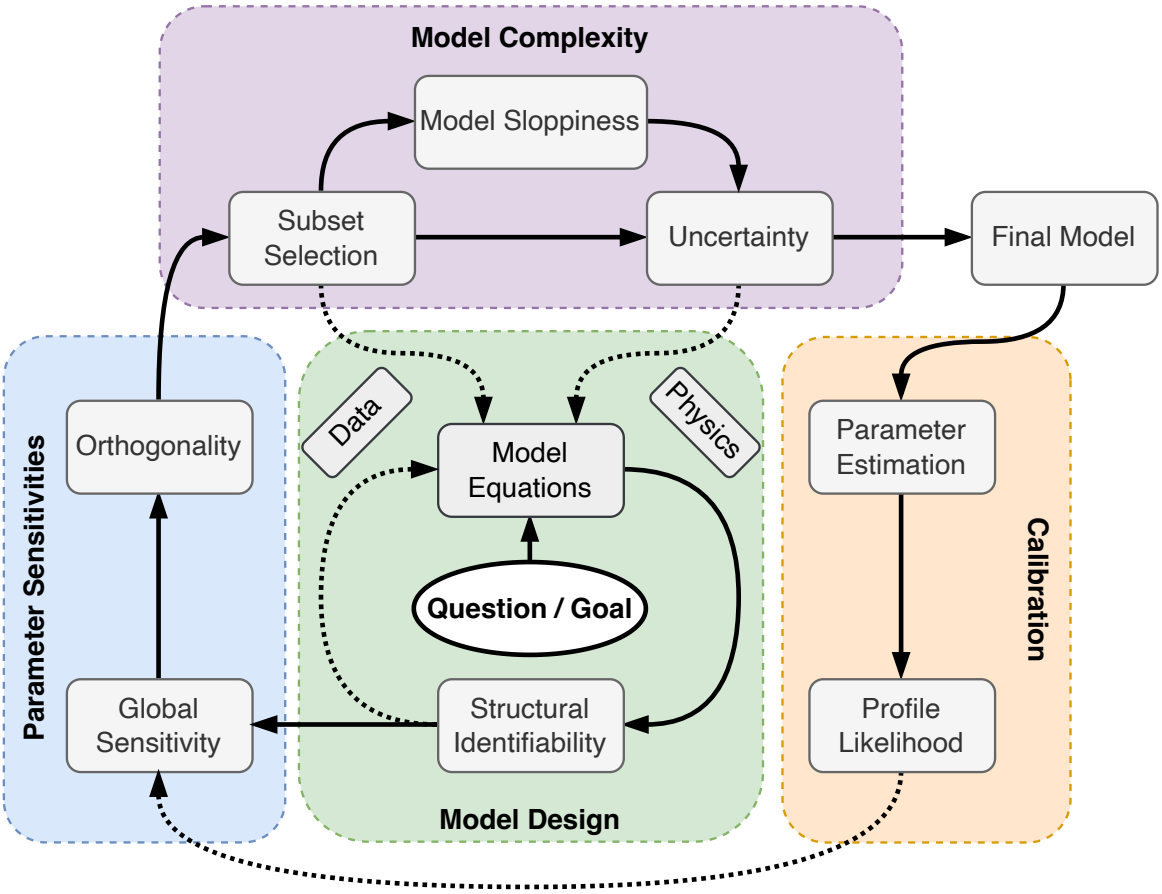

Fig. 9.1 **A schematic representation of the personalisation process** : this represents the stages which a lumped parameter cardiovascular model must go through, to ensure unique personalisation.

Chapter 10

Conclusions & Future Work

Science is organised knowledge. Wisdom is organised life.
— HERBERT SPENCER, The Art of Education

10.1 Conclusions

This thesis focuses on defining best practices for the uncertainty quantification stage of the personalisation process for cardiovascular lumped parameter models. While the focus in this work has been cardiac, the techniques and best practices defined in this work can be applied to any domain in which an dynamical system is investigated. Chapters 5 - 8 progressively align with the principal aims of method refinement, parameter subset reduction and parameter identification, as initially outlined in Chapter 1 and summarised below. We have examined

1. The impact of different statistical estimators, sampling methodologies and convergence when performing a global sensitivity analysis of LPMs,

2. The impact of varying model outputs have on the personalisation process and applied the theory of model sloppiness to gain novel insights into model behaviour,

3. The stability of personalisable subsets of input parameters, to varying sensitivity methods and, on the back of this, developed a new methodology which provides insight into the non-linearity associated with a model response surface.

4. The unscented Kalman filter as a method for parameter estimation in the personalisation process.

Chapter 5 considered the intricacies of changing sampling methodologies and variance-based total order estimators, aiming to establish best practices for practical identifiability studies. Through a thorough empirical assessment of total order estimators and sampling methodologies, we gained insight into their strengths and weaknesses. We have indicated how the received wisdom of sample sizes of $k > 500$ is insufficient to ensure converged sensitivity indices. We have highlighted how the provision of sensitivity indices has to become a convergence driven investigation as in CFD to ensure the validity of parameter interpretations.

Once best practices for sensitivity indices were established in Chapter 5, Chapter 6 showed how changing model outputs can affect parameter interpretations. We performed the first sloppy analysis of a cardiovascular LPM to obtain insight into the response surface structure and have shown how input parameter identifiability is not consistent conceived when subject to varied measurement data and how it depends on the chosen experimental design. Sloppiness is present in LPMs, when the chosen experimental design contains continuous measurements. Possibly the most important conclusion from this work has been how the personalisation of a digital twin to encompass a person's complete physiological envelope necessitates invasive tests to obtain continuous measurements. Although this approach offers an increased number of identifiable parameters with potentials status as biomarkers, it comes at the expense of creating a sloppy system which in turn increases the difficulty in parameter identification. Conversely, discrete metrics may provide a simpler personalisation approach, yielding less identifiable but more targeted biomarkers, due to the absence of sloppiness in the system.

Given the improved appreciation of how the personalisation state of cardiovascular models is dependent on the outputs chosen and convergence of sensitivity indices. Chapter 7 extended the subset selection method of Li et al., [19], to encompass the global nature of the model personalisation process and revealed how a different set of globally identifiable input parameters could be obtained with different sensitivity metrics, and provided alternative perspectives. Assessing the stability of this identifiable input parameter subset, we employed various global and local measures of input parameter sensitivity, revealing how alternative sensitivity methods which map input parameter space in contrasting ways lead to subtly different identifiable input parameter subsets, which was driven mainly by the dissimilar orthogonality between input parameters. In this chapter we were also able to show that the subset selection method is robust to the initial identifiable parameter choice with the same subset of identifiable parameters being obtained each time. Finally in this chapter we have presented a novel, intuitive input parameter hyper-surface structure investigation,

utilising Sobol indices. The connection with Sobol index error evaluation provides a guide for mapping of the complexity of input parameter space, with a view to aid the inverse problem.

Chapter 8 considered how the computationally efficient, continuous sensitivity of model input parameters has led to a novel explanation for the exceptional capability of the UKF to accurately estimate input parameter values within a single cardiac cycle. With highlighting how the more sensitive parameters during each cycle are obtained more efficiently. This insight contributes to our understanding of the UKF's robustness and efficacy. Our research showcases potential clinical applications of the UKF. By utilising patient-specific measurements and employing the close to real-time UKF, it becomes feasible to monitor a patient's physiological state almost in real time. Our tool has the capacity to Help medical professionals promptly to identify the onset of a (patho)physiological condition, thus reducing the necessity for invasive procedures and ultimately improving patient care.

10.2 Future Work

The main conclusions of this work have focused around laying the theoretical foundations of the personalisation process utilising lumped parameter models. Future work should address application and development of UQ for cardiovascular and systems biology models.

10.2.1 Model Redundancy Investigation

The question of the complexity of a model needed for an investigation is still very open. Our investigations in chapter 6 showed how different model outputs can change the interpretations of model parameters coupling this with the best practices of GSA developed in chapter 5. One could utilise the concept of effective dimensions [523] and minimally disruptive curves [524]. These methods allow one to ask when does an ordinary differential equation model become overly complex, given a fixed set of output data? A cardiovascular example of this would be if one was building a LPM to assess the severity of coronary artery disease, questions surrounding the need for represented systemic, pulmonary, cerebral or venous circulation or only the coronary anatomy could be answered with these metrics. These methods allow one to provide the answer as to when does the added model complexity become ineffective in the models contribution to a fixed set of outputs.

10.2.2 Application of the uncertainty quantification framework

The personalisation framework defined in figure 9.1 defines some tentative best practices for LPM calibration. Future work should revolve around the application of this process to determine if we can obtain a clinically competent computational model. Firstly, one should investigate the stages omitted in this thesis, structural identifiability and practical identifiability. It will be interesting to see the workflow's ability to calibrate parameters to a patient data over a long period of time. Further investigations should be performed to examine the minimum time required to perform a full model personalisation to see if this could be applied routinely. Such an undertaking could have applications outside of of cardiovascular problems. In metabolic studies involving type 2 diabetic patients, it is often important to personalise a meal response in order to predict the amount of insulin needed. The uncertainty quantification workflow developed here is agnostic to application; thus investigation in other areas of systems biology may prove fruitful.

10.2.3 Graphics processing unit investigation

Graphical processing units (GPUs) are well-suited for performing single model executions with multiple different initial conditions or input parameter sets [525]. Across all aspects of the personalisation process, especially in global sensitivity analysis and parameter optimisation, multiple independent model executions are needed to quantify the variability and uncertainty present within the system. If one could leverage the computational advantages of a GPU the whole sensitivity analysis pipeline could make uncertainty quantification possible in a clinically acceptable timeline. Recently work which led to the creation of DiffEqGPU.jl has shown that multi core single node CPU model computation is 150x slower than computation on a single GPU [526]. This means that we would be able to utilise the efficient Julia solvers and the GPU hardware making the Julia lang an ideal language for model personalisation.

10.2.4 Universal differential equations

The question of model complexity may also be approached with the introduction of neural networks. Discussed in detail in the previous chapter, the application of universal differential equations would allow us to investigate to what degree our models exhibit discrepancy with clinical data. Given a some patient data, one could construct a series of tests in which models of increasing anatomical fidelity are optimised to clinical data. An error metric is then constructed between the model solutions and the clinical data, to quantify the quality of

fit. This test is then repeated however a neural network is added to the models previously invested and the error metric score is compared between the two scenarios. My conjecture is that one would observe that the simpler physiology model with the additional neural network would return a smaller error metric, compared to unguided high fidelity models.

References

[1] Cmglee. Circulatory system smil, 2024. This work is licensed under the Creative Commons Attribution 4.0 International License. To view a copy of this license, visit http://creativecommons.org/licenses/by/4.0/.

[2] Wapcaplet, Yaddah. Diagram of the human heart, 2024. This work is licensed under the Creative Commons Attribution 4.0 International License. To view a copy of this license, visit http://creativecommons.org/licenses/by/4.0/.

[3] Mikael Häggström, M.D. Coronary arteries, 2021. This work is licensed under the Creative Commons Attribution 4.0 International License. To view a copy of this license, visit http://creativecommons.org/licenses/by/4.0/.

[4] Abraham Noordergraaf. *Circulatory system dynamics*, volume 1. Elsevier, 2012.

[5] Walter F Boron and Emile L Boulpaep. *Medical physiology E-book*. Elsevier Health Sciences, 2016.

[6] Zachary P. Christensen. Cardiac cycle (pressure volume loop), 2018. This work is licensed under the Creative Commons Attribution 3.0 International License. To view a copy of this license, visit http://creativecommons.org/licenses/by/3.0/.

[7] Steven A Niederer, Joost Lumens, and Natalia A Trayanova. Computational models in cardiology. *Nature reviews cardiology*, 16(2):100–111, 2019.

[8] Frans N Van de Vosse and Nikos Stergiopulos. Pulse wave propagation in the arterial tree. *Annual Review of Fluid Mechanics*, 43:467–499, 2011.

[9] Paul D Morris, Andrew Narracott, Hendrik von Tengg-Kobligk, Daniel Alejandro Silva Soto, Sarah Hsiao, Angela Lungu, Paul Evans, Neil W Bressloff, Patricia V Lawford, D Rodney Hose, et al. Computational fluid dynamics modelling in cardiovascular medicine. *Heart*, 102(1):18–28, 2016.

[10] Lucas O Müller, Fredrik E Fossan, Anders T Bråten, Arve Jørgensen, Rune Wiseth, and Leif R Hellevik. Impact of baseline coronary flow and its distribution on fractional flow reserve prediction. *International journal for numerical methods in biomedical engineering*, 37(11):e3246, 2021.

[11] Nico Westerhof, Jan-Willem Lankhaar, and Berend E Westerhof. The arterial windkessel. *Medical & biological engineering & computing*, 47(2):131–141, 2009.

[12] Attonio. Lumpedparametercardiovascularmodel, 2024. This work is licensed under the Creative Commons Attribution 4.0 International License. To view a copy of this license, visit http://creativecommons.org/licenses/by/4.0/.

[13] Daniel P Loucks and Eelco Van Beek. *Water resource systems planning and management: An introduction to methods, models, and applications*. Springer, 2017.

[14] Sanjay Pant, Chiara Corsini, Catriona Baker, Tain-Yen Hsia, Giancarlo Pennati, Irene E Vignon-Clementel, Modeling of Congenital Hearts Alliance (MOCHA) Investigators, et al. Data assimilation and modelling of patient-specific single-ventricle physiology with and without valve regurgitation. *Journal of biomechanics*, 49(11):2162–2173, 2016.

[15] André I Khuri and Siuli Mukhopadhyay. Response surface methodology. *Wiley interdisciplinary reviews: Computational statistics*, 2(2):128–149, 2010.

[16] Andrea Saltelli and Paola Annoni. How to avoid a perfunctory sensitivity analysis. *Environmental Modelling & Software*, 25(12):1508–1517, 2010.

[17] Franz-Georg Wieland, Adrian L Hauber, Marcus Rosenblatt, Christian Tönsing, and Jens Timmer. On structural and practical identifiability. *Current Opinion in Systems Biology*, 25:60–69, 2021.

[18] Andrew White, Malachi Tolman, Howard D Thames, Hubert Rodney Withers, Kathy A Mason, and Mark K Transtrum. The limitations of model-based experimental design and parameter estimation in sloppy systems. *PLoS computational biology*, 12(12):e1005227, 2016.

[19] Rujun Li, Michael A Henson, and Michael J Kurtz. Selection of model parameters for off-line parameter estimation. *IEEE Transactions on control systems technology*, 12(3):402–412, 2004.

[20] Patrick Segers, Nikos Stergiopulos, and Nico Westerhof. Quantification of the contribution of cardiac and arterial remodeling to hypertension. *Hypertension*, 36(5):760–765, 2000.

[21] Sanjay Pant, Chiara Corsini, Catriona Baker, Tain-Yen Hsia, Giancarlo Pennati, and Irene E Vignon-Clementel. Inverse problems in reduced order models of cardiovascular haemodynamics: aspects of data assimilation and heart rate variability. *Journal of The Royal Society Interface*, 14(126):20160513, 2017.

[22] Daniel Canuto, Joe L Pantoja, Joyce Han, Erik P Dutson, and Jeff D Eldredge. An ensemble kalman filter approach to parameter estimation for patient-specific cardiovascular flow modeling. *Theoretical and Computational Fluid Dynamics*, 34:521–544, 2020.

[23] Kirma Sembulingam and Prema Sembulingam. *Essentials of medical physiology*. JP Medical Ltd, 2012.

[24] Arnold M Katz. *Physiology of the Heart*. Lippincott Williams & Wilkins, 2010.

[25] Thomas Eschenhagen, Alexandra Eder, Ingra Vollert, and Arne Hansen. Physiological aspects of cardiac tissue engineering. *American Journal of Physiology-Heart and Circulatory Physiology*, 303(2):H133–H143, 2012.

[26] Heinrich R Schelbert. Anatomy and physiology of coronary blood flow. *Journal of nuclear cardiology*, 17(4):545–554, 2010.

[27] Michael Michail and Adam J Brown. Physiology of the normal heart. *Medicine*, 46(8):427–430, 2018.

[28] Annemarieke de Vlaming, Kimberly Sauls, Zoltan Hajdu, Richard P Visconti, Agnes Nagy Mehesz, Robert A Levine, Susan A Slaugenhaupt, Albert Hagège, Adrian H Chester, Roger R Markwald, et al. Atrioventricular valve development: new perspectives on an old theme. *Differentiation*, 84(1):103–116, 2012.

[29] Barry J Maron and Grover M Hutchins. The development of the semilunar valves in the human heart. *The American journal of pathology*, 74(2):331, 1974.

[30] JU Hidalgo, SB Nadler, and T Bloch. The use of the electronic digital computer to determine best fit of blood volume formulas. *Journal of Nuclear Medicine*, 3(2):94–99, 1962.

[31] Samuel B Nadler, John U Hidalgo, and Ted Bloch. Prediction of blood volume in normal human adults. *Surgery*, 51(2):224–232, 1962.

[32] Delafield Du Bois and Eugene F Du Bois. Clinical calorimetry: tenth paper a formula to estimate the approximate surface area if height and weight be known. *Archives of internal medicine*, 17(6_2):863–871, 1916.

[33] Richard F Burton. Estimating body surface area from mass and height: theory and the formula of du bois and du bois. *Annals of human biology*, 35(2):170–184, 2008.

[34] Marat Fudim, David M Kaye, Barry A Borlaug, Sanjiv J Shah, Stuart Rich, Navin K Kapur, Maria Rosa Costanzo, Michael I Brener, Kenji Sunagawa, and Daniel Burkhoff. Venous tone and stressed blood volume in heart failure: Jacc review topic of the week. *Journal of the American College of Cardiology*, 79(18):1858–1869, 2022.

[35] J E W Beneken and B DeWit. A physical approach to hemodynamic aspects of the human cardiovascular system. In A Guyton and E Reeve, editors, *Physical Bases of Circulatory Transport: Regulation and Exchange*, pages 1–45. Saunders, Philadelphia, PA, 1966.

[36] Philip I Aaronson, Jeremy PT Ward, and Michelle J Connolly. *The cardiovascular system at a glance*. John Wiley & Sons, 2020.

[37] Elisabete Pinto. Blood pressure and ageing. *Postgraduate medical journal*, 83(976):109–114, 2007.

[38] Carl John Wiggers. *Modern aspects of the circulation in health and disease*. Lea & Febiger, 1923.

[39] Sudeh Cheraghi-Sohi, Fiona Holland, Hardeep Singh, Avril Danczak, Aneez Esmail, Rebecca Lauren Morris, Nicola Small, Richard Williams, Carl de Wet, Stephen M Campbell, et al. Incidence, origins and avoidable harm of missed opportunities in diagnosis: longitudinal patient record review in 21 english general practices. *BMJ Quality & Safety*, 30(12):977–985, 2021.

[40] Hardeep Singh, Traber Davis Giardina, Ashley ND Meyer, Samuel N Forjuoh, Michael D Reis, and Eric J Thomas. Types and origins of diagnostic errors in primary care settings. *JAMA internal medicine*, 173(6):418–425, 2013.

[41] Camille Lakhlifi, François-Xavier Lejeune, Marion Rouault, Mehdi Khamassi, and Benjamin Rohaut. Illusion of knowledge in statistics among clinicians: evaluating the alignment between objective accuracy and subjective confidence, an online survey. *Cognitive Research: Principles and Implications*, 8(1):23, 2023.

[42] H Llewelyn, HA Ang, K Lewis, and A Al-Abdullah. The diagnostic process. *Oxford Handbook of Clinical Diagnosis*, 2014.

[43] Maria Victoria Schneider. Defining systems biology: a brief overview of the term and field. *In silico systems biology*, pages 1–11, 2013.

[44] Daniela Fliegner, Christoph Gerdes, Jörg Meding, and Johannes-Peter Stasch. Translational in vivo models for cardiovascular diseases. *New Approaches to Drug Discovery*, pages 223–234, 2016.

[45] Jordi Alastruey, Kim H Parker, Spencer J Sherwin, et al. Arterial pulse wave haemodynamics. In *11th international conference on pressure surges*, volume 30, pages 401–443. Virtual PiE Led t/a BHR Group Lisbon, Portugal, 2012.

[46] Natalia A Trayanova. Whole-heart modeling: applications to cardiac electrophysiology and electromechanics. *Circulation research*, 108(1):113–128, 2011.

[47] Lucas O Müller and Eleuterio F Toro. A global multiscale mathematical model for the human circulation with emphasis on the venous system. *International journal for numerical methods in biomedical engineering*, 30(7):681–725, 2014.

[48] Yubing Shi, Theodosios Korakianitis, and Christopher Bowles. Numerical simulation of cardiovascular dynamics with different types of vad assistance. *Journal of biomechanics*, 40(13):2919–2933, 2007.

[49] Stefano Romagnoli, Zaccaria Ricci, Diego Quattrone, Lorenzo Tofani, Omar Tujjar, Gianluca Villa, Salvatore M Romano, and A Raffaele De Gaudio. Accuracy of invasive arterial pressure monitoring in cardiovascular patients: an observational study. *Critical care*, 18:1–11, 2014.

[50] Ross McFarlane and Irina V Biktasheva. High performance computing for the simulation of cardiac electrophysiology. In *2008 The Third International Conference on Software Engineering Advances*, pages 13–18. IEEE, 2008.

[51] Shinya Goto, Darren K McGuire, and Shinichi Goto. The future role of high-performance computing in cardiovascular medicine and science-impact of multi-dimensional data analysis. *Journal of atherosclerosis and thrombosis*, 29(5):559–562, 2022.

[52] Lev Davidovich Landau and Evgenii Mikhailovich Lifshitz. *Fluid mechanics: Landau And Lifshitz: course of theoretical physics, Volume 6*, volume 6. Elsevier, 2013.

[53] Alfio Quarteroni, Andrea Manzoni, Christian Vergara, et al. *Mathematical modelling of the human cardiovascular system: data, numerical approximation, clinical applications*, volume 33. Cambridge University Press, 2019.

[54] Avner Friedman. *Mathematical biology*, volume 127. American Mathematical Soc., 2018.

[55] Leah Edelstein-Keshet. *Mathematical models in biology*. SIAM, 2005.

[56] Nitesh Kumar, Shiva Kumar, and Gowrava Shenoy B. Advances in the application of computational fluid dynamics in cardiovascular flow. *Cogent Engineering*, 10(1):2178367, 2023.

[57] Lucian Mihai Itu, Puneet Sharma, and Constantin Suciu. *Patient-specific hemodynamic computations: application to personalized diagnosis of cardiovascular pathologies*. Springer, 2017.

[58] Steven A Niederer and Nic P Smith. Using physiologically based models for clinical translation: predictive modelling, data interpretation or something in-between? *The Journal of physiology*, 594(23):6849–6863, 2016.

[59] Julie K Shade, Adityo Prakosa, Dan M Popescu, Rebecca Yu, David R Okada, Jonathan Chrispin, and Natalia A Trayanova. Predicting risk of sudden cardiac death in patients with cardiac sarcoidosis using multimodality imaging and personalized heart modeling in a multivariable classifier. *Science Advances*, 7(31):eabi8020, 2021.

[60] Nic Smith, Adelaide de Vecchi, Matthew McCormick, David Nordsletten, Oscar Camara, Alejandro F Frangi, Hervé Delingette, Maxime Sermesant, Jatin Relan, Nicholas Ayache, et al. euheart: personalized and integrated cardiac care using patient-specific cardiovascular modelling. *Interface focus*, 1(3):349–364, 2011.

[61] Jordi Heijman, Henry Sutanto, Harry JGM Crijns, Stanley Nattel, and Natalia A Trayanova. Computational models of atrial fibrillation: Achievements, challenges, and perspectives for improving clinical care. *Cardiovascular Research*, 117(7):1682–1699, 2021.

[62] Gary R Mirams, Steven A Niederer, and Richard H Clayton. The fickle heart: uncertainty quantification in cardiac and cardiovascular modelling and simulation, 2020.

[63] John B West. Ibn al-nafis, the pulmonary circulation, and the islamic golden age. *Journal of Applied Physiology*, 105(6):1877–1880, 2008.

[64] Henry S Badeer. Hemodynamics for medical students. *Advances in physiology education*, 25(1):44–52, 2001.

[65] Leonhard Euler. Principia pro motu sanguinis per arterias determinando. *Opera postuma*, pages 814–823, 1862.

[66] Thomas Young. Xiii. hydraulic investigations, subservient to an intended croonian lecture on the motion of the blood. *Philosophical Transactions of the Royal society of London*, pages 164–186, 1808.

[67] Ed Hagenbach. Ueber die bestimmung der zähigkeit einer flüssigkeit durch den ausfluss aus röhren. *Annalen der Physik*, 185(3):385–426, 1860.

[68] JC Stettler, P Niederer, M Anliker, and M Casty. Theoretical analysis of arterial hemodynamics including the influence of bifurcations: Part ii: Critical evaluation of theoretical model and comparison with noninvasive measurements of flow patterns in normal and pathological cases. *Annals of biomedical engineering*, 9:165–175, 1981.

[69] Ernst Heinrich Weber and Wilhelm Eduard Weber. *Wellenlehre auf Experimente gegründet oder über die Wellen tropfbarer Flüssigkeiten mit Anwendung auf die Schall-und Lichtwellen*. Fleischer, 1825.

[70] Wilhelm Weber. Theorie der durch wasser oder andere inkompressibele flüssigkeiten in elastischen röhren fortgepflanzten wellen. *Wilhelm Weber's Werke: Erster Band: Akustik Mechanik Optik und Wärmelehre*, pages 548–552, 1892.

[71] Otto Frank. Grundform des pulses. *Z Biol*, 37:483–526, 1899.

[72] Konrad Witzig. *Uber erzwungene Wellenbewegungen zaher, inkompressibler Flussigkeiten in elastischen Rohren*. PhD thesis, Universitat Bern, 1914.

[73] JR Womersley. Mathematical theory of oscillating flow in an elastic tube. *The Journal of physiology*, 127(2):37–8P, 1955.

[74] John R Womersley. *An elastic tube theory of pulse transmission and oscillatory flow in mammalian arteries*. Wright Air Development Center, 1957.

[75] SC Ling and HB Atabek. A nonlinear analysis of pulsatile flow in arteries. *Journal of Fluid Mechanics*, 55(3):493–511, 1972.

[76] Robert R Schaller. Moore's law: past, present and future. *IEEE spectrum*, 34(6):52–59, 1997.

[77] Matthew Hirschhorn, Vakhtang Tchantchaleishvili, Randy Stevens, Joseph Rossano, and Amy Throckmorton. Fluid–structure interaction modeling in cardiovascular medicine–a systematic review 2017–2019. *Medical engineering & physics*, 78:1–13, 2020.

[78] Liuyang Feng, Hao Gao, and Xiaoyu Luo. Whole-heart modelling with valves in a fluid–structure interaction framework. *Computer Methods in Applied Mechanics and Engineering*, 420:116724, 2024.

[79] Alberto Zingaro, Michele Bucelli, Roberto Piersanti, Francesco Regazzoni, Alfio Quarteroni, et al. An electromechanics-driven fluid dynamics model for the simulation of the whole human heart. *Journal of Computational Physics*, page 112885, 2024.

[80] Sara Calandrini and Eugenio Aulisa. Fluid-structure interaction simulations of venous valves: A monolithic ale method for large structural displacements. *International journal for numerical methods in biomedical engineering*, 35(2):e3156, 2019.

[81] Tsuyoshi Ohashi, Hao Liu, and Takami Yamaguchi. Computational fluid dynamic simulation of the flow through venous valve. *Clinical application of computational mechanics to the cardiovascular system*, pages 186–189, 2000.

[82] Daniel J Taylor, Jeroen Feher, Krzysztof Czechowicz, Ian Halliday, DR Hose, Rebecca Gosling, Louise Aubiniere-Robb, Marcel van't Veer, Danielle CJ Keulards, Pim Tonino, et al. Validation of a novel numerical model to predict regionalized blood flow in the coronary arteries. *European Heart Journal-Digital Health*, 4(2):81–89, 2023.

[83] Zhonghua Sun and Lei Xu. Computational fluid dynamics in coronary artery disease. *Computerized medical imaging and graphics*, 38(8):651–663, 2014.

[84] Marcelo A Castro, Christopher M Putman, and Juan R Cebral. Patient-specific computational modeling of cerebral aneurysms with multiple avenues of flow from 3d rotational angiography images. *Academic radiology*, 13(7):811–821, 2006.

[85] Luca Antiga, Bogdan Ene-Iordache, and Andrea Remuzzi. Computational geometry for patient-specific reconstruction and meshing of blood vessels from mr and ct angiography. *IEEE transactions on medical imaging*, 22(5):674–684, 2003.

[86] Wen-Yih Isaac Tseng, Mao-Yuan Marine Su, and Yao-Hui Elton Tseng. Introduction to cardiovascular magnetic resonance: technical principles and clinical applications. *Acta Cardiologica Sinica*, 32(2):129, 2016.

[87] Alessia Lucca, Luigi Fraccarollo, Fredrik E Fossan, Anders T Bråten, Silvia Pozzi, Christian Vergara, and Lucas O Müller. Impact of pressure guidewire on model-based ffr prediction. *Cardiovascular Engineering and Technology*, pages 1–13, 2024.

[88] Yu Zhu, Saeed Mirsadraee, Ulrich Rosendahl, John Pepper, and Xiao Yun Xu. Fluid-structure interaction simulations of repaired type a aortic dissection: a comprehensive comparison with rigid wall models. *Frontiers in Physiology*, 13:913457, 2022.

[89] Shohei Miyazaki, Keiichi Itatani, Toyoki Furusawa, Teruyasu Nishino, Masataka Sugiyama, Yasuo Takehara, and Satoshi Yasukochi. Validation of numerical simulation methods in aortic arch using 4d flow mri. *Heart and vessels*, 32:1032–1044, 2017.

[90] DB Camasão and DJMTB Mantovani. The mechanical characterization of blood vessels and their substitutes in the continuous quest for physiological-relevant performances. a critical review. *Materials Today Bio*, 10:100106, 2021.

[91] Daniel Jodko, Mateusz Jeckowski, and Zbigniew Tyfa. Fluid structure interaction versus rigid-wall approach in the study of the symptomatic stenosed carotid artery: Importance of wall compliance and resilience of loose connective tissue. *International Journal for Numerical Methods in Biomedical Engineering*, 38(8):e3630, 2022.

[92] Malenka M Bissell, Francesca Raimondi, Lamia Ait Ali, Bradley D Allen, Alex J Barker, Ann Bolger, Nicholas Burris, Carl-Johan Carhäll, Jeremy D Collins, Tino Ebbers, et al. 4d flow cardiovascular magnetic resonance consensus statement: 2023 update. *Journal of Cardiovascular Magnetic Resonance*, 25(1):40, 2023.

[93] Noriko Oyama-Manabe, Tadao Aikawa, Satonori Tsuneta, and Osamu Manabe. Clinical applications of 4d flow mr imaging in aortic valvular and congenital heart disease. *Magnetic Resonance in Medical Sciences*, 21(2):319–326, 2022.

[94] Tânia Pereira, Carlos Correia, and Joao Cardoso. Novel methods for pulse wave velocity measurement. *Journal of medical and biological engineering*, 35(5):555–565, 2015.

[95] Paul D Morris, Frans N van de Vosse, Patricia V Lawford, D Rodney Hose, and Julian P Gunn. "virtual"(computed) fractional flow reserve: current challenges and limitations. *JACC: Cardiovascular Interventions*, 8(8):1009–1017, 2015.

[96] Writing Committee Members, Martha Gulati, Phillip D Levy, Debabrata Mukherjee, Ezra Amsterdam, Deepak L Bhatt, Kim K Birtcher, Ron Blankstein, Jack Boyd, Renee P Bullock-Palmer, et al. 2021 aha/acc/ase/chest/saem/scct/scmr guideline for the evaluation and diagnosis of chest pain: a report of the american college of cardiology/american heart association joint committee on clinical practice guidelines. *Journal of the American College of Cardiology*, 78(22):e187–e285, 2021.

[97] Franz-Josef Neumann, Miguel Sousa-Uva, Anders Ahlsson, Fernando Alfonso, Adrian P Banning, Umberto Benedetto, Robert A Byrne, Jean-Philippe Collet, Volkmar Falk, Stuart J Head, et al. 2018 esc/eacts guidelines on myocardial revascularization. *European heart journal*, 40(2):87–165, 2019.

[98] MM Dupin, I Halliday, CM Care, and LL Munn. Lattice boltzmann modelling of blood cell dynamics. *International Journal of Computational Fluid Dynamics*, 22(7):481–492, 2008.

[99] James Spendlove, Xu Xu, Oliver J Halliday, Torsten Schenkel, and Ian Halliday. Chromodynamic multirelaxation-time lattice boltzmann scheme for fluids with density difference. *Physical Review E*, 102(1):013309, 2020.

[100] James Spendlove, Xu Xu, Torsten Schenkel, Michael Seaton, and Ian Halliday. Chromodynamic multi-component lattice boltzmann equation scheme for axial symmetry. *Journal of Physics A: Mathematical and Theoretical*, 53(14):145001, 2020.

[101] Michael M Dupin, Ian Halliday, Chris M Care, Lyuba Alboul, and Lance L Munn. Modeling the flow of dense suspensions of deformable particles in three dimensions. *Physical Review E—Statistical, Nonlinear, and Soft Matter Physics*, 75(6):066707, 2007.

[102] Xu Xu, Kallum Burgin, Meredith A Ellis, and Ian Halliday. Benchmarking of three-dimensional multicomponent lattice boltzmann equation. *Physical Review E*, 96(5):053308, 2017.

[103] James Spendlove, Xu Xu, Torsten Schenkel, JP Gunn, and Ian Halliday. Chromodynamic lattice boltzmann method for the simulation of drops, erythrocytes, and other vesicles. *Communications in computational physics*, 33(1):283–309, 2023.

[104] James Spendlove, Xu Xu, Torsten Schenkel, MA Seaton, Ian Halliday, and JP Gunn. Three-dimensional single framework multicomponent lattice boltzmann equation method for vesicle hydrodynamics. *Physics of Fluids*, 33(7), 2021.

[105] Giuseppe Pontrelli, Ian Halliday, Simone Melchionna, Tim J Spencer, and Sauro Succi. Lattice boltzmann method as a computational framework for multiscale haemodynamics. *Mathematical and Computer Modelling of Dynamical Systems*, 20(5):470–490, 2014.

[106] Kallum Burgin, James Spendlove, Xu Xu, and Ian Halliday. Kinematics of chromodynamic multicomponent lattice boltzmann simulation with a large density contrast. *Physical Review E*, 100(4):043310, 2019.

[107] Ian Halliday, Xu Xu, and Kallum Burgin. Shear viscosity of a two-dimensional emulsion of drops using a multiple-relaxation-time-step lattice boltzmann method. *Physical Review E*, 95(2):023301, 2017.

[108] Ian Halliday, SV Lishchuk, TJ Spencer, G Pontrelli, and CM Care. Multiple-component lattice boltzmann equation for fluid-filled vesicles in flow. *Physical Review E—Statistical, Nonlinear, and Soft Matter Physics*, 87(2):023307, 2013.

[109] Giuseppe Pontrelli, Carola S König, Ian Halliday, Timothy J Spencer, Michael W Collins, Quan Long, and Sauro Succi. Modelling wall shear stress in small arteries using the lattice boltzmann method: influence of the endothelial wall profile. *Medical engineering & physics*, 33(7):832–839, 2011.

[110] Maarten Heusinkveld, Koen Reesink, Theo Arts, Wouter Huberts, and Tammo Delhaas. P125: Use of vascular adaptation in response to mechanical loading facilitates personalisation of a one-dimensional pulse wave propagation model. *Artery Research*, 20(1):79–80, 2017.

[111] JMT Keijsers, CAD Leguy, Wouter Huberts, AJ Narracott, J Rittweger, and FN Van de Vosse. A 1d pulse wave propagation model of the hemodynamics of calf muscle pump function. *International journal for numerical methods in biomedical engineering*, 31(7):e02714, 2015.

[112] Reference Values for Arterial Stiffness' Collaboration. Determinants of pulse wave velocity in healthy people and in the presence of cardiovascular risk factors:'establishing normal and reference values'. *European heart journal*, 31(19):2338–2350, 2010.

[113] John W Lambert. On the nonlinearities of fluid flow in nonrigid tubes. *Journal of the Franklin Institute*, 266(2):83–102, 1958.

[114] ACL Barnard, WA Hunt, WP Timlake, and E Varley. A theory of fluid flow in compliant tubes. *Biophysical journal*, 6(6):717–724, 1966.

[115] Thomas JR Hughes and J Lubliner. On the one-dimensional theory of blood flow in the larger vessels. *Mathematical Biosciences*, 18(1-2):161–170, 1973.

[116] Annemette Sofie Olufsen. *Modeling the arterial system with reference to an anesthesia simulator*. PhD thesis, Roskilde Universitet, 1998.

[117] Zheng Duanmu, Weiwei Chen, Hao Gao, Xilan Yang, Xiaoyu Luo, and Nicholas A Hill. A one-dimensional hemodynamic model of the coronary arterial tree. *Frontiers in Physiology*, 10:853, 2019.

[118] Marvin Fritz, Tobias Köppl, John Tinsley Oden, Andreas Wagner, Barbara Wohlmuth, and Chengyue Wu. A 1d–0d–3d coupled model for simulating blood flow and transport processes in breast tissue. *International Journal for Numerical Methods in Biomedical Engineering*, 38(7):e3612, 2022.

[119] Daniel J Taylor, Harry Saxton, Ian Halliday, Tom Newman, Jeroen Feher, Rebecca Gosling, Andrew J Narracott, Denise van Kemenade, Marcel van't Veer, Pim AL Tonino, et al. Evaluation of models of sequestration flow in coronary arteries—physiology versus anatomy? *Computers in Biology and Medicine*, 173:108299, 2024.

[120] C Zervides and AD Giannoukas. Computational phlebology: reviewing computer models of the venous system. *Phlebology*, 28(4):209–218, 2013.

[121] Etienne Boileau, Perumal Nithiarasu, Pablo J Blanco, Lucas O Müller, Fredrik Eikeland Fossan, Leif Rune Hellevik, Wouter P Donders, Wouter Huberts, Marie Willemet, and Jordi Alastruey. A benchmark study of numerical schemes for one-dimensional arterial blood flow modelling. *International journal for numerical methods in biomedical engineering*, 31(10):e02732, 2015.

[122] Alberto Coccarelli, Jason M Carson, Ankush Aggarwal, and Sanjay Pant. A framework for incorporating 3d hyperelastic vascular wall models in 1d blood flow simulations. *Biomechanics and Modeling in Mechanobiology*, 20:1231–1249, 2021.

[123] Nan Xiao, Jordi Alastruey, and C Alberto Figueroa. A systematic comparison between 1-d and 3-d hemodynamics in compliant arterial models. *International journal for numerical methods in biomedical engineering*, 30(2):204–231, 2014.

[124] Jay Aodh Mackenzie. *A 1D model for the pulmonary and coronary circulation accounting for time-varying external pressure*. PhD thesis, University of Glasgow, 2021.

[125] L Mihaela Paun and Dirk Husmeier. Markov chain monte carlo with gaussian processes for fast parameter estimation and uncertainty quantification in a 1d fluid-dynamics model of the pulmonary circulation. *International journal for numerical methods in biomedical engineering*, 37(2):e3421, 2021.

[126] Federica Caforio, Christoph M Augustin, Jordi Alastruey, Matthias AF Gsell, and Gernot Plank. A coupling strategy for a first 3d-1d model of the cardiovascular system to study the effects of pulse wave propagation on cardiac function. *Computational Mechanics*, 70(4):703–722, 2022.

[127] Tobias Köppl, Ettore Vidotto, and Barbara Wohlmuth. A 3d-1d coupled blood flow and oxygen transport model to generate microvascular networks. *International journal for numerical methods in biomedical engineering*, 36(10):e3386, 2020.

[128] Pablo J Blanco, MR Pivello, SA Urquiza, and RA Feijóo. On the potentialities of 3d–1d coupled models in hemodynamics simulations. *Journal of biomechanics*, 42(7):919–930, 2009.

[129] Alessandro Melis, Richard H Clayton, and Alberto Marzo. Bayesian sensitivity analysis of a 1d vascular model with gaussian process emulators. *International Journal for Numerical Methods in Biomedical Engineering*, 33(12):e2882, 2017.

[130] Leif Rune Hellevik, Jan Vierendeels, T Kiserud, N Stergiopulos, F Irgens, Erik Dick, K Riemslagh, and Pascal Verdonck. An assessment of ductus venosus tapering and wave transmission from the fetal heart. *Biomechanics and modeling in mechanobiology*, 8:509–517, 2009.

[131] Jonathan P Mynard, Daniel J Penny, and Joseph J Smolich. Scalability and in vivo validation of a multiscale numerical model of the left coronary circulation. *American Journal of Physiology-Heart and Circulatory Physiology*, 306(4):H517–H528, 2014.

[132] Philippe Reymond, Fabrice Merenda, Fabienne Perren, Daniel Rufenacht, and Nikos Stergiopulos. Validation of a one-dimensional model of the systemic arterial tree. *American Journal of Physiology-Heart and Circulatory Physiology*, 297(1):H208–H222, 2009.

[133] Aimee M Torres Rojas and Sylvie Lorente. 1d-model of the human liver circulatory system. *Computer Methods and Programs in Biomedicine*, 238:107612, 2023.

[134] Lucas O Müller, Pablo J Blanco, Sansuke M Watanabe, and Raúl A Feijóo. A high-order local time stepping finite volume solver for one-dimensional blood flow simulations: application to the adan model. *International Journal for Numerical Methods in Biomedical Engineering*, 32(10):e02761, 2016.

[135] Mário Sansuke Maranhão Watanabe. Adan: um modelo anatomicamente detalhado da rede arterial humana para hemodinâmica computacional, 2013.

[136] Pablo Javier Blanco, Carlos Alberto Bulant, Lucas O Müller, GD Maso Talou, C Guedes Bezerra, Pedro A Lemos, and Raúl Antonino Feijóo. Comparison of 1d and 3d models for the estimation of fractional flow reserve. *Scientific reports*, 8(1):17275, 2018.

[137] G Landes. Einige untersuchungen an elektrischen analogieschaltungen zum kreitslaufsystem. *Z Biol*, 101:418–429, 1943.

[138] R Burattini and G Gnudi. Computer identification of models for the arterial tree input impedance: comparison between two new simple models and first experimental results. *Medical and Biological Engineering and Computing*, 20(2):134–144, 1982.

[139] Patrick Segers, ER Rietzschel, ML De Buyzere, N Stergiopulos, N Westerhof, LM Van Bortel, Thierry Gillebert, and PR Verdonck. Three-and four-element windkessel models: assessment of their fitting performance in a large cohort of healthy middle-aged individuals. *Proceedings of the Institution of Mechanical Engineers, Part H: Journal of Engineering in Medicine*, 222(4):417–428, 2008.

[140] Massimo Capoccia. Development and characterization of the arterial w indkessel and its role during left ventricular assist device assistance. *Artificial organs*, 39(8):E138–E153, 2015.

[141] Luca Formaggia and Alessandro Veneziani. Reduced and multiscale models for the human cardiovascular system. *Lecture notes VKI lecture series*, 7, 2003.

[142] Vuk Milišić and Alfio Quarteroni. Analysis of lumped parameter models for blood flow simulations and their relation with 1d models. *ESAIM: Mathematical modelling and numerical analysis*, 38(4):613–632, 2004.

[143] RAFAEL Beyar, MARK J Hausknecht, HENRY R Halperin, FC Yin, and MYRON L Weisfeldt. Interaction between cardiac chambers and thoracic pressure in intact circulation. *American Journal of Physiology-Heart and Circulatory Physiology*, 253(5):H1240–H1252, 1987.

[144] SV Frolov, SV Sindeev, VA Lischouk, D Sh Gazizova, D Liepsch, and A Balasso. A lumped parameter model of cardiovascular system with pulsating heart for diagnostic studies. *Journal of Mechanics in Medicine and Biology*, 17(03):1750056, 2017.

[145] Ketan Naik and PH Bhathawala. Mathematical modeling of human cardiovascular system: A lumped parameter approach and simulation. *International Journal of Mathematical, Computational, Physical, Electrical and Computer Engineering*, 11(2):72–84, 2017.

[146] Yubing Shi and Theodosios Korakianitis. Impeller-pump model derived from conservation laws applied to the simulation of the cardiovascular system coupled to heart-assist pumps. *Computers in Biology and Medicine*, 93:127–138, 2018.

[147] SE Leefe and CR Gentle. A review of the in vitro evaluation of conduitmounted cardiac valve prostheses. *Medical engineering & physics*, 17(7):497–506, 1995.

[148] Hiroyuki Suga and Kiichi Sagawa. Instantaneous pressure-volume relationships and their ratio in the excised, supported canine left ventricle. *Circulation research*, 35(1):117–126, 1974.

[149] R Peter Hoskins, V Patricia Lawford, and J Barry Doyle. *Cardiovascular biomechanics*. Springer, 2017.

[150] Kristy Peterson, Edwin T Ozawa, George M Pantalos, and M Keith Sharp. Numerical simulation of the influence of gravity and posture on cardiac performance. *Annals of biomedical engineering*, 30:247–259, 2002.

[151] Yan Fu, Aike Qiao, Yao Yang, and Xiangming Fan. Numerical simulation of the effect of pulmonary vascular resistance on the hemodynamics of reoperation after failure of one and a half ventricle repair. *Frontiers in physiology*, 11:207, 2020.

[152] Martin Žáček and Egon Krause. Numerical simulation of the blood flow in the human cardiovascular system. *Journal of biomechanics*, 29(1):13–20, 1996.

[153] Jürgen Werner, Daniel Bohringer, and Martin Hexamer. Simulation and prediction of cardiotherapeutical phenomena from a pulsatile model coupled to the guyton circulatory model. *IEEE transactions on biomedical engineering*, 49(5):430–439, 2002.

[154] Peter HM Bovendeerd, Petra Borsje, Theo Arts, and Frans N van De Vosse. Dependence of intramyocardial pressure and coronary flow on ventricular loading and contractility: a model study. *Annals of biomedical engineering*, 34:1833–1845, 2006.

[155] Silvio Cavalcanti and Luigi Yuri Di Marco. Numerical simulation of the hemodynamic response to hemodialysis-induced hypovolemia. *Artificial Organs*, 23(12):1063–1073, 1999.

[156] Thomas Heldt, Jolie L Chang, George C Verghese, and Roger G Mark. Cycle-averaged models of cardiovascular dynamics. *IFAC Proceedings Volumes*, 36(15):387–392, 2003.

[157] T Heldt and YB Chernyak. Analytical solution to a minimal cardiovascular model. In *2006 Computers in Cardiology*, pages 785–788. IEEE, 2006.

[158] Kaname Sato, Koichi Takamizawa, Yosuke Ogawa, Yu Tanaka, Kazuhiro Shiraga, Hitomi Masuda, Hikoro Matsui, Ryo Inuzuka, and Hideaki Senzaki. Hemodynamic simulation of complete transposition of the great arteries for optimal treatment strategies based on its circulatory physiology. *American Journal of Physiology-Heart and Circulatory Physiology*, 2024.

[159] Ryno Laubscher, Johan van der Merwe, Jacques Liebenberg, and Philip Herbst. Dynamic simulation of aortic valve stenosis using a lumped parameter cardiovascular system model with flow regime dependent valve pressure loss characteristics. *Medical Engineering & Physics*, 106:103838, 2022.

[160] Yuxin Zhu, Wanning Ge, Tingting Wu, Liudi Zhang, and Polin Hsu. An analytic method to investigate hemodynamics of the cardiovascular system–single ventricular system. *The International Journal of Artificial Organs*, 46(12):654–669, 2023.

[161] Brian D Hoit, Yanfu Shao, Marjorie Gabel, and Richard A Walsh. In vivo assessment of left atrial contractile performance in normal and pathological conditions using a time-varying elastance model. *Circulation*, 89(4):1829–1838, 1994.

[162] Giulia Comunale, Paolo Peruzzo, Biagio Castaldi, Renato Razzolini, Giovanni Di Salvo, Massimo A Padalino, and Francesca M Susin. Understanding and recognition of the right ventricular function and dysfunction via a numerical study. *Scientific reports*, 11(1):3709, 2021.

[163] BJ Bellhouse. Fluid mechanics of a model mitral valve and left ventricle. *Cardiovascular research*, 6(2):199–210, 1972.

[164] Gary Drzewiecki, Jia-Jung Wang, JK-J Li, Joseph Kedem, and Harvey Weiss. Modeling of mechanical dysfunction in regional stunned myocardium of the left ventricle. *IEEE transactions on biomedical engineering*, 43(12):1151–1163, 1996.

[165] Tiffany Camp. Evaluation of fluid diodes as pulmonary heart valve replacements, 2009.

[166] Sabine Paeme, Katherine T Moorhead, J Geoffrey Chase, Bernard Lambermont, Philippe Kolh, Vincent D'orio, Luc Pierard, Marie Moonen, Patrizio Lancellotti, Pierre C Dauby, et al. Mathematical multi-scale model of the cardiovascular system including mitral valve dynamics. application to ischemic mitral insufficiency. *Biomedical engineering online*, 10:1–20, 2011.

[167] Michael S Sacks and Jun Liao. *Advances in heart valve biomechanics*. Springer, 2018.

[168] Yubing Shi, Tony JH Yeo, and Yong Zhao. Numerical simulation of a systemic flow test rig. *ASAIO journal*, 50(1):54–64, 2004.

[169] Theodosios Korakianitis and Yubing Shi. Numerical simulation of cardiovascular dynamics with healthy and diseased heart valves. *Journal of biomechanics*, 39(11):1964–1982, 2006.

[170] JP Mynard, MR Davidson, DJ Penny, and JJ2946553 Smolich. A simple, versatile valve model for use in lumped parameter and one-dimensional cardiovascular models. *International Journal for Numerical Methods in Biomedical Engineering*, 28(6-7):626–641, 2012.

[171] Mette S Olufsen. Structured tree outflow condition for blood flow in larger systemic arteries. *American journal of physiology-Heart and circulatory physiology*, 276(1):H257–H268, 1999.

[172] Hyun Jin Kim, IE Vignon-Clementel, JS Coogan, CA Figueroa, KE Jansen, and CA Taylor. Patient-specific modeling of blood flow and pressure in human coronary arteries. *Annals of biomedical engineering*, 38:3195–3209, 2010.

[173] Jesse W Gerringer, Julie C Wagner, Daniela Vélez-Rendón, and Daniela Valdez-Jasso. Lumped-parameter models of the pulmonary vasculature during the progression of pulmonary arterial hypertension. *Physiological reports*, 6(3):e13586, 2018.

[174] Bao Li, Wenxin Wang, Boyan Mao, and Youjun Liu. A method to personalize the lumped parameter model of coronary artery. *International Journal of Computational Methods*, 16(03):1842004, 2019.

[175] Magdalena Otta, Ian Halliday, Janice Tsui, Chung Lim, Zbigniew R Struzik, and Andrew Narracott. Sensitivity analysis of a model of lower limb haemodynamics. In *International Conference on Computational Science*, pages 65–77. Springer, 2022.

[176] Bart Spronck, Esther GHJ Martens, Erik D Gommer, and Frans N van de Vosse. A lumped parameter model of cerebral blood flow control combining cerebral autoregulation and neurovascular coupling. *American Journal of Physiology-Heart and Circulatory Physiology*, 303(9):H1143–H1153, 2012.

[177] Mauro Ursino. Interaction between carotid baroregulation and the pulsating heart: a mathematical model. *American Journal of Physiology-Heart and Circulatory Physiology*, 275(5):H1733–H1747, 1998.

[178] Giulia Comunale, Francesca M Susin, and Jonathan P Mynard. A female-specific cardiovascular lumped-parameter model. In *2020 42nd Annual International Conference of the IEEE Engineering in Medicine & Biology Society (EMBC)*, pages 2654–2657. IEEE, 2020.

[179] Bram W Smith, J Geoffrey Chase, Roger I Nokes, Geoffrey M Shaw, and Graeme Wake. Minimal haemodynamic system model including ventricular interaction and valve dynamics. *Medical engineering & physics*, 26(2):131–139, 2004.

[180] Arthur C Guyton, Thomas G Coleman, and Harris J Granger. Circulation: overall regulation. *Annual review of physiology*, 34(1):13–44, 1972.

[181] DIAO Jun-jie, JIANG Wen-tao, LI Zhong-you, WEI Jun-ru, LI Xiao, and MIN Lei. Numerical study of hemodynamics of lumped-parameter model for lower limb amputee, 2023.

[182] Carrie Hahn, Ajay Mahajan, Tsuchin Chu, and M Schoen. A lumped-parameter model to investigate the effect of plantar pressure on arterial blood flow in a diabetic foot. *Proceedings of the Institution of Mechanical Engineers, Part H: Journal of Engineering in Medicine*, 221(6):677–686, 2007.

[183] Hong Tang, Ziyin Dai, Miao Wang, Binbin Guo, Shunyu Wang, Jiabin Wen, and Ting Li. Lumped-parameter circuit platform for simulating typical cases of pulmonary hypertensions from point of hemodynamics. *Journal of cardiovascular translational research*, 13:826–852, 2020.

[184] G Fragomeni, A Merola, R Serra, S De Franciscis, and F Amato. A nonlinear lumped parameters model to analyze the dynamics of venous reflux. In *2008 30th Annual International Conference of the IEEE Engineering in Medicine and Biology Society*, pages 1407–1410. IEEE, 2008.

[185] Lorenzo Civilla, Agnese Sbrollini, Laura Burattini, Micaela Morettini, et al. An integrated lumped-parameter model of the cardiovascular system for the simulation of acute ischemic stroke: description of instantaneous changes in hemodynamics. *Mathematical Biosciences and Engineering*, 18(4):3993–4010, 2021.

[186] Mohsen Abdi, Alireza Karimi, Mahdi Navidbakhsh, Gila Pirzad Jahromi, and Kamran Hassani. A lumped parameter mathematical model to analyze the effects of tachycardia and bradycardia on the cardiovascular system. *International Journal of Numerical Modelling: Electronic Networks, Devices and Fields*, 28(3):346–357, 2015.

[187] Zheng Duanmu, Min Yin, Xueling Fan, Xilan Yang, and Xiaoyu Luo. A patient-specific lumped-parameter model of coronary circulation. *Scientific reports*, 8(1):874, 2018.

[188] Tijmen Koopsen, Nick Van Osta, Tim Van Loon, Frans A Van Nieuwenhoven, Frits W Prinzen, Bas R Van Klarenbosch, Feddo P Kirkels, Arco J Teske, Kevin Vernooy, Tammo Delhaas, et al. A lumped two-compartment model for simulation of ventricular pump and tissue mechanics in ischemic heart disease. *Frontiers in physiology*, 13:782592, 2022.

[189] Caterina Guiot, PG Pianta, C Cancelli, and TJ Pedley. Prediction of coronary blood flow with a numerical model based on collapsible tube dynamics. *American Journal of Physiology-Heart and Circulatory Physiology*, 258(5):H1606–H1614, 1990.

[190] Shuji Shimizu, Dai Une, Toru Kawada, Yohsuke Hayama, Atsunori Kamiya, Toshiaki Shishido, and Masaru Sugimachi. Lumped parameter model for hemodynamic simulation of congenital heart diseases. *The journal of physiological sciences*, 68:103–111, 2018.

[191] Thomas Heldt, Eun B Shim, Roger D Kamm, and Roger G Mark. Computational modeling of cardiovascular response to orthostatic stress. *Journal of applied physiology*, 92(3):1239–1254, 2002.

[192] Francesco Migliavacca, Giancarlo Pennati, Gabriele Dubini, Roberto Fumero, Riccardo Pietrabissa, Gonzalo Urcelay, Edward L Bove, Tain-Yen Hsia, and Marc R de Leval. Modeling of the norwood circulation: effects of shunt size, vascular resistances, and heart rate. *American Journal of Physiology-Heart and Circulatory Physiology*, 280(5):H2076–H2086, 2001.

[193] Roland Burns. *Advanced control engineering*. Elsevier, 2001.

[194] Sofia Guzzetti, LA Mansilla Alvarez, PJ Blanco, Kevin Thomas Carlberg, and A Veneziani. Propagating uncertainties in large-scale hemodynamics models via network uncertainty quantification and reduced-order modeling. *Computer Methods in Applied Mechanics and Engineering*, 358:112626, 2020.

[195] Pras Pathmanathan, Jonathan M Cordeiro, and Richard A Gray. Comprehensive uncertainty quantification and sensitivity analysis for cardiac action potential models. *Frontiers in physiology*, 10:436778, 2019.

[196] Andrea Saltelli, Marco Ratto, Terry Andres, Francesca Campolongo, Jessica Cariboni, Debora Gatelli, Michaela Saisana, and Stefano Tarantola. *Global sensitivity analysis: the primer*. John Wiley & Sons, 2008.

[197] Bertrand Iooss and Paul Lemaître. A review on global sensitivity analysis methods. *Uncertainty management in simulation-optimization of complex systems: algorithms and applications*, pages 101–122, 2015.

[198] Fredrik E Fossan, Jacob Sturdy, Lucas O Müller, Andreas Strand, Anders T Bråten, Arve Jørgensen, Rune Wiseth, and Leif R Hellevik. Uncertainty quantification and sensitivity analysis for computational ffr estimation in stable coronary artery disease. *Cardiovascular engineering and technology*, 9:597–622, 2018.

[199] Paul A Heidenreich, Justin G Trogdon, Olga A Khavjou, Javed Butler, Kathleen Dracup, Michael D Ezekowitz, Eric Andrew Finkelstein, Yuling Hong, S Claiborne Johnston, Amit Khera, et al. Forecasting the future of cardiovascular disease in the united states: a policy statement from the american heart association. *Circulation*, 123(8):933–944, 2011.

[200] Emelia J Benjamin, Paul Muntner, Alvaro Alonso, Marcio S Bittencourt, Clifton W Callaway, April P Carson, Alanna M Chamberlain, Alexander R Chang, Susan Cheng, Sandeep R Das, et al. Heart disease and stroke statistics—2019 update: a report from the american heart association. *Circulation*, 139(10):e56–e528, 2019.

[201] Jane A Leopold and Joseph Loscalzo. Emerging role of precision medicine in cardiovascular disease. *Circulation research*, 122(9):1302–1315, 2018.

[202] Reinhard Laubenbacher, Anna Niarakis, Tomáš Helikar, Gary An, Bruce Shapiro, Rahuman S Malik-Sheriff, TJ Sego, Adam Knapp, Paul Macklin, and James A Glazier. Building digital twins of the human immune system: toward a roadmap. *NPJ digital medicine*, 5(1):64, 2022.

[203] Eric A Stahlberg, Mohamed Abdel-Rahman, Boris Aguilar, Alireza Asadpoure, Robert A Beckman, Lynn L Borkon, Jeffrey N Bryan, Colleen M Cebulla, Young Hwan Chang, Ansu Chatterjee, et al. Exploring approaches for predictive cancer patient digital twins: Opportunities for collaboration and innovation. *Frontiers in Digital Health*, 4:1007784, 2022.

[204] Jieling Zhao, Ahmed Ghallab, Reham Hassan, Steven Dooley, Jan Georg Hengstler, and Dirk Drasdo. A liver digital twin for in silico testing of cellular and inter-cellular mechanisms in regeneration after drug-induced damage. *Iscience*, 27(2), 2024.

[205] Hui Xiong, Congying Chu, Lingzhong Fan, Ming Song, Jiaqi Zhang, Yawei Ma, Ruonan Zheng, Junyang Zhang, Zhengyi Yang, and Tianzi Jiang. The digital twin brain: A bridge between biological and artificial intelligence. *Intelligent Computing*, 2:0055, 2023.

[206] James K Min, Jonathon Leipsic, Michael J Pencina, Daniel S Berman, Bon-Kwon Koo, Carlos Van Mieghem, Andrejs Erglis, Fay Y Lin, Allison M Dunning, Patricia Apruzzese, et al. Diagnostic accuracy of fractional flow reserve from anatomic ct angiography. *Jama*, 308(12):1237–1245, 2012.

[207] Charles A Taylor, Timothy A Fonte, and James K Min. Computational fluid dynamics applied to cardiac computed tomography for noninvasive quantification of fractional flow reserve: scientific basis. *Journal of the American College of Cardiology*, 61(22):2233–2241, 2013.

[208] Angelo Auricchio and Frits W Prinzen. Enhancing response in the cardiac resynchronization therapy patient: the 3b perspective—bench, bits, and bedside. *JACC: Clinical Electrophysiology*, 3(11):1203–1219, 2017.

[209] Anneloes G Munneke, Joost Lumens, and Tammo Delhaas. Cardiovascular fetal-to-neonatal transition: an in silico model. *Pediatric Research*, 91(1):116–128, 2022.

[210] Cristobal Rodero, Marina Strocchi, Maciej Marciniak, Stefano Longobardi, John Whitaker, Mark D O'Neill, Karli Gillette, Christoph Augustin, Gernot Plank, Edward J Vigmond, et al. Linking statistical shape models and simulated function in the healthy adult human heart. *PLoS computational biology*, 17(4):e1008851, 2021.

[211] Nico HJ Pijls, Pepijn van Schaardenburgh, Ganesh Manoharan, Eric Boersma, Jan-Willem Bech, Marcel van't Veer, Frits Bär, Jan Hoorntje, Jacques Koolen, William Wijns, et al. Percutaneous coronary intervention of functionally nonsignificant stenosis: 5-year follow-up of the defer study. *Journal of the American College of Cardiology*, 49(21):2105–2111, 2007.

[212] Byron N Roberts, Pei-Chi Yang, Steven B Behrens, Jonathan D Moreno, and Colleen E Clancy. Computational approaches to understand cardiac electrophysiology and arrhythmias. *American Journal of Physiology-Heart and Circulatory Physiology*, 303(7):H766–H783, 2012.

[213] Pim AL Tonino, William F Fearon, Bernard De Bruyne, Keith G Oldroyd, Massoud A Leesar, Peter N Ver Lee, Philip A MacCarthy, Marcel Van't Veer, and Nico HJ Pijls. Angiographic versus functional severity of coronary artery stenoses in the fame study: fractional flow reserve versus angiography in multivessel evaluation. *Journal of the American College of Cardiology*, 55(25):2816–2821, 2010.

[214] Mariano Pellicano, Ifat Lavi, Bernard De Bruyne, Hana Vaknin-Assa, Abid Assali, Orna Valtzer, Yonit Lotringer, Giora Weisz, Yaron Almagor, Panagiotis Xaplanteris, et al. Validation study of image-based fractional flow reserve during coronary angiography. *Circulation: Cardiovascular Interventions*, 10(9):e005259, 2017.

[215] Christoph M Augustin, Matthias AF Gsell, Elias Karabelas, Erik Willemen, Frits W Prinzen, Joost Lumens, Edward J Vigmond, and Gernot Plank. A computationally efficient physiologically comprehensive 3d–0d closed-loop model of the heart and circulation. *Computer methods in applied mechanics and engineering*, 386:114092, 2021.

[216] Alexandre Lewalle, Gregory Milburn, Kenneth S Campbell, and Steven A Niederer. Cardiac length-dependent activation driven by force-dependent thick-filament dynamics. *Biophysical Journal*, 2024.

[217] SA Niederer, PJ Hunter, and NP Smith. A quantitative analysis of cardiac myocyte relaxation: a simulation study. *Biophysical journal*, 90(5):1697–1722, 2006.

[218] DA Nordsletten, SA Niederer, MP Nash, PJ Hunter, and NP Smith. Coupling multi-physics models to cardiac mechanics. *Progress in biophysics and molecular biology*, 104(1-3):77–88, 2011.

[219] Åshild Telle, James D Trotter, Xing Cai, Henrik Finsberg, Miroslav Kuchta, Joakim Sundnes, and Samuel T Wall. A cell-based framework for modeling cardiac mechanics. *Biomechanics and Modeling in Mechanobiology*, 22(2):515–539, 2023.

[220] Icilio Cavero and Henry Holzgrefe. Cipa: Ongoing testing, future qualification procedures, and pending issues. *Journal of pharmacological and toxicological methods*, 76:27–37, 2015.

[221] Thomas Colatsky, Bernard Fermini, Gary Gintant, Jennifer B Pierson, Philip Sager, Yuko Sekino, David G Strauss, and Norman Stockbridge. The comprehensive in vitro proarrhythmia assay (cipa) initiative—update on progress. *Journal of pharmacological and toxicological methods*, 81:15–20, 2016.

[222] Tina M Morrison, Pras Pathmanathan, Mariam Adwan, and Edward Margerrison. Advancing regulatory science with computational modeling for medical devices at the fda's office of science and engineering laboratories. *Frontiers in medicine*, 5:241, 2018.

[223] Tina M Morrison, Maureen L Dreher, Srinidhi Nagaraja, Leonardo M Angelone, and Wolfgang Kainz. The role of computational modeling and simulation in the total product life cycle of peripheral vascular devices. *Journal of medical devices*, 11(2):024503, 2017.

[224] Owen Faris and Jeffrey Shuren. An fda viewpoint on unique considerations for medical-device clinical trials. *New England Journal of Medicine*, 376(14):1350–1357, 2017.

[225] Boris P Kovatchev, Marc Breton, Chiara Dalla Man, and Claudio Cobelli. In silico preclinical trials: a proof of concept in closed-loop control of type 1 diabetes, 2009.

[226] Genevieve Coorey, Gemma A Figtree, David F Fletcher, Victoria J Snelson, Stephen Thomas Vernon, David Winlaw, Stuart M Grieve, Alistair McEwan, Jean Yee Hwa Yang, Pierre Qian, et al. The health digital twin to tackle cardiovascular disease—a review of an emerging interdisciplinary field. *NPJ digital medicine*, 5(1):126, 2022.

[227] Steven A Niederer, Michael S Sacks, Mark Girolami, and Karen Willcox. Scaling digital twins from the artisanal to the industrial. *Nature Computational Science*, 1(5):313–320, 2021.

[228] R Laubenbacher, Borna Mehrad, Ilya Shmulevich, and N Trayanova. Digital twins in medicine. *Nature Computational Science*, 4(3):184–191, 2024.

[229] Andre Mourato, Rodrigo Valente, Jose Xavier, Moises Brito, Stephane Avril, Jose Cesar de Sa, Antonio Tomas, and Jose Fragata. Computational modelling and simulation of fluid structure interaction in aortic aneurysms: A systematic review and discussion of the clinical potential. *Applied Sciences*, 12(16):8049, 2022.

[230] Suran Galappaththige, Richard A Gray, Caroline Mendonca Costa, Steven Niederer, and Pras Pathmanathan. Credibility assessment of patient-specific computational modeling using patient-specific cardiac modeling as an exemplar. *PLoS computational biology*, 18(10):e1010541, 2022.

[231] Claudio Capelli, Emilie Sauvage, Giuliano Giusti, Giorgia M Bosi, Hopewell Ntsinjana, Mario Carminati, Graham Derrick, Jan Marek, Sachin Khambadkone, Andrew M Taylor, et al. Patient-specific simulations for planning treatment in congenital heart disease. *Interface Focus*, 8(1):20170021, 2018.

[232] Annamaria Carusi, Kevin Burrage, and Blanca Rodríguez. Bridging experiments, models and simulations: an integrative approach to validation in computational cardiac electrophysiology. *American Journal of Physiology-Heart and Circulatory Physiology*, 303(2):H144–H155, 2012.

[233] ASME V&V40. Assessing credibility of computational modeling through verification and validation: application to medical devices. *The American Society of Mechanical Engineers*, 2018.

[234] Marco Viceconti and Luca Emili. *Toward Good Simulation Practice: Best Practices for the Use of Computational Modelling and Simulation in the Regulatory Process of Biomedical Products*. Springer Nature, 2024.

[235] Massimiliano Zaniboni, Andrew E Pollard, Lin Yang, and Kenneth W Spitzer. Beat-to-beat repolarization variability in ventricular myocytes and its suppression by electrical coupling. *American Journal of Physiology-Heart and Circulatory Physiology*, 278(3):H677–H687, 2000.

[236] Chon Lok Lei, Sanmitra Ghosh, Dominic G Whittaker, Yasser Aboelkassem, Kylie A Beattie, Chris D Cantwell, Tammo Delhaas, Charles Houston, Gustavo Montes Novaes, Alexander V Panfilov, et al. Considering discrepancy when calibrating a mechanistic electrophysiology model. *Philosophical Transactions of the Royal Society A*, 378(2173):20190349, 2020.

[237] D Rodney Hose, Patricia V Lawford, Wouter Huberts, Leif Rune Hellevik, Stig W Omholt, and Frans N van de Vosse. Cardiovascular models for personalised medicine: Where now and where next? *Medical engineering & physics*, 72:38–48, 2019.

[238] Jeffrey W Holmes and Joost Lumens. Clinical applications of patient-specific models: The case for a simple approach. *Journal of cardiovascular translational research*, 11:71–79, 2018.

[239] Wouter Huberts, Stefan GH Heinen, Niek Zonnebeld, Daniel AF van den Heuvel, Jean-Paul PM de Vries, Jan HM Tordoir, D Rodney Hose, Tammo Delhaas, and Frans N van de Vosse. What is needed to make cardiovascular models suitable for clinical decision support? a viewpoint paper. *Journal of computational science*, 24:68–84, 2018.

[240] Jorge Corral-Acero, Francesca Margara, Maciej Marciniak, Cristobal Rodero, Filip Loncaric, Yingjing Feng, Andrew Gilbert, Joao F Fernandes, Hassaan A Bukhari, Ali Wajdan, et al. The 'digital twin'to enable the vision of precision cardiology. *European heart journal*, 41(48):4556–4564, 2020.

[241] Richard A Gray and Pras Pathmanathan. Patient-specific cardiovascular computational modeling: diversity of personalization and challenges. *Journal of cardiovascular translational research*, 11:80–88, 2018.

[242] Marco Viceconti, Francesco Pappalardo, Blanca Rodriguez, Marc Horner, Jeff Bischoff, and Flora Musuamba Tshinanu. In silico trials: Verification, validation and uncertainty quantification of predictive models used in the regulatory evaluation of biomedical products. *Methods*, 185:120–127, 2021.

[243] M Peirlinck, F Sahli Costabal, J Yao, JM Guccione, S Tripathy, Y Wang, D Ozturk, P Segars, TM Morrison, S Levine, et al. Precision medicine in human heart modeling: Perspectives, challenges, and opportunities. *Biomechanics and modeling in mechanobiology*, 20:803–831, 2021.

[244] M Vardhan and A Randles. Application of physics-based flow models in cardiovascular medicine: Current practices and challenges. *Biophysics Reviews*, 2(1), 2021.

[245] Gary R Mirams, Pras Pathmanathan, Richard A Gray, Peter Challenor, and Richard H Clayton. Uncertainty and variability in computational and mathematical models of cardiac physiology. *The Journal of physiology*, 594(23):6833–6847, 2016.

[246] Ross H Johnstone, Eugene TY Chang, Rémi Bardenet, Teun P De Boer, David J Gavaghan, Pras Pathmanathan, Richard H Clayton, and Gary R Mirams. Uncertainty and variability in models of the cardiac action potential: Can we build trustworthy models? *Journal of molecular and cellular cardiology*, 96:49–62, 2016.

[247] Nicolaas Westerhof, Nikolaos Stergiopulos, Mark IM Noble, and Berend E Westerhof. *Snapshots of hemodynamics: an aid for clinical research and graduate education*. Springer, 2018.

[248] Sanjay Pant, Chiara Corsini, Catriona Baker, Tain-Yen Hsia, Giancarlo Pennati, and Irene E Vignon-Clementel. A lumped parameter model to study atrioventricular valve regurgitation in stage 1 and changes across stage 2 surgery in single ventricle patients. *IEEE Transactions on Biomedical Engineering*, 65(11):2450–2458, 2018.

[249] Dong Li, Penghao Jiang, Chen Hu, and Ting Yan. Comparison of local and global sensitivity analysis methods and application to thermal hydraulic phenomena. *Progress in Nuclear Energy*, 158:104612, 2023.

[250] Chuan Qin, Yuqing Jin, Meng Tian, Ping Ju, and Shun Zhou. Comparative study of global sensitivity analysis and local sensitivity analysis in power system parameter identification. *Energies*, 16(16):5915, 2023.

[251] MPR Haaker and Peter JT Verheijen. Local and global sensitivity analysis for a reactor design with parameter uncertainty. *Chemical Engineering Research and Design*, 82(5):591–598, 2004.

[252] Trevor N Johnson, Ben G Small, Eva Gil Berglund, and Karen Rowland Yeo. A best practice framework for applying physiologically-based pharmacokinetic modeling to pediatric drug development. *CPT: Pharmacometrics & Systems Pharmacology*, 10(9):967–972, 2021.

[253] Andrea Saltelli, Ksenia Aleksankina, William Becker, Pamela Fennell, Federico Ferretti, Niels Holst, Sushan Li, and Qiongli Wu. Why so many published sensitivity analyses are false: A systematic review of sensitivity analysis practices. *Environmental modelling & software*, 114:29–39, 2019.

[254] Melanie A Felmlee, Wojciech Krzyzanski, Bridget L Morse, and Marilyn E Morris. Use of a local sensitivity analysis to inform study design based on a mechanistic toxicokinetic model for γ-hydroxybutyric acid. *The AAPS Journal*, 13:240–254, 2011.

[255] Anna A Sher, Ken Wang, Andrew Wathen, Philip John Maybank, Gary R Mirams, David Abramson, Denis Noble, and David J Gavaghan. A local sensitivity analysis method for developing biological models with identifiable parameters: Application to cardiac ionic channel modelling. *Future Generation Computer Systems*, 29(2):591–598, 2013.

[256] Robert A Paulsen, John W Clark, Paul H Murphy, and John A Burdine. Sensitivity analysis and improved identification of a systemic arterial model, 1982.

[257] Laura M Ellwein, Hien T Tran, Cheryl Zapata, Vera Novak, and Mette S Olufsen. Sensitivity analysis and model assessment: mathematical models for arterial blood flow and blood pressure. *Cardiovascular Engineering*, 8:94–108, 2008.

[258] Michael Levin, Jurrki Kuikka, and James B Bassingthwaighte. Sensitivity analysis in optimization of time-distributed parameters for a coronary circulation model. *Medical progress through technology*, 7(2-3):119, 1980.

[259] Toshiro Sato, Stanley M Yamashiro, Daniel Vega, and Fred S Grodins. Parameter sensitivity analysis of a network model of systemic circulatory mechanics. *Annals of Biomedical Engineering*, 2:289–306, 1974.

[260] Ayesha Saleem Khan, Aamir Shahzad, Muhammad Zubair, Abdullah Alvi, and Raheem Gul. Personalized 0d models of normal and stenosed carotid arteries. *Computer methods and programs in biomedicine*, 200:105888, 2021.

[261] Tomasz Lipniacki, Pawel Paszek, Allan R Brasier, Bruce A Luxon, and Marek Kimmel. Stochastic regulation in early immune response. *Biophysical journal*, 90(3):725–742, 2006.

[262] Liesbet Geris, David Gomez-Cabrero, et al. Uncertainty in biology. *Studies in Mechanobiology, Tissue Engineering and Biomaterials*, 10:978–3, 2016.

[263] Adam Mahdi, Jacob Sturdy, Johnny T Ottesen, and Mette S Olufsen. Modeling the afferent dynamics of the baroreflex control system. *PLoS computational biology*, 9(12):e1003384, 2013.

[264] Hiroaki Kitano. Computational systems biology. *Nature*, 420(6912):206–210, 2002.

[265] Ryan N Gutenkunst, Joshua J Waterfall, Fergal P Casey, Kevin S Brown, Christopher R Myers, and James P Sethna. Universally sloppy parameter sensitivities in systems biology models. *PLoS computational biology*, 3(10):e189, 2007.

[266] Fabrice I Mowbray, Donna Manlongat, and Meghna Shukla. Sensitivity analysis: A method to promote certainty and transparency in nursing and health research. *Canadian Journal of Nursing Research*, 54(4):371–376, 2022.

[267] Emanuele Borgonovo and Elmar Plischke. Sensitivity analysis: A review of recent advances. *European Journal of Operational Research*, 248(3):869–887, 2016.

[268] George Qian and Adam Mahdi. Sensitivity analysis methods in the biomedical sciences. *Mathematical biosciences*, 323:108306, 2020.

[269] Raheem Gul, Aamir Shahzad, and Syed Muhammad Jawwad Riaz. A guide to uncertainty and global sensitivity analysis in lumped-parameter models of the cardiovascular system.

[270] Christian Haargaard Olsen, Johnny T Ottesen, Ralph C Smith, and Mette S Olufsen. Parameter subset selection techniques for problems in mathematical biology. *Biological cybernetics*, 113:121–138, 2019.

[271] WP Donders, W Huberts, FN van de Vosse, and T Delhaas. Personalization of models with many model parameters: an efficient sensitivity analysis approach. *International journal for numerical methods in biomedical engineering*, 31(10), 2015.

[272] Vinzenz Gregor Eck, Wouter Paulus Donders, Jacob Sturdy, Jonathan Feinberg, Tammo Delhaas, Leif Rune Hellevik, and Wouter Huberts. A guide to uncertainty quantification and sensitivity analysis for cardiovascular applications. *International journal for numerical methods in biomedical engineering*, 32(8):e02755, 2016.

[273] Jing Yang. Convergence and uncertainty analyses in monte-carlo based sensitivity analysis. *Environmental Modelling & Software*, 26(4):444–457, 2011.

[274] Annie Lumen, Kevin McNally, Nysia George, Jeffrey W Fisher, and George D Loizou. Quantitative global sensitivity analysis of a biologically based dose-response pregnancy model for the thyroid endocrine system. *Frontiers in pharmacology*, 6:139938, 2015.

[275] Nan-Hung Hsieh, Brad Reisfeld, Frederic Y Bois, and Weihsueh A Chiu. Applying a global sensitivity analysis workflow to improve the computational efficiencies in physiologically-based pharmacokinetic modeling. *Frontiers in pharmacology*, 9:588, 2018.

[276] Anna A Sher, Michael T Cooling, Blair Bethwaite, Jefferson Tan, Tom Peachey, Colin Enticott, Slavisa Garic, David J Gavaghan, Denis Noble, David Abramson, et al. A global sensitivity tool for cardiac cell modeling: application to ionic current balance and hypertrophic signaling. In *2010 Annual International Conference of the IEEE Engineering in Medicine and Biology*, pages 1498–1502. IEEE, 2010.

[277] Marion Taconné, Virginie Le Rolle, Kimi P Owashi, Vasileios Panis, Arnaud Hubert, Vincent Auffret, Elena Galli, Alfredo Hernandez, and Erwan Donal. Sensitivity analysis and parameter identification of a cardiovascular model in aortic stenosis. In *2021 Computing in Cardiology (CinC)*, volume 48, pages 1–4. IEEE, 2021.

[278] R Gul, A Shahzad, and M Zubair. Application of 0d model of blood flow to study vessel abnormalities in the human systemic circulation: An in-silico study. *International Journal of Biomathematics*, 11(08):1850106, 2018.

[279] Christian Haargaard Olsen, Hien T Tran, Johnny T Ottesen, Jesper Mehlsen, and Mette S Olufsen. Challenges in practical computation of global sensitivities with application to a baroreceptor reflex model. Technical report, North Carolina State University. Center for Research in Scientific Computation, 2013.

[280] Virginie Le Rolle, David Ojeda, and Alfredo I Hernández. Embedding a cardiac pulsatile model into an integrated model of the cardiovascular regulation for heart failure followup. *IEEE transactions on biomedical engineering*, 58(10):2982–2986, 2011.

[281] David Ojeda, Virginie Le Rolle, Majid Harmouche, Agnes Drochon, Hervé Corbineau, Jean-Philippe Verhoye, and Alfredo I Hernández. Sensitivity analysis and parameter estimation of a coronary circulation model for triple-vessel disease. *IEEE Transactions on Biomedical Engineering*, 61(4):1208–1219, 2014.

[282] Tatsuya Harada, Hajime Kubo, Taketoshi Mori, and Tomomasa Sato. Screening parameters of pulmonary and cardiovascular integrated model with sensitivity analysis. In *2006 International Conference of the IEEE Engineering in Medicine and Biology Society*, pages 210–213. IEEE, 2006.

[283] Mitchel J Colebank, Amanda L Colunga, Macie King, Christopher Schell, Matt Sheldon, Mariam Kharbat, Robert Sternquist, and Mette S Olufsen. Parameter inference in a computational model of hemodynamics in pulmonary hypertension. *arXiv preprint arXiv:2101.06266*, 2021.

[284] Nick van Osta, Aurore Lyon, Feddo Kirkels, Tijmen Koopsen, Tim van Loon, Maarten J Cramer, Arco J Teske, Tammo Delhaas, Wouter Huberts, and Joost Lumens. Parameter subset reduction for patient-specific modelling of arrhythmogenic cardiomyopathy-related mutation carriers in the circadapt model. *Philosophical Transactions of the Royal Society A*, 378(2173):20190347, 2020.

[285] John Walmsley, Theo Arts, Nicolas Derval, Pierre Bordachar, Hubert Cochet, Sylvain Ploux, Frits W Prinzen, Tammo Delhaas, and Joost Lumens. Fast simulation of mechanical heterogeneity in the electrically asynchronous heart using the multipatch module. *PLoS computational biology*, 11(7):e1004284, 2015.

[286] Ilya M Sobol. Global sensitivity indices for nonlinear mathematical models and their monte carlo estimates. *Mathematics and computers in simulation*, 55(1-3):271–280, 2001.

[287] Andrea Saltelli. Making best use of model evaluations to compute sensitivity indices. *Computer physics communications*, 145(2):280–297, 2002.

[288] Jeremy E Oakley and Anthony O'Hagan. Probabilistic sensitivity analysis of complex models: a bayesian approach. *Journal of the Royal Statistical Society Series B: Statistical Methodology*, 66(3):751–769, 2004.

[289] Andrea Saltelli, Paola Annoni, Ivano Azzini, Francesca Campolongo, Marco Ratto, and Stefano Tarantola. Variance based sensitivity analysis of model output. design and estimator for the total sensitivity index. *Computer physics communications*, 181(2):259–270, 2010.

[290] Ivano Azzini, Thierry A Mara, and Rossana Rosati. Comparison of two sets of monte carlo estimators of sobol'indices. *Environmental Modelling & Software*, 144:105167, 2021.

[291] Elmar Plischke and Emanuele Borgonovo. What about totals? alternative approaches to factor fixing. In *Safety, Reliability and Risk Analysis: Beyond the Horizon-Proceedings of the European Safety and Reliability Conference, ESREL*, volume 2014, pages 3339–3344, 2013.

[292] Qian Wang, Joseph HA Guillaume, John D Jakeman, Tao Yang, Takuya Iwanaga, Barry Croke, and Anthony J Jakeman. Assessing the predictive impact of factor fixing with an adaptive uncertainty-based approach. *Environmental Modelling & Software*, 148:105290, 2022.

[293] Arnald Puy, William Becker, Samuele Lo Piano, and Andrea Saltelli. A comprehensive comparison of total-order estimators for global sensitivity analysis. *International Journal for Uncertainty Quantification*, 12(2), 2022.

[294] GEB Archer, Andrea Saltelli, and Ilya Meyerovich Sobol. Sensitivity measures, anova-like techniques and the use of bootstrap. *Journal of Statistical Computation and Simulation*, 58(2):99–120, 1997.

[295] Gareth James, Daniela Witten, Trevor Hastie, Robert Tibshirani, and Jonathan Taylor. Resampling methods. In *An Introduction to Statistical Learning: with Applications in Python*, pages 201–228. Springer, 2023.

[296] Saman Razavi, Anthony Jakeman, Andrea Saltelli, Clementine Prieur, Bertrand Iooss, Emanuele Borgonovo, Elmar Plischke, Samuele Lo Piano, Takuya Iwanaga, William Becker, et al. The future of sensitivity analysis: An essential discipline for systems modeling and policy support. *Environmental Modelling & Software*, 137:104954, 2021.

[297] Jiri Nossent, Pieter Elsen, and Willy Bauwens. Sobol'sensitivity analysis of a complex environmental model. *Environmental Modelling & Software*, 26(12):1515–1525, 2011.

[298] E Benjamin Randall, Nicholas Z Randolph, Alen Alexanderian, and Mette S Olufsen. Global sensitivity analysis informed model reduction and selection applied to a valsalva maneuver model. *Journal of theoretical biology*, 526:110759, 2021.

[299] Lorenzo Sala, Nicolas Golse, Alexandre Joosten, Eric Vibert, and Irene Vignon-Clementel. Sensitivity analysis of a mathematical model simulating the post-hepatectomy hemodynamics response. *Annals of Biomedical Engineering*, 51(1):270–289, 2023.

[300] Nikolai L Bjørdalsbakke, Jacob T Sturdy, David R Hose, and Leif R Hellevik. Parameter estimation for closed-loop lumped parameter models of the systemic circulation using synthetic data. *Mathematical biosciences*, 343:108731, 2022.

[301] Elias Karabelas, Stefano Longobardi, Jana Fuchsberger, Orod Razeghi, Cristobal Rodero, Marina Strocchi, Ronak Rajani, Gundolf Haase, Gernot Plank, and Steven Niederer. Global sensitivity analysis of four chamber heart hemodynamics using surrogate models. *IEEE Transactions on Biomedical Engineering*, 69(10):3216–3223, 2022.

[302] Marina Strocchi, Stefano Longobardi, Christoph M Augustin, Matthias AF Gsell, Argyrios Petras, Christopher A Rinaldi, Edward J Vigmond, Gernot Plank, Chris J Oates, Richard D Wilkinson, et al. Cell to whole organ global sensitivity analysis on a four-chamber heart electromechanics model using gaussian processes emulators. *PLOS Computational Biology*, 19(6):e1011257, 2023.

[303] Aaron Katz and Venkateswaran Sankaran. Mesh quality effects on the accuracy of cfd solutions on unstructured meshes. *Journal of Computational Physics*, 230(20):7670–7686, 2011.

[304] Anna Sher, Steven A Niederer, Gary R Mirams, Anna Kirpichnikova, Richard Allen, Pras Pathmanathan, David J Gavaghan, Piet H Van Der Graaf, and Denis Noble. A quantitative systems pharmacology perspective on the importance of parameter identifiability. *Bulletin of Mathematical Biology*, 84(3):39, 2022.

[305] Anastasia Nasopoulou, Anoop Shetty, Jack Lee, David Nordsletten, C Aldo Rinaldi, Pablo Lamata, and Steven Niederer. Improved identifiability of myocardial material parameters by an energy-based cost function. *Biomechanics and modeling in mechanobiology*, 16:971–988, 2017.

[306] Ben BCB Hui, Socrates Dokos, and Nigel H Lovell. Parameter identifiability of cardiac ionic models using a novel cellml least squares optimization tool. In *2007 29th Annual International Conference of the IEEE Engineering in Medicine and Biology Society*, pages 5307–5310. IEEE, 2007.

[307] Andreas Raue, Johan Karlsson, Maria Pia Saccomani, Mats Jirstrand, and Jens Timmer. Comparison of approaches for parameter identifiability analysis of biological systems. *Bioinformatics*, 30(10):1440–1448, 2014.

[308] Alejandro F Villaverde, Antonio Barreiro, and Antonis Papachristodoulou. Structural identifiability of dynamic systems biology models. *PLoS computational biology*, 12(10):e1005153, 2016.

[309] David LI Janzén, Linnéa Bergenholm, Mats Jirstrand, Joanna Parkinson, James Yates, Neil D Evans, and Michael J Chappell. Parameter identifiability of fundamental pharmacodynamic models. *Frontiers in Physiology*, 7:590, 2016.

[310] Dominique Joubert, JD Stigter, and Jaap Molenaar. Assessing the role of initial conditions in the local structural identifiability of large dynamic models. *Scientific Reports*, 11(1):16902, 2021.

[311] Floriane Anstett-Collin, Lilianne Denis-Vidal, and Gilles Millérioux. A priori identifiability: An overview on definitions and approaches. *Annual Reviews in Control*, 50:139–149, 2020.

[312] C Houston, B Marchand, L Engelbert, and CD Cantwell. Reducing complexity and unidentifiability when modelling human atrial cells. *Philosophical Transactions of the Royal Society A*, 378(2173):20190339, 2020.

[313] Xabier Rey Barreiro and Alejandro F Villaverde. Benchmarking tools for a priori identifiability analysis. *Bioinformatics*, 39(2):btad065, 2023.

[314] Sandra Díaz-Seoane, Antonio Barreiro Blas, and Alejandro F Villaverde. Controllability and accessibility analysis of nonlinear biosystems. *Computer Methods and Programs in Biomedicine*, 242:107837, 2023.

[315] Maria Pia Saccomani, Giuseppina Bellu, Stefania Audoly, and Leontina d'Angió. A new version of daisy to test structural identifiability of biological models. In *Computational Methods in Systems Biology: 17th International Conference, CMSB 2019, Trieste, Italy, September 18–20, 2019, Proceedings 17*, pages 329–334. Springer, 2019.

[316] Jonathan A Kirk, Maria P Saccomani, and Sanjeev G Shroff. A priori identifiability analysis of cardiovascular models. *Cardiovascular engineering and technology*, 4:500–512, 2013.

[317] Salma Bahnasawy, Hesham Al-Sallami, and Stephen Duffull. A minimal model to describe short-term haemodynamic changes of the cardiovascular system. *British Journal of Clinical Pharmacology*, 87(3):1411–1421, 2021.

[318] Antoine Pironet, Pierre C Dauby, J Geoffrey Chase, Paul D Docherty, James A Revie, and Thomas Desaive. Structural identifiability analysis of a cardiovascular system model. *Medical engineering & physics*, 38(5):433–441, 2016.

[319] SY Amy Cheung, Oneeb Majid, James WT Yates, and Leon Aarons. Structural identifiability analysis and reparameterisation (parameter reduction) of a cardiovascular feedback model. *European journal of pharmaceutical sciences*, 46(4):259–271, 2012.

[320] Athanassios Iliadis. Structural identifiability and sensitivity. *Journal of pharmacokinetics and pharmacodynamics*, 46(2):127–135, 2019.

[321] Ronald A Fisher. On the mathematical foundations of theoretical statistics. *Philosophical transactions of the Royal Society of London. Series A, containing papers of a mathematical or physical character*, 222(594-604):309–368, 1922.

[322] Matthew S Shotwell and Richard A Gray. Estimability analysis and optimal design in dynamic multi-scale models of cardiac electrophysiology. *Journal of agricultural, biological, and environmental statistics*, 21:261–276, 2016.

[323] Michael F Rempel and Julie Zhou. On exact k-optimal designs minimizing the condition number. *Communications in Statistics-Theory and Methods*, 43(6):1114–1131, 2014.

[324] Ariel Cintrón-Arias, Harvey Thomas Banks, Alex Capaldi, and Alun L Lloyd. A sensitivity matrix based methodology for inverse problem formulation. *Inverse and Ill Posed Problems*, 2009.

[325] Sanjay Pant. Information sensitivity functions to assess parameter information gain and identifiability of dynamical systems. *Journal of The Royal Society Interface*, 15(142):20170871, 2018.

[326] Berit Floor Lund and Bjarne A Foss. Parameter ranking by orthogonalization—applied to nonlinear mechanistic models. *Automatica*, 44(1):278–281, 2008.

[327] Hong Yue, Martin Brown, Joshua Knowles, Hong Wang, David S Broomhead, and Douglas B Kell. Insights into the behaviour of systems biology models from dynamic sensitivity and identifiability analysis: a case study of an nf-κb signalling pathway. *Molecular BioSystems*, 2(12):640–649, 2006.

[328] Costas Kravaris, Juergen Hahn, and Yunfei Chu. Advances and selected recent developments in state and parameter estimation. *Computers & chemical engineering*, 51:111–123, 2013.

[329] Mette S Olufsen and Johnny T Ottesen. A practical approach to parameter estimation applied to model predicting heart rate regulation. *Journal of mathematical biology*, 67(1):39–68, 2013.

[330] Anna N McGuinness, Aman Tahir, Nadia R Sutton, and Andrew D Marquis. Identifiability of enzyme kinetic parameters in substrate competition: a case study of cd39/ntpdase1. *Purinergic Signalling*, pages 1–15, 2023.

[331] Johnny T Ottesen, Jesper Mehlsen, and Mette S Olufsen. Structural correlation method for model reduction and practical estimation of patient specific parameters illustrated on heart rate regulation. *Mathematical biosciences*, 257:50–59, 2014.

[332] Andrew D Marquis, Andrea Arnold, Caron Dean-Bernhoft, Brian E Carlson, and Mette S Olufsen. Practical identifiability and uncertainty quantification of a pulsatile cardiovascular model. *Mathematical biosciences*, 304:9–24, 2018.

[333] Amanda L Colunga, Mitchel J Colebank, REU Program, and Mette S Olufsen. Parameter inference in a computational model of haemodynamics in pulmonary hypertension. *Journal of the Royal Society Interface*, 20(200):20220735, 2023.

[334] Keegan E Hines, Thomas R Middendorf, and Richard W Aldrich. Determination of parameter identifiability in nonlinear biophysical models: A bayesian approach. *Journal of General Physiology*, 143(3):401–416, 2014.

[335] Maria Pia Saccomani and Karl Thomaseth. The union between structural and practical identifiability makes strength in reducing oncological model complexity: a case study. *Complexity*, 2018(1):2380650, 2018.

[336] Nicholas N Lam, Paul D Docherty, and Rua Murray. Practical identifiability of parametrised models: A review of benefits and limitations of various approaches. *Mathematics and Computers in Simulation*, 199:202–216, 2022.

[337] Matthew J Simpson and Oliver J Maclaren. Profile-wise analysis: a profile likelihood-based workflow for identifiability analysis, estimation, and prediction with mechanistic mathematical models. *PLoS Computational Biology*, 19(9):e1011515, 2023.

[338] Belén Casas, Jonas Lantz, Federica Viola, Gunnar Cedersund, Ann F Bolger, Carl-Johan Carlhäll, Matts Karlsson, and Tino Ebbers. Bridging the gap between measurements and modelling: a cardiovascular functional avatar. *Scientific reports*, 7(1):1–15, 2017.

[339] Mitchel J Colebank and Naomi C Chesler. An in-silico analysis of experimental designs to study ventricular function: A focus on the right ventricle. *PLoS computational biology*, 18(9):e1010017, 2022.

[340] Antoine Pironet, Paul D Docherty, Pierre C Dauby, J Geoffrey Chase, and Thomas Desaive. Practical identifiability analysis of a minimal cardiovascular system model. *Computer methods and programs in biomedicine*, 171:53–65, 2019.

[341] Bryan C Daniels, Yan-Jiun Chen, James P Sethna, Ryan N Gutenkunst, and Christopher R Myers. Sloppiness, robustness, and evolvability in systems biology. *Current opinion in biotechnology*, 19(4):389–395, 2008.

[342] Prem Jagadeesan, Karthik Raman, and Arun K Tangirala. Sloppiness: Fundamental study, new formalism and its application in model assessment. *Plos one*, 18(3):e0282609, 2023.

[343] Martin Fink, Steven A Niederer, Elizabeth M Cherry, Flavio H Fenton, Jussi T Koivumäki, Gunnar Seemann, Rüdiger Thul, Henggui Zhang, Frank B Sachse, Dan Beard, et al. Cardiac cell modelling: observations from the heart of the cardiac physiome project. *Progress in biophysics and molecular biology*, 104(1-3):2–21, 2011.

[344] Dominic G Whittaker, Michael Clerx, Chon Lok Lei, David J Christini, and Gary R Mirams. Calibration of ionic and cellular cardiac electrophysiology models. *Wiley Interdisciplinary Reviews: Systems Biology and Medicine*, 12(4):e1482, 2020.

[345] Dominic G Whittaker, Jiahui Wang, Joseph G Shuttleworth, Ravichandra Venkateshappa, Jacob M Kemp, Thomas W Claydon, and Gary R Mirams. Ion channel model reduction using manifold boundaries. *Journal of the Royal Society Interface*, 19(193):20220193, 2022.

[346] Gloria M Monsalve-Bravo, Brodie AJ Lawson, Christopher Drovandi, Kevin Burrage, Kevin S Brown, Christopher M Baker, Sarah A Vollert, Kerrie Mengersen, Eve McDonald-Madden, and Matthew P Adams. Analysis of sloppiness in model simulations: Unveiling parameter uncertainty when mathematical models are fitted to data. *Science advances*, 8(38):eabm5952, 2022.

[347] Yu-Mei Tan, Rachel R Worley, Jeremy A Leonard, and Jeffrey W Fisher. Challenges associated with applying physiologically based pharmacokinetic modeling for public health decision-making. *Toxicological Sciences*, 162(2):341–348, 2018.

[348] Gianna L Marschmann, Holger Pagel, Philipp Kügler, and Thilo Streck. Equifinality, sloppiness, and emergent structures of mechanistic soil biogeochemical models. *Environmental Modelling & Software*, 122:104518, 2019.

[349] Kapil Gadkar, DC Kirouac, DE Mager, Piet H van der Graaf, and Saroja Ramanujan. A six-stage workflow for robust application of systems pharmacology. *CPT: pharmacometrics & systems pharmacology*, 5(5):235–249, 2016.

[350] Ann C Babtie and Michael PH Stumpf. How to deal with parameters for whole-cell modelling. *Journal of The Royal Society Interface*, 14(133):20170237, 2017.

[351] Kody Law, Andrew Stuart, and Kostas Zygalakis. Data assimilation. *Cham, Switzerland: Springer*, 214:52, 2015.

[352] Simon J Julier. The scaled unscented transformation. In *Proceedings of the 2002 American Control Conference (IEEE Cat. No. CH37301)*, volume 6, pages 4555–4559. IEEE, 2002.

[353] Amirhossein Arzani and Scott TM Dawson. Data-driven cardiovascular flow modelling: examples and opportunities. *Journal of the Royal Society Interface*, 18(175):20200802, 2021.

[354] Simon J Julier and Jeffrey K Uhlmann. Unscented filtering and nonlinear estimation. *Proceedings of the IEEE*, 92(3):401–422, 2004.

[355] Eric A Wan and Rudolph Van Der Merwe. The unscented kalman filter. *Kalman filtering and neural networks*, pages 221–280, 2001.

[356] Huan Huang, Ming Yang, Wangfu Zang, Shunjie Wu, and Yafei Pang. In vitro identification of four-element windkessel models based on iterated unscented kalman filter. *IEEE transactions on biomedical engineering*, 58(9):2672–2680, 2011.

[357] Brett Matzuka, Jesper Mehlsen, Hien Tran, and Mette Sofie Olufsen. Using kalman filtering to predict time-varying parameters in a model predicting baroreflex regulation during head-up tilt. *IEEE Transactions on Biomedical Engineering*, 62(8):1992–2000, 2015.

[358] Damiano Lombardi. Inverse problems in 1d hemodynamics on systemic networks: A sequential approach. *International journal for numerical methods in biomedical engineering*, 30(2):160–179, 2014.

[359] Sanjay Pant, Aleksander Sizarov, Angela Knepper, Gaëtan Gossard, Alberto Noferi, Younes Boudjemline, and Irene Vignon-Clementel. Multiscale modelling of potts shunt as a potential palliative treatment for suprasystemic idiopathic pulmonary artery hypertension: a paediatric case study. *Biomechanics and Modeling in Mechanobiology*, 21(2):471–511, 2022.

[360] Alfio Quarteroni, L Formaggia, and A Veneziani. Cardiovascular mathematics. In *Proceedings of the International Congress of Mathematicians*, volume 1, pages 479–512. European Mathematical Society Madrid, Spain, 2006.

[361] Jon Nerdal. *Navier-Stokes Equations in One and Two Dimensions*. PhD thesis, Louisiana State University and Agricultural & Mechanical College, 2022.

[362] Karim Azer and Charles S Peskin. A one-dimensional model of blood flow in arteries with friction and convection based on the womersley velocity profile. *Cardiovascular Engineering*, 7:51–73, 2007.

[363] Fredrik Berntsson, Arpan Ghosh, VA Kozlov, and SA Nazarov. A one dimensional model of blood flow through a curvilinear artery. *Applied Mathematical Modelling*, 63:633–643, 2018.

[364] L Mihaela Păun, M Umar Qureshi, Mitchel Colebank, Nicholas A Hill, Mette S Olufsen, Mansoor A Haider, and Dirk Husmeier. Mcmc methods for inference in a mathematical model of pulmonary circulation. *Statistica Neerlandica*, 72(3):306–338, 2018.

[365] Rebecca C Gosling, Jacob Sturdy, Paul D Morris, Fredrik Eikeland Fossan, Leif Rune Hellevik, Patricia Lawford, D Rodney Hose, and Julian Gunn. Effect of side branch flow upon physiological indices in coronary artery disease. *Journal of Biomechanics*, 103:109698, 2020.

[366] Charles A Taylor, Kersten Petersen, Nan Xiao, Matthew Sinclair, Ying Bai, Sabrina R Lynch, Adam UpdePac, and Michiel Schaap. Patient-specific modeling of blood flow in the coronary arteries. *Computer Methods in Applied Mechanics and Engineering*, 417:116414, 2023.

[367] NIKOS Stergiopulos, JEAN-JACQUES Meister, and NICO Westerhof. Determinants of stroke volume and systolic and diastolic aortic pressure. *American Journal of Physiology-Heart and Circulatory Physiology*, 270(6):H2050–H2059, 1996.

[368] Nikolai L Bjørdalsbakke, Jacob Sturdy, Emma ML Ingeström, and Leif R Hellevik. Monitoring variability in parameter estimates for lumped parameter models of the systemic circulation using longitudinal hemodynamic measurements. *BioMedical Engineering OnLine*, 22(1):34, 2023.

[369] Yubing Shi, Patricia Lawford, and D Rodney Hose. Construction of lumped-parameter cardiovascular models using the cellml language. *Journal of medical engineering & technology*, 42(7):525–531, 2018.

[370] Theodosios Korakianitis and Yubing Shi. A concentrated parameter model for the human cardiovascular system including heart valve dynamics and atrioventricular interaction. *Medical engineering & physics*, 28(7):613–628, 2006.

[371] Hideaki Senzaki, Chen-Huan Chen, and David A Kass. Single-beat estimation of end-systolic pressure-volume relation in humans: a new method with the potential for noninvasive application. *Circulation*, 94(10):2497–2506, 1996.

[372] Johnny Tom Ottesen and M Danielsen. Modeling ventricular contraction with heart rate changes. *Journal of theoretical biology*, 222(3):337–346, 2003.

[373] Theodosios Korakianitis and Yubing Shi. Numerical comparison of hemodynamics with atrium to aorta and ventricular apex to aorta vad support. *ASAIO Journal*, 53(5):537–548, 2007.

[374] T Arts, P Bovendeerd, T Delhaas, and F Prinzen. Modeling the relation between cardiac pump function and myofiber mechanics. *Journal of biomechanics*, 36(5):731–736, 2003.

[375] Dilson E Rassier. Sarcomere mechanics in striated muscles: from molecules to sarcomeres to cells. *American Journal of Physiology-Cell Physiology*, 313(2):C134–C145, 2017.

[376] Piero Colli Franzone, Luca Franco Pavarino, and Simone Scacchi. *Mathematical cardiac electrophysiology*, volume 13. Springer, 2014.

[377] Steven A Niederer and Nicolas P Smith. An improved numerical method for strong coupling of excitation and contraction models in the heart. *Progress in biophysics and molecular biology*, 96(1-3):90–111, 2008.

[378] Christoph M Augustin, Thomas E Fastl, Aurel Neic, Chiara Bellini, John Whitaker, Ronak Rajani, Mark D O'Neill, Martin J Bishop, Gernot Plank, and Steven A Niederer. The impact of wall thickness and curvature on wall stress in patient-specific electromechanical models of the left atrium. *Biomechanics and modeling in mechanobiology*, 19(3):1015–1034, 2020.

[379] Cesare Corrado, Steven Williams, Gernot Planck, Mark O'Neill, and Steven Niederer. A predictive personalised model for the left atrium. In *2017 Computing in Cardiology (CinC)*, pages 1–4. IEEE, 2017.

[380] Joost Lumens, Tammo Delhaas, Borut Kirn, and Theo Arts. Three-wall segment (triseg) model describing mechanics and hemodynamics of ventricular interaction. *Annals of biomedical engineering*, 37:2234–2255, 2009.

[381] Javier Bermejo, Yolanda Benito, Marta Alhama, Raquel Yotti, Pablo Martínez-Legazpi, Candelas Perez Del Villar, Esther Pérez-David, Ana González-Mansilla, Cristina Santa-Marta, Alicia Barrio, et al. Intraventricular vortex properties in nonischemic dilated cardiomyopathy. *American Journal of Physiology-Heart and Circulatory Physiology*, 306(5):H718–H729, 2014.

[382] Arash Kheradvar, Carsten Rickers, Daisuke Morisawa, Minji Kim, Geu-Ru Hong, and Gianni Pedrizzetti. Diagnostic and prognostic significance of cardiovascular vortex formation. *Journal of cardiology*, 74(5):403–411, 2019.

[383] John J Charonko, Rahul Kumar, Kelley Stewart, William C Little, and Pavlos P Vlachos. Vortices formed on the mitral valve tips aid normal left ventricular filling. *Annals of biomedical engineering*, 41(5):1049–1061, 2013.

[384] Mikhail Prokopenko, Joseph T Lizier, Oliver Obst, and X Rosalind Wang. Relating fisher information to order parameters. *Physical Review E*, 84(4):041116, 2011.

[385] Max D Morris. Factorial sampling plans for preliminary computational experiments. *Technometrics*, 33(2):161–174, 1991.

[386] Francesca Campolongo, Jessica Cariboni, and Andrea Saltelli. An effective screening design for sensitivity analysis of large models. *Environmental modelling & software*, 22(10):1509–1518, 2007.

[387] Francesca Campolongo, Andrea Saltelli, and Jessica Cariboni. From screening to quantitative sensitivity analysis. a unified approach. *Computer physics communications*, 182(4):978–988, 2011.

[388] Michiel JW Jansen, Walter AH Rossing, and Richard A Daamen. Monte carlo estimation of uncertainty contributions from several independent multivariate sources. In *Predictability and nonlinear modelling in natural sciences and economics*, pages 334–343. Springer, 1994.

[389] RI Cukier, CM Fortuin, Kurt E Shuler, AG Petschek, and J Ho Schaibly. Study of the sensitivity of coupled reaction systems to uncertainties in rate coefficients. i theory. *The Journal of chemical physics*, 59(8):3873–3878, 1973.

[390] Andrea Saltelli, Stefano Tarantola, and KP-S Chan. A quantitative model-independent method for global sensitivity analysis of model output. *Technometrics*, pages 39–56, 1999.

[391] Thierry Alex Mara. Extension of the rbd-fast method to the computation of global sensitivity indices. *Reliability Engineering & System Safety*, 94(8):1274–1281, 2009.

[392] Alexander McFarlane Mood. *Introduction to the Theory of Statistics.* McGraw-hill, 1950.

[393] IM Soboĺ. Sensitivity estimates for nonlinear mathematical models. *Math. Model. Comput. Exp.*, 1:407, 1993.

[394] VG Eck, J Sturdy, and LR Hellevik. Effects of arterial wall models and measurement uncertainties on cardiovascular model predictions. *Journal of biomechanics*, 50:188–194, 2017.

[395] Bradley Efron and Robert J Tibshirani. *An introduction to the bootstrap*. Chapman and Hall/CRC, 1994.

[396] Various contributors. `QuasiMonteCarlo.jl`. https://github.com/SciML/QuasiMonteCarlo.jl, 2019.

[397] Jeff Bezanson, Alan Edelman, Stefan Karpinski, and Viral B Shah. Julia: A fresh approach to numerical computing. *SIAM review*, 59(1):65–98, 2017.

[398] Alexander Shapiro. Monte carlo sampling methods. *Handbooks in operations research and management science*, 10:353–425, 2003.

[399] Hans Janssen. Monte-carlo based uncertainty analysis: Sampling efficiency and sampling convergence. *Reliability Engineering & System Safety*, 109:123–132, 2013.

[400] Michael D McKay, Richard J Beckman, and William J Conover. A comparison of three methods for selecting values of input variables in the analysis of output from a computer code. *Technometrics*, 42(1):55–61, 2000.

[401] J Nayeem, CN Podder, and MA Salek. Sensitivity analysis and impact of an imperfect vaccine of two strains of hepatitis b virus infection. *Journal of Biological Systems*, pages 1–22, 2023.

[402] Yves Tinda Mangongo, Joseph-Desire Kyemba Bukweli, Justin Dupar Busili Kampempe, Rostin Matendo Mabela, and Justin Manango Wazute Munganga. Stability and global sensitivity analysis of the transmission dynamics of malaria with relapse and ignorant infected humans. *Physica Scripta*, 97(2):024002, 2022.

[403] Marissa Renardy, Louis R Joslyn, Jess A Millar, and Denise E Kirschner. To sobol or not to sobol? the effects of sampling schemes in systems biology applications. *Mathematical biosciences*, 337:108593, 2021.

[404] Min Pang, Ruichen Xu, Zhibing Hu, Jianjian Wang, and Ying Wang. Uncertainty and sensitivity analysis of input conditions in a large shallow lake based on the latin hypercube sampling and morris methods. *Water*, 13(13):1861, 2021.

[405] Qingyu Wang, Takuji Nakashima, Chenguang Lai, Hidemi Mutsuda, Taiga Kanehira, Yasufumi Konishi, and Hiroyuki Okuizumi. Modified algorithms for fast construction of optimal latin-hypercube design. *IEEE Access*, 8:191644–191658, 2020.

[406] William J Morokoff and Russel E Caflisch. Quasi-monte carlo integration. *Journal of computational physics*, 122(2):218–230, 1995.

[407] Russel E Caflisch. Monte carlo and quasi-monte carlo methods. *Acta numerica*, 7:1–49, 1998.

[408] Ishaan L Dalal, Deian Stefan, and Jared Harwayne-Gidansky. Low discrepancy sequences for monte carlo simulations on reconfigurable platforms. In *2008 International Conference on Application-Specific Systems, Architectures and Processors*, pages 108–113. IEEE, 2008.

[409] William Chen and Maxim Skriganov. Upper bounds in classical discrepancy theory. *A Panorama of Discrepancy Theory*, pages 3–69, 2014.

[410] Colas Schretter, Leif Kobbelt, and Paul-Olivier Dehaye. Golden ratio sequences for low-discrepancy sampling. *Journal of Graphics Tools*, 16(2):95–104, 2012.

[411] James N Lyness. Notes on lattice rules. *Journal of Complexity*, 19(3):321–331, 2003.

[412] Il'ya Meerovich Sobol'. On the distribution of points in a cube and the approximate evaluation of integrals. *Zhurnal Vychislitel'noi Matematiki i Matematicheskoi Fiziki*, 7(4):784–802, 1967.

[413] Xifu Sun, Barry Croke, Stephen Roberts, and Anthony Jakeman. Comparing methods of randomizing sobol sequences for improving uncertainty of metrics in variance-based global sensitivity estimation. *Reliability Engineering & System Safety*, 210:107499, 2021.

[414] Sergei Kucherenko, Balazs Feil, Nilay Shah, and Wolfgang Mauntz. The identification of model effective dimensions using global sensitivity analysis. *Reliability Engineering & System Safety*, 96(4):440–449, 2011.

[415] Shu Tezuka. On the necessity of low-effective dimension. *Journal of Complexity*, 21(5):710–721, 2005.

[416] Ivano Azzini, Thierry Mara, and Rossana Rosati. Monte carlo estimators of first-and total-orders sobol'indices. *arXiv preprint arXiv:2006.08232*, 2020.

[417] Toshimitsu Homma and Andrea Saltelli. Importance measures in global sensitivity analysis of nonlinear models. *Reliability Engineering & System Safety*, 52(1):1–17, 1996.

[418] Il'ya Meerovich Sobol'. Global sensitivity indices for the investigation of nonlinear mathematical models. *Matematicheskoe modelirovanie*, 19(11):23–24, 2007.

[419] Michiel JW Jansen. Analysis of variance designs for model output. *Computer Physics Communications*, 117(1-2):35–43, 1999.

[420] Alexandre Janon, Thierry Klein, Agnes Lagnoux, Maëlle Nodet, and Clémentine Prieur. Asymptotic normality and efficiency of two sobol index estimators. *ESAIM: Probability and Statistics*, 18:342–364, 2014.

[421] Ror Bellman and Karl Johan Åström. On structural identifiability. *Mathematical biosciences*, 7(3-4):329–339, 1970.

[422] Hongyu Miao, Xiaohua Xia, Alan S Perelson, and Hulin Wu. On identifiability of nonlinear ode models and applications in viral dynamics. *SIAM review*, 53(1):3–39, 2011.

[423] Lennart Ljung and Torkel Glad. On global identifiability for arbitrary model parametrizations. *automatica*, 30(2):265–276, 1994.

[424] Andreas Raue, Clemens Kreutz, Thomas Maiwald, Julie Bachmann, Marcel Schilling, Ursula Klingmüller, and Jens Timmer. Structural and practical identifiability analysis of partially observed dynamical models by exploiting the profile likelihood. *Bioinformatics*, 25(15):1923–1929, 2009.

[425] Marisa C Eisenberg and Harsh V Jain. A confidence building exercise in data and identifiability: Modeling cancer chemotherapy as a case study. *Journal of theoretical biology*, 431:63–78, 2017.

[426] Mette S Olufsen, Johnny T Ottesen, Hien T Tran, Laura M Ellwein, Lewis A Lipsitz, and Vera Novak. Blood pressure and blood flow variation during postural change from sitting to standing: model development and validation. *Journal of applied physiology*, 99(4):1523–1537, 2005.

[427] G Golub, V Klema, and GW Stewart. Rank degeneracyand least squares problems. In *Rep. STAN-CS-76-559*. Dept. Comput. Sci., Stanford University, 1976.

[428] Katherine J Pearce, Kimberly Nellenbach, Ralph C Smith, Ashley C Brown, and Mansoor A Haider. Modeling and parameter subset selection for fibrin polymerization kinetics with applications to wound healing. *Bulletin of mathematical biology*, 83:1–22, 2021.

[429] James C Spall. Monte carlo computation of the fisher information matrix in nonstandard settings. *Journal of Computational and Graphical Statistics*, 14(4):889–909, 2005.

[430] Svante Wold, Kim Esbensen, and Paul Geladi. Principal component analysis. *Chemometrics and intelligent laboratory systems*, 2(1-3):37–52, 1987.

[431] Sheldon Axler. *Linear algebra done right*. Springer Science & Business Media, 1997.

[432] Paul Bekker and Tom Wansbeek. Identification in parametric models. *A companion to theoretical econometrics*, pages 144–161, 2001.

[433] Mykel J Kochenderfer and Tim A Wheeler. *Algorithms for optimization*. Mit Press, 2019.

[434] Harry Saxton, Torsten Schenkel, Ian Halliday, and Xu Xu. Personalised parameter estimation of the cardiovascular system: Leveraging data assimilation and sensitivity analysis. *Journal of Computational Science*, 74:102158, 2023.

[435] Oana-Teodora Chis, Alejandro F Villaverde, Julio R Banga, and Eva Balsa-Canto. On the relationship between sloppiness and identifiability. *Mathematical biosciences*, 282:147–161, 2016.

[436] Kevin S Brown and James P Sethna. Statistical mechanical approaches to models with many poorly known parameters. *Physical review E*, 68(2):021904, 2003.

[437] Joshua J Waterfall, Fergal P Casey, Ryan N Gutenkunst, Kevin S Brown, Christopher R Myers, Piet W Brouwer, Veit Elser, and James P Sethna. Sloppy-model universality class and the vandermonde matrix. *Physical review letters*, 97(15):150601, 2006.

[438] Mark Asch, Marc Bocquet, and Maëlle Nodet. *Data assimilation: methods, algorithms, and applications*. SIAM, 2016.

[439] Juliane Liepe, Sarah Filippi, Michał Komorowski, and Michael PH Stumpf. Maximizing the information content of experiments in systems biology. *PLoS computational biology*, 9(1):e1002888, 2013.

[440] Daniel Silk, Paul DW Kirk, Chris P Barnes, Tina Toni, and Michael PH Stumpf. Model selection in systems biology depends on experimental design. *PLoS computational biology*, 10(6):e1003650, 2014.

[441] Nicholas J Higham. Analysis of the cholesky decomposition of a semi-definite matrix. *Reliable Numerical Computation*, 1990.

[442] Suresh Chengode. Left ventricular global systolic function assessment by echocardiography. *Annals of cardiac anaesthesia*, 19(Suppl 1):S26, 2016.

[443] Ryan Turner and Carl Edward Rasmussen. Model based learning of sigma points in unscented kalman filtering. *Neurocomputing*, 80:47–53, 2012.

[444] Christopher Rackauckas and Qing Nie. Differentialequations.jl–a performant and feature-rich ecosystem for solving differential equations in julia. *Journal of Open Research Software*, 5(1), 2017.

[445] Christopher Rackauckas and Qing Nie. Confederated modular differential equation apis for accelerated algorithm development and benchmarking. *Advances in Engineering Software*, 132:1–6, 2019.

[446] Vaibhav Kumar Dixit and Christopher Rackauckas. Globalsensitivity.jl: Performant and parallel global sensitivity analysis with julia. *Journal of Open Source Software*, 7(76):4561, 2022.

[447] Torsten Schenkel and Harry Saxton. Circulatorysystemmodels.jl, 2022.

[448] Yingbo Ma, Shashi Gowda, Ranjan Anantharaman, Chris Laughman, Viral Shah, and Chris Rackauckas. Modelingtoolkit: A composable graph transformation system for equation-based modeling, 2021.

[449] Luca Rosalia, Caglar Ozturk, David Van Story, Markus A Horvath, and Ellen T Roche. Object-oriented lumped-parameter modeling of the cardiovascular system for physiological and pathophysiological conditions. *Advanced theory and simulations*, 4(3):2000216, 2021.

[450] Marek Mateják, Tomáš Kulhánek, Jan Šilar, Pavol Privitzer, Filip Ježek, and Jiří Kofránek. Physiolibrary-modelica library for physiology. In *Proceedings of the 10th International Modelica Conference*, volume 96, pages 499–505. Linköping University Electronic Press Lund, 2014.

[451] Gerald Schweiger, Henrik Nilsson, Josef Schoeggl, Wolfgang Birk, and Alfred Posch. Modeling and simulation of large-scale systems: A systematic comparison of modeling paradigms. *Applied Mathematics and Computation*, 365:124713, 2020.

[452] Autumn A Cuellar, Catherine M Lloyd, Poul F Nielsen, David P Bullivant, David P Nickerson, and Peter J Hunter. An overview of cellml 1.1, a biological model description language. *Simulation*, 79(12):740–747, 2003.

[453] Michael Hucka, Andrew Finney, Herbert M Sauro, Hamid Bolouri, John C Doyle, Hiroaki Kitano, Adam P Arkin, Benjamin J Bornstein, Dennis Bray, Athel Cornish-Bowden, et al. The systems biology markup language (sbml): a medium for representation and exchange of biochemical network models. *Bioinformatics*, 19(4):524–531, 2003.

[454] Shahriar Iravanian and others. CellMLToolkit.jl: a Julia library that connects CellML models to SciML. https://github.com/SciML/CellMLToolkit.jl, 2021.

[455] John Tinnerholm, Adrian Pop, and Martin Sjölund. A modular, extensible, and modelica-standard-compliant openmodelica compiler framework in julia supporting structural variability. *Electronics*, 11(11):1772, 2022.

[456] Christopher Rackauckas, Yingbo Ma, Julius Martensen, Collin Warner, Kirill Zubov, Rohit Supekar, Dominic Skinner, Ali Ramadhan, and Alan Edelman. Universal differential equations for scientific machine learning. *arXiv preprint arXiv:2001.04385*, 2020.

[457] Harry Saxton, Ian Halliday, Torsten Schenkel, and Xu Xu. Assessing parameter subset selection methods using a minimalmechanical model of the cardiovascular system. *Available at SSRN 4374559*, 2023.

[458] Tommaso Nannicini. Simulation-based sensitivity analysis for matching estimators. *The stata journal*, 7(3):334–350, 2007.

[459] Samuele Lo Piano, Federico Ferretti, Arnald Puy, Daniel Albrecht, and Andrea Saltelli. Variance-based sensitivity analysis: The quest for better estimators and designs between explorativity and economy. *Reliability Engineering & System Safety*, 206:107300, 2021.

[460] Arnald Puy, Samuele Lo Piano, and Andrea Saltelli. A sensitivity analysis of the pawn sensitivity index. *Environmental Modelling & Software*, 127:104679, 2020.

[461] Sergei Kucherenko, Daniel Albrecht, and Andrea Saltelli. Exploring multi-dimensional spaces: A comparison of latin hypercube and quasi monte carlo sampling techniques. *arXiv preprint arXiv:1505.02350*, 2015.

[462] Jon Herman and Will Usher. Salib: An open-source python library for sensitivity analysis. *Journal of Open Source Software*, 2(9):97, 2017.

[463] Arnald Puy, Samuele Lo Piano, Andrea Saltelli, and Simon A Levin. Sensobol: an r package to compute variance-based sensitivity indices. *arXiv preprint arXiv:2101.10103*, 2021.

[464] Graham Glen and Kristin Isaacs. Estimating sobol sensitivity indices using correlations. *Environmental Modelling & Software*, 37:157–166, 2012.

[465] Thierry A Mara and Stefano Tarantola. Variance-based sensitivity indices for models with dependent inputs. *Reliability Engineering & System Safety*, 107:115–121, 2012.

[466] Stefano Tarantola and Thierry A Mara. Variance-based sensitivity indices of computer models with dependent inputs: The fourier amplitude sensitivity test. *International Journal for Uncertainty Quantification*, 7(6), 2017.

[467] Sergei Kucherenko, Stefano Tarantola, and Paola Annoni. Estimation of global sensitivity indices for models with dependent variables. *Computer physics communications*, 183(4):937–946, 2012.

[468] AIAA Digital Engineering Integration Committee et al. Digital twin: Definition & value—an aiaa and aia position paper. *AIAA: Reston, VA, USA*, 2020.

[469] Natalia A Trayanova and Adityo Prakosa. Up digital and personal: How heart digital twins can transform heart patient care. *Heart Rhythm*, 21(1):89–99, 2024.

[470] Karli Gillette, Matthias AF Gsell, Anton J Prassl, Elias Karabelas, Ursula Reiter, Gert Reiter, Thomas Grandits, Christian Payer, Darko Štern, Martin Urschler, et al. A framework for the generation of digital twins of cardiac electrophysiology from clinical 12-leads ecgs. *Medical Image Analysis*, 71:102080, 2021.

[471] Francesco Viola, Giulio Del Corso, Ruggero De Paulis, and Roberto Verzicco. Gpu accelerated digital twins of the human heart open new routes for cardiovascular research. *Scientific reports*, 13(1):8230, 2023.

[472] Erin P Balogh, Bryan T Miller, John R Ball, and National Academies of Sciences. Technology and tools in the diagnostic process. In *Improving Diagnosis in Health Care*. National Academies Press (US), 2015.

[473] Sean P Murphy, Nasrien E Ibrahim, and James L Januzzi. Heart failure with reduced ejection fraction: a review. *Jama*, 324(5):488–504, 2020.

[474] Anthony M Dart and Bronwyn A Kingwell. Pulse pressure—a review of mechanisms and clinical relevance. *Journal of the American College of Cardiology*, 37(4):975–984, 2001.

[475] Peter D Gatehouse, Jennifer Keegan, Lindsey A Crowe, Sharmeen Masood, Raad H Mohiaddin, Karl-Friedrich Kreitner, and David N Firmin. Applications of phase-contrast flow and velocity imaging in cardiovascular mri. *European radiology*, 15:2172–2184, 2005.

[476] Jamal A Alhashemi, Maurizio Cecconi, and Christoph K Hofer. Cardiac output monitoring: an integrative perspective. *Critical Care*, 15(2):214, 2011.

[477] Kiichi Sagawa. The ventricular pressure-volume diagram revisited. *Circulation Research*, 43(5):677–687, 1978.

[478] Roger E Kirk. Experimental design. *Sage handbook of quantitative methods in psychology*, pages 23–45, 2009.

[479] Albert Tarantola. *Inverse problem theory and methods for model parameter estimation*. SIAM, 2005.

[480] Kyle Strimbu and Jorge A Tavel. What are biomarkers? *Current Opinion in HIV and AIDS*, 5(6):463, 2010.

[481] Clemens Kreutz, Andreas Raue, Daniel Kaschek, and Jens Timmer. Profile likelihood in systems biology. *The FEBS journal*, 280(11):2564–2571, 2013.

[482] Harry Saxton, Xu Xu, Torsten Schenkel, and Ian Halliday. Assessing input parameter hyperspace and parameter identifiability in a cardiovascular system model via sensitivity analysis. *Journal of Computational Science*, 79:102287, 2024.

[483] Pablo J Blanco, Sansuke M Watanabe, Marco Aurélio RF Passos, Pedro A Lemos, and Raúl A Feijóo. An anatomically detailed arterial network model for one-dimensional computational hemodynamics. *IEEE Transactions on biomedical engineering*, 62(2):736–753, 2014.

[484] Lucas O Müller, Sansuke M Watanabe, Eleuterio F Toro, Raúl A Feijóo, and Pablo J Blanco. An anatomically detailed arterial-venous network model. cerebral and coronary circulation. *Frontiers in Physiology*, 14:1162391, 2023.

[485] Harry Saxton, Xu Xu, Torsten Schenkel, Richard H Clayton, and Ian Halliday. Convergence, sampling and total order estimator effects on parameter orthogonality in global sensitivity analysis. *PLOS Computational Biology*, 20(7):e1011946, 2024.

[486] Friederike Schäfer, Jacob Sturdy, and Leif Rune Hellevik. Age and sex-dependent sensitivity analysis of a common carotid artery model. *Biomechanics and Modeling in Mechanobiology*, pages 1–19, 2024.

[487] Matteo Salvador, Marina Strocchi, Francesco Regazzoni, Christoph M Augustin, Luca Dede', Steven A Niederer, and Alfio Quarteroni. Whole-heart electromechanical simulations using latent neural ordinary differential equations. *NPJ Digital Medicine*, 7(1):90, 2024.

[488] Harvey Thomas Banks, Shuhua Hu, and W Clayton Thompson. *Modeling and inverse problems in the presence of uncertainty*. CRC Press, 2014.

[489] Henry Voelzke, Carsten O Schmidt, Sebastian E Baumeister, Till Ittermann, Glenn Fung, Janina Krafczyk-Korth, Wolfgang Hoffmann, Matthias Schwab, Henriette E Meyer zu Schwabedissen, Marcus Doerr, et al. Personalized cardiovascular medicine: concepts and methodological considerations. *Nature Reviews Cardiology*, 10(6):308–316, 2013.

[490] Amanda lee Colunga. *Mathematical Analysis of Cardiovascular Hemodynamics in Disease*. North Carolina State University, 2023.

[491] Sam Coveney and Richard H Clayton. Sensitivity and uncertainty analysis of two human atrial cardiac cell models using gaussian process emulators. *Frontiers in Physiology*, 11:364, 2020.

[492] John Norton. An introduction to sensitivity assessment of simulation models. *Environmental Modelling & Software*, 69:166–174, 2015.

[493] Anqi Wang and Dimitri P Solomatine. Practical experience of sensitivity analysis: Comparing six methods, on three hydrological models, with three performance criteria. *Water*, 11(5):1062, 2019.

[494] Dan Gabriel Cacuci. Motivation: Overcoming the curse of dimensionality in sensitivity analysis, uncertainty quantification, and predictive modeling. In *The nth-Order Comprehensive Adjoint Sensitivity Analysis Methodology, Volume I: Overcoming the Curse of Dimensionality: Linear Systems*, pages 1–44. Springer, 2022.

[495] Jitendra R Raol, Gopalrathnam Girija, and Jatinder Singh. *Modelling and parameter estimation of dynamic systems*, volume 65. Iet, 2004.

[496] Libera Fresiello, Gianfranco Ferrari, Arianna Di Molfetta, K Zieliński, A Tzallas, Steven Jacobs, Marek Darowski, Maciej Kozarski, Bart Meyns, Nikolaos S Katertsidis, et al. A cardiovascular simulator tailored for training and clinical uses. *Journal of Biomedical Informatics*, 57:100–112, 2015.

[497] Bernd Saugel, Karim Kouz, Agnes S Meidert, Leonie Schulte-Uentrop, and Stefano Romagnoli. How to measure blood pressure using an arterial catheter: a systematic 5-step approach. *Critical Care*, 24:1–10, 2020.

[498] Zahra Keshavarz-Motamed. A diagnostic, monitoring, and predictive tool for patients with complex valvular, vascular and ventricular diseases. *Scientific Reports*, 10(1):1–19, 2020.

[499] Elliott M Antman and Joseph Loscalzo. Precision medicine in cardiology. *Nature Reviews Cardiology*, 13(10):591–602, 2016.

[500] Anand Ambhore, Swee-Guan Teo, Abdul Razakjr Bin Omar, and Kian-Keong Poh. Ecg series. importance of qt interval in clinical practice. *Singapore medical journal*, 55(12):607, 2014.

[501] Josef Kautzner. Qt interval measurements. *Cardiac electrophysiology review*, 6:273–277, 2002.

[502] Harry Saxton, Xu Xu, Ian Halliday, and Torsten Schenkel. New perspectives on sensitivity and identifiability analysis using the unscented kalman filter, 2023.

[503] Edgar Hernando Sepúlveda Oviedo, Leonardo Enrique Bermeo Clavijo, and Luis Carlos Méndez Córdoba. Openmodelica-based virtual simulator for the cardiovascular and respiratory physiology of a neonate. *Journal of Medical Engineering & Technology*, 46(3):179–197, 2022.

[504] Katarzyna Buszko, Sławomir Kujawski, Julia L Newton, and Paweł Zalewski. Hemodynamic response to the head-up tilt test in patients with syncope as a predictor of the test outcome: A meta-analysis approach. *Frontiers in physiology*, 10:184, 2019.

[505] Carin Basirun, Melanie L Ferlazzo, Nicholas R Howell, Guo-Jun Liu, Ryan J Middleton, Boris Martinac, S Anand Narayanan, Kate Poole, Carmine Gentile, and Joshua Chou. Microgravity× radiation: A space mechanobiology approach toward cardiovascular function and disease. *Frontiers in Cell and Developmental Biology*, 9:750775, 2021.

[506] Ahmed S Abutaleb and J Melbin. The estimation of the cardiac time-varying parameters during the ejection phase of the cardiac cycle using the ito calculus. *Cardiovascular Engineering*, 10:118–127, 2010.

[507] Sourabh Katoch, Sumit Singh Chauhan, and Vijay Kumar. A review on genetic algorithm: past, present, and future. *Multimedia Tools and Applications*, 80:8091–8126, 2021.

[508] Zhe Chen et al. Bayesian filtering: From kalman filters to particle filters, and beyond. *Statistics*, 182(1):1–69, 2003.

[509] Marco D Mazzeo and Peter V Coveney. Hemelb: A high performance parallel lattice-boltzmann code for large scale fluid flow in complex geometries. *Computer Physics Communications*, 178(12):894–914, 2008.

[510] I Zacharoudiou, JWS McCullough, and Peter V Coveney. Development and performance of a hemelb gpu code for human-scale blood flow simulation. *Computer Physics Communications*, 282:108548, 2023.

[511] Eugene TY Chang, Mark Strong, and Richard H Clayton. Bayesian sensitivity analysis of a cardiac cell model using a gaussian process emulator. *PloS one*, 10(6):e0130252, 2015.

[512] Sam Coveney, Cesare Corrado, Jeremy E Oakley, Richard D Wilkinson, Steven A Niederer, and Richard H Clayton. Bayesian calibration of electrophysiology models using restitution curve emulators. *Frontiers in Physiology*, 12:693015, 2021.

[513] Thomas Grandits, Christoph M Augustin, Gundolf Haase, Norbert Jost, Gary R Mirams, Steven A Niederer, Gernot Plank, András Varró, László Virág, and Alexander Jung. Neural network emulation of the human ventricular cardiomyocyte action potential for more efficient computations in pharmacological studies. *Elife*, 12:RP91911, 2024.

[514] Elias C Massoud. Emulation of environmental models using polynomial chaos expansion. *Environmental modelling & software*, 111:421–431, 2019.

[515] Chang K Park and Kwang-Il Ahn. A new approach for measuring uncertainty importance and distributional sensitivity in probabilistic safety assessment. *Reliability Engineering & System Safety*, 46(3):253–261, 1994.

[516] Ronald L Iman and Stephen C Hora. A robust measure of uncertainty importance for use in fault tree system analysis. *Risk analysis*, 10(3):401–406, 1990.

[517] Art B Owen. Sobol'indices and shapley value. *SIAM/ASA Journal on Uncertainty Quantification*, 2(1):245–251, 2014.

[518] Eunhye Song, Barry L Nelson, and Jeremy Staum. Shapley effects for global sensitivity analysis: Theory and computation. *SIAM/ASA Journal on Uncertainty Quantification*, 4(1):1060–1083, 2016.

[519] Javier Castro, Daniel Gómez, and Juan Tejada. Polynomial calculation of the shapley value based on sampling. *Computers & Operations Research*, 36(5):1726–1730, 2009.

[520] Maziar Raissi, Paris Perdikaris, and George E Karniadakis. Physics-informed neural networks: A deep learning framework for solving forward and inverse problems involving nonlinear partial differential equations. *Journal of Computational physics*, 378:686–707, 2019.

[521] Sifan Wang, Yujun Teng, and Paris Perdikaris. Understanding and mitigating gradient flow pathologies in physics-informed neural networks. *SIAM Journal on Scientific Computing*, 43(5):A3055–A3081, 2021.

[522] Maziar Raissi, Paris Perdikaris, and George Em Karniadakis. Multistep neural networks for data-driven discovery of nonlinear dynamical systems. *arXiv preprint arXiv:1801.01236*, 2018.

[523] Arnald Puy, Pierfrancesco Beneventano, Simon A Levin, Samuele Lo Piano, Tommaso Portaluri, and Andrea Saltelli. Models with higher effective dimensions tend to produce more uncertain estimates. *Science Advances*, 8(42):eabn9450, 2022.

[524] Dhruva V Raman, James Anderson, and Antonis Papachristodoulou. Delineating parameter unidentifiabilities in complex models. *Physical Review E*, 95(3):032314, 2017.

[525] Dániel Nagy, Lambert Plavecz, and Ferenc Hegedűs. The art of solving a large number of non-stiff, low-dimensional ordinary differential equation systems on gpus and cpus. *Communications in Nonlinear Science and Numerical Simulation*, 112:106521, 2022.

[526] Utkarsh Utkarsh, Valentin Churavy, Yingbo Ma, Tim Besard, Prakitr Srisuma, Tim Gymnich, Adam R Gerlach, Alan Edelman, George Barbastathis, Richard D Braatz, et al. Automated translation and accelerated solving of differential equations on multiple gpu platforms. *Computer Methods in Applied Mechanics and Engineering*, 419:116591, 2024.

[527] George K Batchelor. On steady laminar flow with closed streamlines at large reynolds number. *Journal of Fluid Mechanics*, 1(2):177–190, 1956.

Appendix A

1D Model Derivation

A.1 Numerical Scheme Derivation

Following treatment based upon Olufsen [116], Chapter 7, and Hughes and Lubliner [115]. In our analysis we will eventually make simplifications for absence of any body force on fluid and constant (time-independent) boundary shape. Notation for boundary regions and corresponding unit normal's, expressed in cylindrical polar co-ordinates is given in table A.1 below. Note that the system's axial symmetry implies $\hat{n}_\theta = 0$ for all parts of the boundary,

Table A.1 **Boundary normal unit vectors and notations**: Expressed here within cylindrical polar co-ordinates, using accepted notation, relative to the co-ordinate system orientation in which $\hat{e}_z$ is the streamwise (artery centre-line) direction. All normal's are positive pointing away from the enclosed volume. In this table, $R_z = \frac{dR}{dz}$ which is a known function of streamwise co-ordinate, z.

	Boundary Element Location			
	Inlet	Luminal	Outlet	z
Unit normal, $\hat{n}$	$-\hat{e}_z$	$\frac{(R_z\hat{e}_z+\hat{e}_r)}{\sqrt{1+R_z^2}}$	$\hat{e}_z$	$\hat{e}_z$
Identifier	$\partial\Omega_i$	$\partial\Omega_l$	$\partial\Omega_o$	$\partial\Omega_z$

A.2 Conservation Relations in the Presence of Leak

Hughes and Lubliner apply Reynolds' transport theorem [527] to the leaking artery to show that for some arbitrary scalar function $\xi(r,z,t)$ [115]

$$\frac{\partial}{\partial t}A\xi + \frac{\partial}{\partial z}A(\xi\bar{u_z}) = \iint_{\partial\Omega_x}\frac{D\xi}{Dt}dA + \oint_{C(z)}\xi(\underline{u}-\underline{v})\cdot\hat{n}dl \tag{A.1}$$

Later, we will set time derivatives to zero. Above, $\underline{u}$ ($\underline{v}$) denotes fluid (boundary) motion, $C(z)$ identifies a contour in the luminal boundary lying within a plane perpendicular to the z-axis (axis of symmetry), A is the smallest area bounded by $C(z)$ and the overbar denotes a cross-sectional area average

$$\bar{\xi} = \frac{1}{A} \iint_{\partial\Omega_z} \xi \, dA$$

A.2.1 Volume Balance

Set $\xi = 1$ in equation A.1 from which it is immediate that

$$\frac{\partial A}{\partial t} + \frac{\partial}{\partial z} A\bar{u}_z + \psi = 0, \quad \psi = -\oint_{C(z)} w_n dl \tag{A.2}$$

where $w_n = (\underline{u} - \underline{v}) \cdot \hat{n}$ is the relative normal component of the fluid motion at the boundary. Accordingly, sink term $\psi(z)$ represents the volumetric flux per unit length of fluid leaving the domain at streamwise location z.

A.2.2 Streamwise Momentum Balance

Set $\xi = v_z(r,z,t)$ in equation A.1 from which it is immediate that

$$\frac{\partial}{\partial t} A\bar{u}_z + \frac{\partial}{\partial z} A\bar{u_z^2} + \psi_p = \iint_{\partial\Omega_z} \frac{Du_z}{Dt} dA, \quad \psi_p = -\oint_{C(z)} u_z w_n dl. \tag{A.3}$$

The material derivative in the above may be replaced from the (right hand side) of an approximate form of the z-component of the curvilinear Navier-Stokes equations, following Hughes and Lubliner [115]

$$\iint_{\partial\Omega_z} \frac{Du_z}{Dt} dA = -\frac{A}{\rho} \frac{\partial \bar{p}}{\partial z} + \frac{\eta}{\rho} \oint_{C(z)} (\hat{n} \cdot \underline{\nabla}) \, u_z dl$$

and expanding the directional derivative in the integrand and substituting we find

$$\frac{\partial}{\partial t} A\bar{u}_z + \frac{\partial}{\partial z} A\bar{u_z^2} + \frac{A}{\rho} \frac{\partial \bar{p}}{\partial z} + \psi_p = \frac{\eta}{\rho} \oint_{C(z)} \frac{\left(R_z \frac{\partial u_z}{\partial z} + \frac{\partial u_z}{\partial r} \right)}{\sqrt{1 + R_z^2}} dl.$$

Following Olufson [116], we next suppose the dominant term in the first integration on the right hand side to be $\frac{\partial u_z}{\partial r}$, assume cylindrical symmetry (so that R_z is constant on contour

$C(z)$) and transpose all terms to the left hand side

$$\frac{\partial}{\partial t}A\bar{u}_z + \frac{\partial}{\partial z}A\bar{u_z^2} + \frac{A}{\rho}\frac{\partial \bar{p}}{\partial z} + \psi_p - \frac{2\pi\eta R(z)}{\rho\sqrt{1+R_z^2}}\left[\frac{\partial u_z}{\partial r}\right]_{\partial\Omega_L(z)} = 0. \tag{A.4}$$

Momentum sink term will be related to the volume sink term (Equation A.2) below. Finally, we introduce the convective acceleration parameter, implicitly defined as follows

$$\chi\bar{u_z}^2 = \frac{1}{A}\iint_{A(z)} u_z^2 dA$$

Of course, χ can be evaluated only based upon assumptions made regarding the transverse variation of the velocity profile. We return to this point shortly. The momentum conservation equation may now be written as follows

$$\frac{\partial}{\partial t}A\bar{u}_z + \frac{\partial}{\partial z}\left(\chi A\bar{u_z}^2\right) + \frac{A}{\rho}\frac{\partial \bar{p}}{\partial z} + \psi_p - \frac{2\pi\eta R(z)}{\rho\sqrt{1+R_z^2}}\left[\frac{\partial u_z}{\partial r}\right]_{\partial\Omega_L(z)} = 0. \tag{A.5}$$

in which χ is the momentum correction coefficient [116]. We now assume the following transverse velocity profile within the artery, which enforces a no-slip condition at the boundary ($u_z(z,R) = 0$) and has a blunting which is controlled by the parameter ζ [198].

$$u_z(z,r) = u(z)\left(\frac{\zeta+2}{\zeta}\right)\left[1-\left(\frac{r}{R(z)}\right)^{\zeta}\right], \quad 0 \le r \le R(z), \quad \zeta \in [1,9], \tag{A.6}$$

A no-slip condition at luminal boundary of course inconsistent with any leak and following equation. We return to this matter shortly. For the moment, this profile underwrites the following results

$$\bar{u}_z = u(z), \quad \chi = \left(\frac{\zeta+2}{\zeta+1}\right), \quad \left[\frac{\partial u_z}{\partial r}\right]_{\partial\Omega_L(z)} = -\frac{\bar{u}_z(\zeta+2)}{R(z)}, \quad \psi_p = 0. \tag{A.7}$$

The last result for the momentum sink follows immediately from Equation A.3.

To obtain a preliminary form of the momentum conservation equation, we substitute Equations A.7 into Equation A.4, yielding

$$\frac{\partial}{\partial t}A\bar{u}_z + \frac{\partial}{\partial z}\left(\chi A\bar{u_z}^2\right) + \frac{A}{\rho}\frac{\partial \bar{p}}{\partial z} + \frac{2\pi\eta(\zeta+2)\bar{u}_z}{\rho\sqrt{1+R_z^2}} = 0. \tag{A.8}$$

We have used this form of momentum conservation recently, to compare what we designate physiological and anatomical leak [119].

To obtain an alternative form for the momentum conservation equation, we assume a flat profile with the velocity at the boundary given at all points within the domain and at the boundary by $\bar{u_z}$. Of course this messes-up the gradient term $\left[\frac{\partial u_z}{\partial r}\right]_{\partial\Omega_L(z)}$. Overlooking this, we now have for the momentum source term, from (the second) Equation A.3 the following simplification

$$\psi_p(z) = \oint_{C(z)} u_z w_n dl \rightarrow \oint_{C(z)} \bar{u_z} w_n dl = \bar{u_z} \oint_{C(z)} w_n dl = \bar{u_z}\psi(z)$$

A second form for the momentum conservation equation now follows

$$\frac{\partial}{\partial t}A\bar{u_z} + \frac{\partial}{\partial z}\left(\chi A\bar{u_z}^2\right) + \frac{A}{\rho}\frac{\partial \bar{p}}{\partial z} + \bar{u_z}\psi(z) + \frac{2\pi\eta(\zeta+2)\bar{u_z}}{\rho\sqrt{1+R_z^2}} = 0. \tag{A.9}$$

This is the form of momentum conservation assumed in this work.

A self-consistent way to obtain a momentum conservation equation is to assume a profile which is structured, with a formal slip velocity at the boundary. Note that we don't mean molecular slip here.

A.3 Hughes and Lubliner Result

Return to equation A.4, before the introduction of the convective acceleration parameter, expand the time derivative.....

$$\bar{u_z}\frac{\partial}{\partial t}A + A\frac{\partial}{\partial t}\bar{u_z} + \frac{\partial}{\partial z}\left(\chi A\bar{u_z}^2\right) + \frac{A}{\rho}\frac{\partial \bar{p}}{\partial z} + \psi_p - \frac{2\pi\eta R(z)}{\rho\sqrt{1+R_x^2}}\left[\frac{\partial u_z}{\partial r}\right]_{\partial\Omega_L(z)} = 0. \tag{A.10}$$

...and use Equation A.2 to eliminate the area derivative

$$A\frac{\partial}{\partial t}\hat{u_z} - \bar{u_z}\left(\frac{\partial}{\partial z}A\bar{u_z} + \psi\right) + \frac{\partial}{\partial z}A\bar{u_z^2} + \frac{A}{\rho}\frac{\partial \bar{p}}{\partial z} + \psi_p - \frac{2\pi\eta R(z)}{\rho\sqrt{1+R_x^2}}\left[\frac{\partial u_z}{\partial r}\right]_{\partial\Omega_L(z)} = 0. \tag{A.11}$$

...expanding...

$$A\frac{\partial}{\partial t}\hat{u_z} - \bar{u_z}\frac{\partial}{\partial z}A\bar{u_z} - \bar{u_z}\psi + \frac{\partial}{\partial z}A\bar{u_z^2} + \frac{A}{\rho}\frac{\partial \bar{p}}{\partial z} + \psi_p - \frac{2\pi\eta R(z)}{\rho\sqrt{1+R_z^2}}\left[\frac{\partial u_z}{\partial r}\right]_{\partial\Omega_L(z)} = 0. \tag{A.12}$$

...and using the product rule (backwards) in the second term...

$$A\frac{\partial}{\partial t}\hat{u_z} - \frac{\partial}{\partial z}\left(A\bar{u_z}^2\right) + A\bar{u_z}\frac{\partial \bar{u_z}}{\partial z} - \bar{u_z}\psi + \frac{\partial}{\partial z}A\bar{u_z^2} + \frac{A}{\rho}\frac{\partial \bar{p}}{\partial z} + \psi_p - \frac{2\pi\eta R(z)}{\rho\sqrt{1+R_z^2}}\left[\frac{\partial u_z}{\partial r}\right]_{\partial\Omega_L(z)} = 0. \tag{A.13}$$

.....and grouping terms, we obtain.....

$$A\left(\frac{D\bar{u_z}}{Dt}\right) + \frac{\partial}{\partial z}\left(A(\bar{u_z^2} - \bar{u_z}^2)\right) + \frac{A}{\rho}\frac{\partial \bar{p}}{\partial z} - \bar{u_z}\psi + \psi_p - \frac{2\pi\eta R(z)}{\rho\sqrt{1+R_z^2}}\left[\frac{\partial u_z}{\partial r}\right]_{\partial\Omega_L(z)} = 0. \tag{A.14}$$

At this point, we re-introduce assumptions about the form of the velocity profile, but consistently this time. The profile of Fossan et al. [198] will serve (equation A.6). Accordingly, we loose the term ψ_p (as discussed above, any profile meeting the slip condition will have this effect) but we retain the term in ψ which was introduced from the volume conservation equation

$$A\left(\frac{D\bar{u_z}}{Dt}\right) + (\chi-1)\frac{\partial}{\partial z}A\bar{u_z}^2 + \frac{A}{\rho}\frac{\partial \bar{p}}{\partial z} - \bar{u_z}\psi + \frac{2\pi\eta(\zeta+2)\bar{u_z}}{\rho\sqrt{1+R_z^2}} = 0. \tag{A.15}$$

One final spot of faffing will suffice;

$$\left(\frac{D\bar{u_z}}{Dt}\right) + \frac{(\chi-1)}{A}\frac{\partial}{\partial z}A\bar{u_z}^2 + \frac{1}{\rho}\frac{\partial \bar{p}}{\partial z} = \frac{\bar{u_z}}{A}\left(\psi + \frac{2\pi\eta(\zeta+2)}{\rho\sqrt{1+R_z^2}}\right) \tag{A.16}$$

The latter is Hughes and Lubliner's result.

To further expose the difference between this and Olufson's formulation, let us set $\bar{u_z} = \frac{Q}{A}$ and multiply by A, whereupon the last equation becomes

$$A\frac{D}{Dt}\left(\frac{Q}{A}\right) + (\chi-1)\frac{\partial}{\partial z}\left(\frac{Q^2}{A}\right) + \frac{A}{\rho}\frac{\partial \bar{p}}{\partial z} = \frac{Q}{A}\left(\psi + \frac{2\pi\eta(\zeta+2)}{\rho\sqrt{1+R_z^2}}\right) \tag{A.17}$$

In the steady limit, replacing the material derivative with $\bar{u_z}\frac{\partial}{\partial z}$

$$Q\frac{\partial}{\partial z}\left(\frac{Q}{A}\right) + (\chi-1)\frac{\partial}{\partial z}\left(\frac{Q^2}{A}\right) + \frac{A}{\rho}\frac{\partial \bar{p}}{\partial z} = \frac{Q}{A}\left(\psi + \frac{2\pi\eta(\zeta+2)}{\rho\sqrt{1+R_z^2}}\right) \tag{A.18}$$

A.4 Viscous Boundary Force After Olufson

We consider Olufson's boundary force contribution to the momentum balance in order to assess the correct form of the surface element. The viscous force over the whole boundary is

given by the following contraction of the stress tensor evaluated at the boundary

$$\begin{aligned}\iint_{\partial\Omega}\sigma_{z\alpha}\hat{n}_\alpha dA = &-\iint_{\partial\Omega_i}\sigma_{zz}dA \\ &+\iint_{\partial\Omega_l}\left(\frac{\sigma_{zz}R_x+\sigma_{zr}}{\sqrt{1+R_z^2}}\right)dA \\ &+\iint_{\partial\Omega_o}\sigma_{zz}dA.\end{aligned} \tag{A.19}$$

Above, the Einstein convention is used. Substituting the symmetry-adapted expressions for the components of the stress [52] we straightforwardly obtain

$$\begin{aligned}\iint_{\partial\Omega}\sigma_{z\alpha}\hat{n}_\alpha dA = &-\iint_{\partial\Omega_i}\left(-p+2\eta\frac{\partial u_z}{\partial z}\right)dA \\ &+\iint_{\partial\Omega_l}\left(\frac{\left(-p+2\eta\frac{\partial u_z}{\partial z}\right)R_z+\eta\left(\frac{\partial u_z}{\partial r}+\frac{\partial u_r}{\partial z}\right)}{\sqrt{1+R_z^2}}\right)dA \\ &+\iint_{\partial\Omega_o}\left(-p+2\eta\frac{\partial u_z}{\partial z}\right)dA.\end{aligned} \tag{A.20}$$

Assuming there is no convective acceleration at the inlet and outlet and resolving the luminal integration we obtain

$$\begin{aligned}\iint_{\partial\Omega}\sigma_{z\alpha}\hat{n}_\alpha dA = &\iint_{\partial\Omega_i}pdA-\iint_{\partial\Omega_o}pdA \\ &+\int_0^L\left(\int_0^{2\pi}\frac{\left(-p+2\eta\frac{\partial u_z}{\partial z}\right)R_z+\eta\left(\frac{\partial u_z}{\partial r}+\frac{\partial u_r}{\partial z}\right)}{\sqrt{1+R_z^2}}Rd\theta\right)dz.\end{aligned} \tag{A.21}$$

Noting that $p(L,r)-p(0,r)=\int_0^L\frac{\partial}{\partial z}p(\xi,r)d\xi$ and that the integration limits are everywhere constant, we transform the pressure terms on the right hand side

$$\begin{aligned}\iint_{\partial\Omega}\sigma_{z\alpha}\hat{n}_\alpha dA = &-\int_0^L\left(\iint_{\partial\Omega_x}\frac{\partial p}{\partial\xi}dA\right)d\xi \\ &+\int_0^L\left(\int_0^{2\pi}\frac{\left(-p+2\eta\frac{\partial u_z}{\partial z}\right)R_z+\eta\left(\frac{\partial u_z}{\partial r}+\frac{\partial u_r}{\partial z}\right)}{\sqrt{1+R_z^2}}Rd\theta\right)dz.\end{aligned} \tag{A.22}$$

Finally, we retain terms to leading order in taper parameter, R_z and neglect the derivative $\frac{\partial u_r}{\partial z}$ relative to $\frac{\partial u_z}{\partial r}$

$$\iint_{\partial\Omega} \sigma_{z\alpha}\hat{n}_\alpha dA \approx -\int_0^L \left(\iint_{\partial\Omega_z} \frac{\partial p}{\partial \xi} dA\right) d\xi + 2\pi\eta \int_0^L \frac{\partial u_z}{\partial r} R\sqrt{1+R_z^2}^{-1} dz. \tag{A.23}$$

A.5 Numerical Scheme

For the sake of completeness we restate the 1D Navier-Stokes equations with leak accounting for vessel taper and slip

$$\begin{aligned}
&\frac{dQ}{dz} + \psi = 0,\ Q(z) = Q(0)\Big(\frac{A(z)}{A(0)}\Big)^{\frac{c}{2}},\\
&\frac{d}{dz}\Big(\delta\frac{Q^2}{A}\Big) + \frac{A}{\rho}\frac{dP}{dz} + \frac{2(\zeta+2)\pi\mu}{\rho}\frac{Q}{A}\left(1+\Big(\frac{dR}{dz}\Big)^2\right)^{-1/2} + \alpha\frac{Q}{A}\psi = 0,\\
&Q(0) = Q_0,\ P(0) = P_0,\ \alpha \in [0.4, 1.0],\ \delta = \frac{\zeta+2}{\zeta+1}
\end{aligned} \tag{A.24}$$

We now find the sink ψ in terms of area

$$\begin{aligned}
\psi &= -\frac{dQ}{dz} && \text{[By definition]}\\
&= -\frac{d}{dz}\left(Q_0\Big(\frac{A}{A_0}\Big)^{\frac{c}{2}}\right)\\
&= -\frac{Q_0}{A_0^{\frac{c}{2}}}\frac{c}{2}A^{\frac{c}{2}-1}\frac{dA}{dz}
\end{aligned} \tag{A.25}$$

using $K = \frac{2(\zeta+2)\pi\mu}{\rho}$, the momentum equation can be written as

$$\frac{d}{dz}\Big(\delta\frac{Q^2}{A}\Big) + \frac{A}{\rho}\frac{dP}{dz} + K\left(1+\Big(\frac{dR}{dz}\Big)^2\right)^{-1/2}\frac{Q}{A} + \alpha\frac{Q}{A}\psi = 0 \tag{A.26}$$

Expanding the derivative and subbing in the expression for ψ

$$-\delta Q^2 A^{-2}\frac{dA}{dz} + \delta\frac{2Q}{A}\frac{dQ}{dz} + \frac{A}{\rho}\frac{dP}{dz} + K\left(1+\Big(\frac{dR}{dz}\Big)^2\right)^{-1/2}\frac{Q}{A} - \alpha\frac{Q}{A}\frac{Q_0}{A_0^{\frac{c}{2}}}\frac{c}{2}A^{\frac{c}{2}-1}\frac{dA}{dz} = 0 \tag{A.27}$$

Using $Q = Q_0\Big(\frac{A}{A_0}\Big)^{\frac{c}{2}}$ and $\frac{dQ}{dz} = \frac{Q_0}{A_0^{\frac{c}{2}}}\frac{c}{2}A^{\frac{c}{2}-1}\frac{dA}{dz}$

$$-\delta Q_0^2 \frac{A^{c-2}}{A_0^c}\frac{dA}{dz} + \frac{2\delta Q_0}{A}\frac{A^{c/2}}{A_0^{c/2}}\frac{Q_0 c}{2A_0^{c/2}}A^{c/2-1}\frac{dA}{dz} + \frac{A}{\rho}\frac{dP}{dz} + \frac{KQ_0A^{c/2-1}}{A_0^{c/2}}\left(1+\left(\frac{dR}{dz}\right)^2\right)^{-1/2} - \alpha\frac{Q_0A^{c/2-1}}{A_0^{c/2}}\frac{Q_0 c}{2A_0^{c/2}}A^{c/2-1}\frac{dA}{dz} = 0 \tag{A.28}$$

Simplifying terms

$$-\delta Q_0^2 \frac{A^{c-2}}{A_0^c}\frac{dA}{dz} + \frac{\delta Q_0^2 c}{A_0^c}A^{c-2}\frac{dA}{dz} + \frac{A}{\rho}\frac{dP}{dz} + \frac{KQ_0A^{c/2-1}}{A_0^{c/2}}\left(1+\left(\frac{dR}{dz}\right)^2\right)^{-1/2} - \frac{\alpha Q_0^2 c}{2A_0^c}A^{c-2}\frac{dA}{dz} = 0 \tag{A.29}$$

Factorise a common $\frac{Q_0^2A^{c-2}}{A_0^c}\frac{dA}{dz}$ out

$$\frac{Q_0^2A^{c-2}}{A_0^c}\frac{dA}{dz}\left(-\delta+\delta c-\frac{\alpha c}{2}\right) + \frac{A}{\rho}\frac{dP}{dz} + \frac{KQ_0A^{c/2-1}}{A_0^{c/2}}\left(1+\left(\frac{dR}{dz}\right)^2\right)^{-1/2} = 0 \tag{A.30}$$

Divide and multiply through by A & ρ respectively

$$\frac{\rho Q_0^2A^{c-3}}{A_0^c}\frac{dA}{dz}\left(-\delta+\delta c-\frac{\alpha c}{2}\right) + \frac{dP}{dz} + \frac{\rho KQ_0A^{c/2-2}}{A_0^{c/2}}\left(1+\left(\frac{dR}{dz}\right)^2\right)^{-1/2} = 0 \tag{A.31}$$

Integrating the above between vessel segment x_i and x_{i+1}

$$\left(-\delta+\delta c-\frac{\alpha c}{2}\right)\frac{\rho Q_0^2}{A_0^c}\int_{x_i}^{x_{i+1}}A^{c-3}\frac{dA}{dz}dz + \int_{x_i}^{x_{i+1}}\frac{dP}{dz}dz + \frac{\rho KQ_0}{A_0^{c/2}}\int_{x_i}^{x_{i+1}}A^{c/2-2}\left(1+\left(\frac{dR}{dz}\right)^2\right)^{-1/2}dz = 0 \tag{A.32}$$

Utilise that $\int A^{c-3}\frac{dA}{dz}dz = \frac{A^{c-2}}{c-2}$

$$\left(-\delta+\delta c-\frac{\alpha c}{2}\right)\frac{\rho Q_0^2}{(c-2)A_0^c}\left(A_{i+1}^{c-2}-A_i^{c-2}\right) + P_{i+1} - P_i + \frac{\rho KQ_0}{A_0^{c/2}}\int_{x_i}^{x_{i+1}}A^{c/2-2}\left(1+\left(\frac{dR}{dz}\right)^2\right)^{-1/2}dz = 0 \tag{A.33}$$

Writing A_{i+1}^{c-2} as $\frac{A_{i+1}^{c}}{A_{i+1}^{2}}$ and utilising

$$Q = Q_0 \frac{A^{c/2}}{A_0^{c/2}}, K = \frac{2(\zeta+2)\pi\mu}{\rho} \tag{A.34}$$

Simplifying terms

$$\begin{aligned}\left(-\frac{\delta\rho}{c-2}+\frac{\rho\delta c}{c-2}-\frac{\rho\alpha c}{2(c-2)}\right)\left(\frac{Q_{i+1}^2}{A_{i+1}^2}-\frac{Q_i^2}{A_i^2}\right)+P_{i+1}-P_i \\ +2(\zeta+2)\pi\mu\int_{x_i}^{x_{i+1}}\frac{Q}{A^2}\left(1+\left(\frac{dR}{dz}\right)^2\right)^{-1/2}dz=0\end{aligned} \tag{A.35}$$

We will aim for a formulation in terms of vessel area

$$\begin{aligned}&A=\pi R^2 \rightarrow R=\frac{A^{1/2}}{\pi^{1/2}} \\ &\left(\frac{dR}{dz}\right)^2=\left(\frac{d}{dz}\left(\frac{A^{1/2}}{\pi^{1/2}}\right)\right)^2=\left(\frac{A^{-1/2}}{2\pi^{1/2}}\frac{dA}{dz}\right)^2=\frac{A^{-1}}{4\pi}\left(\frac{dA}{dz}\right)^2\end{aligned} \tag{A.36}$$

Write to clearly identify the inertia and viscous terms. All in terms of area and flow.

$$\begin{aligned}P_i-P_{i+1}=\rho\left[\frac{2\delta(c-1)-\alpha c}{2(c-2)}\right]\left(\frac{Q_{i+1}^2}{A_{i+1}^2}-\frac{Q_i^2}{A_i^2}\right) \\ +2(\zeta+2)\pi\mu\int_{x_i}^{x_{i+1}}\frac{Q}{A^2}\left(1+\frac{1}{4\pi A}\left(\frac{dA}{dz}\right)^2\right)^{-1/2}dz\end{aligned} \tag{A.37}$$

Applying the trapezoidal rule we obtain a computational scheme of:

$$\begin{aligned}\Delta P_i &= \rho\left[\frac{2\delta(c-1)-\alpha c}{2(c-2)}\right]\left(\frac{Q_{i+1}^2}{A_{i+1}^2}-\frac{Q_i^2}{A_i^2}\right) \\ &+\pi\mu(\zeta+2)\Delta z\left[\frac{Q_{i+1}}{A_{i+1}^2}\left(1+\frac{1}{4\pi A_{i+1}}\left(\frac{A_{i+2}-A_{i+1}}{\Delta z}\right)^2\right)^{-1/2}\right. \\ &\left.+\frac{Q_i}{A_i^2}\left(1+\frac{1}{4\pi A_i}\left(\frac{A_{i+1}-A_i}{\Delta z}\right)^2\right)^{-1/2}\right] \\ P_{i+1} &= P_i-\Delta P_i\end{aligned} \tag{A.38}$$

Where Δz is each vessel segment length. This numerical scheme is valid for the healthy parts of the vessel.